ULTRASONIC PROCESSING OF ALUMINIUM ALLOY MELTS

Ph.D. THESIS

by

NEERAJ SRIVASTAVA

DEPARTMENT OF METALLURGICAL AND MATERIALS ENGINEERING
INDIAN INSTITUTE OF TECHNOLOGY ROORKEE
ROORKEE – 247667, INDIA
APRIL, 2018

ULTRASONIC PROCESSING OF ALUMINIUM ALLOY MELTS

A THESIS

Submitted in partial fulfilment of the requirements for the award of the degree

of

DOCTOR OF PHILOSOPHY

in

METALLURGICAL AND MATERIALS ENGINEERING

by

NEERAJ SRIVASTAVA

DEPARTMENT OF METALLURGICAL AND MATERIALS ENGINEERING
INDIAN INSTITUTE OF TECHNOLOGY ROORKEE
ROORKEE – 247667, INDIA
APRIL, 2018

INDIAN INSTITUTE OF TECHNOLOGY ROORKEE
ROORKEE

CANDIDATE'S DECLARATION

I hereby certify that the work which is being presented in the thesis entitled **"ULTRASONIC PROCESSING OF ALUMINIUM ALLOY MELTS"** in partial fulfilment of the requirements for the award of the degree of Doctor of Philosophy and submitted in the Department of Metallurgical and Materials Engineering, Indian Institute of Technology Roorkee, Roorkee is an authentic record of my own work carried out during the period from July, 2012 to April, 2018 under the supervision of Dr. G. P. Chaudhari, Associate Professor, Department of Metallurgical and Materials Engineering, Indian Institute of Technology Roorkee, Roorkee.

The matter presented in this thesis has not been submitted by me for the award of any other degree of this or any other Institution.

(NEERAJ SRIVASTAVA)

This is to certify that the above statement made by the candidate is correct to the best of my knowledge.

(**G. P. Chaudhari)**
Date: ___/___/_____ **Supervisor**

The Ph.D. Viva-Voce Examination of **Mr. NEERAJ SRIVASTAVA**, Research Scholar, has been held on……...

Chairman SRC **Signature of External Examiner**

This is to certify that the student has made all the corrections in the thesis.

Signature of Supervisor **Head of Deptt/Chairman ODC**

ABSTRACT

Grain refinement from solidification processing is an effective and inexpensive method of obtaining improved mechanical properties in light alloys. The combined effect of solute and ultrasound-assisted solidification technique can play a vital role in grain refinement of cast aluminium alloys. A systematic experimental study has been made of the combined influence of solute content (1 wt.%, 2 wt.%, 3 wt.%, and 5 wt.%) and ultrasonic intensity (0, 88, 350, 790, 1400 W/cm^2) on grain refinement of Al-Si, Al-Cu and Al-Ni binary alloys. The results indicate that the grain refinement in Al-3wt.%Ni alloy is larger than Al-3wt.%Si alloy with application of ultrasonic treatment although the growth restriction factor value of silicon (Si) solute is higher than nickel (Ni) solute in pure aluminium. These observations prompted the investigation regarding the grain refinement mechanisms in aluminium based hypoeutectic alloys. For that, the grain refining efficiency of different solutes was analyzed using various factors such as the freezing range (ΔT), StJohn's model and constitutional supercooling parameter (P). The mechanisms for ultrasonic grain refinement of aluminium alloys are discussed based on experimental findings. Ultrasonication resulted in more activated nucleants in Al-Cu alloys than in Al-Si and Al-Ni alloys by the StJohn's model. In particular, high solute content can ensure achievement of homogeneous and consistent grain morphology in ultrasonic grain refinement. In addition, excellent grain refinement was achieved in both the Al-5wt.%Cu alloy which has an equilibrium freezing range of 100ºC and the Al-5wt.%Ni alloy which has an equilibrium freezing range of just 5ºC at the same applied ultrasonic intensity (1400 W/cm^2). Constitutional supercooling parameter truly explains the grain refinement mechanism in Al-Ni alloys with ultrasonic treatment (UST), which have near-eutectic compositions as compared to the Al-Cu and Al-Si alloys studied. Evidently, such discrepancy in average grain size with content of solute cannot be completely described by using growth restriction factor (Q), ΔT, and P values alone. A combination of high solute content and high ultrasonic intensity produces significant grain refinement, including significant refinement of eutectic structures that formed in the Al-5wt.%Si alloy, Al-5wt.%Cu alloy and Al-5wt.%Ni alloy. UST enhanced the mechanical properties of USTed aluminium alloys as compared to respective as-cast aluminium alloys.

Effect of temperatures of high power ultrasonic processing temperature (700°C, 725°C, 750°C, and 775°C) on the distribution of 1 wt.% Al_2O_3 nano-particles in Al6061 alloy melt is studied. Al6061 alloy composites are fabricated by varying the weight percentage (1, 2 and 3 wt.%) of Al_2O_3 nano-particles at ultrasonic processing temperature of 775°C. From the microstructural examination, it is observed that nano particles are better dispersed in the alloy matrix with increasing ultrasonic processing temperature. Some agglomerated reinforcement particles are seen at lower ultrasonic processing temperature of 700°C. As compared to the base alloy, mechanical properties like hardness, 0.2% offset yield strength, and ultimate tensile strength increased significantly with processing temperature. This is attributed mainly to the coefficient of thermal expansion mismatch between the alloy matrix and the Al_2O_3 particles, followed by Orowan strengthening, and to a lesser extent to the Hall–Petch strengthening mechanism.

UST of the melt resulted in better dispersion of Al_2O_3 particles up to 2 wt.% additions. Al6061-2wt.%Al_2O_3 composite showed good mechanical properties with yield strength and ultimate tensile strength values, which are 81% and 53% higher than the base alloy. Al6061-3wt.%Al_2O_3 composite showed poor yield strength and ultimate tensile strength as compared to Al6061-1wt.%Al_2O_3 and Al6061-2wt.%Al_2O_3 composites due to agglomeration of particles. A comparison is made between the experimental yield strengths of the nano composites and the theoretical yield strengths calculated by coefficients of thermal expansion mismatch, Hall-patch, load bearing effect and Orowan strengthening models.

The proposed thesis consists of seven chapters:

Chapter 1 contains a brief introduction to aluminium alloys and different techniques used for increasing the mechanical properties of aluminium alloys from grain refinement and other strengthening routes.

Chapter 2 gives a comprehensive literature review on grain refinement of as-cast and with UST aluminium alloys. It summarizes the effect of content of solute, nano-particles and ultrasonic intensity on microstructure and mechanical properties of aluminium alloys as given in open literature. It contains brief theory of solidification, effects of ultrasound in molten metals and an overview of strengthening mechanisms. It also defines objectives of the present work based on the literature review, scope of the work and the methodology adopted in the present investigation.

Chapter 3 deals with the details of experimental procedure carried out in line with the scope of the work. The procedures of specimen preparation for microstructural studies (scanning electron

microscopy, optical microscopy and transmission electron microscopy) and mechanical testing (hardness and tensile test) are explained.

Chapter 4 deals with effect of the combined influence of solute content (1 wt.%, 2 wt.%, 3 wt.%, 5 wt.%) and ultrasonic intensity (0, 88, 350, 790, 1400 W/cm^2) on grain refinement of Al-Si, Al-Cu and Al-Ni binary alloys. The resulting microstructure of each aluminium alloy is characterized and the combined effect of solute content and UST is discussed.

Mechanisms for ultrasonic grain refinement of aluminium alloys are discussed in **Chapter 5**. Grain refining efficiency of different solutes is analyzed using the StJohn's model, ΔT, and P. All these factors are calculated from conventional technique and Scheil-Gulliver solidification simulation.

Chapter 6 deals with the effect of UST on the eutectic phase and mechanical properties (hardness and tensile strength) of the Al-Si, Al-Cu and Al-Ni binary alloys of varying solute contents (1 wt.%, 2 wt.%, 3 wt.%, 5 wt.%).

In Chapter 7, the effect of temperature of high power ultrasonic processing (700ºC, 725ºC, 750ºC, and 775ºC) on the distribution of 1wt.% Al_2O_3 nano-particles in Al6061 alloy melt is studied. Al6061 alloy is also fabricated with varying the content of nanoparticles (2 and 3 wt.%) at ultrasonic processing temperature of 775ºC. The microstructural features and mechanical properties of nano composites are characterized. Various strengthening mechanisms in the ultrasonically processed nano composites are analyzed.

Eighth and ninth chapters deal with conclusions and scope for future work, respectively.

ACKNOWLEDGEMENT

Sometimes words are not enough to say the thoughts or feelings but if anyone shares them, it becomes the cause of his cordial happiness, which spreads.

First, I would like to express my deepest gratitude, sincere thanks and acknowledgement to my respected supervisor Dr. G. P. Chaudhari, Associate Professor, Department of Metallurgical and Materials Engineering, Indian Institute of Technology Roorkee, for showing his faith in me and giving me the wonderful opportunity of doing research under his supervision. His thorough knowledge, invaluable advices, indelible inspiration, constant encouragement, constructive criticism, and persistent support has shaped this thesis to its present form. His guidance helped me in all the time of research and writing of this thesis. To him, I shall remain, professionally and emotionally obliged. I could not have imagined having a better advisor and mentor for my Ph.D. work then him.

I am grateful to the respected committee members Prof. Ujwal Prakash, Prof. P.K. Ghosh, Prof. S.K. Nath, Prof. B.S.S. Daniel, and Dr. Inderdeep Singh for sparing their valuable time in monitoring the work progress and providing imperative comments and precious suggestions from time to time, which helped me, a lot.

Respected Prof. Anjan Sil (Head, Department of Metallurgical and Materials Engineering) is gratefully acknowledged for providing me the necessary research facilities and important ambience to complete this work. I would also like to thank Prof. M. Qian, R.M.I.T. University, Australia, for his valuable comments and suggestions throughout my research work. I thank all the faculty members of the Department of Metallurgical and Material Engineering and non – teaching staff, Mr. R.K. Sharma, Mr. Rajendra Sharma, Mr. Kuldeep Sharma, Mr. Naresh Sharma, and Mr. Sukhmal Giri for generously providing me the guidance and various research related resources on time.

Thanks are also due to my seniors, colleagues and friends Dr. Pramod P. Bhingole, Dr. Ashish W. Selokar, Dr. Amarendra, Dr. Sunil Rajput, Dr. Brij Kishore, Dr. Sanjeev Kumar, Dr. Surya Deo, Dr. Gajendra, Dr. Abhishek Rajput, Dr. Sandan Sharma, Rahul Gupta, Dr. Vijay

Sharma, Himanshu Kala, Guru Praksah, Aniruddha Malakar, Nitin, Nitesh, Manoj, Abhishek, Anuj, Vishal for making my stay a pleasant experience.

I cannot thank enough to my parents, Late Shri. S. D. Srivastava and Smt. Shushila Devi, and my brother and bhabi Shri. Ajai Srivastava & Smt. Ruchi Srivastava, Shri. Vineet Srivastava & Smt. Roli Srivastava, Shri. Jitendra Srivastava & Smt. Pooja Srivastava and my heart loving nephews and nieces, for their support both morally and spiritually, and for their patience, love, guidance, encouragement, and prayers during this research period. Special thanks to my soul mate and wife Nishi Srivastava for her support and love that I cannot express in my words.

Above all, to the Great Almighty, the author of knowledge and wisdom, for His everlasting love and strength that He bestowed upon me throughout this journey.

Neeraj Srivastava

Date:___/____/_____

TABLE OF CONTENT

LIST OF FIGURES

LIST OF TABLES

LIST OF ABBREVIATIONS AND SYMBOLS

TiB_2	Titanium Diboride
Zr	Zirconium
Q	Growth restriction factor
Al	Aluminium
Nb	Niobium
V	Vanadium
Si	Silicon
Cu	Copper
Ni	Nickel
Mg	Magnesium
B	Boron
Fe	Iron
C	Carbon
Cr	Chromium
Sc	Scandium
Mn	Manganese
Zn	Zinc
UST	Ultrasonic treatment
α-Al	Primary phase of aluminium
Ti	Titanium
W	Tungsten
atm	atmospheric pressure
K	Kelvin
wt.%	Weight percentage
vol.%	Volume percentage
°C	Degree Celsius
CTE	Coefficient of thermal expansion
G	Gibbs free energy
H	Enthalpy

T	Absolute temperature
S	Entropy
G_l	Free energy of liquid
G_s	Free energy of solid
ΔG	Free energy change for a liquid to solid transformation
T_m	Melting point of the metal
U	Net energy change
γ_{SL}	Surface energy between the solid and liquid
γ_{NS}	Surface energies between the nucleating surface and solid
γ_{NL}	Surface energies between the nucleating surface and liquid
ΔH	Latent heat of fusion per unit volume
r^*	Critical radius
θ	Wetting angle
ΔT	Undercooling
Δs_f	Entropy of fusion
m	Liquidus slope
k	Partition coefficient
C_0	Alloy composition in binary alloy
P	Supercooling parameter
ΔT_c	Constitutional undercooling
f_s	Fraction of solid
RGS	Relative grain size
d	Grain size
a	Potency of solute
b	Number of active nucleants
K/s	Kelvin per second
USTed	Ultrasonically treated
µm	Micro Meter
kW	Kilowatt
MMCs	Metal matrix composites

Al_2O_3	Alumina
B_4C	Boron Carbide
SiC	Silicon Carbide
TiC	Titanium Carbide
nm	Nano Meter
P/M	Powder metallurgy
P	Pressure
V_L	Specific volume of liquid phase
V_S	Specific volumes of solid phase
P_d	Pressure required for the fragmentation of crystals
σ_{mp}	Strength of the material near the melting point
H_2	Hydrogen
f	Frequency
ρ	Density of molten metal
c	Speed of sound
A	Amplitude
I	Ultrasonic intensity
mm	Millimeter
NC700	One weight percentage of nano-sized alumina were fabricated at temperature of 700ºC using ultrasonic treatment
NC725	One weight percentage of nano-sized alumina were fabricated at temperature of 725ºC using ultrasonic treatment
NC750	One weight percentage of nano-sized alumina were fabricated at temperature of 750ºC using ultrasonic treatment
NC775	One weight percentage of nano-sized alumina were fabricated at temperature of 775ºC using ultrasonic treatment
NC775MS	One weight percentage of nano-sized alumina were fabricated at temperature of 775ºC using manual stirring
2NC775	Two weight percentage of nano-sized alumina were fabricated at temperature of 775ºC using ultrasonic treatment

3NC775	Three weight percentage of nano-sized alumina were fabricated at temperature of 775ºC using ultrasonic treatment
SEM	Scanning electron microscope
TEM	Transmission electron microscope
EBSD	Electron back scattered diffraction
kV	kilovolt
EDS	Energy dispersive X-ray spectroscopy
XRD	X-ray diffraction
kg	Kilogram
Q_T	Growth restriction factor value obtained from using the Scheil-Gulliver solidification simulation
C_m	Maximum solubility of solute in liquid
C_e	Eutectic composition of alloy
H	Hardness
1Si	as-cast Al-1wt.%Si
2Si	as-cast Al-2wt.%Si
3Si	as-cast Al-3wt.%Si
5Si	as-cast Al-5wt.%Si
1Cu	as-cast Al-1wt.%Cu
2Cu	as-cast Al-2wt.%Cu
3Cu	as-cast Al-3wt.%Cu
5Cu	as-cast Al-5wt.%Cu
1Ni	as-cast Al-1wt.%Ni
2Ni	as-cast Al-2wt.%Ni
3Ni	as-cast Al-3wt.%Ni
5Ni	as-cast Al-5wt.%Ni
1Si-UST	Ultrasonically treated Al-1wt.%Si
2Si-UST	Ultrasonically treated Al-2wt.%Si
3Si-UST	Ultrasonically treated Al-3wt.%Si
5Si-UST	Ultrasonically treated Al-5wt.%Si
1Cu-UST	Ultrasonically treated Al-1wt.%Cu

2Cu-UST	Ultrasonically treated Al-2wt.%Cu
3Cu-UST	Ultrasonically treated Al-3wt.%Cu
5Cu-UST	Ultrasonically treated Al-5wt.%Cu
1Ni-UST	Ultrasonically treated Al-1wt.%Ni
2Ni-UST	Ultrasonically treated Al-2wt.%Ni
3Ni-UST	Ultrasonically treated Al-3wt.%Ni
5Ni-UST	Ultrasonically treated Al-5wt.%Ni
$\sigma_{0.2}$	Yield stress
UTS	Ultimate tensile strength
V_p	Volume fraction of nano-particles
η_m	Viscosity of molten matrix
η_c	Viscosity of composite
R	Universal gas constant
σ_{sv}	Surface energy of solid in vapor phase
σ_{lv}	Surface energy of liquid in vapor phase
σ_{sl}	Surface energy of solid in liquid phase
$\Delta\sigma_{Hall-Petch}$	Increment of yield strength of composite due to grain refinement strengthening mechanism
$\triangle\ \sigma_{Orwan}$	Increment of yield strength of composite due to Orowan strengthening mechanism
λ	Average inter-particle spacing
D	Average diameter of nano-particles
G	Shear modulus
b	Burgers vector
$\triangle\ \sigma_{CTE}$	Increment of yield strength of composite due to thermal mismatch strengthening mechanism
$\Delta\sigma_{LOAD}$	Increment of yield strength of composite due load bearing strengthening mechanism
$\Delta\alpha$	Difference in CTE between the matrix and the reinforcing particles

ΔT	Difference between stress free homologous temperature and room temperature
σ_m	Yield strength of the base alloy
$\sigma_{y,c}$	Yield strength of the composite

CHAPTER 1

INTRODUCTION

Aluminium alloys are widely employed in automobile and aerospace industries because of their lightweight, good strength, excellent corrosion resistance, and low cost [1–4]. In addition, Al alloys are easy to recycle from scrap thereby reducing the greenhouse gas emissions [5–7]. Grain refinement is a useful technique for aluminium alloys for enhancing the mechanical properties and quality of metal castings [8,9]. A fine and uniform grain structure imparts good yield strength, high toughness, and improved machinability [10,11]. Various techniques have been used for grain refinement of the aluminium alloys. These techniques depend upon the processing temperature. Therefore, these can be classified into three categories- cryogenic temperature processing, room temperature processing, and solidification processing.

In solidification processing, grain refinement can be achieved by increasing thermal undercooling through increasing cooling rates, constitutional undercooling through addition of selected solute elements, or by increasing the number of effective heterogeneous nuclei through inoculation [12,13]. Earlier research mainly focused on the grain refinement of peritectic based aluminium alloy systems due to better grain refinement results observed in these alloys [13–16]. For example, adding TiB_2 [17] and zirconium [18] into pure aluminium significantly reduced the grain size of as-cast aluminium. It is observed that driving force for nucleation is larger in peritectic based aluminium alloys as compared to eutectic-based aluminium alloys at similar value of growth restriction factor (Q) and undercooling. As a result, finer microstructures are observed in peritectic based aluminium alloys [19]. Wang et al. [18] observed that addition of peritectic forming zicronium, niobium, and vanadium solutes significantly reduced the average grain size of as-cast aluminium. On the other hand, the grain refining efficiency is poor for silicon, copper and magnesium containing eutectic-based alloys having a similar values of growth restriction factor (Q) [20]. Among the eutectic aluminium alloys, it was reported that the grain refinement in Al-Mg alloys is larger as compared to Al-Si and Al-Cu alloys at the similar values of growth restriction factor (Q) [21,22]. Various methods have been employed during solidification for grain refinement of alloys, including rheocasting, inoculation, and physical

methods such as mechanical stirring, electromagnetic vibrations, and use of ultrasound vibrations [23–27]. Wang et al. observed that the nucleation efficiency of eutectic alloys can be changed with the application of UST [28]. UST can refine the grain structure of hypoeutectic alloys, which can give superior mechanical properties and these alloys can be used in automobile and structural applications.

The chief possible influences of UST on the properties of as cast materials are [27,29–31]:

1. Decrease in grain size and primary & secondary arm spacing;
2. Promotion of columnar to equiaxed transition;
3. Influence on the size, amount, and distribution of secondary phases;
4. Promotion of uniformity in the dispersion of non-metallic inclusions and particles;
5. Reduction in dendritic segregation and enhancement in the material homogeneity;

A number of studies have focused on UST of aluminium alloy melts. Puga et al. observed that the grain morphology of cast AlSi9Cu3 alloy changed from dendritic to globular upon UST and the grain size of α-Al decreased significantly from 700 μm to 41μm [32]. Feng et al. showed that the dendritic morphology of the primary α-Al in Al-23%Si alloy changed to the equiaxed one after the UST [33]. Jian et al. obtained a globular and refined microstructure in A356 alloy by UST [34]. Tuan et al. showed that applying UST at 720°C resulted in a uniform grain structure in an Al-Mg-Sc alloy [35]. Atamanenko et al. studied the effect of UST in both the liquid state and the semisolid state in Al-Cu, Al-Zr-Ti and Al-Zr-V alloys. Ultrasonic refinement of these alloys depended on the amplitude of the sonotrode, UST time, and volume of the melt [16]. Das and Kotadia demonstrated that the α-Al phase in LM6 alloy can be modified into globular grains by UST [36]. Li et al. observed that UST refined the microstructure of Al-1%Si alloy (herein all compositions are given in wt.%) [24]. Recently, Wang et al. showed that there is no effect of UST on grain refinement of Al-2%Cu alloy, when the UST is applied above the liquidus temperature [37]. This finding suggests that ultrasonic grain refinement occurs within the liquidus-solidus range. Accordingly, the freezing range of an alloy can be an important factor that affects ultrasonic grain refinement.

Another method of improving the mechanical properties of aluminium alloys is by adding micron size and nano-sized particles in aluminium alloys [38,39]. Generally micron sized particles are used to enhance the yield strength and ultimate tensile strength of the aluminium alloy matrix, but the ductility of the composite degrades significantly [40]. As compared to

micron size particles, nano particle reinforcements can improve the mechanical properties more efficiently from particle strengthening mechanisms while retaining good ductility [41,42]. Nano-sized spheres reduce the critical solidification velocity for particle engulfment and thus provide better dispersion [43,44].

In literature, there are two efficient methods for adding the nano-particles in metal matrix via solid-state processing (e.g. powder metallurgy) and liquid-state solidification processing [45,46]. In the powder metallurgy method, high shear stress is used to shear the clusters of nano-particles, which is produced by high-energy ball milling [45,47]. Powder metallurgy method can be used to disperse low volume fraction of nano-particles reinforcement (< 2 vol. %) in the metal matrix. However, when the volume fraction of nano-particles reinforcement in metal matrix is greater than 2 vol.%, the agglomeration and non-uniform distribution of particles is observed by increasing the duration of high-energy ball milling [47,48].

There are also major challenges in reinforcement of the nano-particles via liquid state solidification processing. These are [45,49]:

1. Non-oxide nano-sized reinforcements easily degrade or oxidize when nano-particles are introduced into the molten metal at high temperature.
2. Nano-sized reinforcements has tendency to float into the melt due to the poor wettability of the nano-sized reinforcements with the molten metal.
3. Nano-sized reinforcements tend to form agglomerates or clusters in molten metal due to the lack of a repulsive force and attractive Van der Waals force.
4. In solidification, nano-sized reinforcements are generally pushed to the grain boundary by solidification fronts.

Due to above challenges, a uniform dispersion of nano-sized reinforcement in metal matrix is less observed by solidification processing even in specimens with a low content of nano-sized reinforcement in literature [45]. In literature, various processing methods for reinforcing the nano-sized particles in aluminium alloys matrix have been examined via solidification processing method. Yang et al. added SiC nano-particles to A356 alloy using an ultrasonic assisted casting method, wherein the ultrasonic nonlinear effects helped in efficiently dispersing the SiC nano-particles in the A356 alloy matrix [40]. Sajjadi et al. used a stir casting technique to disperse nano-sized alumina particles in pure aluminium matrix [50]. Akbari et al. fabricated the A356/1.5 vol.% nano-Al_2O_3 reinforced composite by stir casting technique. The

tensile properties of the composites enhanced as compared to the base alloy [51]. Ezatpour et al. investigated the influences of reinforcing alumina nano-particles (0.5, 1 and 1.5 wt.%) to Al6061 alloy using the stir casting method [52]. Sajjadi et al. observed the microstructure evolution and mechanical properties of A356 alloy/Al_2O_3 composites using stir and compo-casting techniques [53]. Su et al. fabricated the Al/Al_2O_3 nano-composites using ultrasonic solidification technique [54]. Mula et al. investigated the mechanical properties of Al–2%Al_2O_3 nano-composite using non-contact ultrasonic solidification technique [54].

Stir casting is an established, economical, most productive and industrially feasible method for fabricating aluminium alloy composites [53,55]. However, it is ineffective in dispersing the nano particles uniformly in metal matrix due to poor wetting of the nano particles by the molten metal, and formation of clusters of nano particles in molten metal from the Van der Waals attraction force [40,56]. For overcoming these difficulties, it is suggested that ultrasound assisted solidification is a promising method. High intensity shock waves generated by UST break the clusters of nano particles and improve the wettability thereby ensuring their uniform dispersion in the melt [40,54,57,58].

As discussed earlier, both the UST and the solute content affect the microstructural evolution during solidification in aluminium alloys. However, a systematic study of the combined effect of solute content and UST in aluminium alloys is lacking in literature (a study on Mg alloys was reported by Qian et al. in 2010 [59]). In this research, the grain refinement in Al-Si, Al-Cu and Al-Ni alloys is studied by varying the respective solute content (1%, 2%, 3% and 5%) and the applied ultrasonic intensity (88, 350, 790 and 1400 W/cm^2). The resulting microstructure of each aluminium alloy is characterized and the combined effect of solute content and UST is discussed. The resulting grain structure with the application of UST in binary aluminium alloys is studied in light of well-established grain refinement theories. Effect of UST on the eutectic phase and mechanical properties of aluminium alloys is also investigated.

Temperature of the melt and content of reinforcement play an important role in particle dispersion [54]. There is little work on the dispersion of nano-particles in aluminium alloys from ultrasonic solidification technique at different processing temperatures. Therefore, there is a need to study the effect of ultrasonic processing temperature on the incorporation and dispersion of nano particles, and the resultant inter-particle spacing in the composites. In this research, ultrasound assisted solidification is used to fabricate Al6061-1wt.%Al_2O_3 composites by varying

the processing temperatures (700°C, 725°C, 750°C, and 775°C). Microstructural and mechanical properties of composites are studied. Al6061 alloy composites reinforced with three weight fractions (1, 2, and 3 wt.%) of alumina nano-particles are also fabricated with UST at ultrasonic processing temperature of 775ºC and effect of nano-particles on the microstructure and tensile properties of aluminium alloy composites is studied. Effect of various mechanisms i.e. Orowan strengthening, Hall-Petch strengthening, and coefficient of thermal expansion (CTE) mismatch between the matrix and the particles on the strengthening of the composites is analyzed. To estimate the theoretical yield strength of composites, different strengthening models are used. The experimental and theoretical yield strength of composites is compared.

CHAPTER 2

LITERATURE REVIEW

This chapter gives a comprehensive literature review on basic theories/models of solidification, the effect of solute content on the grain refinement of as-cast and USTed aluminium alloys and studies involving processing methods that are best for dispersing the nano-particles in aluminium alloy melts. It also defines objectives of the present work based on the literature review, scope of the work and the methodology adopted in the present investigation.

Microstructures consisting of fine equiaxed grains generally exhibit a combination of good strength and good ductility [60,61]. Further, if an alloy solidifies with the globular grained structure, it has many benefits including isotropic microstructure and properties, less micro-segregation, and reduced tendency of hot tearing susceptibility, enhanced resistance to corrosion, and enhancement of mechanical properties [16,62,63]. Thus, grain size reduction is an easy and inexpensive way to enhance the mechanical properties of aluminium alloys [64]. Many techniques are used to achieve grain refinement in aluminium alloys.

Among the solidification processing methods, the basic mechanism and models for grain refinement are described here:

2.1. Grain Refinement Theories/ Models

`For last 50 years, many theories and models are reported for understanding the grain nucleation and growth mechanisms in solidification of light alloys [65]. These models and theories are deliberated here.

2.1.1. Classical Nucleation theory

2.1.1.1. Nucleation and Growth Mechanisms

A phase system is characterized by Gibbs *free energy,* which is *represented in* the equation 2.1.

$$G = H - TS \ldots\ldots\ldots\ldots\ldots\ldots\ldots\ldots\ldots \quad (2.1)$$

Where H is the enthalpy, T *is* the absolute temperature, and S is the entropy.

For any phase, *G* varies with *T* as shown in Figure 2.1 that shows the variation of *G* for a pure metal with respect to *T*.

Phase transformations in the system are indicated when the lines for two states (parent and product phase) cross each other: a system can decrease its free energy *G* by shifting to the lower line. The free energy difference between the lines is called the *driving force,* as shown in Figure 2.1. G_l and G_s denote the free energy of liquid and solid for pure metals respectively. The free energy change (ΔG) for a liquid to solid transformation is depend up-on the melting point (T_m) of the metal [65].

Above T_m, $\Delta G > 0$;

at T_m, $\Delta G = 0$;

below T_m, $\Delta G < 0$.

Nucleation and growth are two steps in the transformation of phase. When $\Delta G < 0$, very tiny particles are formed due to thermal fluctuations that will not be dissolved in the parent matrix. This is called nucleation. In growth, size of the particles is increased.

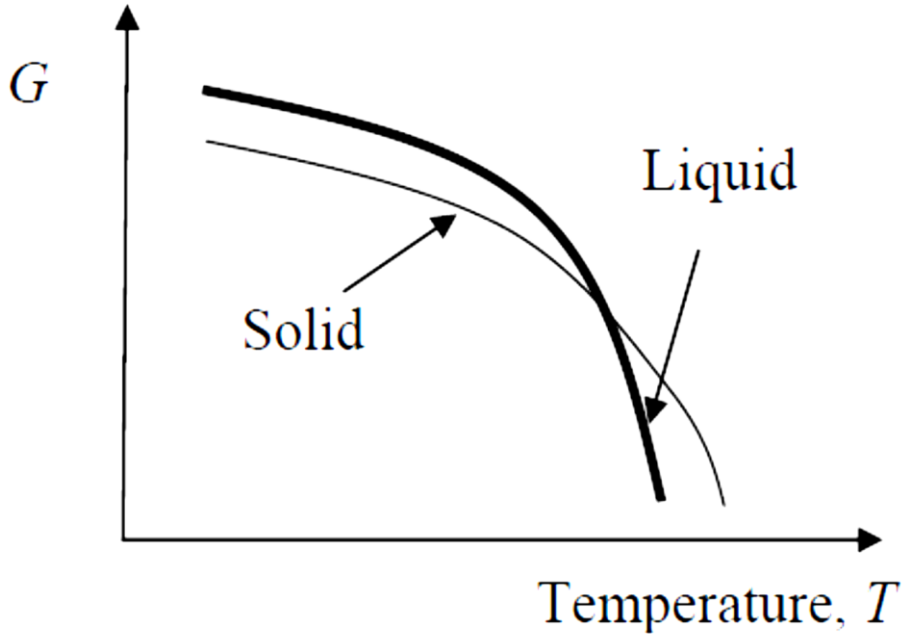

Figure 2.1. Free energy change between solid to liquid [65].

2.1.1.2. Homogeneous Nucleation

In homogeneous nucleation, the probability of nucleation remains constant throughout the volume of the parent phase. In other words, homogeneous nucleation occurs below the

liquidus temperature of the pure metal at a given volume. According to equation 2.2, change in internal energy (U) can be represented in terms of surface energy and volume free energy for spherical as shown in Figure 2.2 [65,66].

Net energy change = Volume free energy + Surface energy

$$U = \frac{4}{3}\pi r^3 \Delta G + 4\pi r^2 \Upsilon_{SL} \ldots\ldots\ldots\ldots\ldots\ldots \quad (2.2)$$

where ΔG is driving force for solidification, r is the radius of spherical particles and Υ_{SL} is the specific surface energy.

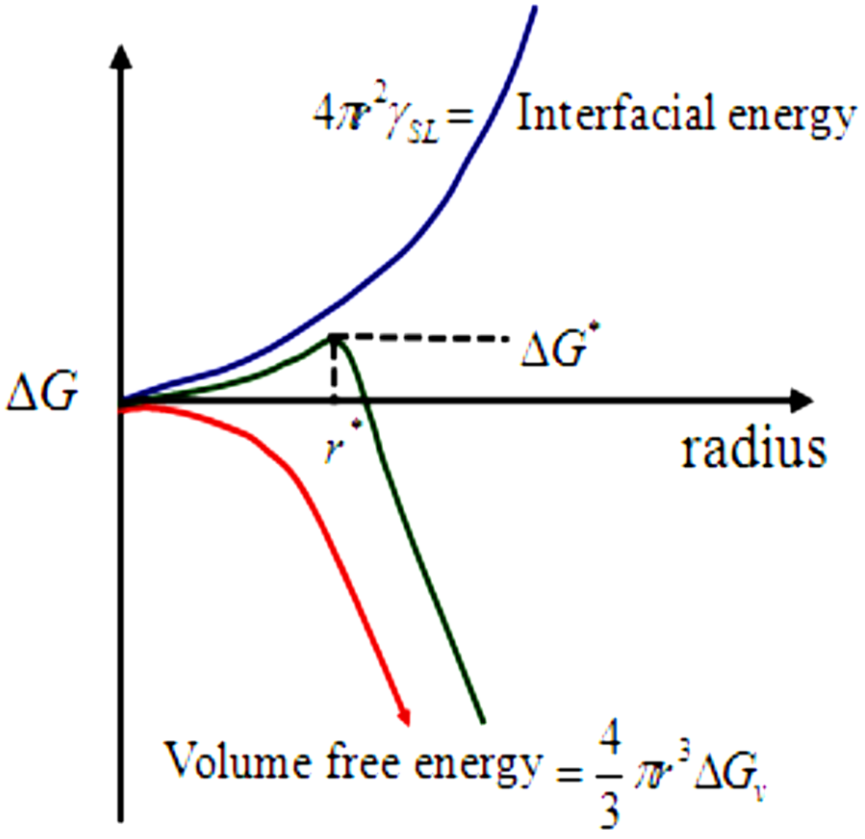

Figure 2.2. The free energy change (ΔG) related with homogeneous nucleation of a sphere of radius r [65].

In equation 2.3, driving force for solidification can be expressed as [65]:

$$\Delta G = \frac{\Delta H \Delta T}{T_m} \ldots\ldots\ldots\ldots\ldots\ldots\ldots\ldots\ldots\ldots\ldots\ldots \quad (2.3)$$

where ΔH is the latent heat of fusion per unit volume at the melting point, ΔT is the undercooling (difference between the solidification temperature and melting temperature (equilibrium liquidus temperature)), and T_m is the melting point.

For maximum U, differentiating U with respect to r gives:

$$\frac{\partial U}{\partial r} = 0 \text{..... (2.4)}$$

and, free energy of nucleation is

$$U^* = \frac{16\pi {\Upsilon_{SL}}^3}{3(\Upsilon_{SL})^2} \text{..... (2.5)}$$

Thus, the critical radius of nucleus is derived from equation 2.6.

Critical radius $$r^* = -\frac{2\Upsilon_{SL}}{\Delta G} \text{..... (2.6)}$$

2.1.1.3. Heterogeneous nucleation

In heterogeneous nucleation, the probability of nucleation is much higher in preferred sites as compared to other sites. These preferred sites being the container wall containing the liquid, inclusions and grain boundaries in solid. Heterogeneous nucleation on a matrix is typically studied in terms of a classical model with a solid embryo (a form of a spherical cap) making a contact angle θ as shown in Figure 2.3. In Figure 2.3, surface energies ($\Upsilon_{SL}, \Upsilon_{NS}\ and\ \Upsilon_{NL}$) are chiefly interacting. Surface energy between the solid and liquid is denoted by Υ_{SL}. The wetting or contact angle (θ) can be determined from the equilibrium between surface tension forces acting on the periphery of the solid particle [12,65,66]. The energy barrier for heterogeneous nucleation U^*_{het} turns out to be:

$$U^*_{het} = \frac{1}{4} U^*_{homo}(2 - 3cos\theta + cos^3\theta) \text{..... (2.7)}$$

In heterogeneous nucleation, the energy barrier is much smaller as compared to homogeneous nucleation at small wetting angle. Wetting angle should be low for easier heterogeneous nucleation. Hypothetically, if the value of wetting angle becomes zero, there will be no energy barrier for heterogeneous nucleation. For this, specific particles are used in solidification processes in industries. These particles are known as inoculants [12,67,68].

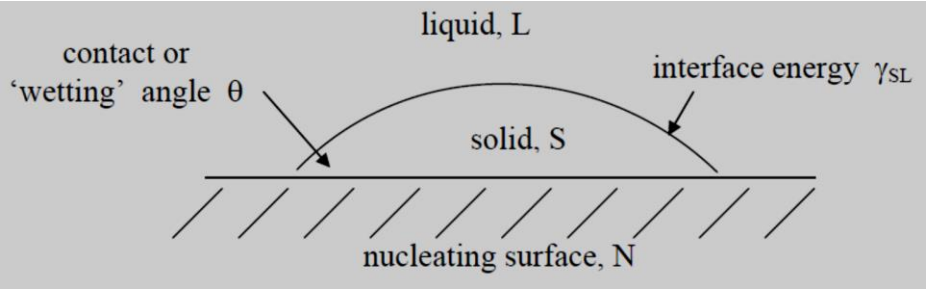

Figure 2.3: Schematic diagram of wetting angle between the flat mould walls and the nucleating surface [12,67,68].

2.1.2. Various grain refinement models in literature

According to classical nucleation theory, the creation of a stable nucleus mainly depends on the competition between the driving force for the phase change from liquid to solid (the volume free energy) and the energy that is required for creating a new interface. The equation of free energy barrier for nucleation on a heterogeneous substrate in terms of undercooling (ΔT) and the surface energy of new interface (σ) is [65]:

$$\Delta G = \left(\frac{16\pi}{3}\right)\left(\frac{\sigma^3}{\Delta s_f \Delta T^2}\right) f(\theta) \ldots\ldots\ldots\ldots\ldots (2.8)$$

Where Δs_f is the entropy of fusion and θ is the wetting angle between the liquid phase and the heterogeneous nucleation substrate.

According to Equation (2.8), ΔG can be decreased by decreasing θ or increasing ΔT. When wetting angle between the substrate and melt is low, the free energy barrier to nucleation is lower even at relatively small undercooling [65]. Therefore, the probability of nucleation will be more at a smaller undercooling for low wetting angles. Equation 2.8 is not valid for wetting angle less than 10° [69].

Free energy barrier for nucleation is a function of the amount of solute and the nucleus size, which further complicates the alloy system analysis [65]. Effect of solute on free energy barrier may depend upon the lattice mismatch between the substrate and the matrix, and mixing entropy influences [69]. Greer et al. suggested that effectiveness of a grain refiner may be improved at a distinctive average diameter of particle [13].

Easton and StJohn [69] observed that mainly two mechanisms are responsible for grain refinement in solidification. First mechanism is observed at the wall of the casting as the result of initial undercooling and the other mechanism occurs in the bulk of the molten metal due to

effect of constitutional undercooling. Constitutional undercooling retards the dissolution or further promotes the growth of crystals, which are nucleated at or near the wall so that the survived nuclei move inside into the bulk of the casting. Constitutional undercooling which is developed at the interface of these first grains helps in the propagation of nucleation wave in everywhere the bulk of the melt [70]. A minor modification to the constitutional undercooling mechanism is suggested by Winegard and Chalmers [71]. Easton and StJohn's model investigated the effect of both alloy composition and potency of nucleants on the grain size. Both growth restriction factor (*Q*) and supercooling parameters (*P*) are used for studying the effect of solute on the grain size [13,72]. The expressions for *Q* and *P* are written as:

$$Q = m(k-1)C_0 \ldots\ldots\ldots\ldots\ldots \quad (2.9)$$

$$P = \frac{m(k-1)C_0}{k} \ldots\ldots\ldots\ldots\ldots\ldots \quad (2.10)$$

Where m is the slope of the liquidus, *k* is the partition coefficient, and C_0 is the alloy composition in binary alloy.

Maxwell and Hellawell were the first to propose growth restriction factor (*Q*) [73]. It was observed that growth restriction factor is proportional to amount of constitutional undercooling that can be produced [73]. Spittle and Sadli [72] used the supercooling parameter for analyzing the grain refining efficiency of eutectic-based alloys. Easton and StJohn [74] observed that supercooling parameter does not clarify the grain refinement mechanism for peritectic-based alloys (titanium solute in pure aluminium). Hunt [75] proposed that the value of $m(k-1)C_0$ is the difference between solidus temperature and liquidus temperature at a solute concentration of kC_0. Chai et al. [76] suggested that growth restriction factor is inversely proportional to the growth rate of dendrite. They also proposed that the factor $m(k-1)C_0$ can be added for the various elements present in an alloy system. Desnain et al. [77] estimated the value of growth restriction factor for multi-component system using Maxwell and Hellawell's model [73]. Easton and StJohn [69] proposed a model for estimating growth restriction factor and supercooling parameter. It was assumed that the negative thermal gradient is negligible at the grain–liquid interface due to unconstrained growth as compared to the amount of constitutional undercooling, that there are enough substrates extant, and that nucleation starts when the constitutional undercooling is achieved [69,78]. This model derives the expression of growth restriction factor (*Q*) and supercooling parameter (*P*) [69].

$$\Delta T_c = \frac{mC_0(k-1)}{k} = P \ldots\ldots\ldots\ldots\ldots\ldots\ldots (2.11)$$

$$\frac{dT_c}{df_s} = mC_0(k-1) = Q \ldots\ldots\ldots\ldots\ldots\ldots (2.12)$$

Equation 2.12 is true for either equilibrium or non-equilibrium Scheil solidification.

For studying the effect of solute on grain size, this model introduced a new term, which is called relative grain size (RGS) to compare and determine the effect of solute content [69]. RGS is the fraction of solid (f_{sn}), when the constitutional undercooling (ΔT_c) achieves the required undercooling (ΔT_n) for nucleation [69,78].

$$RGS = f_{sn} = \left(\frac{mC_0}{mC_0 - \Delta T_n}\right)^{1/p} \ldots\ldots\ldots\ldots\ldots (2.13)$$

Equation 2.13 can be used for any binary alloys system.

Another model was proposed for analyzing the grain refining efficiency of solute in terms of potency by assuming that the constitutional influences on the grain size are closely related to the initial rate of development of constitutional undercooling according to equation 2.12 [79–81]. This model is expressed as:

$$d = a + b/Q \ldots\ldots\ldots\ldots\ldots\ldots\ldots\ldots\ldots (2.14)$$

Here slope *(b)* represents the potency of solute. Higher value of *b* means lower potency. Intercept *(a)* represents the number of active nucleants. Theoretically, if the value of *a* is zero, the number of active nucleants will be infinite.

2.2. Effect of solute content on grain refinement of aluminium alloys

For the last several decades, it has been reported that the processing condition and alloy constitution are significant factors affecting the grain size of alloys [64,82]. It was observed that the grain structure of metal is changed from columnar to equiaxed by adding solutes in the metal during solidification processing [17,83]. The research is maily focused on peritcectic based aluminium alloys. There has been less work reported on the effect of solute in eutectic based aluminium alloys. The effect of solute in eutectcic based aluminium alloys reported in the literature is summarized as follows.

Martinez-Villalobos et al. [84] analyzed the effect of nickel solute in aluminium alloys at different solute contents (hypoeutectic, eutectic and hypereutectic alloys) and also studied the

influence of rapid solidification on the morphology and dispersion of intermetallic phases. Their results showed that hypoeutectic Al-Ni alloy had α-Al rich phase surrounded by eutectic phase. Eutectic phase was entirely composed of small needles of intermetallic compound (Al_3Ni) surrounded by α-Al phase. For hypereutectic alloy, the microstructure consists of coarse intermetallic compound (Al_3Ni) which is enclosed by the eutectic phase. By increasing the content of solute (Ni), grain size decreased significantly. Globular grains and uniform distribution of intermetallic phase were observed using rapid solidification method.

Turchin et al. [85] investigated the macro and microstructure of Al–4.5%Cu alloy during solidification under the conditions of controlled melt flow. Their results indicated that columnar grains were observed during solidification in flowing melt and equiaxed grains were observed by increasing the melt flow in the regions with flow recirculation. Chaus et al. [86] studied the effect of rapid quenching on microstructure and mechanical properties of Al-Si alloy. Refined grain size, and refined eutectic phase and primary Si were observed using rapid quenching technology. Coarse plate-like eutectic Si phase was changed to a fine morphology at a higher cooling rate during solidification. Mechanical properties of alloys improved by rapid quenching technique.

Eskin et al. [87] observed the combined effect of solute content (1 to 4 wt.%) and cooling rate (0.1-20 K/s) on the microstructure of binary Al–Cu alloys. Their results indicated that the grain size and dendrite arms spacing decreased with increasing solute content of copper and increasing the cooling rate. By increasing the content of solute (Cu), the amount of non-equilibrium eutectics increased which depended in a complicated way on the cooling rate. It increased with increasing the cooling rate from 0 to 1K/s and then decreased from 1 to 10 K/s.

Haghayeghi et al. [88] studied the influence of processing temperature and relaxation time after liquid shearing on the microstructure of the Al–10wt.%Mg alloy. The maximum grain size of the processed alloy was 40 μm in all relaxation time parameter (30, 45, 60 and 90 s). Therefore, there was no effect of the relaxation time on the shearing phenomenon for grain refinement.

Li et al. [89] studied the influence of solute content (Mg) on the microstructure of Al–Mg alloys. Al-Mg alloys at different solute contents of Mg (0, 0.2, 0.7, 1.0, 3.0, 5.0 and 7 wt. %) were fabricated. Average grain size of Al-Mg alloy decreased significantly up to 1 wt.% of solute (Mg), while there was no effect on the grain size above 1 wt.% of solute.

Silva et al. [90] observed the effect of solute contents on the microstructure of Al-Ni hypoeutectic alloys. Al-Ni alloys were fabricated under unsteady-state solidification condition by varying the amount of solute (1, 3 and 5 wt.%). Their results showed that primary dendrite spacing decreased with increasing amount of solute. The microstructure consisted of α-Al dendritic phase and eutectic mixture (α-Al + Al_3Ni).

2.3. Effect of solute content and UST on grain refinement of aluminium alloys

Grain refinement is a useful technique for control of grain morphology and grain size of alloy during solidification. During last several decades, various methods have been employed during solidification for grain refinement of lightweight alloys like rapid quenching, spray forming [91,92], inoculation and physical methods such as mechanical stirring, electromagnetic vibrations, and ultrasonic vibrations. UST is one of the easy and useful physical methods to refine grain size of lightweight alloys during the solidification process [3-6].

Abramov et al. [93] studied the effect of UST on microstructure and mechanical properties of hypoeutectic Al–7Si alloy. Application of UST changed the microstructure to sub-dendritic structure from the dendritic structure, refined the Si inclusions and improved the mechanical properties of alloy.

Atamanenko et al. [94] studied the effect of melt temperature and UST on Al-4wt.%Cu alloy without and with adding the grain refiners (0.05 wt.% of Al-5Ti-1B). UST was employed in the melt by varying the ultrasonic power (2 to 5 kW) for 10 s at 700°C temperature. Upon increasing the power of UST, the grain size of alloys reduced without and with addition of grain refiner. Atamanenko et al. [95] further reported that the grain size and dendritic arm spacing decreased with UST in Al-4wt.%Cu and Al-11wt.%Cu alloys during continuous and semi-solid processing of UST. In case of Al-4wt.%Cu alloy, cavitation aided grain refinement was the dominant mechanism and for Al-11wt.%Cu alloy, grain refinement occurred due to influence of primary nucleation by UST.

Jung et al. [96] examined the effect of UST on the microstructure of Al-Si alloys having different Si contents (12, 15, and 18 wt.%). UST was employed into the melt for 60 s in the temperature range of 700-750°C for the 12 wt.% Si alloy and 750-800°C for 15 wt.% Si and 18 wt.% Si alloys. UST reduced the average grain size of the alloy and changed the morphology of α-Al grain from dendritic to equiaxed. UST also refined the size of eutectic Si phase and primary Si particles. Das and Kotadia [36] studied the effect of UST on the microstructure of LM6 alloy.

Their results showed that UST eliminated dendritic α-Al phase and globular grains were produced. Very fine Si platelets were observed in the intergranular spaces near the ultrasonic horn.

Ferguson et al. [97] studied the effect of UST, pouring temperature, and cooling rate on the microstructure of A356 alloy. A356 alloy samples were fabricated under three experimental processing conditions-

a) Melt cast at different pouring temperatures (610, 750, 850, and 950°C) and then poured into the steel mold without UST horn.
b) UST horn (without preheat) inserted into the melt for 30 and 60 s accompanied with UST. After that, horn was removed and melt held in the electric resistance furnace for 0, 60 and 120 s and then cast into a steel mold.
c) UST horn (without preheat) inserted into the melt for 30 and 60 s without UST. After that probe was removed and melt was immediately quenched into the steel mold.

The results showed that grain size decreased at lower pouring temperature without immersion of ultrasonic horn for as-cast samples. For as-cast samples with immersion of ultrasonic horn, grain size decreased with increasing ultrasonic horn immersion time, which definitely proved the chill effect of the cold horn. For UST samples, the grain size significantly decreased.

Feng et al. [33] reported the influence of UST on the microstructure of hypereutectic Al-23wt.%Si alloy. UST was applied to the melt in the temperature range of 680-700°C for 10 min, after which the crucible with melt was withdrawn from the furnace and quenched into water. The morphology of the α-Al phase changed from dendritic to equiaxed structure with the application of UST. UST also refined the primary silicon phase.

Fukui et al. [98] reported the influence of UST on the microstructure of Al-18Si alloy. In experiment, aluminium alloy was melted at 750°C in alumina crucible. UST was applied at different temperatures of 583°C, 587°C, 592°C, 597°C, and 601°C for 10 s. After UST, sample was quenched into water. The results indicated that the as-cast sample quenched at 583°C had fine dendritic α-Al phase and eutectic structure. The α-Al phase, silicon grains and fine eutectic structure was observed in sample USTed at 583°C. At lower UST processing temperatures (583, 587°C), globular α-Al grains were observed, and at higher UST processing temperatures (597, 601°C), dendritic α-Al phase was observed.

Jia and Nastac [62] reported the effect of UST on the microstructure of A356 alloy. In their experiments, A356 alloy was melted in electric furnace. Ultrasonic probe was inserted into the melt for 15 min. The results showed more equiaxed dendritic structure after UST. UST also refined the size of the eutectic phase. Jian et al. [34] studied the influence of UST on A356 alloy melt at different stages of solidification. Three type of experiments were performed with application of UST into the melt, which are mentioned here:

a) UST was applied to the A356 alloy melt in temperature range from 634°C to 574.8°C and then it was cooled in the furnace. This was called as continuous cooling treatment.
b) In second type of experiment which was named as intermittent treatment, UST was applied to the melt in the temperature range of 614 to 574.8°C for varying durations of 5, 10 and 20 s.
c) In isothermal treatment, UST was performed at various solid fractions for different ultrasonic durations of 5, 10 and 20 s.

In continuous cooling, UST time of 20 s was enough for produce globular grains of α-Al. Better results were obtained in intermittent treatment as compared to continuous cooling and isothermal treatment. Isothermal UST with a short duration into the mushy zone decreased the average grain size of α-Al but failed to yield globular grains.

Jian et al. [99] reported the effect of UST on microstructure of A356 alloy. Globular α-Al grains were obtained after application of UST. The morphology of eutectic silicon changed to fine structure form a coarse acicular plate-like structure with the application of UST. The length and width of eutectic silicon decreased from 26 μm to 2 μm and from 2.7 μm to 0.6 μm, respectively. Jian et al. [100] observed the influence of UST on the microstructure of Al7050 alloy. UST was employed into the melt (a) in liquid state (670 to 655°C), (b) after the melt starts to crystallize (640 to 625°C), and (c) in mixed solid-liquid slurry state (625 to 590°C). Results indicated that UST showed a little effect on the grain refinement in liquid state processing, while significant refinement was observed in temperature range of 640-625°C. α-Al grains were also refined efficiently in the temperature range of 625-590°C.

Jiang et al. [101] studied the grain refinement mechanism for cast aluminium alloys under the influence of UST. Equiaxed microstructure was obtained when the molten melt was treated with ultrasonic vibration using a preheated ultrasonic radiator. It was seen that the equiaxed region occurred only in a small area at below the radiating face of ultrasonic horn (immersed in

chilled state), and coarse dendritic grains were observed at other positions below the radiating face. In this study, cavitation-promoted nucleation was the mechanism responsible for grain refinement.

Khalifa et al. [102] investigated the effect of UST on eutectic silicon and iron-based intermetallic phases in 380, 384, 356 and 356 (with 0.8% Fe) grade Al-Si alloys. Isothermal UST was carried out at different temperatures (620, 605, 600 and 595°C) on the 380 alloy for 4 s, and at 623°C on the 356 and 356 (with 0.8% Fe) alloys for 5 and 15 s. The results indicated that more compacted Si particles were formed after UST near the ultrasonic horn. At higher temperatures, no effect of UST was observed on eutectic silicon phase. UST changed the morphology of iron-based intermetallic phases from large plate-like particles to compacted form, when UST was applied 10°C above the liquidus temperature. UST did not have much effect on the morphology of iron-based intermetallic phases at higher temperatures.

Khalifa et al. [103] studied the influence of UST on the size and morphology of the α-Al phase in A356 alloy by varying the UST time and ultrasonic processing temperature. UST refined the solidification microstructure when the melt was ultrasonically treated near the liquidus temperature. Fine non-dendritic globular grains in the range of 53-72 μm were observed. Khalifa [104] further studied the microstructural characterization of Al-4wt.%Mg alloy under the application of ultrasound vibrations. Non-dendritic aluminium grains were observed, when continuous ultrasonic vibrations were applied to the liquid for 2-3 minutes during solidification in temperature range from 660°C to 615°C. Dendrite fragmentation mechanism was responsible for the grain refinement.

Kotadia and Das [26] reported the effect of UST on the primary α-Al phase, primary-Si and eutectic phase of hypoeutectic (Al–7wt.%Si) and hypereutectic (Al–16wt.%Si) alloys. Their results showed that dendrite to equiaxed transformation of α-Al phase was observed upon UST of hypoeutectic alloy and UST refined and uniformly dispersed the eutectic Si phase. For hypereutectic alloy, UST refined and better dispersed the primary silicon particles. It was suggested that the refinement of the primary α-Al phase occurred due to cavitation enhanced heterogeneous nucleation mechanism. Eutectic spheriodisation was observed near the ultrasonic horn because of strong fluid flow due to cavitation effect.

Li et al. [105] studied the influence of UST on the microstructure of Al-l.65wt.%Si alloy. In their experiment, ultrasonic probe preheated to 600°C was inserted into the melt (750°C) for

different UST durations (20, 40, 60, 80, 100 and 120 s). It was observed that the macrostructure had a columnar grain structure in the outer region of ingots, an equiaxed grain structure region in central area below the ultrasonic probe, and a coarse columnar grain structure at the top of ingot when UST time was 20 s. When the UST time was increased to 40 and 60 s, the columnar grain structure in the outer region of ingots decreased and equiaxed grain structure region in central area of the ingots increased. When the UST time was increased to 80 and 100 s, many fine and homogeneous equiaxed grains were seen in the ingot section, the columnar grain structure in the outer region of ingots was reduced, and equiaxed grain area in the central region of ingots further increased.

Li et al. [106] reported the effect of UST on microstructure of A1075 alloy with the effect of grain refiner (Al–5Ti–0.25C alloy). UST was applied to the alloy melt (A1075 and Al–5Ti–0.25C alloy) at different temperatures (850 and 720°C) for 5 min. UST refined the $TiAl_3$ phase and uniformly distributed the TiC phase into aluminium matrix. Cavitation and acoustic streaming effects were responsible for the microstructural refinement.

Matsuda et al. [107] evaluated the effect of UST on the grain size of Al-4wt.%Si alloy. UST was applied at different conditions- (a) above liquidus temperature, (b) during undercooling before recalescence, (c) during recalescence, and (d) after recalescence for verifying the grain refinement mechanism. Grain refinement in aluminium alloy was not observed, when UST was applied after recalescence. Dendrite fragmentation mechanism did not initiate just under the liquidus temperature. It was observed that the grain refinement occurred due to an increase in the number density of non-equilibrium nuclei, when UST was applied above the liquidus temperature. Average grain size of aluminium alloy decreased upon UST during (b) and (c). The experimental results indicated enhanced nucleation, but the cause for this is not clear from their study.

Puga et al. [32] observed the effect of UST on microstructure of AlSi9Cu3 alloy at different UST processing temperatures. UST was performed at various temperatures (615, 620, 630 and 640°C) and different levels of ultrasonic power (200, 400 and 600 W) for 120 s with a preheated ultrasonic horn. UST led to the formation of globular α-Al grains and finer eutectic Si phase, whose size depended on the UST temperature and ultrasonic power. Use of higher UST temperatures and lower ultrasonic power produced rosette-like α-Al grains and exhibited inferior grain refinement efficiency. Puga et al. [108] reported the effect of UST on microstructure of

AlSi9Cu3(Fe) alloy. UST was applied continuously between 680°C and 580°C at different degree of ultrasonic power (200, 400 and 600 W). UST produced more refined α-Al and eutectic Si phases upon increasing the ultrasonic power. Globular α-Al microstructure was obtained at maximum ultrasonic power (600 W) with average grain size of 36 μm.

Wang et al. [37] examined the influence of UST and melt temperature in Al–2wt.%Cu alloy. Significant refinement was observed when UST was applied at a temperature that was 20°C above the liquidus temperature. No grain refinement was detected in the alloy, when ultrasonic vibration was introduced from above the liquidus temperature and ceased just above the liquidus temperature. Wang et al. [28] investigated the combined effect of Al3Ti1B master alloy and UST on the microstructure of Al-2wt.%Cu alloy. Significant grain refinement was observed when UST was applied at 40°C above the liquidus temperature (655°C) and stopped at 653°C for 4 minutes in Al-2wt.%Cu alloy without and with adding the master alloy. UST altered the nucleation efficiency of the master alloy by increasing the number of activated TiB_2 particles.

Wang et al. [14] studied the effect of UST on Al–0.4wt.%Ti alloy. They selected three temperature zones for application of UST- (a) above liquidus temperature (810 to 770°C), (b) across the liquidus temperature (770 to 730°C), and (c) below the liquidus temperature (730 to 690°C). Size of the Al_3Ti intermetallic phase refined in all the temperature zones. Cavitation-enhanced nucleation mechanism was responsible for refinement of intermetallic phase when UST was applied above the liquidus temperature. Cavitation-induced fragmentation mechanism dominated for refinement below the liquidus temperature.

Effect of UST applied at different pouring temperatures on the microstructures of Al-1wt.%Mg-0.3wt.%Sc alloy was studied by Tuan et al. [35]. Substantial grain refinement was observed in alloy after UST as compared to the as-cast alloy. Cavitation-enhanced heterogeneous nucleation mechanism was responsible for grain refinement of alloy. Yu et al. [109] investigated the influence of UST on the microstructure and mechanical properties of Al–23wt.%Si alloy. Grain size of α-Al decreased with UST as compared to as-cast alloy. UST also refined and uniformly distributed the primary silicon phase. As a result, ultimate tensile strength of the alloy increased.

Zhang et al. [110] analyzed the role of UST on Al–Cu, AA7075, Al–Ti, Al–Zr–Ti and AA2024 alloys cooled using different cooling rates. UST refined the microstructures and intermetallic phases when UST was applied in the solidification range. Grain refinement of Al

alloy depended upon the undercooling. With larger undercooling, more grain refinement occurred.

Zhang et al. [111] investigated the effect of isothermal and continuous cooling UST on the microstructure of hypoeutectic (Al-5wt.%Si), hypereutectic (Al-17wt.%Si) and near-eutectic (Al-11wt.%Si) alloys at different ultrasonic processing temperatures (650, 670, 700 and 720 ºC). Refined grain size was observed with UST done during continuous cooling. In hypoeutectic Al-Si alloy, cavitation-assisted fragmentation mechanism was found to be responsible for the grain refinement of alloy. A substantial refinement of primary silicon crystals was also observed in hypereutectic alloys when UST was applied near the liquidus temperature. However, application of UST during further solidification might have resulted in coarsening and agglomeration of primary Si.

Zhang et al. [112] observed the morphology of α-Al phase and size of primary intermetallic compound formed under different ultrasound intensities in Al-0.4wt.%Zr-0.12 wt.%Ti alloys. UST was applied for 10-20 s from temperature 790°C to 750°C into the melt. 4.0, 3.5, 3, 2.5, and 2.0 kW of ultrasonic generator power were employed. They studied the mechanisms responsible for the formation of these primary intermetallic phases under UST. UST refined the α-Al phase and the eutectic silicon phase coarsened during solidification processing. For grain refinement, cavitation dendritic fragmentation mechanism was responsible.

Zhang et al. [113] reported the effect of UST on the microstructure and mechanical properties of A356 alloy by varying the ultrasonic power (0.6, 0.8, 1.0 and 1.2 kW). UST was done to the melt for 10 min. With UST, morphology of α-Al and Si phases improved and their size decreased. It was observed that sharp and long dendrite-shaped silicon phase turned into smooth particle shape or short-rod shape with size of about 3–8 μm at maximum ultrasonic power of 1.2 kW.

2.4. Processing methods for dispersing the micro and nano-particles in light alloy melts

Adding the ceramic particles in to light alloys enhances their strength, high temperature strength, and wear resistance [114–116]. There are several established techniques for adding the ceramic particles in to metal alloy matrix. These conventional routes are mechanical alloying, powder metallurgy, squeeze casting, compocasting, spray deposition, stir casting, and ultrasound assisted solidification [40,115–121]. Processing route affects the mechanical properties of the alloy matrix composites. These conventional routes are mainly classified in to solid-state

processing route and liquid state processing route [45]. Each has to fabricate metal matrix composites (MMCs) with definite combinations of alloy matrix and ceramic particles. Therefore, a lot of research is mainly done for designing the processing routes to fabricate MMCs. Several researchers reported that liquid state processing route is a simple and effective method for fabricating large quantities of MMCs [45]. Table 2.1 shows different processing methods used for successfully adding the ceramic particles into the molten metal.

Table 2.1: Summary of research work for adding ceramic particles in to the metal matrix.

Cited work	**Alloy/ Materials studied**	**Reinforcement particles**	**Solidification method**
Ghosh et al. [38]	Al-Mg	Al_2O_3 particles (45-212 µm)	Stir casting
Ghosh and Ray [122]	Al-Mg	Al_2O_3 particles (45-212 µm)	Compocasting
Kumaran et al. [123]	6351 Al alloy	Hybrid 0, 5 & 10 wt.% of B_4C and 5 wt.% SiC	Stir casting
Kumaran et al. [124]	6351 Al alloy	Hybrid 0, 5 & 10 wt.% of B_4C and 5 wt.% SiC	Stir casting
Yamanoglu et al. [125]	Al-Cu-Mg	4 wt.% SiC (650 nm)	Stir casting
Uju and Oguocha [126]	A535 Alloy	5 wt.% Fly Ash and 5 wt.% SiC	Proprietary stir casting
Alaneme and Aluko [127]	Al6063	3, 6, 9 and 12 vol.% SiC (30 µm)	Double stir casting
Khan et al. [128]	Al-5%Mg	10 and 20 vol.% B_4C	Stir casting
Ozden et al. [129]	Al2124, Al5083, and Al6063	10 wt.% SiC (167 µm)	Stir casting
Yılmaz and Buytoz [130]	Al-Cu-Mg-Si alloy	5, 7, 10 and 15 vol.% Al_2O_3 (20µm)	Stir casting

Baradeswaran and Elaya Perumal [131]	Al7075	5, 10, 15 and 20 vol.% B_4C (20 μm)	Stir casting
Li and Langdon [132]	Al 7005	20 vol.% Al_2O_3 (20 μm)	Proprietary casting
Mazahery and Shabani [133]	A356	SiC (50 nm and 16 μm)	P/M and Stir Casting
Narasimha Murthy et al. [118]	AA2024	2 and 3 wt.% Fly Ash (23 nm)	P/M and UST
Su et al. [54]	Al 2024	Al_2O_3 (65 nm)	P/M and UST
Li and Langdon [134]	Al 6061	20 vol.% Al_2O_3 (20μm)	Proprietary casting
S. G. et al. [44]	AA 6061	TiC	Stir casting
A. G. Rao et al. [45]	AA 6061	10 wt.% B_4C (25 μm)	Centrifugal Casting
El-Sabbagh et al. [135]	AA 6061	15 vol.% SiC (15 and 8 μm)	Stir cast
Benal and Shivanand [136]	Al 6061	9 wt.% of SiC (60 μm) and 0, 1, 3 , 5 wt.% of E-glass fibre (2-3 mm)	Stir cast
Srivatsan [137]	Al2024	10 and 15 vol.% of Al_2O_3	Proprietary casting
Ezatpour et al. [138]	Al 6061	0.5, 1 and 1.5 wt.% Al_2O_3 (40 nm)	P/M and Stir casting
Mahadevan et al. [139]	AA 6061	15 vol.% SiC (23 μm)	Stir cast
Mula et al. [140]	Pure Al	2, 3.57 and 4.69 wt.% of Al_2O_3 (10 nm)	Non-contacting UST
Mula et al. [141]	Pure Al	2 wt.% of Al_2O_3 (10 nm)	Non-contacting UST

Nie et al. [142]	AZ91	1 vol.% SiC (60 nm)	UST
Nie et al. [143]	AZ91	0.5, 1 and 2 vol.% SiC (60 nm)	UST
Nie et al. [56]	AZ91D	0.5, 1 and 2 vol.% SiC (1 μm)	UST
Cao et al. [144]	Mg-(2,4)Al-1Si	2 wt.% SiC (50 nm)	UST
Xuan and Nastac [145]	A356	1 wt.% Al_2O_3 (20 nm)	UST
Jia et al. [115]	A356	1 wt.% β-SiC (50 nm) or Al_2O_3 (20 nm).	UST
Li et al. [119]	A356	1 wt.% SiC (30 nm)	UST
Harichandran and Selvakumar [116]	Pure Al	2, 4, 6, 8 and 10 wt.% B_4C (80 nm)	UST

Among above processing methods, stir casting is a simple, effective and economical method for adding the micron sized particles in molten metal [38,146]. This method is also competent for forming the near net-structure MMCs into a complex structure by conventional foundry techniques [147]. Micron-sized ceramic particles are extensively used in the fabrication of MMCs [40]. Micron-sized particles enhance strength but reduce the ductility of the composite [148]. Due to poor ductility of MMCs reinforced with micron size particles, their application is limited. For overcoming these problems, nowadays nano-particles are used for fabricating the MMCs [40]. It is observed that nano-particles can significantly enhance the mechanical properties of composites as compared to micron-size particles [45,119]. Nano-particles also retain the ductility of the matrix. It was reported that low content of nano-particle reinforcements is enough for enhancing the mechanical properties of composites as compared to micron-sized particles [45,56]. Recently, it was found that nano-particles can effectively promote the heterogeneous nucleation sites under solidification and hinder the grain growth because of Zener pinning effect during solidification [149,150]. Several strengthening mechanisms are observed in nano-composites that are responsible for increasing the yield strength of composites as compared to their base alloy. These mechanisms are Orowan strengthening [151], Hall-Petch strengthening, coefficient of thermal expansion (CTE) mismatch strengthening, and load bearing

mechanism [152–156]. For understanding the contribution of these strengthening mechanisms, several models are proposed that estimate the yield strength of composites. These models are Arithmetic summation method [157,158], Quadratic method [157,159,160], Compounding method, Zheng and Chen model, and other models [157,160].

However, it is extremely difficult to uniformly disperse the nano-particles in molten metal by stir casting method because nano-particles have a large surface to volume ratio and poor wettability in molten metal, which readily stimulate the agglomeration and clustering of particles [115,119,120,161]. It is propounded that ultrasonic solidification method is promising processing route to uniformly disperse the nano-particles in aluminium and magnesium alloys because of the acoustic streaming and ultrasonic cavitation effect. UST also has potential for minimizing melt oxidation by decreasing the processing time [41,45,57,144]. UST produces nonlinear effects such as cavitation and acoustic streaming into the liquid [18]. Acoustic streaming could enhance the transfer of small particles in to the molten metal, equalize the concentration of the solute in the melt and the temperature, and fragment the dendritic structure [40,46,115,145]. The basic mechanism of UST in molten metal is described below.

2.5. Effects of ultrasonication in molten metals

When high intensity ultrasound propagates through liquid melts, some phenomena like acoustic streaming and cavitation arise in the molten metal, which causes change in the morphology of the solidifying phases [162,163]. Some known metallurgical effects are observed during the treatment of molten metal under the application of power ultrasound. These effects are as follows [162,163]:

i. Solidification under ultrasonic field
    a) Reduction in grain size
    b) Non-dendritic solidification
ii. Refining of melts
    a) Ultrasonic degassing of melts
    b) Fine filtration in the ultrasonic field (USFIRALS process)
iii. Dispersion of other substances into the melts
iv. Acceleration of rate processes
v. Other metallurgical and related effects

When ultrasonic waves are transmitted through a medium, its molecular structure is alternately stretched and compressed [30]. If the negative pressure during the stretching phase or rarefaction phase is strong enough to overcome intermolecular binding forces, it can tear apart the medium resulting in tiny cavities (micro bubbles). The cavities so formed can grow under tensile stresses in the succeeding cycles. Eventually they collapse with the release of large magnitude of energy as depicted in Figure 2.4. This phenomenon produces hot spots [31]. These local transient hot spots have very high temperatures (>5000 K) and large pressure (>1000 atm) which could significantly increase the wettability between the nano-particles and the molten metal and could break up the clustering of nano-particles [45,46,54,54,57,164]. In addition, the powerful acoustic streaming produced by UST can promote the uniform dispersion of nano-particles into the molten metal [41,45,115,144].

The important factors controlling the intensity of cavitation are[165,166] :

Ultrasonic frequency: The lower the frequency, the more intense will be the cavitation occurrence.

Ultrasonic power: The amount of cavitation per unit of time and volume is determined by the power level. Increase in power increases the number of cavitation events. When cavitation occurs in a melt, the occurrence of pulsating cavitation bubbles can cause the dispersion of crystals and increase in the nucleation rate of crystallization.

Two mechanisms have been proposed for grain refinement of alloys using UST. These mechanisms are cavitation enhanced nucleation and cavitation assisted dendrite fragmentation [30,32,34,110,167,168]. UST may affect nucleation in several ways. Pressure influences the liquidus temperature of an alloy [162]. If ultrasonic energy is applied to a melt near its liquidus temperature, some regions in the molten alloy may be superheated while other regions may be undercooled. Each location the melt undergoes change from superheating to undercooling at high frequencies. This may result in the formation of an increased number of solid nuclei [170]. Another possibility is that the grain refiners added to the melt may also be affected by ultrasonic vibration, since each foreign particle can act as a nucleus and is most effective under a certain undercooling. Nucleation under the action of ultrasound vibrations may also occur in the melt at a temperature higher than the liquidus, corresponding to the increase in the pressure [8,25].

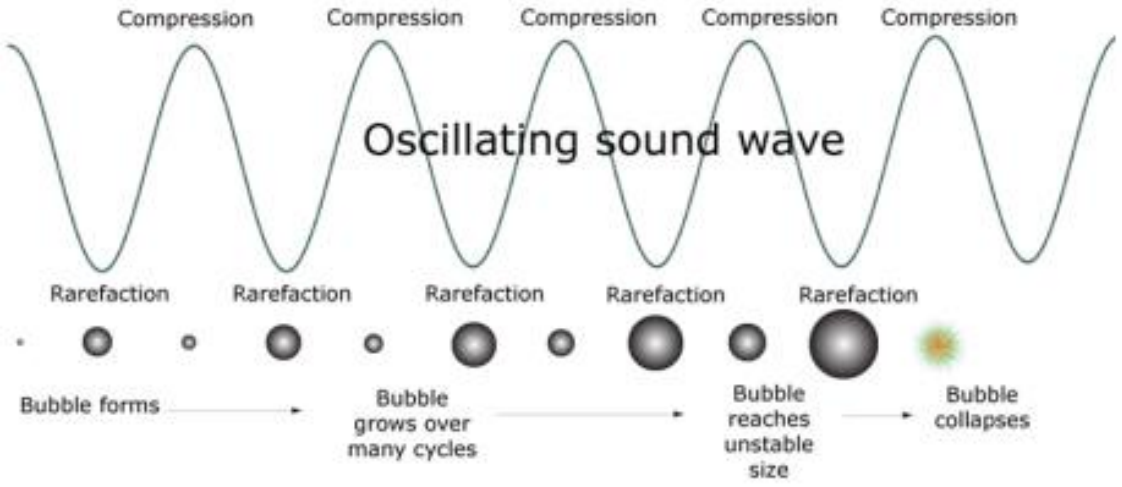

Figure 2.4. Cavitation phenomena in the melt [169].

2.5.1. Cavitation enhanced nucleation

Possible mechanisms of crystal nucleation due to cavitation are [27]:

1. From the surface of the expanding cavity, the liquid evaporates to cause cooling of the surface
2. An increase in the melting point is produced from positive pressure pulse associated with cavity collapse
3. Cooling is caused by negative pressure associated with cavity collapse

Cavitation- enhanced nucleation is interpreted in terms of two different mechanisms discussed below [170,171]:

2.5.1.1. Pressure pulse melting point (T_m) mechanism

Cavitation bubbles produced in liquid metal start to collapse, inducing the pressure pulse waves, resulting in an increase of solid-liquid equilibrium temperature. Undercooling of the liquid phase occurs due to increase in pressure and consequently the melting point is increased, which is explained by the Clausius–Clapeyron equation (2.15) [31,172].

$$\frac{dT_m}{dP} = \frac{T_m(V_L - V_S)}{\Delta H} \quad \text{..... (2.15)}$$

Where, ΔH is the latent heat of freezing in $J.g^{-1}$, P is pressure in 10^5 Pa, T_m is freezing point in K, V_S, and V_L are the specific volumes of solid and liquid phases in $cm^3.g^{-1}$, respectively. Nucleation rate increases due to an increase in T_m, which is equivalent to increasing the undercooling.

2.5.1.2. Cavitation enhanced inclusion wetting

In this case, the pressure pulse fills the cavities and cracks on the surfaces of the substrates such as the mould, or impurities by molten metal. Therefore, enhanced nucleation results from these defects that can act as effective nucleation sites [162].

2.5.1.3. Cavitation induced endothermic vaporization theory

This mechanism involves undercooling of the molten metal at the surface of bubble. During cavitation, the expansion of gas inside the cavitation bubbles leads to increase the bubble size and decrease the bubble temperature, which will cause undercooling at the bubble surface and, as a result, form nuclei on the bubble's surface. When these bubbles collapse, a significant number of nuclei are produced into the melt and this promotes the heterogeneous nucleation in the melt [27].

2.5.2. Cavitation assisted dendrite fragmentation

The convection and shock waves created in the solidifying melt during ultrasonic vibration can promote dendrite fragmentation, which causes melting at a dendrite root, where the solutes are segregated. The melting at a dendrite root may be a result of local temperature increase. Diffusion of solutes away from the dendrite roots would lead to a reduction of the solute concentration and increase in the local temperature. Stirring can also promote dendrite fragmentation, since it produces local temperature variations and promotes diffusion of solutes in the liquid. Furthermore, the local pressure fluctuations given by equations (2.16) and (2.17) lead to fluctuations in the melting temperature which results in the melting of the dendrite roots.

$$p_{max} = p_0 + \sqrt{2\rho cI} \quad \ldots\ldots\ldots\ldots\ldots\ldots\ldots\ldots \quad (2.16)$$

$$p_{min} = p_0 - \sqrt{2\rho cI} \quad \ldots\ldots\ldots\ldots\ldots\ldots\ldots\ldots \quad (2.17)$$

These fluctuations should aid in the melting of the dendrite roots. This will lead to more homogeneous microstructure with smaller grain size. However, if the applied ultrasonic field is strong enough to produce cavitation, then a major origin of grain refinement is the fragmentation

of crystals to produce new nuclei [30,32,34,110,167,168]. Abramov studied the destruction/fragmentation of growing crystals due to cavitation induced by ultrasound [163]. Equation (2.18) shows the pressure (P_d) required for the fragmentation of crystals [172].

$$P_d = \frac{1}{4}\left(\frac{r}{l}\right)^2 \sigma_{mp} \approx \gamma\sigma_{mp} \quad \text{..... (2.18)}$$

Where σ_{mp} is strength of the material near the melting point, and *l* and *r* are the length and radius of the crystal, respectively. Table 2.2 shows that the ultrasonic intensity required for the crystal dispersion scales with the γ parameter. Both the alloy strength and the crystal morphology influences the dispersion of growing crystals. Table 2.2 also reveals how the crystal morphology is related to the ultrasound intensity [163,172].

Table 2.2. Crystal geometry and ultrasound intensity necessary for crystal dispersion [172].

Crystal growth velocity (μm.s^{-1})	**Crystal length (mm)**	**Crystal radius (mm)**	$\boldsymbol{\gamma \times 10^{-2}}$	**Ultrasound intensity (W.cm^{-2})**
5	0.2	0.05	6.25	30
16	0.4	0.06	2.25	20
25	0.6	0.08	1.78	15
50	1.0	0.12	1.44	10
100	1.6	0.20	1.55	10

It is also reported that UST helps the degassing of the melt and decrease the porosity of the cast-structure [173–178]. Mechanism of ultrasonic degassing is described as follows.

2.5.3. Ultrasonic degassing of melts

The interaction of high intensity ultrasound with liquid reduces the amount of gas dissolved in liquid, leading to degassing. This effect can be used for degassing metal melts. Ultrasonic degassing of melts by UST is an environmentally clean and comparatively cheap technique. In this technique, Hydrogen is removed from the molten aluminium with the help of UST. The mechanism of ultrasonic degassing is dependent on the phenomenon of ultrasonic cavitation in the molten metal. When ultrasonic horn is applied into the melt, ultrasonic waves

produce tensile and compressive stress in the alternate cycle, which forms large number of tiny cavities in the melt at higher ultrasonic vibration. The surface area of pulsating bubbles in rarefaction phase is several times greater than compression phase. At this time, the hydrogen gas diffuses from the surrounding melt in to the bubbles. The amount of hydrogen gas that enters in to the bubble in rarefaction phase is larger than the amount of hydrogen gas leaving the bubble in compression phase, as shown in Figure 2.5. This is called rectified mass diffusion effect [169,179], due to which the bubble gains significant amount of hydrogen gas over several cycles. Due to hydrodynamic buoyancy force, large bubbles can float to the surface of the molten metal and escape from the surface [169].

An experiment was carried out for finding out the rates of removal of hydrogen from Al-Si-Mg alloy by using different processes like chlorine salts processing, UST, vacuum degassing, combined UST and vacuum degassing and it was observed that combined UST and vacuum degassing gives promising results (as shown in Figure 2.6 and Table 2.3) [27,181].

2.6. Research gaps and Problem Formulation

Increasing volumes of aluminium alloys are used in automobile and aerospace applications for satisfying the demands for fuel efficiency and to achieve low carbon dioxide gas emissions. Therefore, time-to-time modifications on aluminium alloys have been made by changing the composition, processing methods, and particle size of reinforcements in composites for achieving better mechanical properties. However, the demand for continuous improvement in performance of aluminium alloys, through its improvement of mechanical behavior, in automobile and aerospace application is ever increasing.

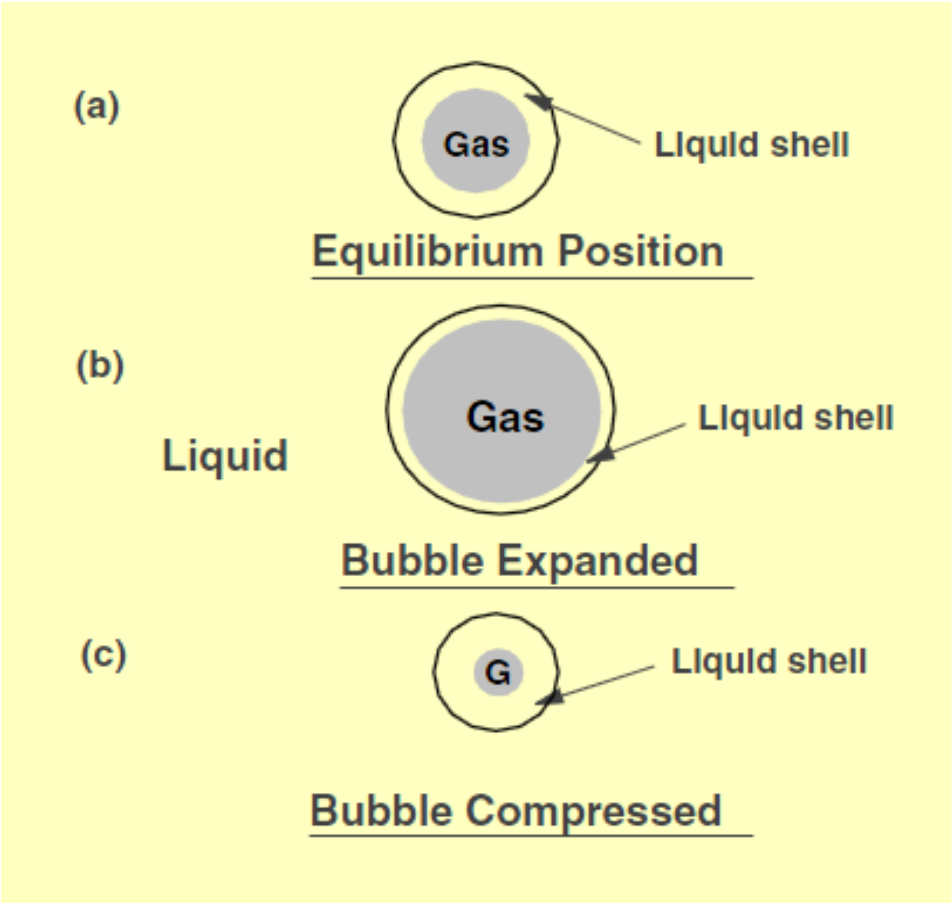

Figure 2.5. Schematic of rectified diffusion [180].

Table 2.3. Comparison of efficiencies of degassing techniques used in industry for Al-Si-Mg alloy [27,181].

Degassing techniques	**H_2 (cm^3 per 100 g)**	**Density (10^3 $Kg.m^{-3}$)**	**Porosity number**
Ultrasonic degassing	0.17	2.706	1-2
Vacuum degassing	0.20	2.681	1-2
Argon purging	0.26	2.667	2-3
C_2Cl_6	0.30	2.665	2-3
Universal flux	0.26	2.663	3-4
Initial melt	0.35	2.660	4

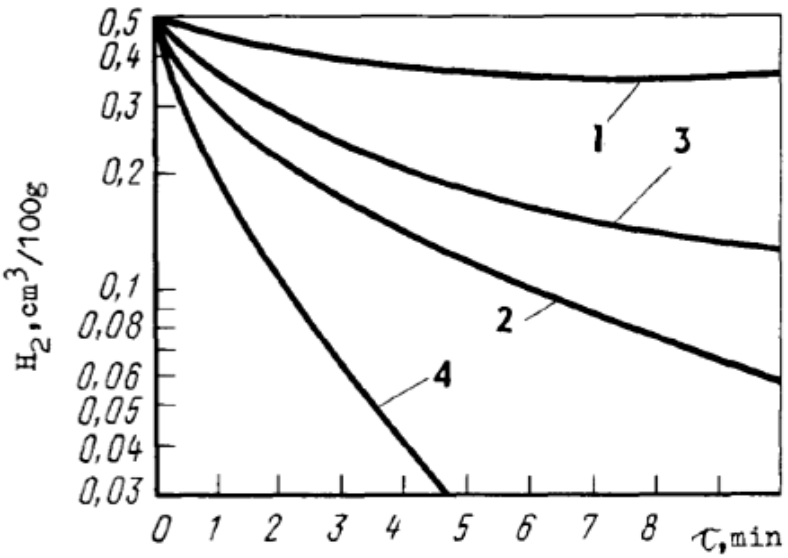

Figure 2.6. Rates of removal of hydrogen from Al-Si-Mg alloy (1) chlorine salts processing, (2) UST, (3) vacuum degassing, (4) combined UST and vacuum degassing [27,181].

An exhaustive review of the literature on aluminium and its alloys with effect of solute, ceramic particles, and UST has been carried out, and based on the identified research gaps the problem formulation is made in the present work. The important findings on aluminium alloys from the literature are summarized below:

In literature, previous studies mainly dealt with grain refinement of the peritectic based aluminium alloys (Al-Ti, Al-Cr and Al-V) without and with UST. There is little work done on the grain refinement of eutectic-based aluminium alloys by using ultrasound solidification technique. Grain refinement mechanism in off-eutectic and hypoeutectic aluminium alloys with the application of UST is scarcely reported. A systematic study of the combined effect of solute content and UST in microstructural evolution of aluminium alloys is lacking in literature. It was observed that the nucleation efficiency of eutectic alloys could be changed with the application of UST. UST has potential to refine the grain structure of hypoeutectic alloys, which will show superior mechanical properties and could be used in automobile and structural applications.

It is known that UST efficiency is changed with ultrasonic processing temperature. Therefore, melt temperature or melt viscosity can play a vital role in dispersing the nano-particles in aluminium alloy melts. There is little work on the dispersion of nano-particles in aluminium alloys from ultrasonic solidification technique by using different processing temperatures.

Therefore, there is a need to study the effect of ultrasonic processing temperature on the incorporation and dispersion of nano-particles, and the resultant inter-particle spacing in the composites.

Thus the objectives of this work are:

1. To study the combined effect of solute content and UST on microstructure of binary aluminium alloys.
2. To investigate the dominant grain refinement mechanism.
3. To study the mechanical behavior of ultrasonically treated binary aluminium alloys.
4. To investigate the dispersion of nano-particles in aluminium alloy when UST is performed.
5. To study the structure-mechanical property relationship in ultrasonically treated nano-particles dispersed aluminium alloy composites.

CHAPTER 3

EXPERIMENTAL PROCEDURE AND INSTRUMENTS

This chapter describes the details of experimental procedures carried out in line with the scope of the work. The procedures of specimen preparation for microstructural characterization (scanning electron microscopy, optical microscopy and transmission electron microscopy) and mechanical testing (hardness and tensile test) are explained.

3.1. Materials

Pure aluminium was procured from Hindalco, India. Both pure copper and nickel were procured from Hindustan Copper Limited, India. The nominal composition of commercially available Al6061 alloy procured from Hindalco, India is given in Table 3.1. It melting range is 580°C-660ºC. γ-Al_2O_3 powder (30-70 nm) was procured from Sigma –Aldrich, India.

Table 3.1. Chemical composition of the Al6061 alloy.

Mg	Si	Mn	Cu	Fe	Ti	Zn	Cr	Al
0.88	0.70	0.33	0.29	0.18	0.02	0.003	0.006	97.591

3.2. Experimental procedure

For fabricating the Al-x %Si, Al-x %Cu and Al-x %Ni alloys (x = 1, 2, 3 and 5 wt.%), the experimental setup used is as shown in Figure 3.1. A 20 kHz ultrasonic generator was used to generate vibrations in molten Al alloys using a 1.5 kW capacity ultrasonic generator unit (Model VCX 1500, Sonics and Materials, USA). The diameter and length of the niobium (Nb) acoustic radiator were 19 mm and 175 mm respectively. It should be noted that the frequency of the Nb radiator changes during UST with an increase in temperature due to being immersed in the melt and with an increase solid fraction in the melt as solidification goes on. However, the

variations are comparable for all the binary aluminium alloys processed in this work. The ultrasonic intensity is given by Equation (3.1) according to Eskin [27]:

$$I = \frac{1}{2}\rho c(2\pi f A)^2 \quad \ldots\ldots\ldots\ldots\ldots\ldots\ldots\ldots\ldots\ldots (3.1)$$

Where ρ is the density of molten metal, c is the speed of sound in the melt, f is the frequency and A is the amplitude. Four amplitudes of ultrasonic horn vibrations were selected; viz. 24 μm, 18 μm, 12 μm and 6 μm (measured using a contactless vibrometer at room temperature). They gave intensity values of about 1400 W/cm^2, 790 W/cm^2, 350 W/cm^2 and 88 W/cm^2 by using Equation (3.1), where c ≈ 1.3×10^3 ms^{-1} in molten aluminium according to Eskin [27] and the density of molten aluminium was taken as ρ = 2375 kgm^{-3}. Eskin [27] determined that the threshold ultrasonic intensity required to produce cavitation in molten aluminium is about 80 W/cm^2. The lowest ultrasonic intensity of 88 W/cm^2 used in this research thus still exceeds this threshold intensity.

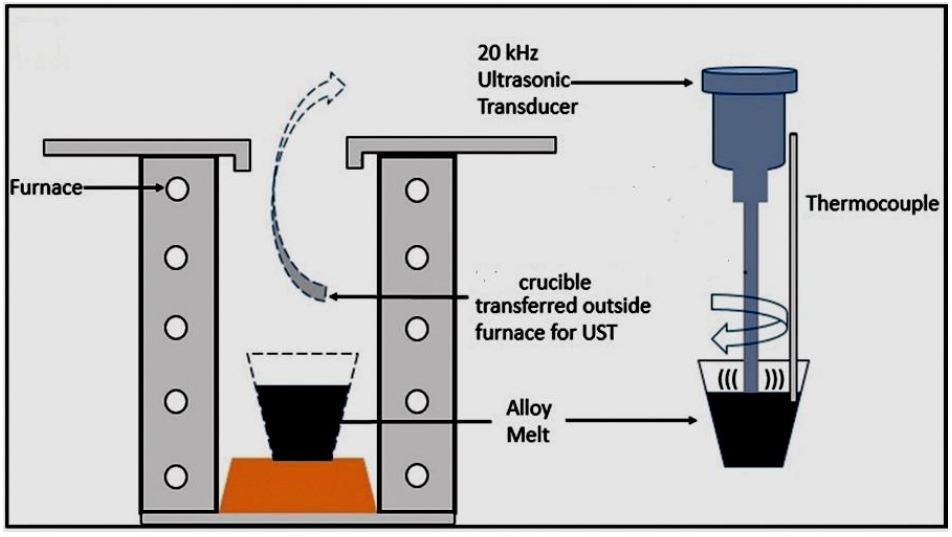

Figure 3.1. Experimental set-up for ultrasonic processing of binary aluminium alloys.

Binary alloys of Al-Si, Al-Cu and Al-Ni with solute contents of 1%, 2%, 3% and 5% were selected for ultrasonic grain refinement. Table 3.2 lists the basic data of the Al-Si, Al-Cu and Al-Ni systems as per the ASM Handbook Vol. 3 Alloy Phase Diagrams (1992) [182]. Phase diagrams of Al-Si, Al-Cu and Al-Ni binary alloys are shown in Figures 3.2, 3.3, and 3.4, respectively [182]. In principle, all four selected Al-x%Cu (x = 1, 2, 3, 5) alloys are off-eutectic

alloys (<5.65 % Cu, Table 3.2) while all four selected Al-x%Ni (x = 1, 2, 3, 5) alloys are hypoeutectic alloys (>0.24 % Ni, Table 3.2). As for the four selected Al-Si alloys, Al-1%Si is off-eutectic (<1.65 % Si, Table 3.1) while the rest three (Al-2%Si, Al-3%Si and Al-5%Si) are all hypoeutectic.

Table 3.2. Basic data of the Al-Si, Al-Cu and Al-Ni alloy systems (k = equilibrium solute partition coefficient; m = liquidus slope).

Alloy system	Eutectic point	Maximum solubility in α-Al
Al-Si	577°C, 12.6 % Si	1.65 % Si
Al-Cu	548.2°C, 33.2 % Cu	5.65 % Cu
Al-Ni	639.9°C, 5.7 % Ni	0.24 % Ni

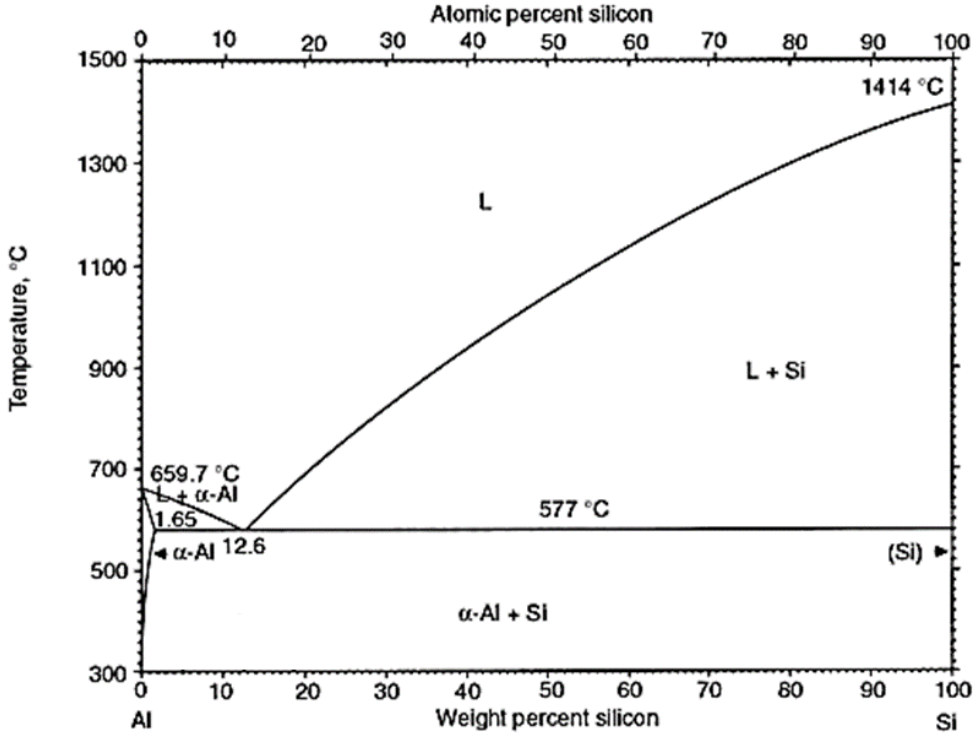

Figure 3.2. Phase diagram of binary Al-Si alloy [182].

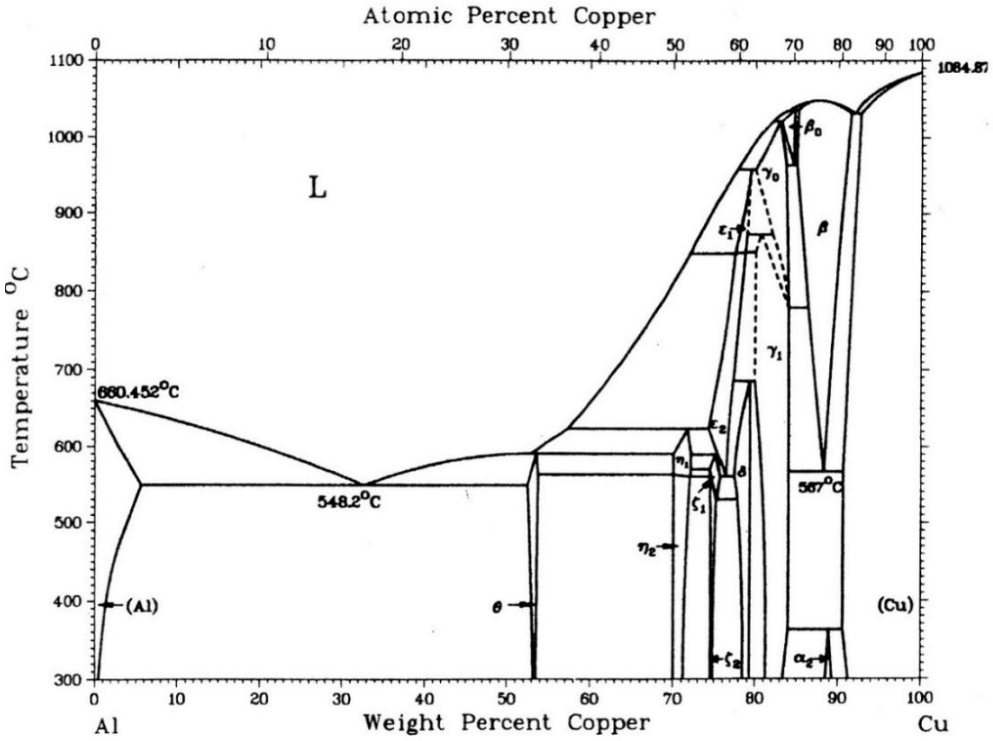

Figure 3.3. Phase diagram of binary Al-Cu alloy [182].

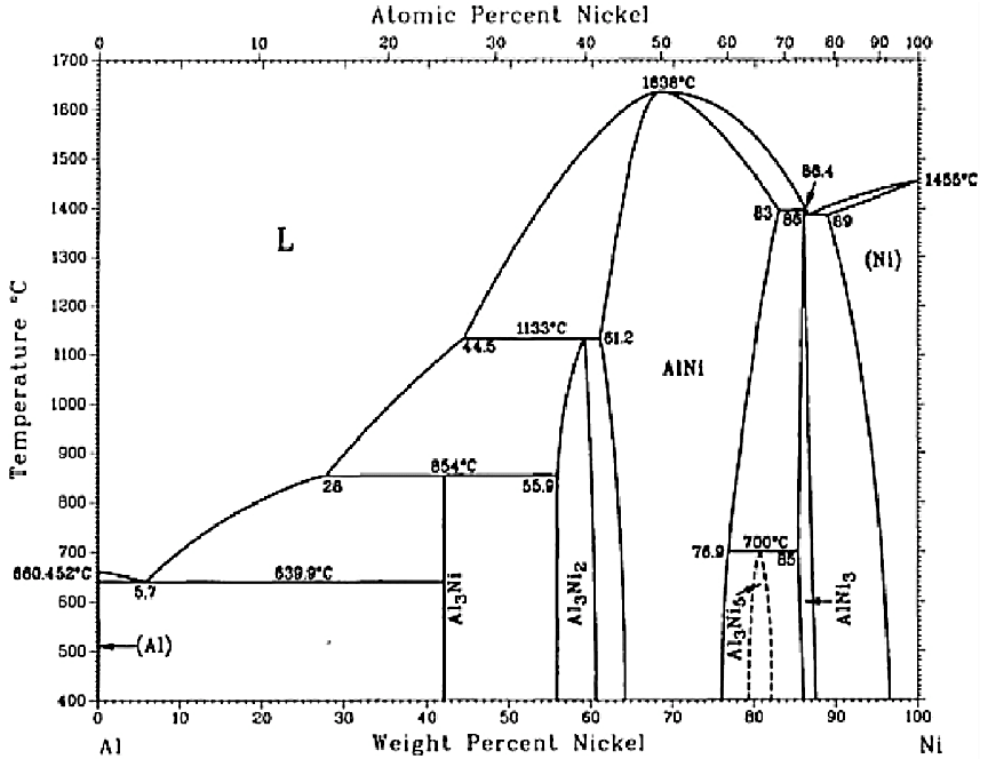

Figure 3.4. Phase diagram of binary Al-Ni alloy [182].

Commercial purity aluminium and respective master alloys were used to make Al–Si, Al-Cu and Al-Ni alloys. In each experiment, 300 grams of the aluminium and master alloy were melted in a graphite crucible (inside diameter: 60 mm) in an electric resistance furnace at 700±5°C, which is at least 40°C higher than the liquidus of each alloy. The melt was held for 30 min to allow for complete dissolution. A thermocouple was placed into the melt to record the cooling process during solidification. The Nb ultrasonic horn was preheated to ~700°C prior to ultrasonic processing. The crucible was withdrawn from the furnace at 700°C and placed on refractory bricks. The Nb ultrasonic horn was then immersed into the melt and the UST system was switched on until solidification was nearly complete. A control sample was cast for each composition under identical conditions but without UST, which is referred to as "as-cast" alloy.

Figure 3.5 shows the schematic experimental setup for the fabrication of aluminium alloy nano-composites by ultrasound assisted solidification technique. It consists of an electric resistance furnace, ultrasonic unit, and thermocouple, along with controlled argon atmosphere. A 19 mm diameter niobium probe was used to transmit 20 kHz ultrasonic waves generated with a 1.5 kW capacity ultrasonic generator unit (Model VCX 1500, Sonics and Materials, USA).

In each experiment, 300 g of Al6061 alloy was heated to UST processing temperature in a graphite crucible (3 mm thickness, 60 mm diameter, and 80 mm length). Upon reaching the UST temperature, Al_2O_3 nano-particles wrapped in aluminium foil were fed into the bottom of the crucible with the help of a plunger. The melt was manually stirred with graphite rod for about 5 min at approximately 45 revolutions per min for initial mixing of the powder and the melt. Ultrasonic probe was inserted into molten metal to a depth of 15-20 mm for 3 min. The processed melt was immediately poured into a steel mold preheated to 400ºC. During UST of molten metal, temperature and time were controlled.

Al6061 matrix nano-composites with one wt.% of nano-sized Al_2O_3 were fabricated at different temperatures of 700ºC, 725ºC, 750ºC and 775ºC using UST. These nano-composites with UST are named as NC700, NC725, NC750, and NC775 respectively. In order to isolate the effect of UST, one control specimen was cast after manual stirring at 775ºC and is named as NC775MS. In this case, all other casting conditions were maintained identical. Best mechanical properties were observed in composites ultrasonically processed at 775ºC. Therefore, two more Al6061 alloy nano-composites were also fabricated with 2 and 3 wt.% of nano-particles at

ultrasonic processing temperature of 775ºC. These USTed nano-composites are named as 2NC775 and 3NC775 respectively.

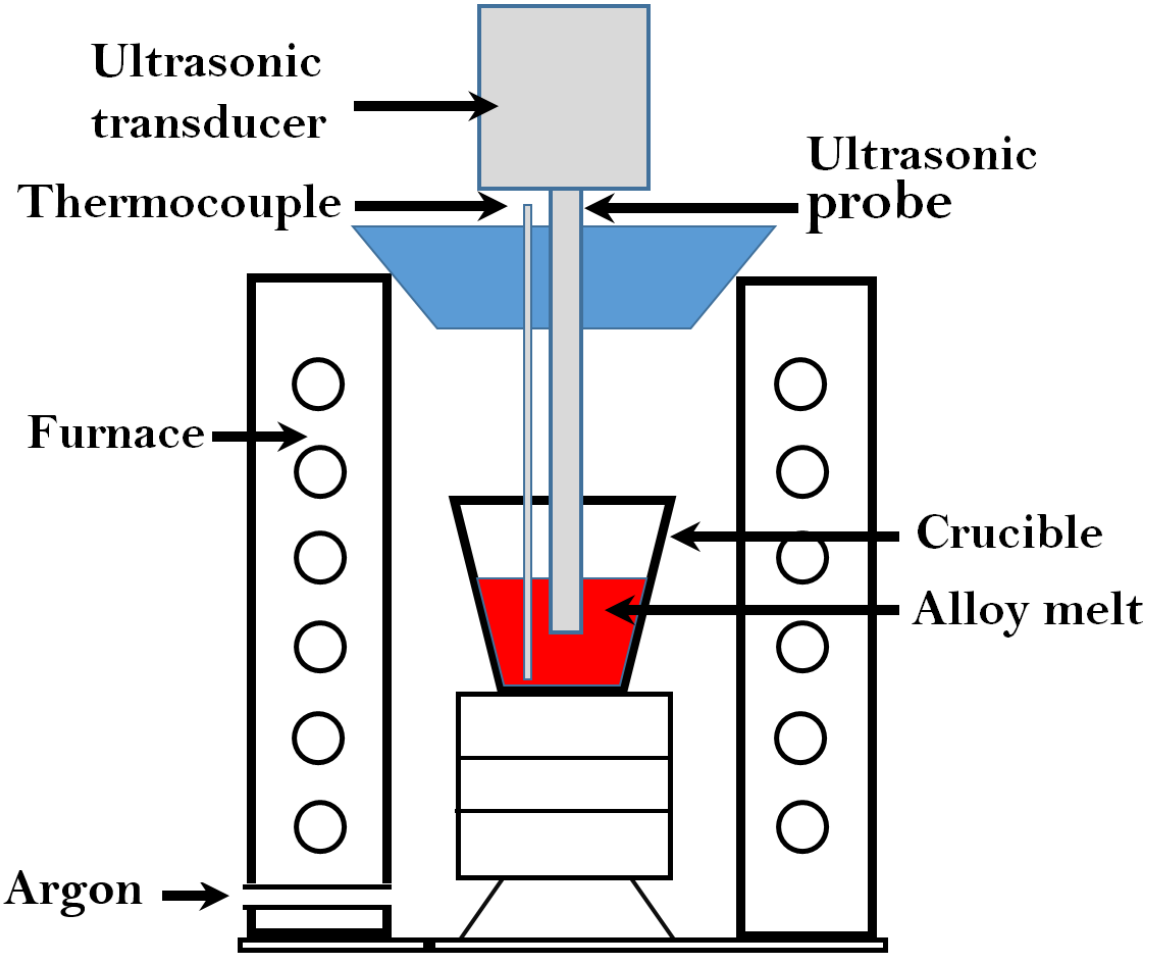

Figure 3.5. Experimental set-up for ultrasonic processing of composites.

3.3. Flow diagram of work

Figure 3.6 shows the flow diagram of present research work. In present work, about ~200 castings including duplicates were made for fabricating 70 actual cast compositions.

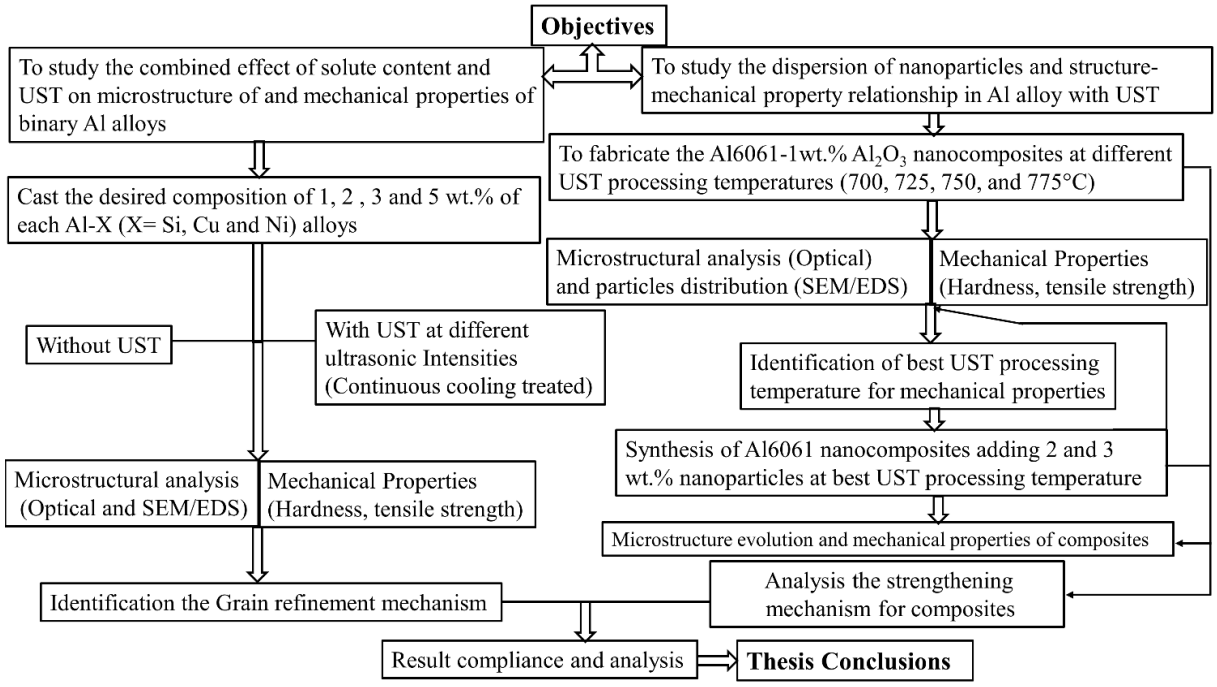

Figure 3.6. Flow diagram of present work.

3.4. Microstructural Characterization

3.4.1. Optical metallography

For metallographic examination, samples were cut from the center of the longitudinal section of each casting for binary aluminium alloys and aluminium alloy composites. Specimen preparation involved grinding in belt grinder using emery paper of 100 grit size followed by manual polishing using 320, 800, 1200, 1500 and 2000 grit-size emery papers. Subsequently, cloth polishing was performed on velvet cloth using a mixture of magnesium oxide powder and water. These polished specimens were cleaned in ultrasonic cleaner using acetone. All specimens were etched using Keller reagent. The chemical composition of the Keller reagent is 2 ml HF, 3 ml HCl, 20 ml HNO_3, and 175 ml water.

A Leica DMI5000 M optical microscope and a Zeiss scanning electron microscope (SEM) operated in secondary electron imaging mode were used for microstructural examination. Mean linear intercept method and ImageJ software were used to determine the average grain size for binary aluminium alloys and aluminium alloy composites. Average inter particle distance in aluminium alloy composites was measured by ImageJ software.

3.4.1.1. TEM sample preparation

Electron microscopy of specimens was also performed using a transmission electron microscope (TEM) (Tecnai G2 20 S-TWIN at 200 kV). TEM provides information about the size, morphological, compositional, and crystallographic characteristics. In the present study, TEM study was used for the analysis of alumina nano powder and dislocations in Al6061 alloy composites. For TEM specimen preparation, a low speed diamond saw was used for cutting thin slice (1-2 mm). This thin slice was glued to an aluminium piece (18 × 18 × 15 mm). Then slice was thinned down using paper polishing with 1500 grit size emery paper. When the thickness of the specimen was reduced to about 100 µm, the specimen was removed from the surface of aluminium piece using acetone. Finally, a specimen punch was used for cutting the 3 mm diameter disc. A Fischione Model 110 twinjet electro-polisher was used for preparing thin foils for TEM examination. For that, the specimen was placed in twin-jet polisher in an electrolytic solution consisting of 20% perchloric acid and 80% methanol. The bath was maintained at a temperature of -20°C using a mixture of liquid nitrogen and methanol. Twinjet polishing was performed for 20-30 s at a voltage of 12V.

3.4.2. Instruments used in microstructural characterization

3.4.2.1. Diamond Cutter

Buehler Isomet 4000-diamond wheel cutter used for cutting the specimens with precision is shown in Figure 3.7. The feed rate and wheel rotation speed of the diamond cutter can be adjusted as per the property of materials.

Figure 3.7. Diamond cutter IsoMet 4000 for cutting the sample.

3.4.2.2. Optical microscopy

A Leica DMI5000 M microscope was used for optical microscopy (Figure 3.8). Microstructures were captured digitally at different magnifications (5x, 10x, 20x, 50x, and 100x) at various locations in the specimens. In general, this instrument has light source, objective lens, condenser and ocular or eyepiece. A recording device can replace the eyepieces. In research, optical microscopy is used for the inspection, analysis, and testing of microstructure of materials.

3.4.2.3. Scanning electron microscope

Figure 3.9 shows the image of ZEISS EVO 18 scanning electron microscope (SEM). The SEM with energy dispersive X-ray spectroscopy (EDS) acquired the microstructural characteristics and elemental analysis of the binary aluminium alloys and aluminium alloy composites specimens. The fracture surface analysis was performed for identifying the type of fracture that occurs during tensile tests. An Oxford EDS spectrometer was used for detecting different elements of aluminium alloys and aluminium alloy composites.

Figure 3.8. Leica (DMI5000 M) optical microscope was used for optical microscopy.

3.4.2.4. Transmission electron microscope:

A TECNAI G2 20 S-TWIN (FEI Netherlands) TEM (Figure 3.10) was used for revealing alumina nano-particles in Al60601 alloy composites. The TEM was operated at an accelerating voltage of 200 kV.

Figure 3.9. ZEISS EVO 18 Special Edition scanning electron microscope used for characterization of binary aluminium alloys and aluminium alloy composites.

Figure 3.10. Transmission electron microscope (FEI Netherlands) used for characterization of aluminium alloy composites.

3.4.2.5. X-ray diffraction (XRD)

XRD is an analytical method used to for phase identification, phase quantification, and for determining the lattice parameter, crystallite size, and dislocation density of the materials. XRD (Rigaku SmartLab) equipment used in present research work for analysis the phase identification of binary aluminium alloys is shown in Figure 3.11. X-ray diffraction patterns were obtained by using Cu Kα radiation (wavelength -1.54 Å) with 2θ ranging from 10º to 120º. For all the diffraction peaks and corresponding values of 2θ, the inter-planer spacing, d, was calculated using the Bragg's law. For identifying the various phases, JCPDS X-ray diffraction database was used.

Figure 3.11. XRD (Rigaku SmartLab) used for characterization of binary aluminium alloys.

3.5. Mechanical testing

Different mechanical testing procedures used for aluminium alloys and aluminium alloy composites are discussed in the following sections.

3.5.1. Hardness tester

Hardness of polished samples was measured using FIE-VM50 PC Vickers hardness tester (Figure 3.12) by applying 1 kg load for a dwell time of 10 s. At least five hardness readings were measured and the average hardness is reported along with standard deviation.

Figure 3.12. Vickers hardness testing machine (FIE Model VM 50) used for the measuring the hardness of aluminium alloys and aluminium alloy composites.

3.5.2 Tensile testing machine

For tensile tests, specimens with a diameter of 4 mm and gauge length of 20 mm were machined and tested using a Tinius Olsen tensile testing machine (H25 K-S) using a constant crosshead speed of 1 mm/min at room temperature, as shown in Figure 3.13. Tensile testing was performed according to ASTM B557 standard. Three samples were tested for each composite/alloy. Tensile strength and ductility of the aluminium alloys and aluminium alloy composites were evaluated from the stress-strain data.

Figure 3.13. H25 K-S Tinius Olsen tensile testing machine used for the tensile testing of aluminium alloys and aluminium alloy composites.

CHAPTER 4

GRAIN REFINEMENT ON BINARY ALUMINIUM ALLOYS

In this chapter**,** the influence of UST and content of solute (1, 2, 3, and 5 wt.%) on the grain refinement of Al-Si, Al-Cu and Al-Ni alloys is examined. Ultrasonic intensities of 0, 88 W/cm^2, 350 W/cm^2, 790 W/cm^2, and 1400 W/cm^2 were applied during continuous cooling. Resulting microstructure of each aluminium alloy is characterized and the combined effect of solute content and UST is discussed.

4.1. Introduction

Al-Si alloys are widely used in automotive and aerospace applications due to their low thermal expansion coefficient, high specific strength, better mechanical properties, and excellent wear and corrosion resistance [26,60,183,184]. Al-Si alloys are mostly used as a foundry alloys [185,186].

Al-Cu alloys are used in automobile, defense, structural, and aircraft applications. Therefore, there is increasing demand in the industries to develop Al-Cu alloys, which show superior creep strength, high strength, stiffness, good fracture toughness, and low heat resistance [187,188]. Addition of Cu solute as a chief alloying element can help to enhance the strength and hardness of aluminium alloys [189,190].

In Al-Ni alloys, reactions between aluminium and nickel form a series of intermetallic of nickel aluminides compounds such as Al_3Ni_2, Al_3Ni, $AlNi_3$, and AlNi [191]. Eutectic reaction occurs at 640°C and at eutectic composition of 6.1 wt.%, producing a eutectic mixture of α-Al and Al_3Ni [84,191]. This intermetallic phase has good mechanical properties and corrosion resistance at elevated temperature. Al-Ni alloys is generally used in engineering and nanotechnology applications such as coatings in turbine blades, sensors and nano-heaters [191,192].

4.2. Results and discussion

4.2.1. Characterization of phases

For understanding the mechanism of grain refinement of Al-Si, Al-Cu, Al-Ni alloys, XRD analyses of cast Al alloys samples were carried out to determine the phases present. Figures 4.1, 4.2, and 4.3 show the XRD spectra of the Al-Si, Al-Cu, Al-Ni alloys samples, respectively. In each alloy, the peak intensity of secondary phase increased with increasing of solute content due to increasing amount of secondary phase. Figure 4.1 shows that the phase constituents in all four Al-Si alloys are primary α-Al phase and secondary silicon phase.

The XRD spectra of Al-Cu alloys show primary α-Al phase and secondary Al_2Cu phase, as shown in Figure 4.2.

Figure 4.3 shows primary α-Al phase and secondary Al_3Ni phase in Al-Ni alloys. Small intensity peak of Al_3Ni phase is observed in c and d spectra. These observed phases in binary aluminium alloys are also verified from the phase diagram of Al-Si alloy, Al-Cu alloy, and Al-Ni alloy, which are shown in Figure 3.2, Figure 3.3, and Figure 3.4, respectively.

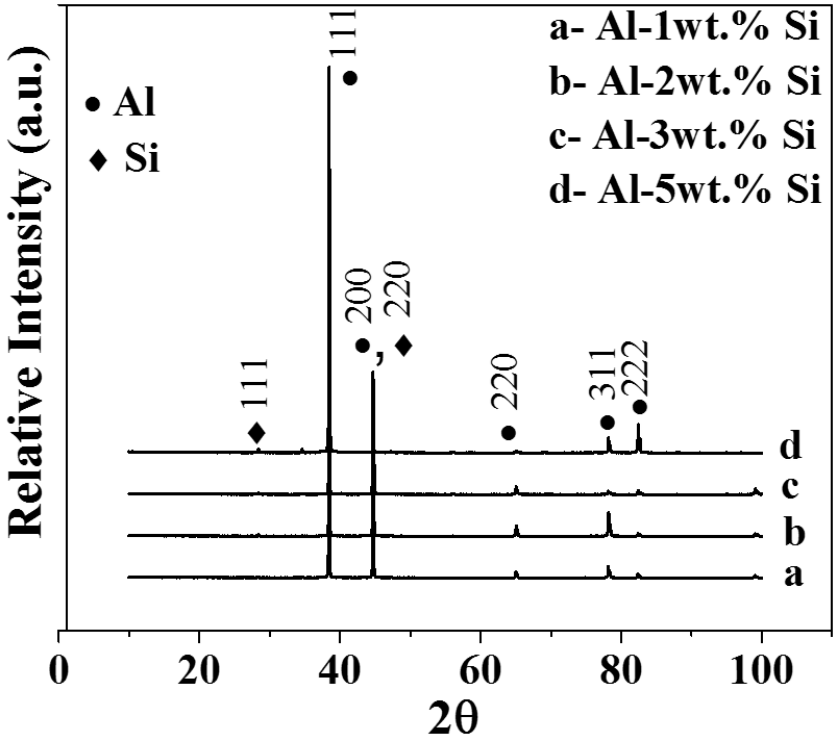

Figure 4.1. XRD patterns of as-cast Al-Si binary alloys.

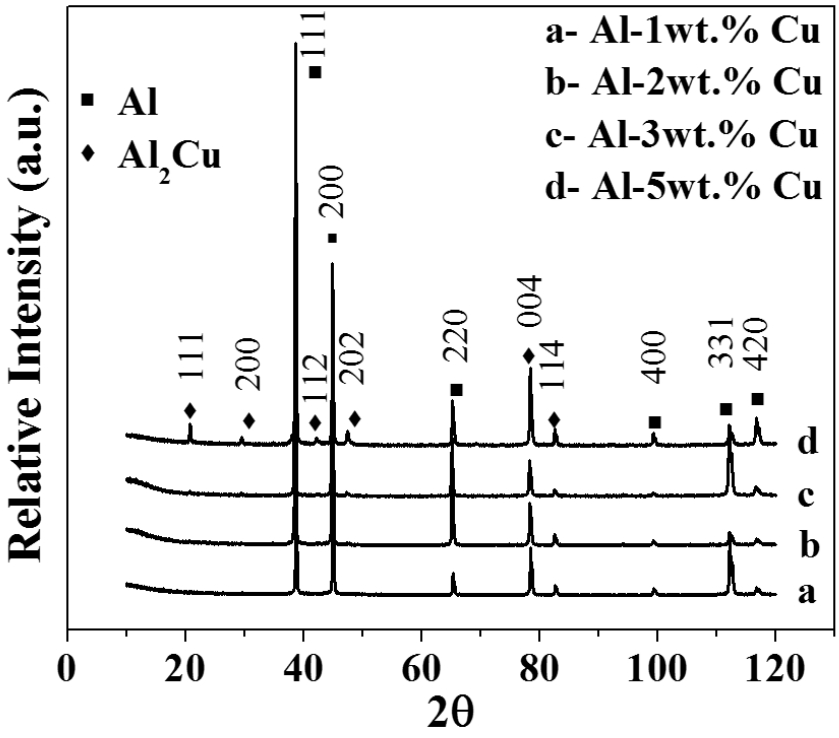

Figure 4.2. XRD patterns of as-cast Al-Cu binary alloys.

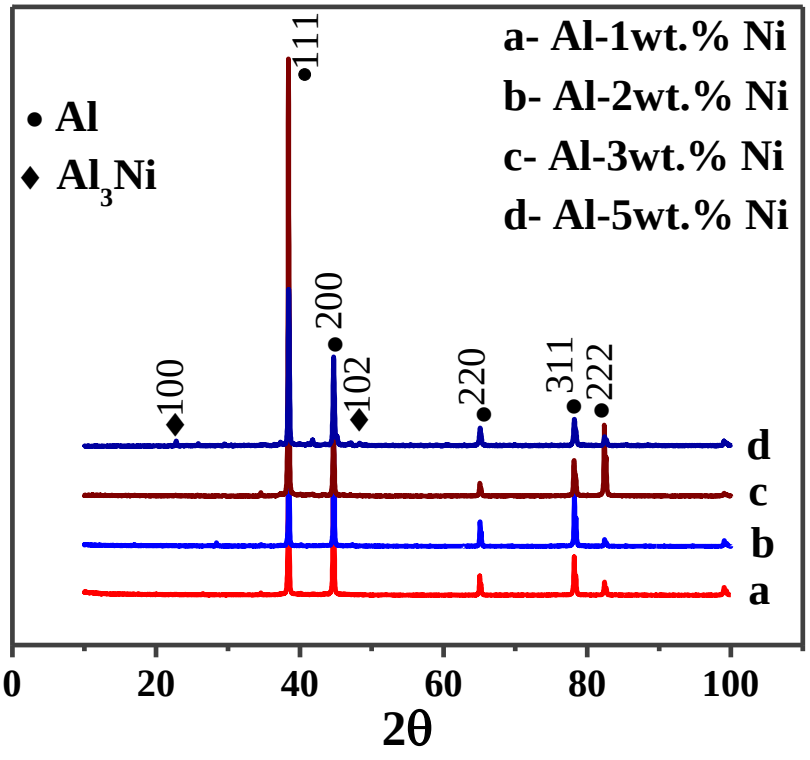

Figure 4.3. XRD patterns of as-cast Al-Ni binary alloys.

4.2.2. Effect of applied ultrasonic intensity and solute content on microstructure of binary Al-Si, Al-Cu, and Al-Ni alloys

Figure 4.4 shows representative optical micrographs of the as-cast Al−(1-5)%Si alloys. Dendritic grains are prominent and the grain structure varies noticeably in each alloy in terms of both grain size and morphology. Dendritic arm spacing and length is decreased by increasing the amount of solute. Primary α-Al phase in Al-1wt.%Si alloy has a larger average grain size of 1625 µm (Figure 4.4a) as compared to 1300, 1078 and 768 µm grain size in Al-2wt.%Si alloy (Figure 4.4b), Al-3wt.%Si alloy (Figure 4.4c), and Al-5wt.%Si alloy (Figure 4.4d), respectively.

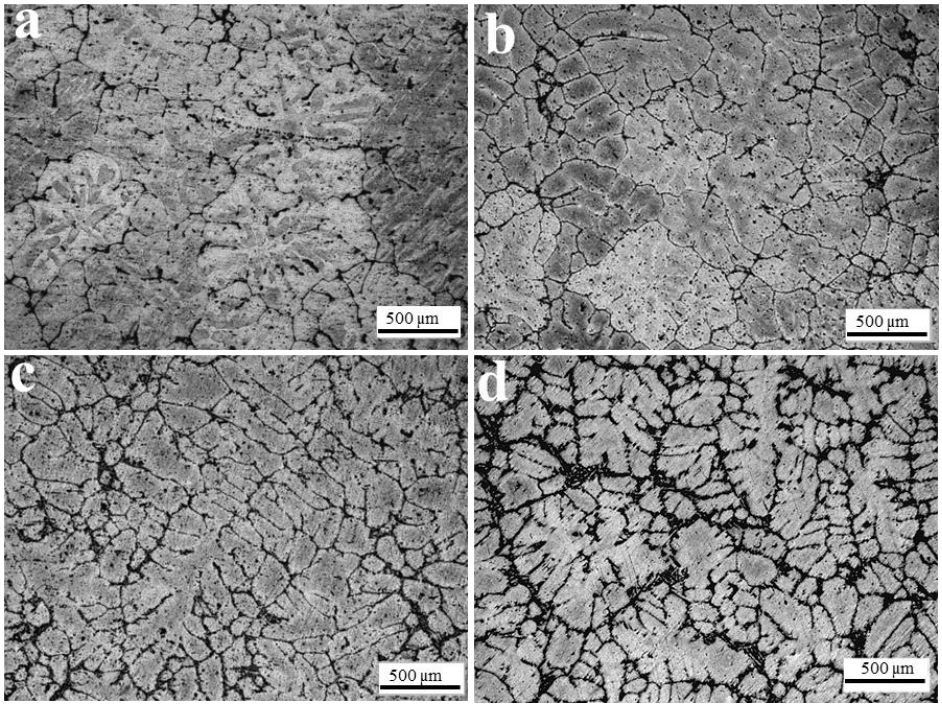

Figure 4.4. Optical micrographs of as-cast Al-Si alloys containing (a) 1 (b) 2 (c) 3, and (d) 5 wt.% Si.

Figure 4.5 shows the SEM micrograph with corresponding EDS spectrum of as-cast Al-5wt.%Si alloy. SEM/EDS analyses were used to help identify the secondary or intermetallic phase present in Al-5wt.%Si alloy. The secondary phase observed in the Al-5wt.%Si alloy is silicon (Figure 4.5). For Al-Si alloy, the microstructure is composed of α-Al dendrites and a eutectic phase. According to the amount of solute (Si), Al-Si alloys can be divided into three categories. These categories are hypoeutectic Al-Si alloys, eutectic Al-Si alloys and

hypereutectic Al-Si alloys. In hypoeutectic Al-Si alloys, range of silicon content is from 1.65 wt.% to less than 12.6 wt.% Si. Compositions of 12.6 wt.% Si and more than 12.6 wt.% Si are categorized as eutectic Al-Si alloy and hypereutectic Al-Si alloys. Phase diagram of the binary Al-Si alloy is shown in Figure 3.2. The eutectic reaction in the Al-Si system is a change of liquid to a solid solution and nearly pure silicon [193]. i.e.

$$L \rightarrow Al_{eut} + Si_{eut} \ldots\ldots\ldots\ldots\ldots\ldots\ldots\ldots \quad (4.1)$$

Dendritic α-Al phase forms at the liquidus temperature of the alloy [193]. At the eutectic temperature, eutectic silicon nucleates in the solute field ahead of the growing α-Al dendrites. Once nucleated, the eutectic silicon grows as flakes into the eutectic liquid. The liquid surrounding the eutectic silicon flakes become enriched with aluminium as it is being depleted of silicon; consequently, eutectic aluminium nucleates and grows on the edges and tips of the eutectic silicon flakes [193]. Finally, aluminium dendrites stop growing upon impingement with the growing eutectic aluminium grains.

It is observed from Figure 4.5 that coarse acicular and long plate-like eutectic silicon phase is distributed non-uniformly among the α-Al dendrites in the as-cast Al-5wt.%Si alloy. The grain boundaries between the eutectic phase and the primary α-Al are hackly type.

Figures 4.6, 4.7, 4.8 and 4.9 show optical micrographs of the Al−(1-5)%Si cast with UST using ultrasonic intensity of 88 W/cm^2, 350 W/cm^2, 790 W/cm^2, and 1400 W/cm^2 processed under continuous cooling condition. These structures reveal finer grains with UST as compared to as-cast Al-Si alloys. Distinct changes in both grain size and morphology are observed after UST.

Figure 4.6 shows the micrograph of Al-Si alloys processed using ultrasonic intensity of 88 W/cm^2. These microstructures show that the grain size of the primary α-Al phase decreases gradually with increasing the amount of solute at a fixed ultrasonic intensity. Upon UST, the dendritic structure that is observed in as-cast Al-Si alloys is changed in to equiaxed structure. However, the morphology of the grain is somewhat coarse possibly because of relatively lower ultrasonic intensity. Average grain size decreased to 241 μm (Figure 4.6d) in USTed Al-5wt.%Si alloy from 768 μm (Figure 4.4d) size of as-cast Al-5wt.%Si alloy. The grain size of USTed Al-1wt.%Si (350 μm), Al-2wt.%Si (312 μm) and Al-3wt.%Si (275 μm) alloys is smaller than respective as-cast alloys.

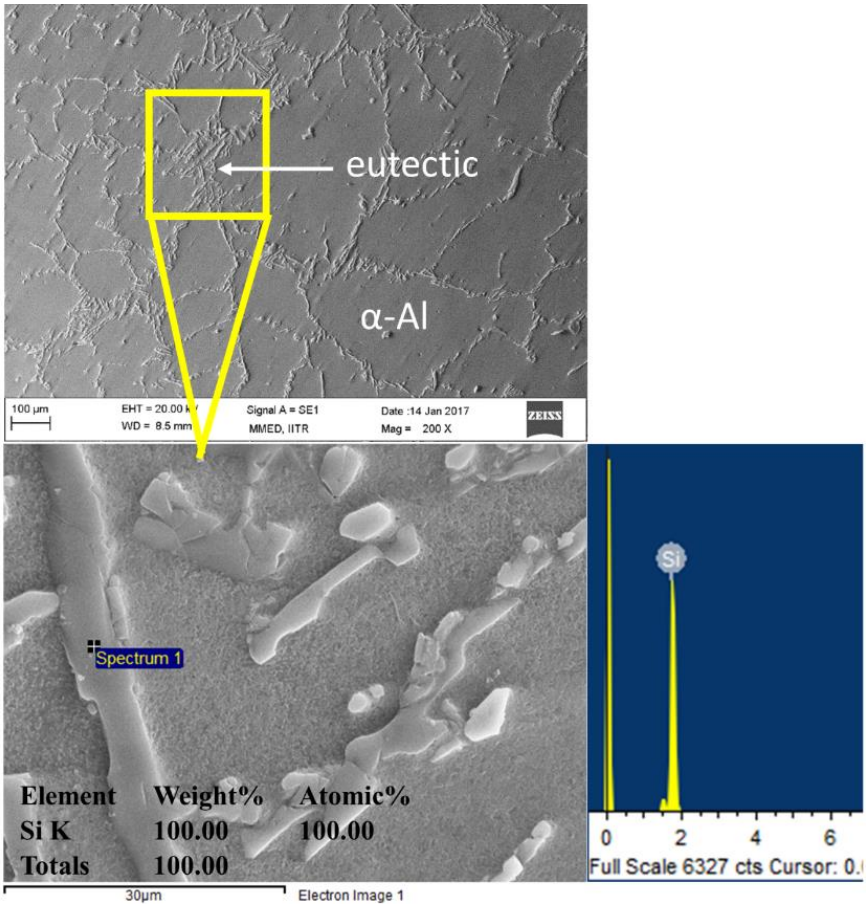

Figure 4.5. SEM images and EDS spectrum of the secondary or intermetallic phases observed in as-cast Al-5wt.%Si alloy.

Figure 4.7 shows optical micrographs of Al-Si alloys processed using ultrasonic intensity of 350 W/cm^2. When ultrasonic intensity increases from 88 W/cm^2 to 350 W/cm^2, grains of α-Al become more fine and globular and the average grain size decreased to 190 µm (350 W/cm^2) from 241 µm (88 W/cm^2) in Al-5wt.%Si alloy. A similar trend in average grain size is observed with different contents of solute.

There is a marginal difference in grain size of alloys USTed using ultrasonic intensity of 790 W/cm^2 (Figure 4.8) and 1400 W/cm^2 (Figure 4.9) at a fixed amount of solute. At the maximum ultrasonic intensity (1400 W/cm^2), more fine and globular α-Al grains with an average grain size of 124 µm are obtained in Al-5wt.%Si alloy (Figure 4.9d) as compared to samples treated with lower ultrasonic intensity levels of 88, 350, and 790 W/cm^2.

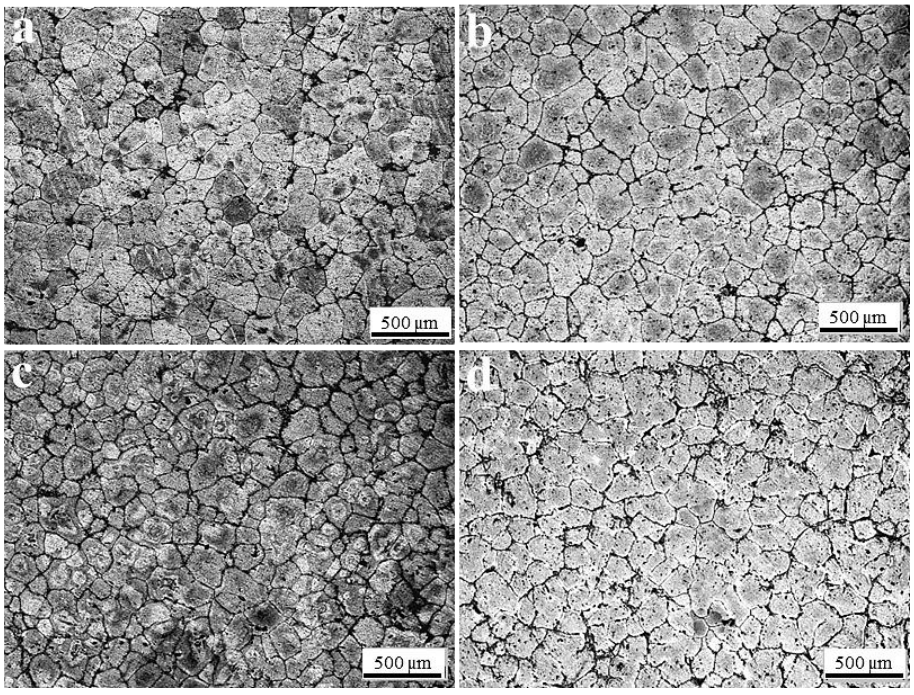

Figure 4.6. Optical micrographs of Al-Si alloys containing (a) 1, (b) 2, (c) 3, and (d) 5 wt.% Si solidified with UST using ultrasonic intensity of 88 W/cm^2.

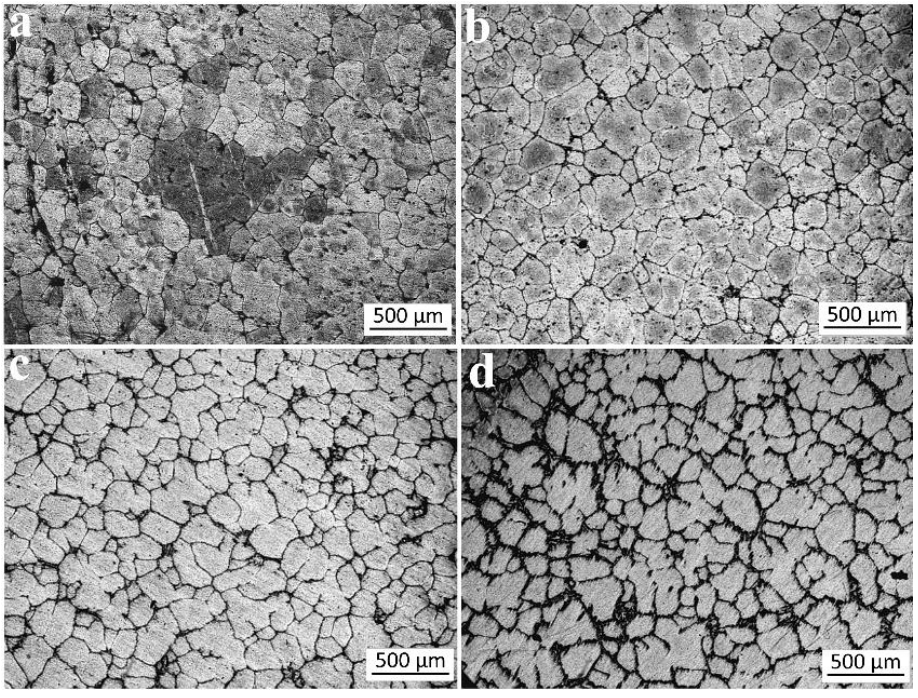

Figure 4.7. Optical micrographs of Al-Si alloys containing (a) 1, (b) 2, (c) 3, and (d) 5 wt.% Si solidified with UST using ultrasonic intensity of 350 W/cm^2.

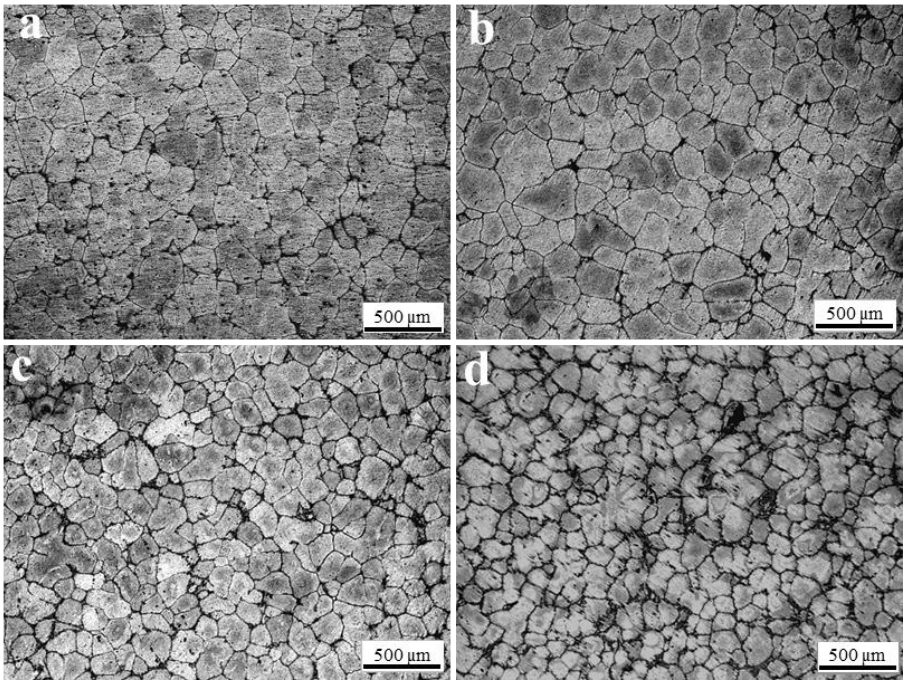

Figure 4.8. Optical micrographs of Al-Si alloys containing (a) 1, (b) 2, (c) 3, and (d) 5 wt.% Si solidified with UST using ultrasonic intensity of 790 W/cm^2.

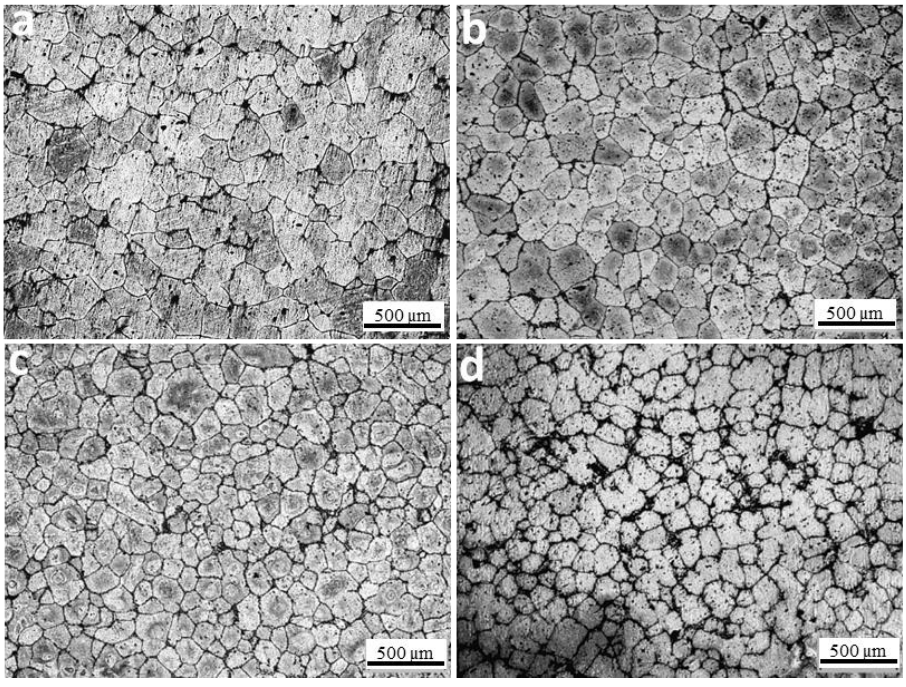

Figure 4.9. Optical micrographs of Al-Si alloys containing (a) 1, (b) 2, (c) 3, and (d) 5 wt.% Si solidified with UST using ultrasonic intensity of 1400 W/cm^2.

Figures 4.10, 4.11, 4.12, 4.13, 4.14 and 4.15 show optical micrographs of as-cast and USTed Al−(1-5)%Cu alloys while Figs 4.16, 4.17, 4.18, 4.19, 4.20 and 4.21 show the cases for as-cast and with UST Al−(1-5)%Ni alloys. Dendritic structures are dominant in all the as-cast Al-Cu alloys (Figure 4.10) and Al-Ni alloys (Figure 4.16). Smallest average grain size of 738 µm is obtained in as-cast Al-5wt.%Cu alloy (Figure 4.10d).

Figure 4.11 shows the SEM micrographs of as-cast Al-5wt.%Cu alloy. The atomic ratio of Al to Cu obtained from the EDS spectrum suggests that the intermetallic phase in Al-5wt.%Cu alloy is Al_2Cu compound (Figure 4.11). Microstructure consists of α-Al dendrites and inter-dendritic eutectic phase (α-Al+ Al_2Cu). Such non-equilibrium eutectic phase is also reported in Al-0.92wt.%Cu alloy, Al-2.12wt.%Cu alloy, Al-3.24wt.%Cu alloy, and Al-4.23wt.%Cu alloy [87], and in Al-2.53wt.%Cu alloy [194] .

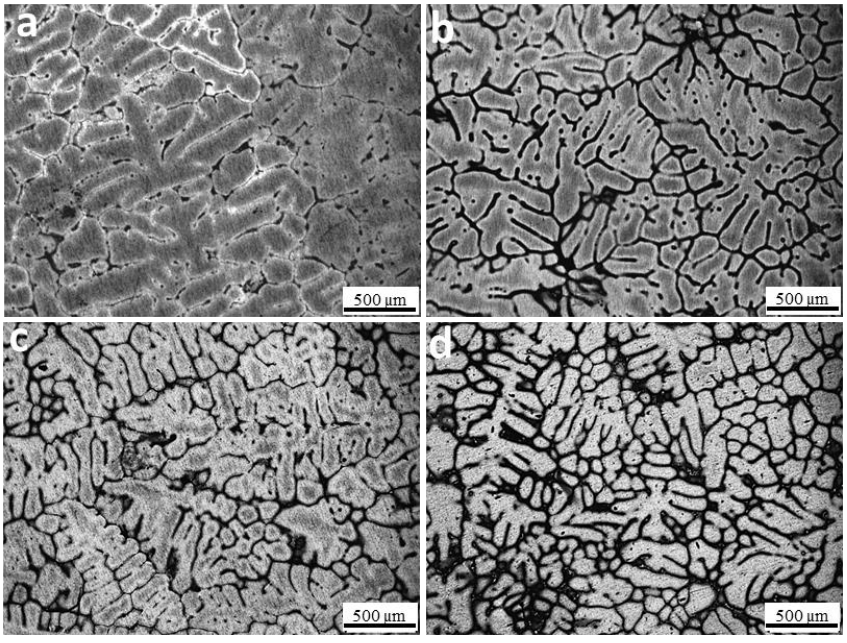

Figure 4.10. Optical micrographs of as-cast Al-Cu alloys containing (a) 1 (b) 2 (c) 3, and (d) 5 wt.% Cu.

Figures 4.12, 4.13, 4.14 and 4.15 show optical micrographs of Al-Cu alloys treated using ultrasonic intensity of 88 W/cm^2, 350 W/cm^2, 790 W/cm^2, and 1400 W/cm^2 during continuous cooling UST. Finer and globular grains are observed in Al-5wt.%Cu alloy at highest ultrasonic intensity of 1400 W /cm^2 employed in this work.

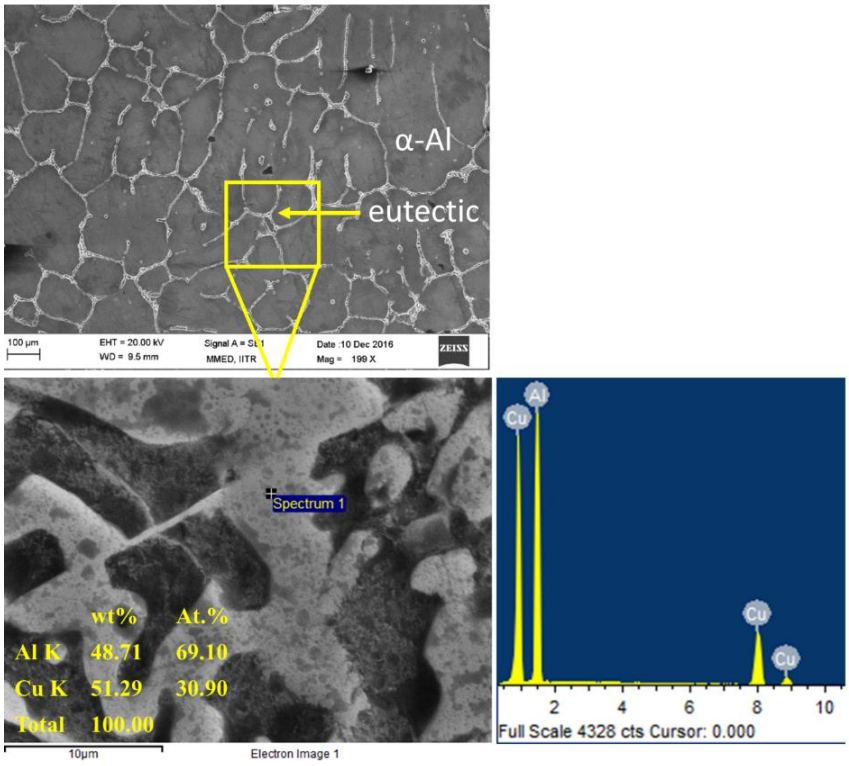

Figure 4.11. SEM images and EDS spectrum of the secondary or intermetallic phases observed in as-cast Al-5wt.%Cu alloy.

Figure 4.12 shows the micrographs of Al-Cu alloys USTed using ultrasonic intensity of 88 W/cm^2. Grain size of primary α-Al phase decreased with increase in solute content. α-Al phase has finer dendritic structure as compared to as-cast alloy in all four Al-Cu alloys. Largest grain size of 920 µm is obtained in Al-1wt.%Cu alloy (Figure 4.12a). Grain sizes of Al-2wt.%Cu alloy, Al-3wt.%Cu alloy and Al-5wt.%Cu alloy are 722 µm (Figure 4.12b), 643 µm (Figure 4.12c) and 410 µm (Figure 4.12d), respectively. The coarse dendritic structure, which is observed in as-cast Al-1wt.% Cu alloy and Al-2wt.% Cu alloy, is changed to fine dendritic or rosette type structure by applying the UST. More fine dendrites and some equiaxed grains are obtained at 3 wt.% of solute, and the density of equiaxed grains are higher at the largest amount of solute (5 wt.%) used in this work. As compared to Al-Si alloys, grain refinement efficiency of Al-Cu alloys is poor at lower ultrasonic intensity (88 W/cm^2). Grain refinement efficiency of alloy is mainly dependent upon the potency of solute and other factors, which are discussed in Chapter 5.

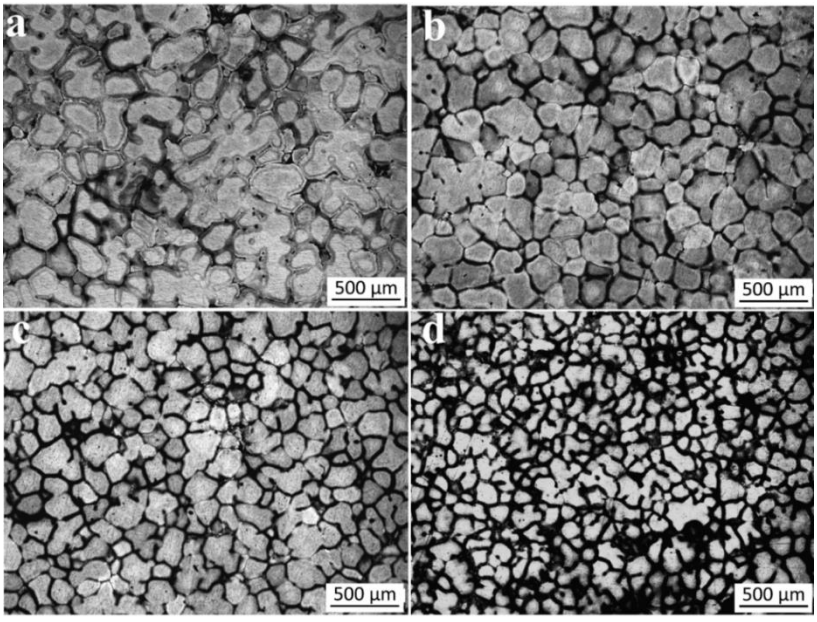

Figure 4.12. Optical micrographs of Al-Cu alloys containing (a) 1, (b) 2, (c) 3, and (d) 5 wt.% Cu solidified with UST using ultrasonic intensity of 88 W/cm^2.

Figure 4.13 shows the optical micrographs of Al-Cu alloys USTed using ultrasonic intensity of 350 W/cm^2. By increasing the ultrasonic intensity from 88 W/cm^2 to 350 W/cm^2, mixed type of microstructure is observed in Al-Cu alloys (Figure 4.13). Al-1wt.%Cu alloy and Al-2wt.%Cu alloy show small dendrites or rosette-like grains (Figure 4.13a and b). For Al-3wt.%Cu alloy and Al-5wt.%Cu alloy, mixed type of structure is observed with some equiaxed grain structure and few small dendrites or rosette-like grains (Figure 4.13c and d). For a fixed intensity, equiaxed grains are more in Al-5wt.%Cu alloy as compared to other alloys. Average grain size of Al-5wt.%Cu alloy (208 µm) (Figure 4.13d) is smaller than Al-1wt.%Cu alloy (650 µm) (Figure 4.13a), Al-2wt.%Cu alloy (413 µm) (Figure 4.13b), and Al-3wt.%Cu alloy (388 µm) (Figure 4.13c). The applied ultrasonic intensity of 350 W/cm^2 is over four times is more than the threshold intensity.

UST performed using ultrasonic intensity of 790 W/cm^2 produced more equiaxed grains and fewer small sized dendritic grains as compared to microstructures of specimens USTed at lower ultrasonic intensity values of 350 W/cm^2 and 88 W/cm^2 (Figure 4.14). UST at the intensity of 1400 W/cm^2 resulted in finest and equiaxed grains in Al-3wt.%Cu alloy and Al-5wt.%Cu alloy. An average grain size of 107 µm (Figure 4.15d) was achieved in the Al-5wt.%Cu alloy

after UST. However, small dendrites or rosette-like grains are still visible at Al-1wt.%Cu alloy and Al-2wt.%Cu alloy (Figure 4.15a and b).

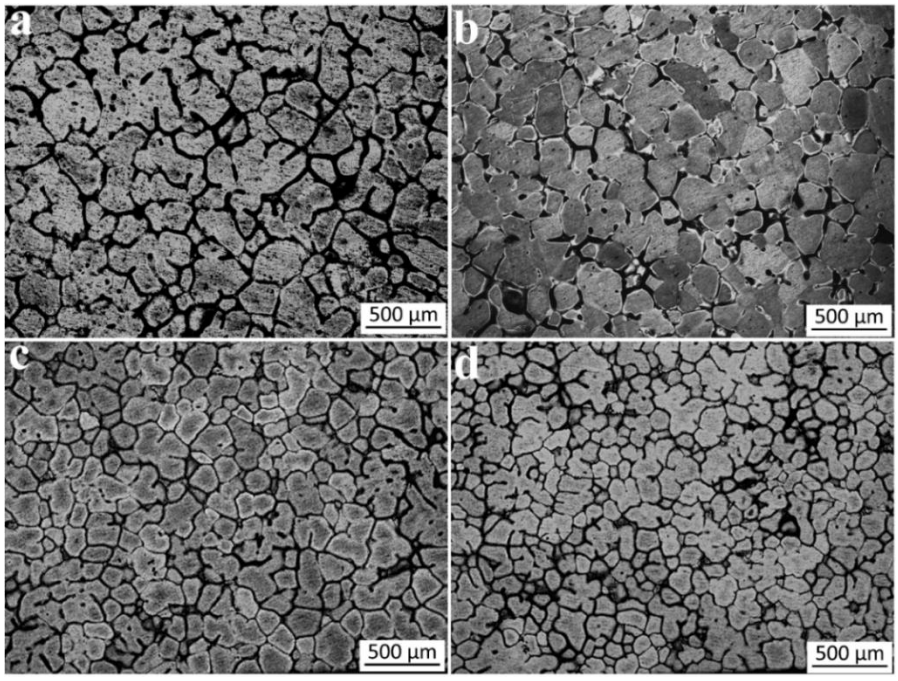

Figure 4.13. Optical micrographs of Al-Cu alloys containing (a) 1, (b) 2, (c) 3, and (d) 5 wt.% Cu solidified with UST using ultrasonic intensity of 350 W/cm^2.

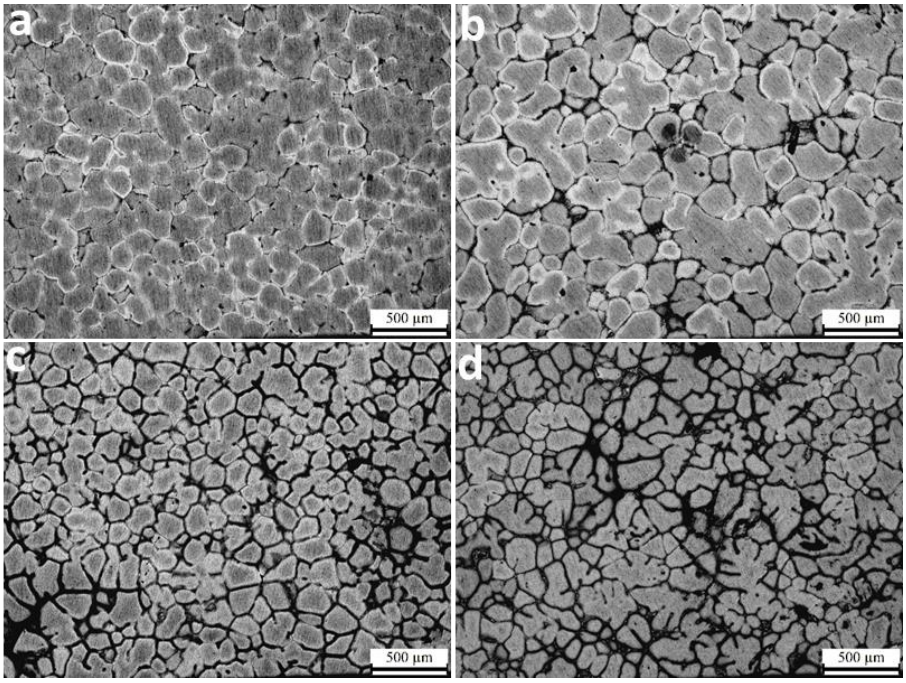

Figure 4.14. Optical micrographs of Al-Cu alloys containing (a) 1, (b) 2, (c) 3, and (d) 5 wt.% Cu solidified with UST using ultrasonic intensity of 790 W/cm^2.

In as-cast Al-Ni alloys, dendrite arm spacing and dendritic arm length decreased in Al-Ni alloys up to 3 wt.% of solute (Figure 4.16). Upon adding 5 wt.% nickel in pure aluminium, there is no further decrease in the dendrite arm spacing and dendritic arm length as compared to Al-3wt.%Ni alloy. However, extent of grain refinement in Al-5wt.%Ni is higher than Al-1wt.%Ni alloy and Al-2wt.%Ni alloy under all conditions, either as-cast or with UST.

Figure 4.17 shows SEM micrograph and corresponding EDS spectrum of as-cast Al-Ni alloys. The microstructure of as-cast Al-5wt.%Ni alloy consists of dendritic α-Al phase surrounded by (α-Al + Al_3Ni) eutectic. Figure 4.17 also shows the composition of the grain boundary phase. EDS results show that the atomic ratio of Al and Ni is about 1:3, which suggests that the intermetallic phase in the Al-5wt.%Ni alloy is Al_3Ni.

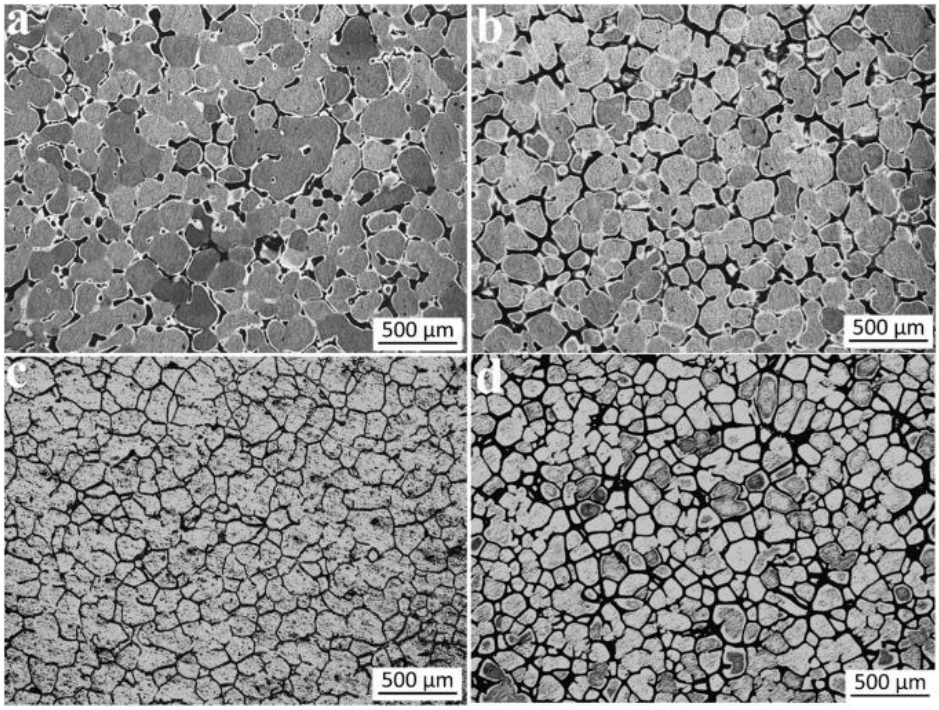

Figure 4.15. Optical micrographs of Al-Cu alloys containing (a) 1, (b) 2, (c) 3, and (d) 5 wt.% Cu solidified with UST using ultrasonic intensity of 1400 W/cm^2.

Figures 4.18, 4.19, 4.20, and 4.21 depict the optical micrographs of Al-Ni alloys cast with UST. Al-Ni alloys showed even more promising response to UST where the grain morphology changed from dendritic to nearly globular even at the low solute levels at all the ultrasonic intensity levels. Grain size is drastically reduced as compared to respective as-cast Al-Ni alloys. Stronger grain refinement effect with an average grain size of 120 µm is observed in the Al-3wt.%Ni alloy at maximum ultrasonic intensity, as shown in Figure 4.21c. In all the conditions,

either as-cast or with UST, the grain refinement in Al-3wt.%Ni alloy is more as compared to Al-5wt.% Ni alloy.

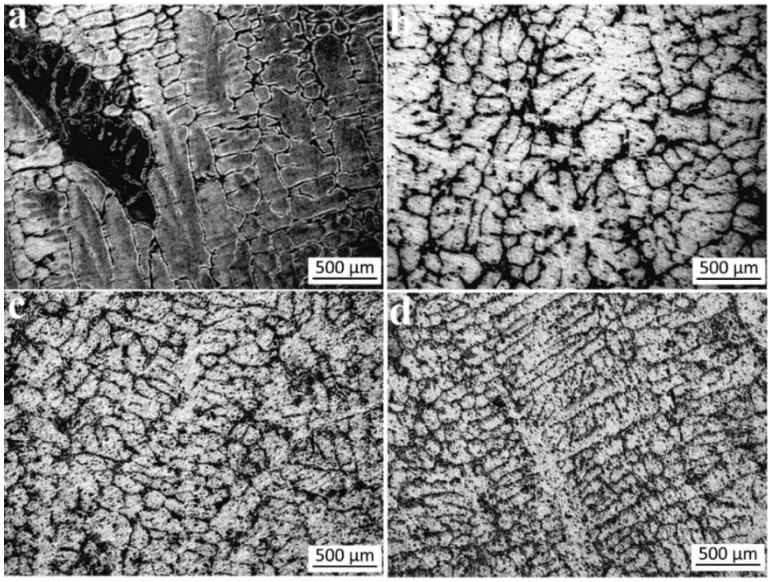

Figure 4.16. Optical micrographs of as-cast Al-Ni alloys containing (a) 1 (b) 2 (c) 3, and (d) 5 wt.% Ni.

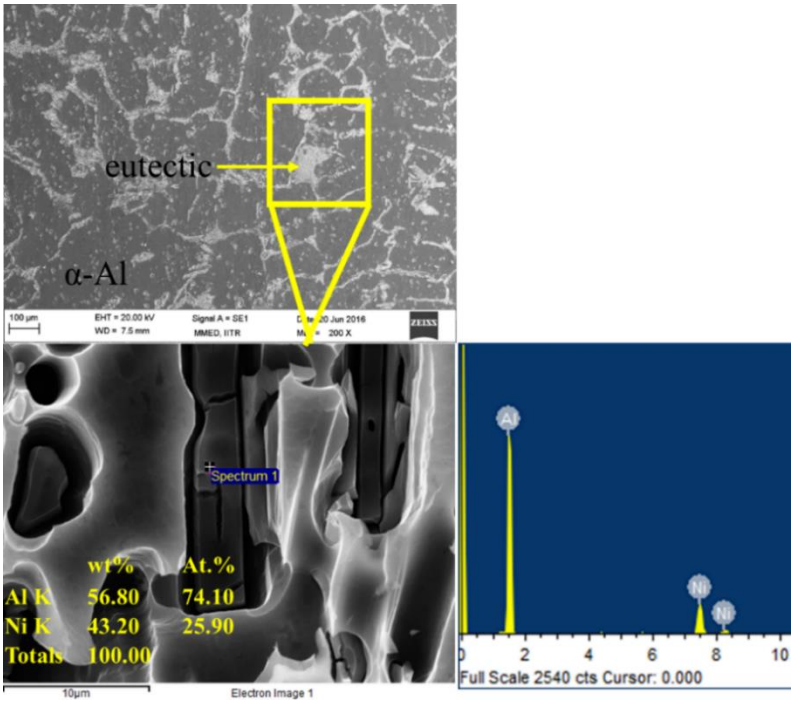

Figure 4.17. SEM images and EDS spectrum of the secondary or intermetallic phases observed in as-cast Al-5wt.%Ni alloy.

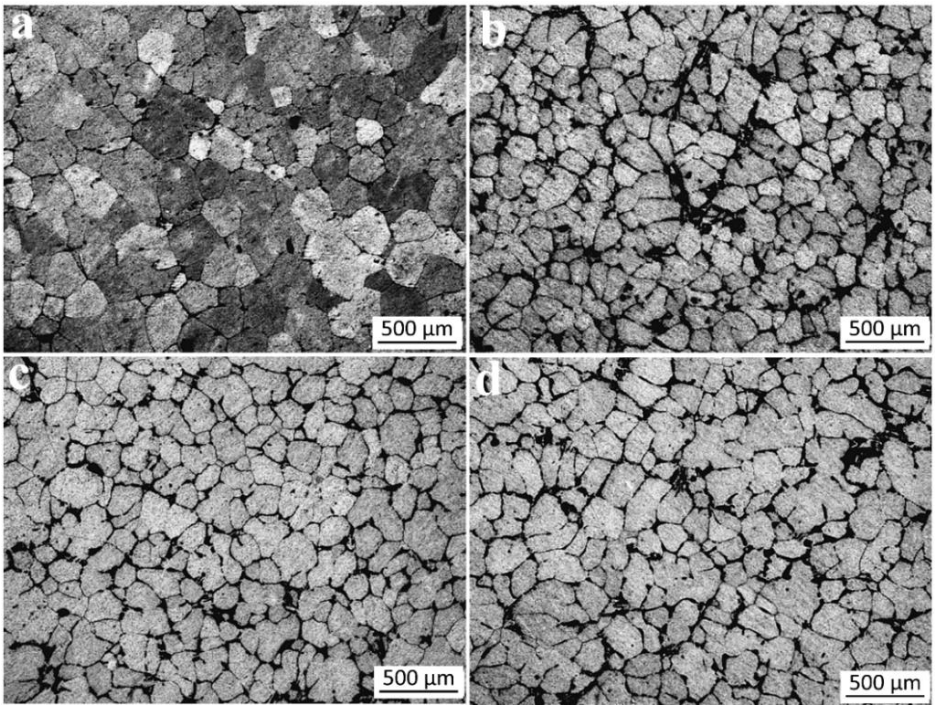

Figure 4.18. Optical micrographs of Al-Ni alloys containing (a) 1, (b) 2, (c) 3, and (d) 5 wt.% Ni solidified with UST using ultrasonic intensity of 88 W/cm^2.

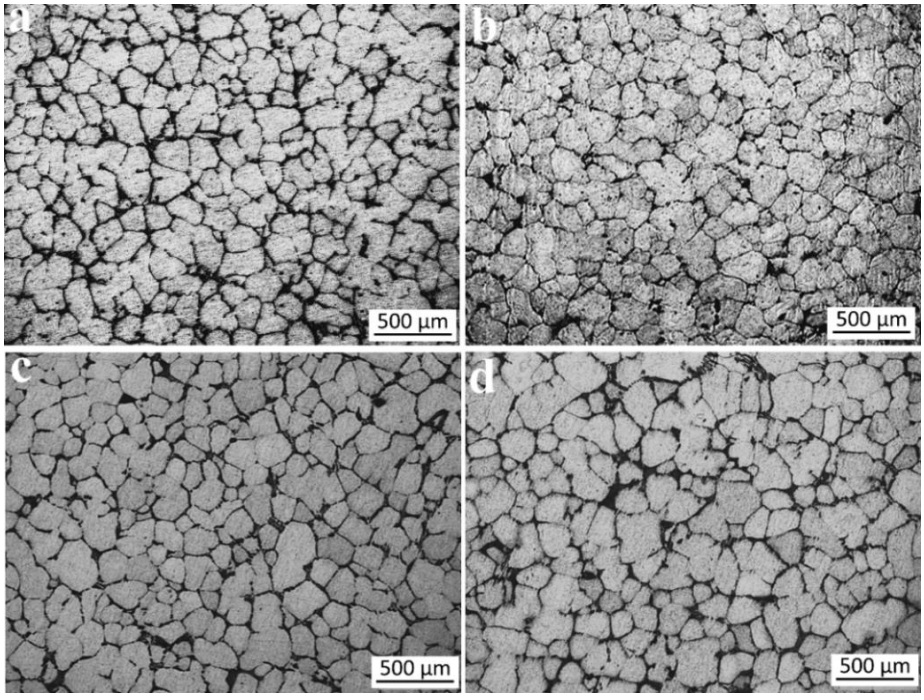

Figure 4.19. Optical micrographs of Al-Ni alloys containing (a) 1, (b) 2, (c) 3, and (d) 5 wt.% Ni solidified with UST using ultrasonic intensity of 350 W/cm^2.

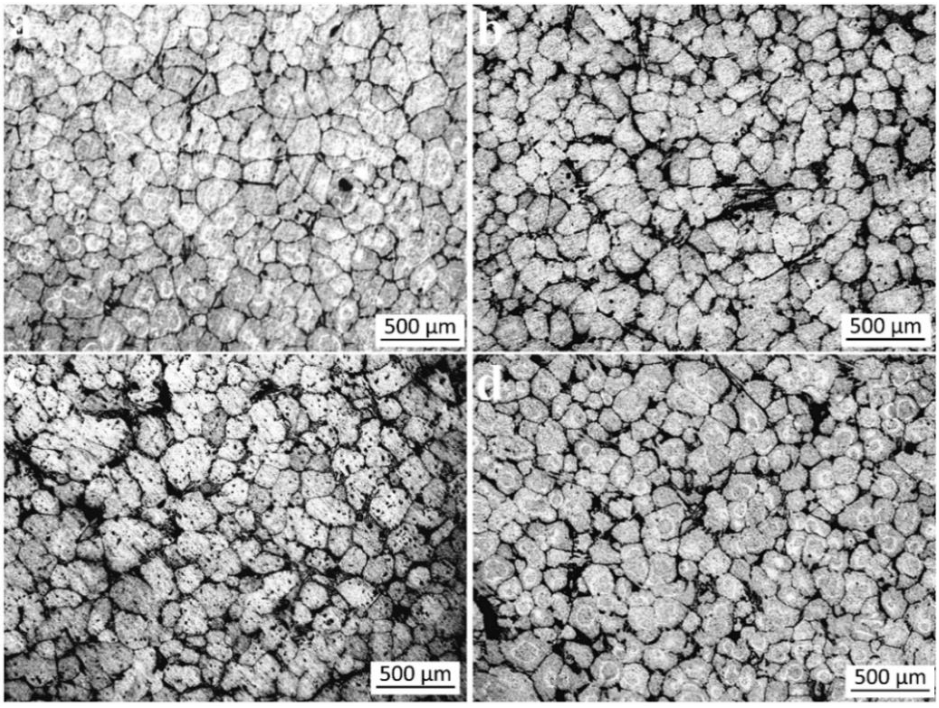

Figure 4.20. Optical micrographs of Al-Ni alloys containing (a) 1, (b) 2, (c) 3, and (d) 5 wt.% Ni solidified with UST using ultrasonic intensity of 790 W/cm^2.

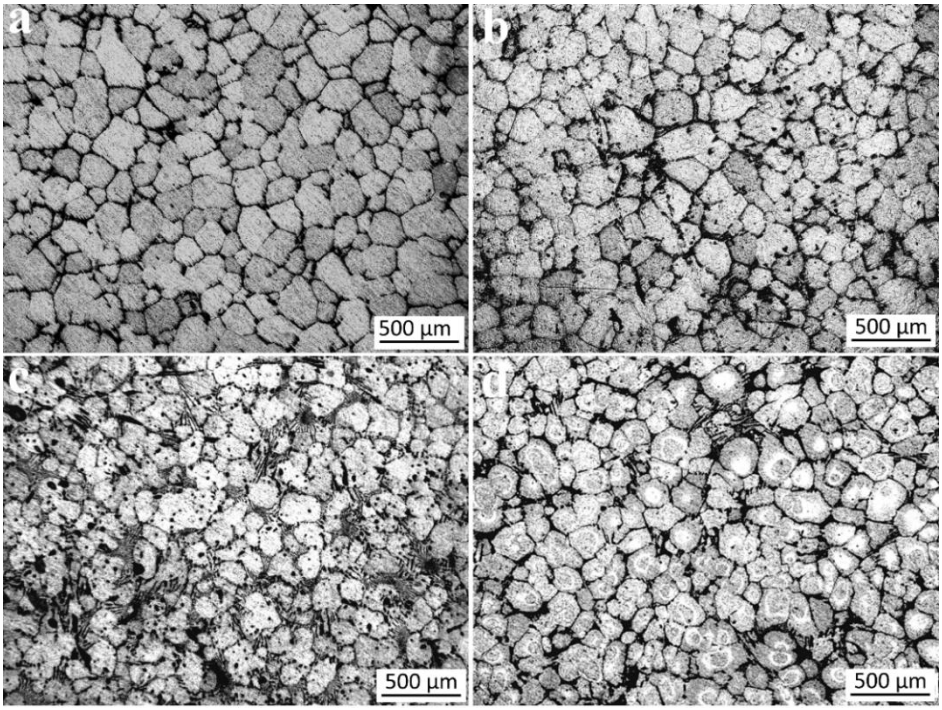

Figure 4.21. Optical micrographs of Al-Ni alloys containing (a) 1, (b) 2, (c) 3, and (d) 5 wt.% Ni solidified with UST using ultrasonic intensity of 1400 W/cm^2.

The relative effect of each factor, i.e. solute content and ultrasonic intensity, is evaluated by estimating the percentage decrease in grain size induced by each factor, as shown in Figure 4.22. For as-cast Al-Si alloys, increasing Si content by 5 times from 1% to 5% reduced the grain size by ~52% (Figure 4.22a). While at 1wt.%Si, increasing ultrasonic intensity by 15 times from 88 W/cm^2 to 1400 W/cm^2 resulted in a decrease in average grain size by ~37%. The decrease in average grain size is ~48% in the case of Al-5wt.%Si alloy (Figure 4.22b). As for as-cast Al-Cu alloys, increasing Cu content from 1% to 5% reduced the average grain size by 58% (Figure 4.22c). Similarly, increasing ultrasonic intensity from 88 W/cm^2 to 1400 W/cm^2 reduced the average grain size by 66% at 1 wt.% Cu, (Figure 4.22d) and by 85% at 5 wt.% Cu, which is much more pronounced than the cases with 1wt.% Si and 5 wt.% Si. The smallest grain size obtained (107 μm) is at 5 wt.% Cu with UST intensity of 1400 W/cm^2. As regards as-cast Al-Ni alloys (Figure 4.22e), the average grain size decreased by 23% with increasing Ni content from 1% to 5%. At 5wt.%Ni, the grain size is reduced by ~40% with increasing ultrasonic intensity from 88 W/cm^2 to 1400 W/cm^2 (Figure 4.22f).

Another observation of the role of solute in ultrasonic grain refinement is its influence on grain morphology. In addition to grain size reductions, solute content has also affected the consistency in grain morphology in the microstructure after UST. At low solute contents (e.g., 1% and 2%), although equiaxed grains can be achieved by UST as shown in Figure 4.15 (a, b), it has been found that the grain morphology is often inhomogeneous and inconsistent. In contrast, at the highest solute content (e.g. 5%), the grain morphology is homogeneous and consistent throughout each sample after UST, particularly at the highest applied ultrasonic intensity level (i.e., 1400 W/cm^2). This is an important advantage of combining the highest solute content with the highest ultrasonic intensity. In general, the combined use of the highest solute content and highest ultrasonic intensity produces highest grain refinement. This is consistent with observations reported by Qian et al. [59] on ultrasonic grain refinement of Mg-Al and Mg-Zn alloys.

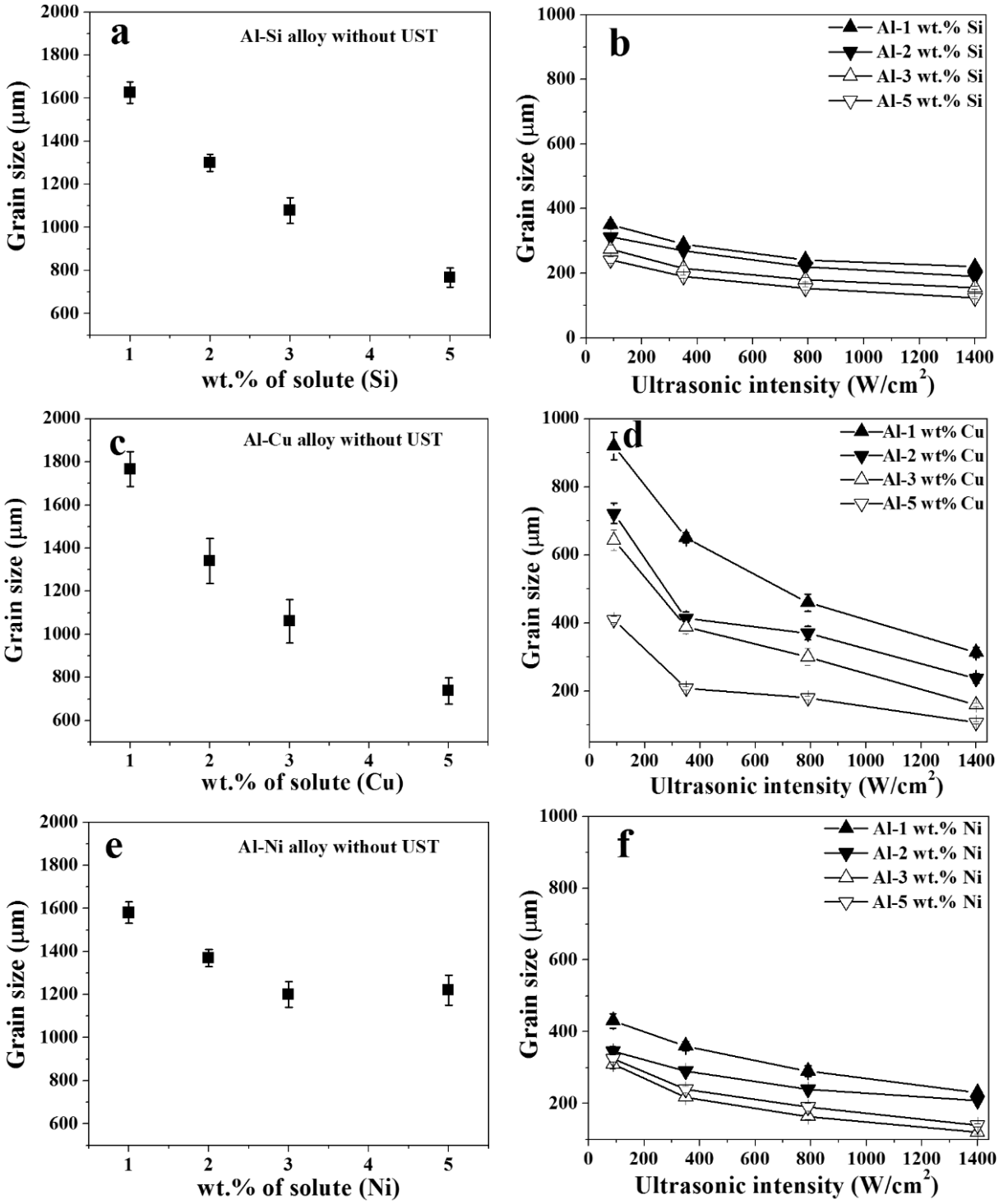

Figure 4.22. Variations of average grain size with solute content for Al-Si alloys- (a) as-cast and (b) with UST, Al-Cu alloys- (c) as-cast and (d) with UST, and Al-Ni alloys- (e) as-cast and (f) with UST.

4.2.3. Effect of UST and solute content on grain density

From the changes in microstructure, several researchers have studied the influence of solute and ultrasonic intensity in terms of grain density [28,59,195]. Grain density is more closely linked with nucleation than grain size [59,195]. Figures 4.23, 4.24, 4.25 show the variations in grain density of Al-Si, Al-Cu and Al-Ni alloys with respect to different levels of ultrasonic intensity (88, 350, 790, and 1400 W/cm^2) and solute contents (1, 2, 3 and 5 wt.%). Grain density values of as-cast and with USTed aluminium alloys are calculated by assuming that the grains are spherical. Grain density of as-cast aluminium alloys is very small, less than five grains/mm^3. That is why they are invisible in the plot. The results show that at a fixed ultrasonic intensity level, the grain density of aluminium alloys increased with increasing solute content, which highlights the important role of solute.

For Al-Si alloys (Figure 4.23), the grain density increased from 45 to 136 grains/mm^3 with increasing solute content from 1 wt.% to 5 wt.% at the minimum ultrasonic intensity of 88 W/cm^2. At the solute content of 5 wt.% Si, the grain density increased from 179 to 867 grains/mm^3 at ultrasonic intensity of 1400 W/cm^2, i.e. the grain density increased by about 6 times upon increasing the ultrasonic intensity 16 times from 88 to 1400 W/cm^2. An almost linear relationship is observed between the grain density and ultrasonic intensity in the range of 88-1400 W/cm^2, for Al-3wt.%Si and Al-5wt.%Si alloys. For Al-1wt.%Si and Al-2wt.%Si alloys, linear relationship is found in the range of 88-790 W/cm^2 and 350-790 W/cm^2, respectively.

For Al-Cu alloys (Figure 4.24), at ultrasonic intensity of 1400 W/cm^2, the grain density increased from 61 to 1554 grains/mm^3 with increasing solute content from 1 wt.% to 5 wt.%. In particular, the grain density of Al-1wt.%Cu alloy, at ultrasonic intensity of 1400 W/cm^2, is thirty times higher than that at 88 W/cm^2. The grain density values of Al-1wt.%Cu alloy, Al-2wt.%Cu alloy, and Al-3wt.%Cu alloys show a nearly linear increase with increasing ultrasonic intensity of 88 to 790 W/cm^2. However, thereupon, there is a sharp change of slope from 790 W/cm^2 to 1400 W/cm^2. By increasing the ultrasonic intensity ~16 times from 88 to 1400 W/cm^2, the grain density in the Al-5wt.%Cu alloy increased by about 58 times. A drastic change of grain density of the Al-5wt.%Cu alloy is observed at ultrasonic intensity of 1400 W/cm^2 as compared to other UST cast alloys. Grain density of Al-5wt.%Cu alloy increased by about 777 times as compared to Al-1wt.%Cu alloy at ultrasonic intensity of 88 W/cm^2.

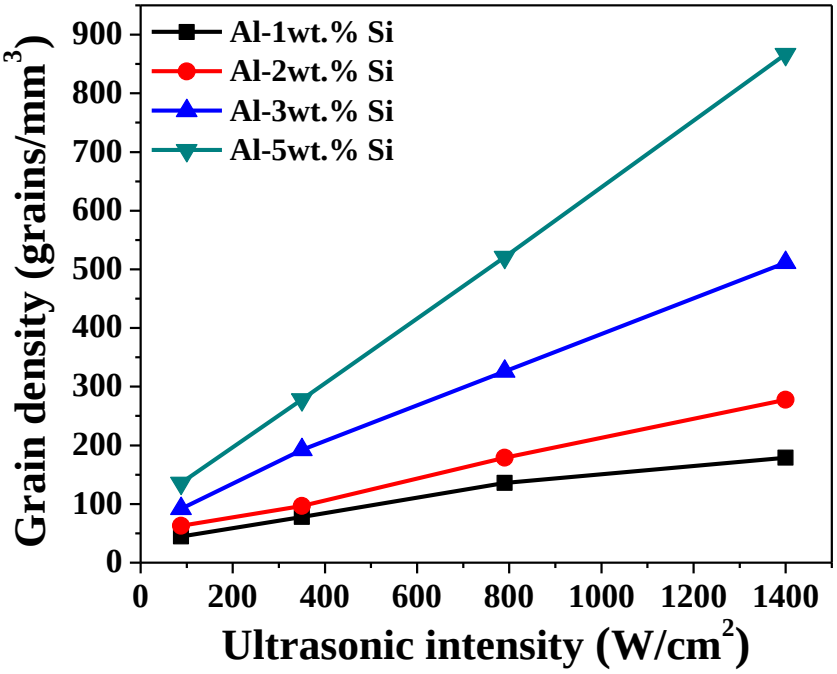

Figure 4.23. Variation of grain density with ultrasonic intensity for Al-Si binary alloys.

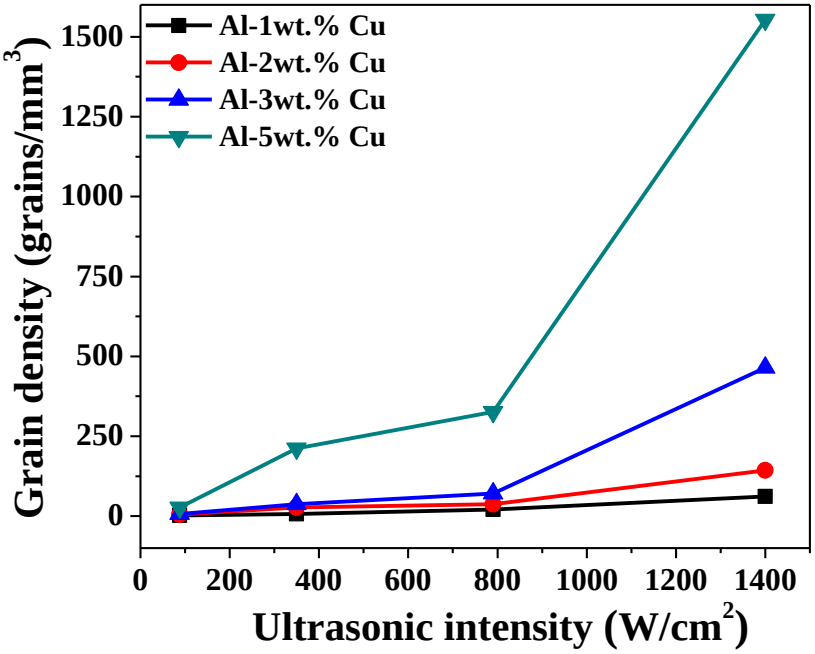

Figure 4.24. Variation of grain density with ultrasonic intensity for Al-Cu binary alloys.

For Al-Ni alloys (Figure 4.25), a linear relationship exists between the grain density and ultrasonic intensity (88-1400 W/cm^2) only for Al-1wt.%Ni and Al-2wt.%Ni alloys. The value of grain density in Al-5wt.%Ni alloy is lower than that of Al-3wt.%Ni alloy but higher than those of Al-1wt.%Ni and Al-2wt.%Ni alloys. At a given solute level of three and 5 wt.% Ni, the grain

density increased by 17 times and 9 times respectively, when the ultrasonic intensity is increased 16 times from 88 to 1400 W/cm^2.

Grain density is significantly increased by increasing both the solute content and ultrasonic intensity. Thus, it is clear that the combined effect of solute and ultrasonic intensity in the grain refining of Al alloys is significant. Qian et al. [59] also reported similar effects of solute content and ultrasonic intensity on the grain density of magnesium alloys.

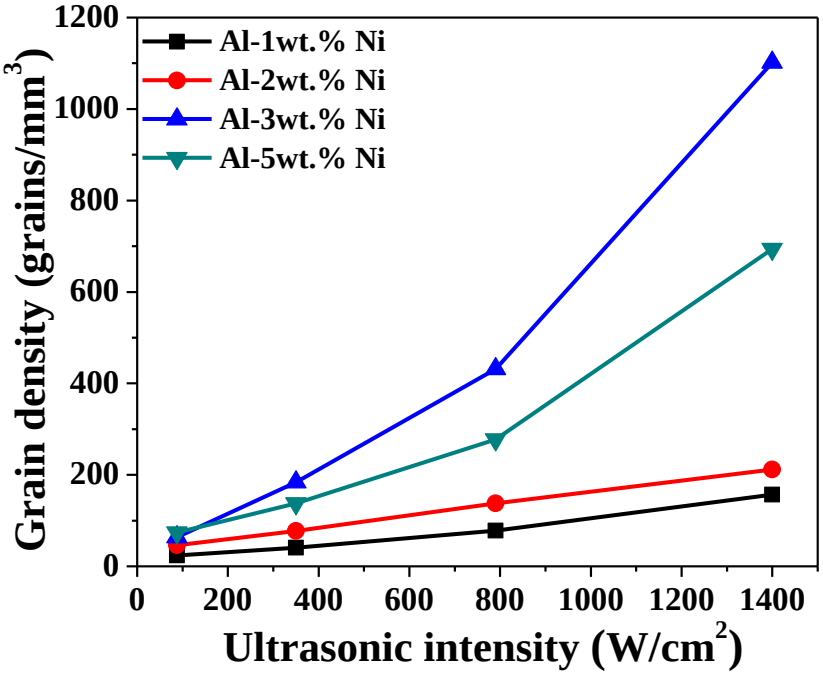

Figure 4.25. Variation in grain density with ultrasonic intensity for Al-Ni binary alloys.

4.2.4. Ultrasonic grain refinement mechanism

Ultrasonic grain refinement mechanisms are briefly described in Chapter 2. However, in literature, there is still no definite evidence available as to which mechanism is dominant in ultrasonic grain refinement of aluminium alloys.

As per Radjai and Miwa [196], ultrasonic irradiation is important to produce the nuclei or crystallites initially, in the volume of the liquid near the ultrasonic horn by enhanced nucleation due to wetting of insoluble nucleating particles and/or due to the pressure pulse mechanism. These nuclei can be subsequently dispersed into other parts of the melt by convection and other dynamic effects such as cavitation and ultrasonic streaming, as per Ramirez et al. [197] and Qian et al. [59]. Wang et al. [37] reported that high intensity UST produced more bulk nuclei in the

irradiated melt than in conventional solidification. These nuclei can be effectively distributed throughout the melt by acoustic streaming, which is related to acoustic pressure (P) defined below by Eskin [27].

$$P = 2\pi\rho Acf \ldots\ldots\ldots\ldots\ldots\ldots \quad (4.1)$$

The acoustic pressures corresponding to the four amplitudes used (24 μm, 18 μm, 12 μm and 6 μm) in this work are 10.6 MPa,7.9 MPa, 5.3 MPa and 2.7 MPa, respectively, which are clearly greater than the threshold value of 1 MPa required for the generation of acoustic streaming in molten aluminium according to Eskin [27]. Thus, acoustic steaming has most likely contributed to the effective distribution of nuclei and therefore extensive grain refinement observed in this work.

Table 4.1 summarizes the common ultrasonic grain refinement mechanisms discussed in literature. The main operating mechanism depends on ultrasonic processing temperature, ultrasonic processing time, and temperature of the horn and nature of the molten alloy. It is often difficult to determine which mechanism is predominant and similar is the case for this research.

Table 4.1. Summary of ultrasonic grain refinement mechanisms reported in literature.

Referred work	**Material**	**Ultrasonic horn**	**UST temperature**	**Mechanism**
Fukui et al [98]	Al-18%Si alloy	Preheated to processing temperature	Semi-solid range	Cavitation enhanced heterogeneous nucleation
Ramirez et al. [82]	AZ31,AZ91 and AJ62	-----	Above liquidus (680°C) for 3 min	Pressure pulse mechanism
Matsuda et al. [107]	Al-4%Si alloy	Preheated to 800°C	Above and below liquidus	Cavitation enhanced heterogeneous nucleation
Atamanenko et al. [95]	Al-11%Cu	----	Continuous cooling	Cavitation enhanced heterogeneous nucleation
Wang et al. [14]	Al-0.4%Ti	Preheated	Above liquidus temperature	Cavitation enhanced heterogeneous nucleation
Wang et al. [28]	Al-2%Cu	Without preheated	695°C to 653°C (liquidus to just below solidus, 655°C)	Cavitation enhanced heterogeneous nucleation

Ramirez et al. [82]	Mg alloy	------	Above liquidus temperature (680°C) for 3 min.	Either cavitation enhanced heterogeneous nucleation or dendritic fragmentation
Youn and Kim [198]	A356 and A390 alloy	Preheated to 400°C	Above liquidus temperature and semi-solid range (1, 5,10, 15 and 20 min)	Cavitation enhanced heterogeneous nucleation
Li et al. [105]	Al-1.65%Si	Preheated to 600°C	Above liquidus (20, 40, 60, 80, 100 and 120 s)	Pressure- pulse mechanism
Kotadia and Das [36]	Al-Si alloy	-------	Continuous cooling	Cavitation enhanced heterogeneous nucleation

4.3. Summary of results

Following conclusions are drawn from this chapter:

1. By increasing the content of solute, the average grain size decreased in as-cast binary aluminium alloys.
2. Average grain size of all the Al alloys decreased with increasing ultrasonic intensity and solute content. Nearly equiaxed grains were obtained in binary Al-Si, Al-Cu and Al-Ni alloys that contained sufficient solute (3% or 5%) and solidified under ultrasonication at the intensity level of 1400 W/cm^2.
3. A combination of high solute content and high-intensity UST during solidification produced significant grain refinement in terms of both grain size and grain morphology for the Al-Si, Al-Cu and Al-Ni systems studied. In addition, high solute content is important to ensure homogenous and consistent grain morphology in ultrasonic grain refinement.

CHAPTER 5

GRAIN REFINEMNT MECHANISMS

In Chapter 4, combined influence of solute concentration and UST on the grain refinement of aluminium-based alloys is studied. In this chapter, grain refining efficiency of different solutes is analyzed by considering the growth restriction factor, StJohn's model, freezing range, and constitutional supercooling parameter.

5.1. Calculation of growth restriction factor

As discussed earlier, binary alloys of Al-Si, Al-Cu and Al-Ni with solute contents of 1%, 2%, 3% and 5% were studied for ultrasonic grain refinement. Table 5.1 shows the values of liquidus slope and equilibrium partition coefficients of the Al-Si, Al-Cu and Al-Ni systems, which are calculated from Figures 3.2, 3.3, and 3.4. The *m(k-1)* parameters for Al-Si, Al-Cu and Al-Ni systems are also listed in Table 5.1.

Table 5.1. Data from the phase diagrams of the Al-Si, Al-Cu and Al-Ni systems (*k*= equilibrium solute partition coefficient; *m*= liquidus slope).

Alloy system	*k*	*m*	m(k-1)
Al-Si	0.130	−6.62	5.759
Al-Cu	0.17	−3.38	2.805
Al-Ni	0.042	−3.6	3.449

Murty et al. observed that solute content plays an important role in grain refinement in multi-component aluminium alloys [12]. StJohn and co-workers showed that both the nuclei and solute play an important role in the grain refinement of both aluminium and magnesium alloys [199]. As discussed in chapter 2, growth restriction factor (*Q*), offers an effective means of analyzing the grain refining efficiency of solutes. It was first used by Maxwell and Hellawell [73] to assess the dependence of grain refinement on alloy system characteristics for Al-Ti, Al-Zr and Al-Cr alloys.

Values of *Q* calculated by using the equation 2.9 are shown in Figure 5.1. Value of *Q* increased with the weight percentage of solute. For 1 wt.% solute, the value of *Q* for Al-Si alloy is two and 1.7 times higher than Al-Cu and Al-Ni alloys, respectively. This is reflected in Figures 4.6, 4.7, 4.8, and 4.9, which show that the grain refinement in Al-Si alloys upon UST is more as compared to Al-Cu alloy at low amount of solute (1% and 2%) due to higher segregating power of silicon in aluminium alloy as compared to solute copper. There is not much difference in values of *Q* between copper and nickel solutes in pure aluminium. However, inconsistent results are observed in terms of growth restriction factor for Al-Si and Al-Ni alloys. Whereas *Q* values are larger for silicon solute at 1 and 2 wt.% as compared to nickel solute, the grain size of these alloys is approximately similar at 1 and 2 wt.% of solute with UST. Further, as mentioned earlier, the grain refinement of Al-3wt.%Ni alloy is larger as compared to Al-3wt.%Si alloy, although the growth restriction factor of silicon solute is approximately two times higher as compared to nickel solute. Therefore, growth restriction factor cannot fully explain the mechanism of grain refinement.

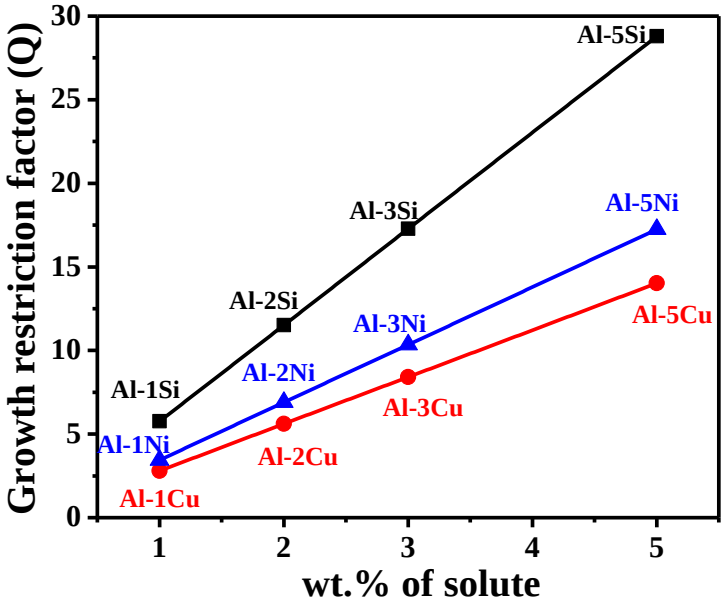

Figure 5.1. Growth restriction factors of Al-Si, Al-Cu and Al-Ni alloys.

For the understanding of grain refinement mechanism, another model was proposed by Easton and StJohn [69] and formulated theoretically by Qian et al. [59] in equation 2.14. Figure 5.2 shows average grain size vs. 1/*Q* for the as-cast and USTed Al-Si, Al-Cu and Al-Ni alloys.

Table 5.2 shows the values of *a* and *b* obtained via best linear fit of the data between grain size and 1/*Q* shown in Figure 5.2. For as-cast alloys, the number of active nucleants (proportional to 1/*a*) is small in each alloy as compared to the same alloy with UST. This is consistent with the coarse grain structures of all the base alloys shown in Figures 4.4, 4.10 and 4.16. The largest intercept ($a \approx 1094$ μm) was obtained for as-cast Al-Ni alloys (Figure 5.2e). This implies that only a small number of active nucleants existed during solidification of as-cast Al-Ni alloys or that the constitutional undercooling was insufficient to activate more nucleants in as-cast Al-Ni alloys. This inference also applies to the base alloys of Al-Si and Al-Cu because of their large values of *a* as shown in Figure 5.2 (a, c). Figure 5.2 (b, d, and f) shows the effect of ultrasonic intensity on the grain refinement of aluminium alloys for a range of *Q* values. Upon increasing the ultrasonic intensity from 88 to 1400 W/cm^2, both the potency of solutes and the number of active nucleants are increased. Consequently, the grain size decreased drastically for all the alloys studied. This can be inferred from the largely decreased values of *a* and *b* upon UST. In Al-Si alloys, increasing ultrasonic intensity from 88 to 1400 W/cm^2 decreased the intercept *a* from 229 μm to 115 μm and the slope *b* from 737 μm°C to 570 μm°C.

For Al-Cu alloys, the intercept *a* and the slope *b* decreased from 386 μm to 78 μm and 1582 μm°C to 697 μm°C, respectively (Table 5.2) upon increasing the ultrasonic intensity from 88 to 1400 W/cm^2. Similarly, for Al-Ni alloys the value of *a* decreased from 277 μm to 109 μm and slope *b* decreased from 585 μm°C to 442 μm°C. The smallest values of *a* and *b* are observed at the highest ultrasonic intensity of 1400 W/cm^2 in all the alloys tested. Different values of *a* and *b* listed in Table 5.2 reflect different degrees of response of each alloy to UST. At maximum ultrasonic intensity of 1400 W/cm^2, the value of *a* is approximately similar for solute (Cu and Ni). Table 5.2 shows that the potency of nickel solute is higher as compared to copper and silicon solute at the highest ultrasonic intensity used in this work.

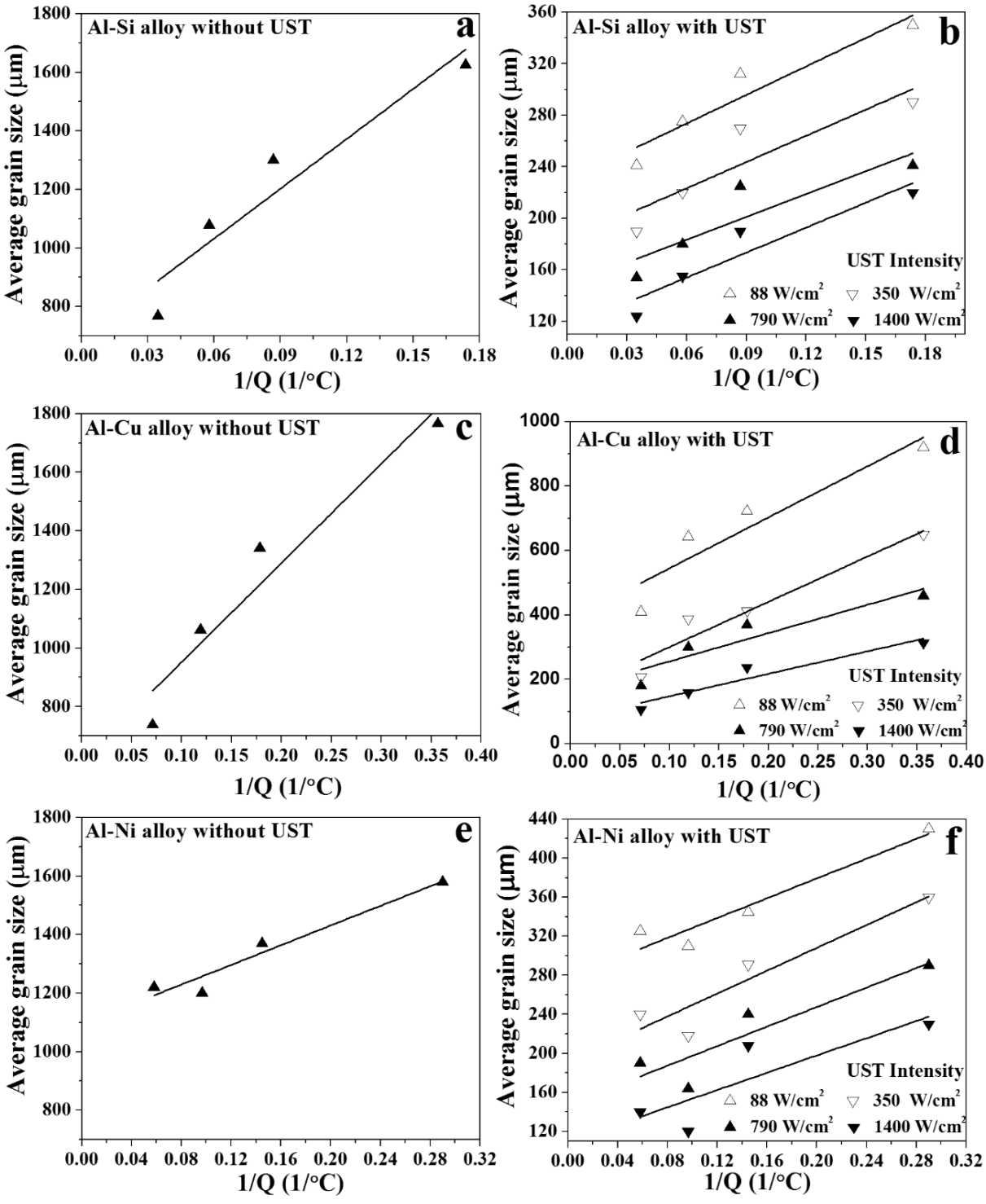

Figure 5.2. Variations of average grain size with 1/*Q* for Al-Si alloys (a) as-cast and (b) with UST, Al-Cu alloys (c) as-cast and (d) with UST, and Al-Ni alloys (e) as-cast and (f) with UST.

Table 5.2. The values of intercept *a* and slope *b* obtained by linear fit of data from Figure 5.2.

Alloy	Ultrasonic intensity (W/cm^2)	Intercept (*a*) (μm)	Slope (*b*) (μm°C)	R^2
Al-Si	As cast	691	5683	0.87
	88	229	737	0.86
	350	182	677	0.71
	790	147	589	0.69
	1400	115	570	0.82
Al-Cu	As cast	612	3388	0.91
	88	386	1582	0.81
	350	160	1405	0.90
	790	152	878	0.79
	1400	78	697	0.89
Al-Ni	As cast	1094	1682	0.91
	88	277	585	0.88
	350	190	507	0.83
	790	147	500	0.74
	1400	109	442	0.59

Schmid-Fetzer and Kozlov proposed a new technique for calculating growth restriction factor (Q_T) in binary and multi-component systems by using Themo-Calc software [200]. It is reported that the conventional technique for calculating *Q* is not accurate [22] and its value is overestimated, which was verified in case of Mg–Mn alloys (Figure 5.3) [200]. Schmid-Fetzer and Kozlov [200] reported that the different values of liquidus slope and partition coefficient are obtained at 3 and 30 wt.% of solute in Mg-Al alloy because of nonlinearity of the liquidus and solidus lines, as a result, the segregating power values varied from 3.59 to 5.44 in Mg–Al alloy (Figure 5.4).

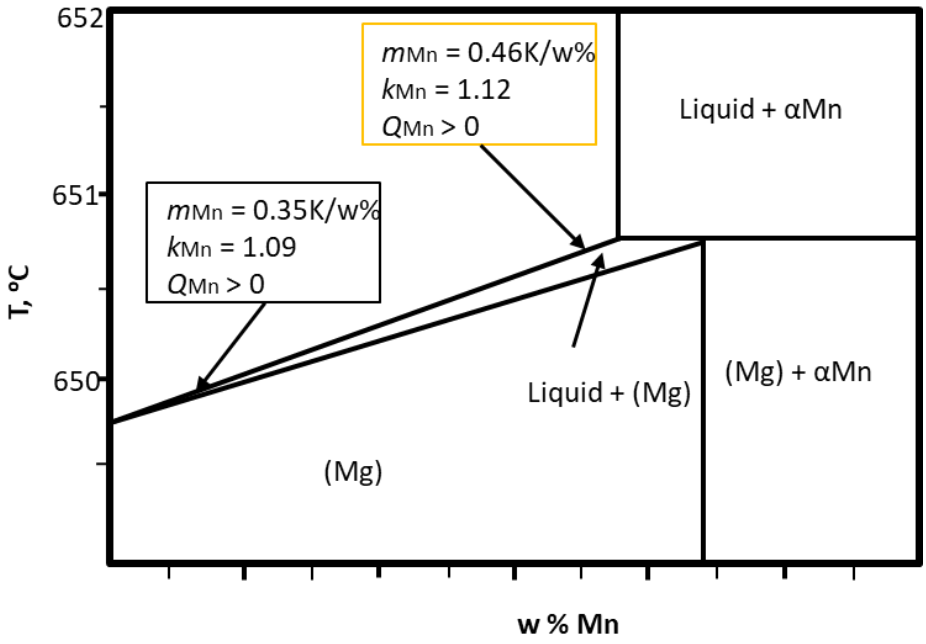

Figure 5.3. Phase diagram of binary Mg–Mn binary alloy (basic data at 0.3 wt% and 1.8 wt.% of solute Mn) [200].

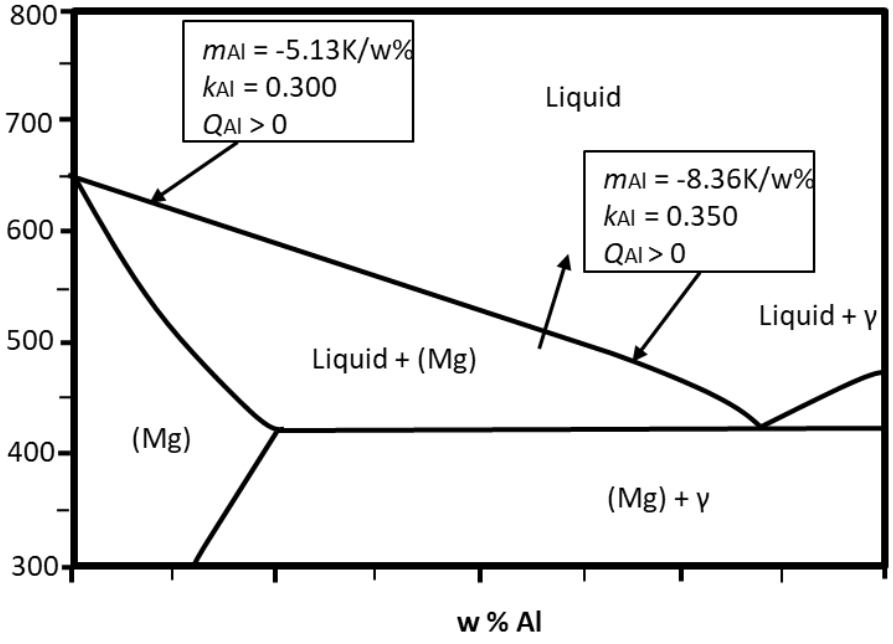

Figure 5.4. Phase diagram of binary Mg–Al binary alloy (basic data at 3 and 30 wt.% of solute Al) [200].

These mathematical inaccuracies in growth restriction factor obtained from conventional technique can significantly affect the calculation of the value of supercooling parameter, *P* for the predicating the grain refining efficiency of solute.

In the present work, the influence of silicon, copper and nickel solutes on grain size of aluminium-based alloys is studied using the growth restriction factor (Q_T) values obtained from the Scheil-Gulliver solidification simulation by using Themo-Calc software. Q_T can be written in terms of the change of the initial rate of the development of constitutional supercooling as a function of solid fraction (f_S) formed, as per equation. 5.1 [69].

$$Q_T = \left(\frac{\partial(\Delta T_{CS})}{\partial f_s}\right)_{f_s \to 0} \quad \text{..... (5.1)}$$

A thermodynamic analysis of Al-Si, Al-Cu and Al-Ni alloys in solidification path is calculated by Scheil-Gulliver simulation from the Thermo-Calc software and it is shown in Figures 5.5, 5.6, and 5.7. For calculation of Q_T, the solid fraction amount must be very small as per equation 5.1. The step size of temperature decrement should satisfy the requirement $f_s \to 0$, with reasonably numerical accuracy of the sampling points. Therefore, temperature step size of 0.01°C is used to simulate Scheil-Gulliver solidification curve for each binary aluminium alloy [200].

Figure 5.5 shows the Scheil-Gulliver solidification curve of binary Al-1wt.%Si alloy, Al-2wt.%Si alloy, Al-3wt.%Si alloy and Al-5wt.%Si alloy, where the composition of the binary alloys is denoted in terms of wt.% rather than mole fraction. It shows that Al-Si alloy contains α-Al phase and eutectic silicon phase. Similarly, Figures 5.6 and 5.7 show the Scheil-Gulliver solidification curve of Al-1wt.%Cu alloy, Al-2wt.%Cu alloy, Al-3wt.%Cu alloy & Al-5wt.%Cu alloy and Al-1wt.%Ni alloy, Al-2wt.%Ni alloy, Al-3wt.%Ni alloy & Al-5wt.%Ni alloy, respectively. All binary alloys contain α-Al phase. Additionally, Al-Cu alloys show eutectic (α-Al + Al_2Cu) mixture and Al-Ni alloys show (α-Al + Al_3Ni) eutectic mixture.

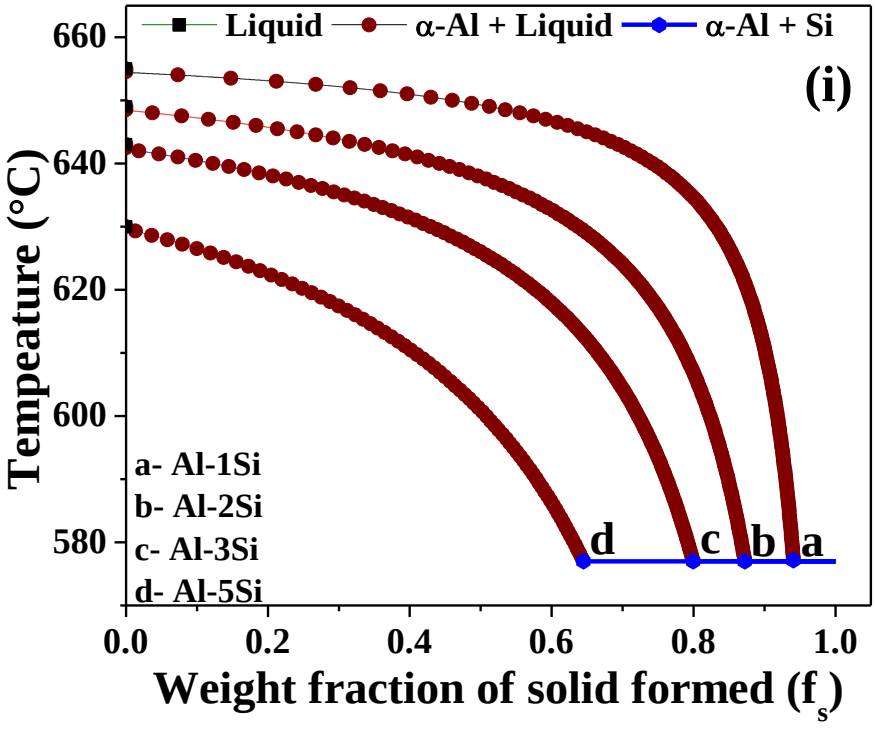

Figure 5.5. Scheil solidification curves for Al-Si alloys.

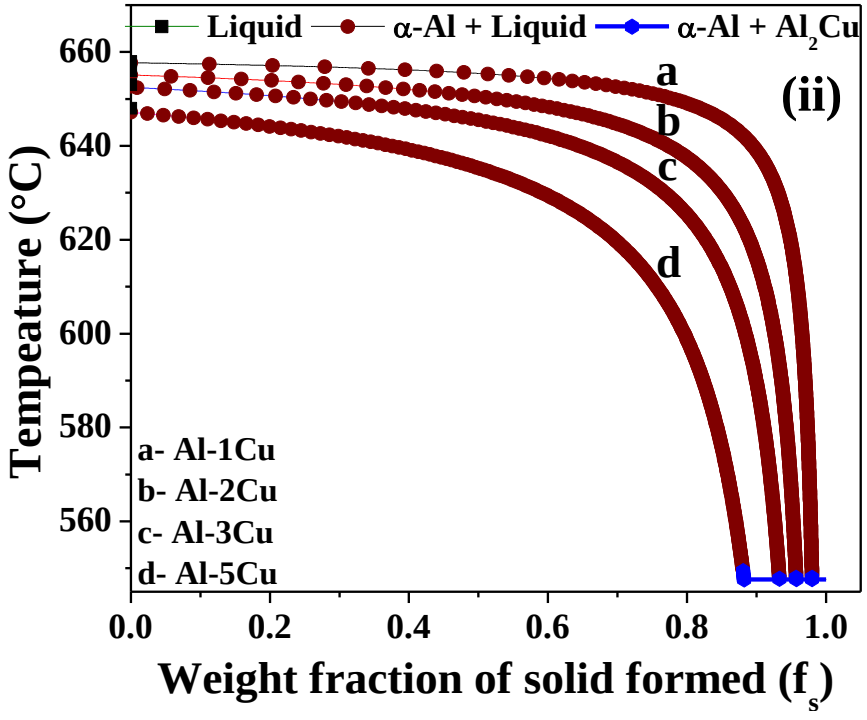

Figure 5.6. Scheil solidification curves for Al-Cu alloys.

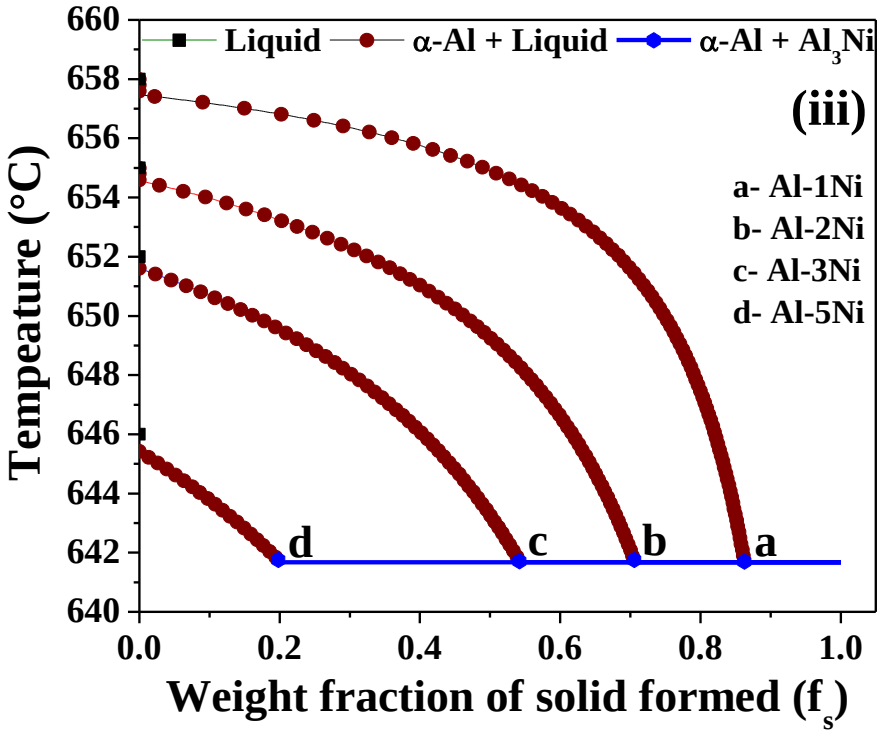

Figure 5.7. Scheil solidification curves for Al-Ni alloys.

Figures 5.8-5.19 show the amount of constitutional undercooling (ΔT_{CS}) produced as a function of the weight fraction of solid for Al-Si, Al-Cu and Al-Ni alloys containing different amounts of solutes. The value of growth restriction factor (Q_T) is obtained from the slope of curves, as shown in Figures 5.8-5.19. A polynomial fit ($\Delta T_{CS} = a + b.f_s + c.f_s^2$) is employed for precise estimation [200]. A comparison of the values of growth restriction factor, which is calculated by conventional technique and Scheil-Gulliver solidification simulation, is shown in Figures 5.20, 5.21, and 5.22. The error percentage between these values of Q and Q_T are shown in Table 5.3. It shows that the value of Q_T increased with weight percentage of solute.

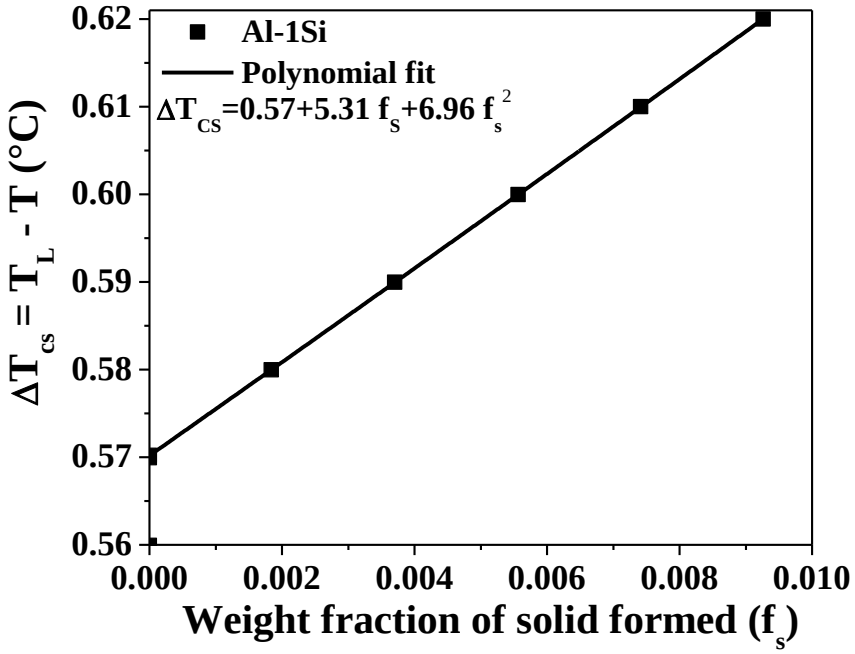

Figure 5.8. Computation of growth restriction factor (Q_T) in Al-1wt.%Si alloy using Scheil solidification simulation.

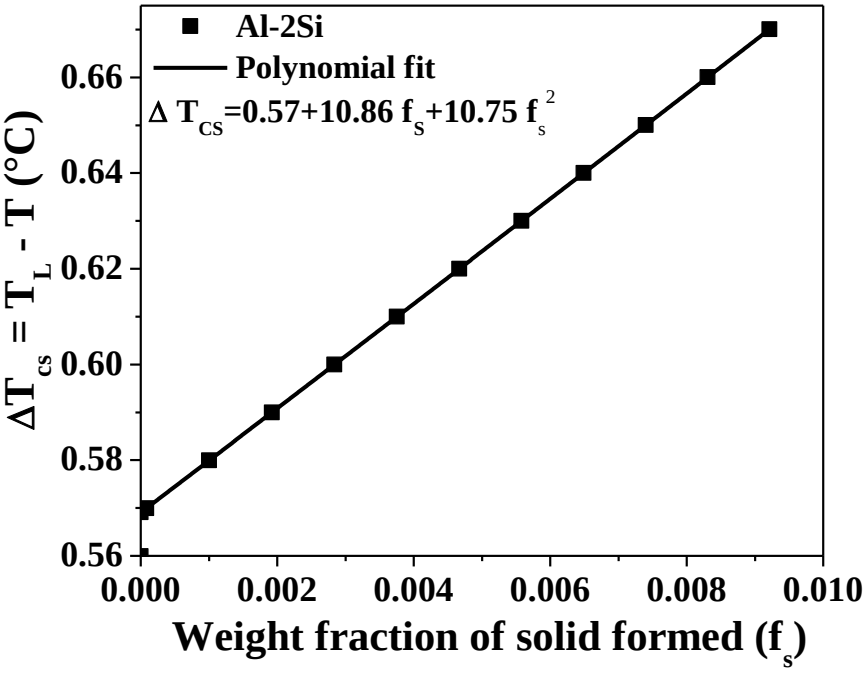

Figure 5.9. Computation of growth restriction factor (Q_T) in Al-2wt.%Si alloy using Scheil solidification simulation.

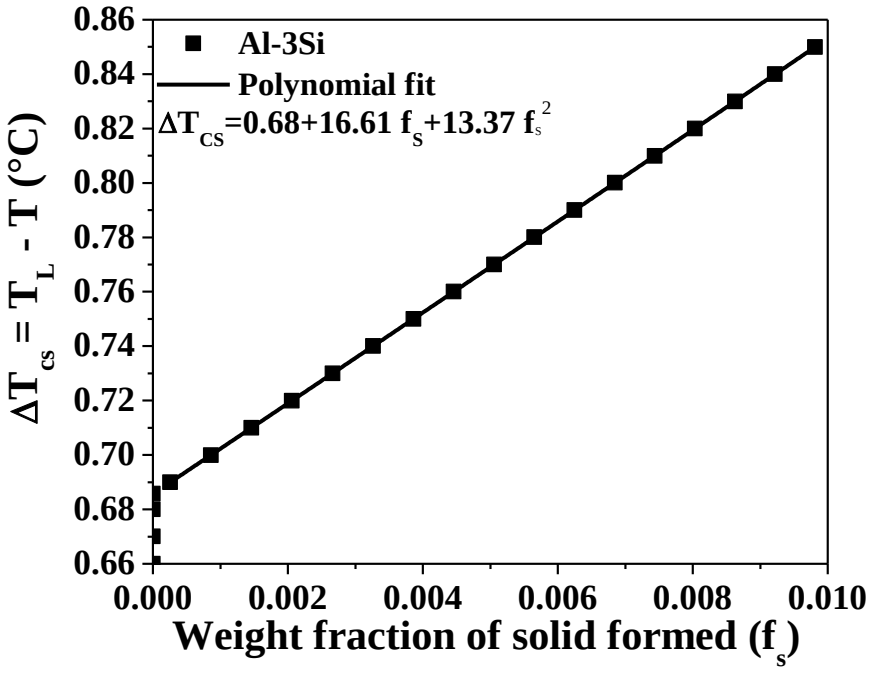

Figure 5.10. Computation of growth restriction factor (Q_T) in Al-3wt.%Si alloy using Scheil solidification simulation.

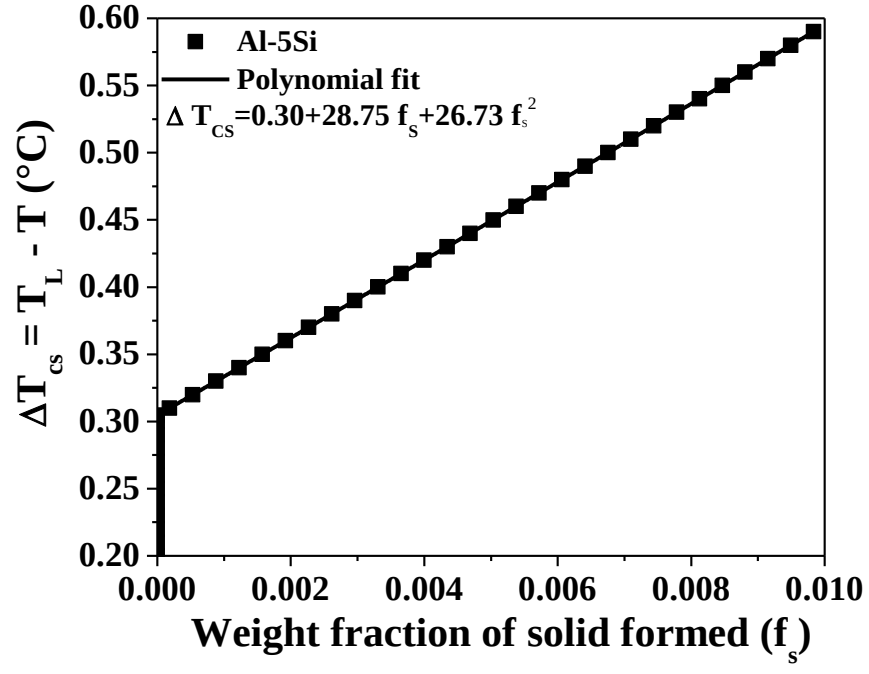

Figure 5.11. Computation of growth restriction factor (Q_T) in Al-5wt.%Si alloy using Scheil solidification simulation.

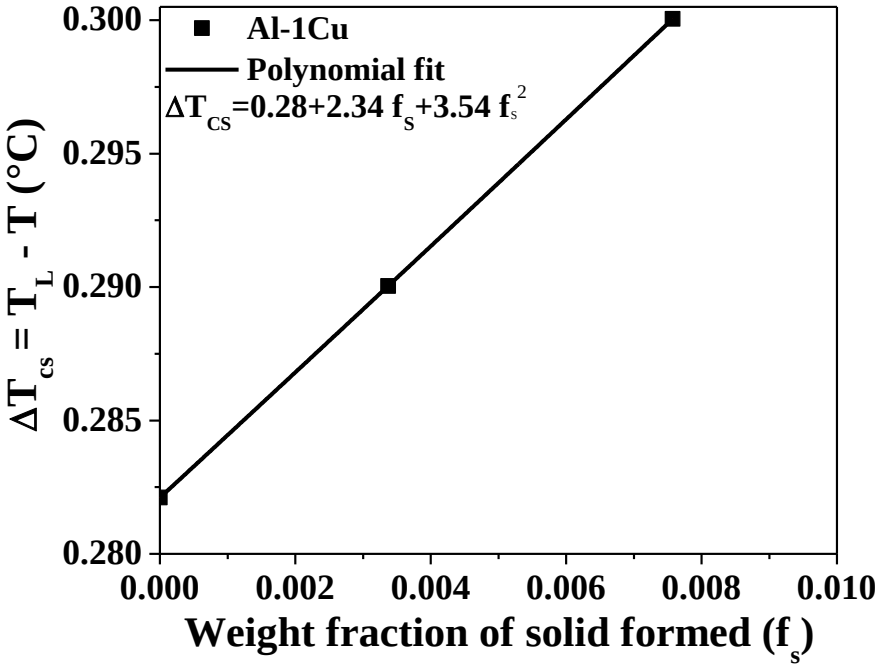

Figure 5.12. Computation of growth restriction factor (Q_T) in Al-1wt.%Cu alloy using Scheil solidification simulation.

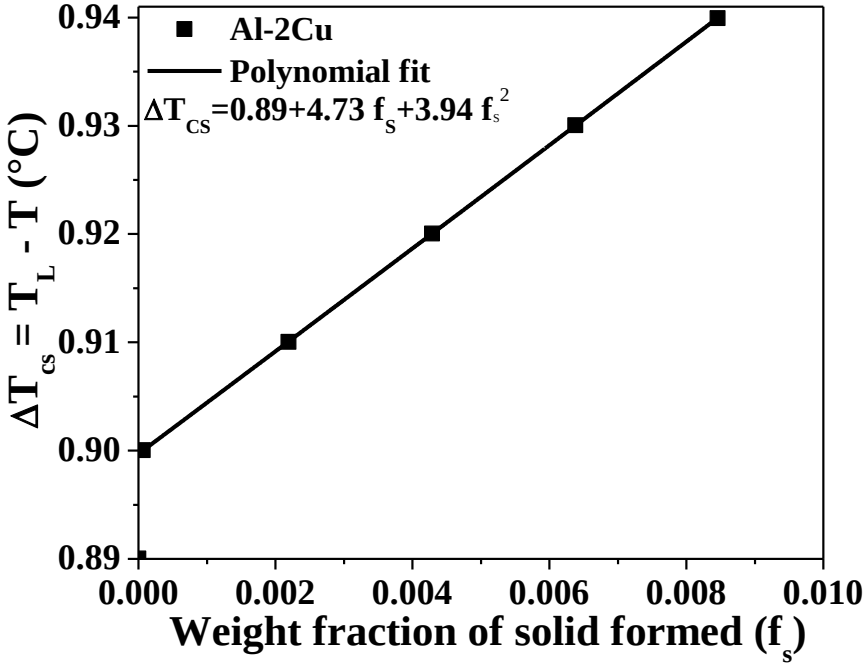

Figure 5.13. Computation of growth restriction factor (Q_T) in Al-2wt.%Cu alloy using Scheil solidification simulation.

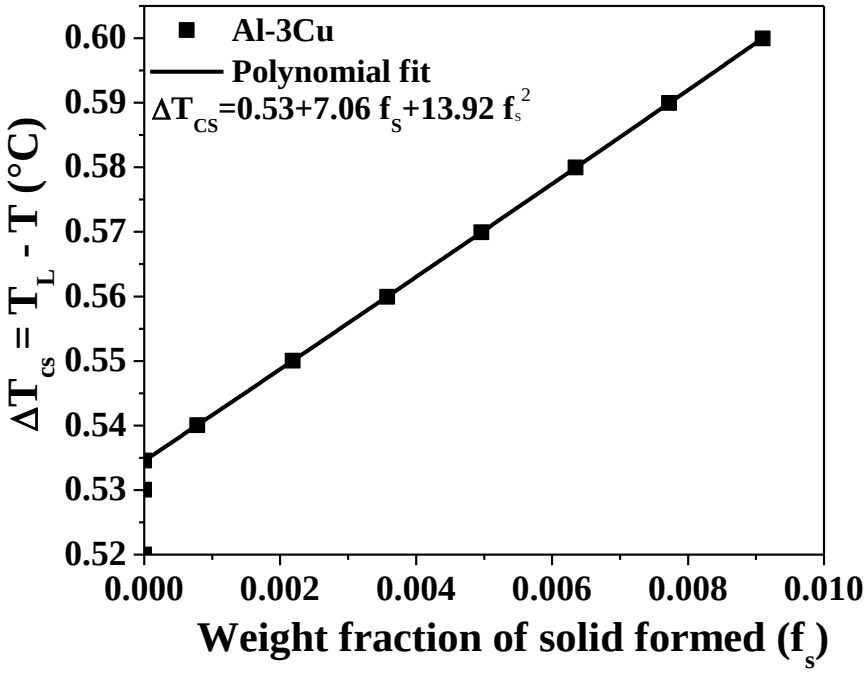

Figure 5.14. Computation of growth restriction factor (Q_T) in Al-3wt.%Cu alloy using Scheil solidification simulation.

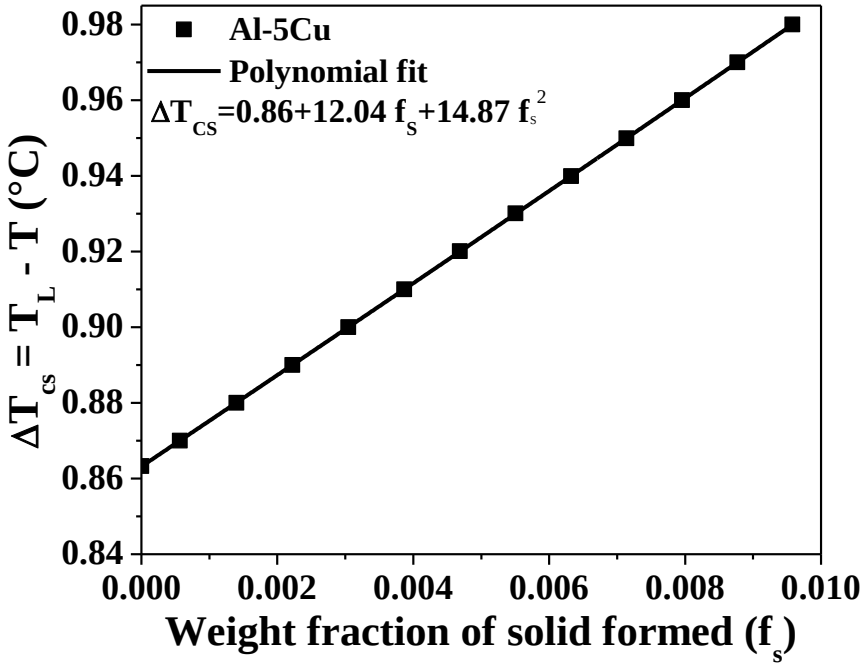

Figure 5.15. Computation of growth restriction factor (Q_T) in Al-5wt.%Cu alloy using Scheil solidification simulation.

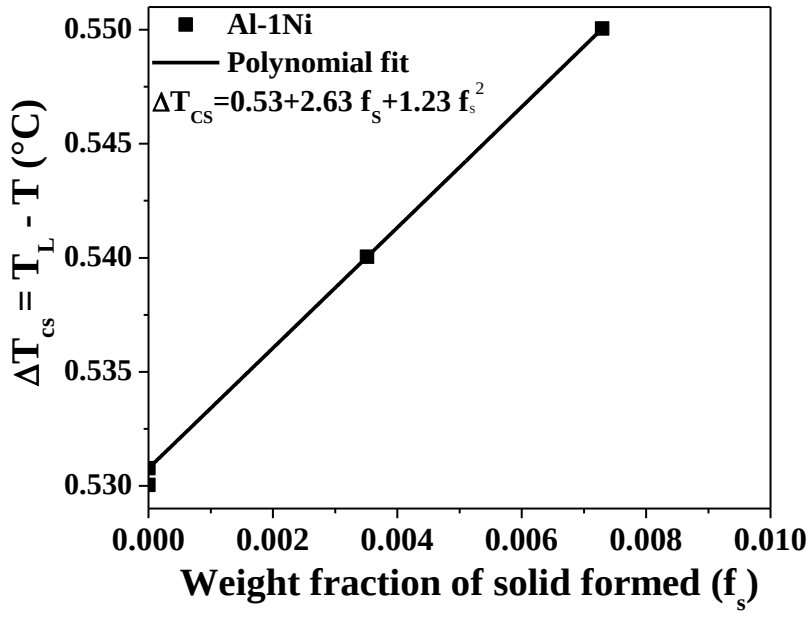

Figure 5.16. Computation of growth restriction factor (Q_T) in Al-1wt.%Ni alloy using Scheil solidification simulation.

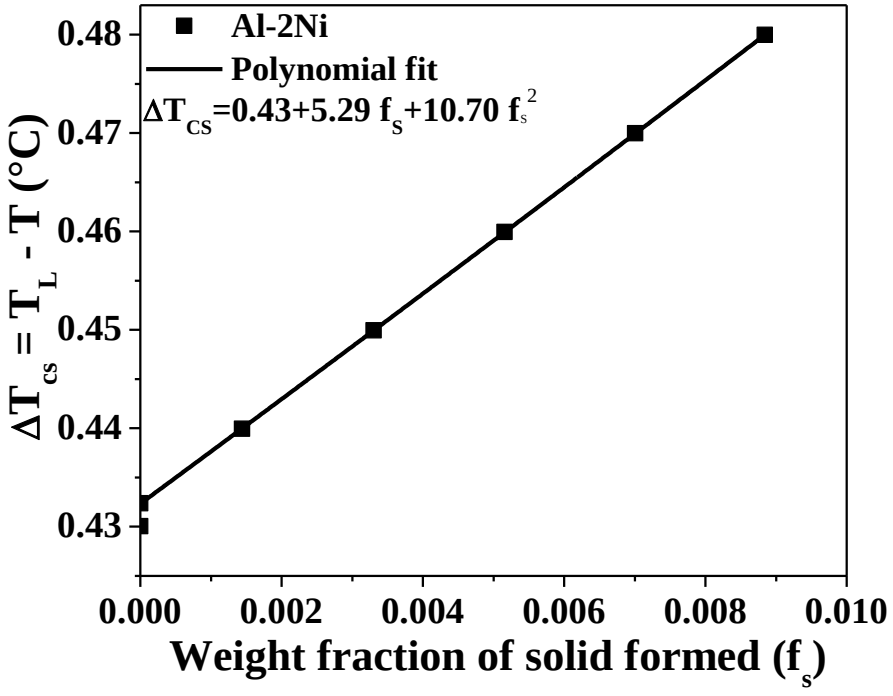

Figure 5.17. Computation of growth restriction factor (Q_T) in Al-2wt.%Ni alloy using Scheil solidification simulation.

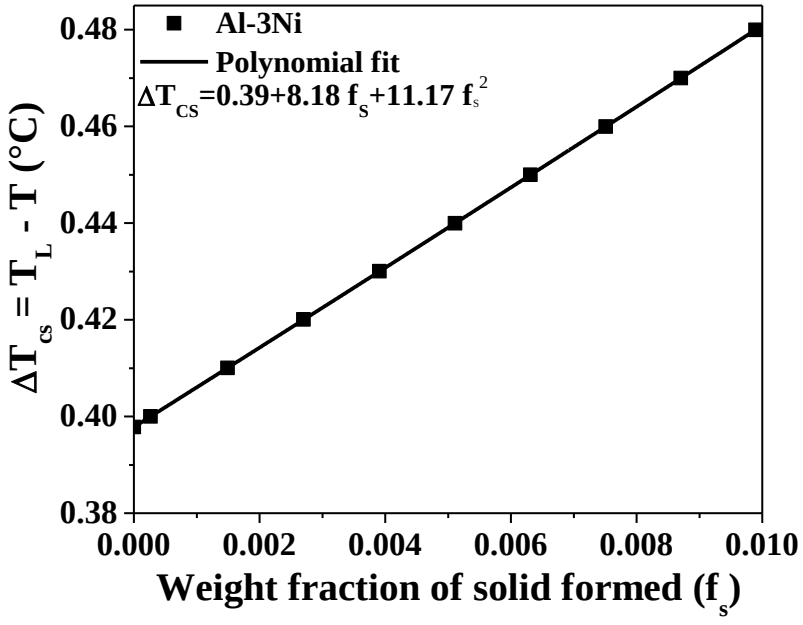

Figure 5.18. Computation of growth restriction factor (Q_T) in Al-3wt.%Ni alloy using Scheil solidification simulation.

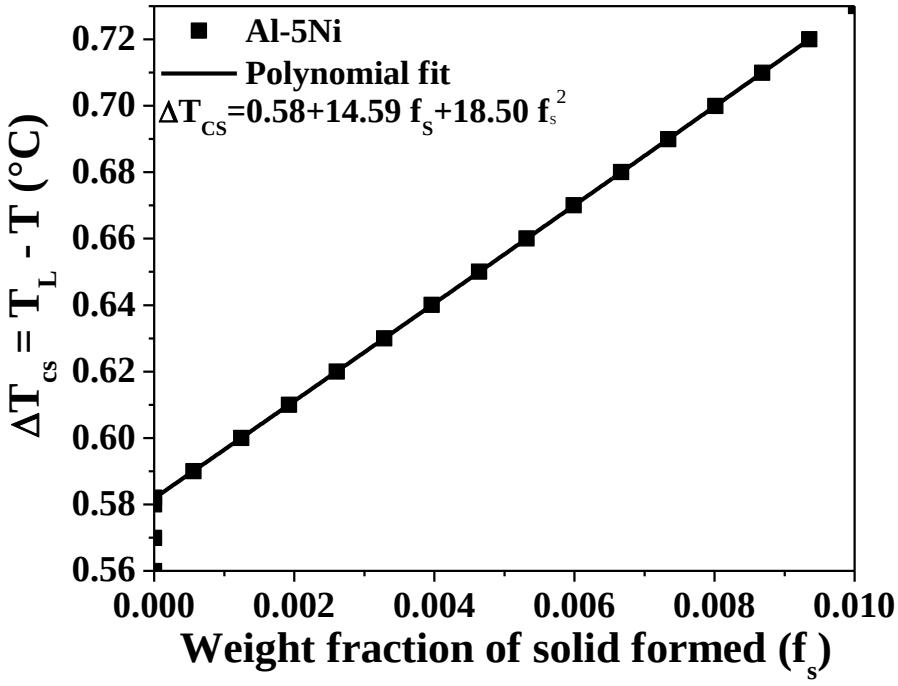

Figure 5.19. Computation of growth restriction factor (Q_T) in Al-5wt.%Ni alloy using Scheil solidification simulation.

Calculated values of Q are overestimated as compared to Q_T for each alloy (Figures 5.20, 5.21, and 5.22). The respective percentage error values are 8.5%, 6%, 4.20% and 0.15% for 1, 2, 3 and 5 wt.% of Si solute in pure Al. Al-Cu alloys have percentage error values, which are 19.87%, 18.6%, 19.19% and 16.48% corresponding to 1%, 2%, 3% and 5% Cu, respectively. For Al-Ni alloys, the % error values are large being 31.14%, 30.4%, 26.5%, and 18.2%, corresponding to 1%Ni, 2%Ni, 3%Ni and 5%Ni, respectively, as shown in Table 5.3. In this work, the composition of Al-Ni alloys lies in the range of near-eutectic alloy, therefore, the % error values are much higher as compared to Al-Si and Al-Cu alloys.

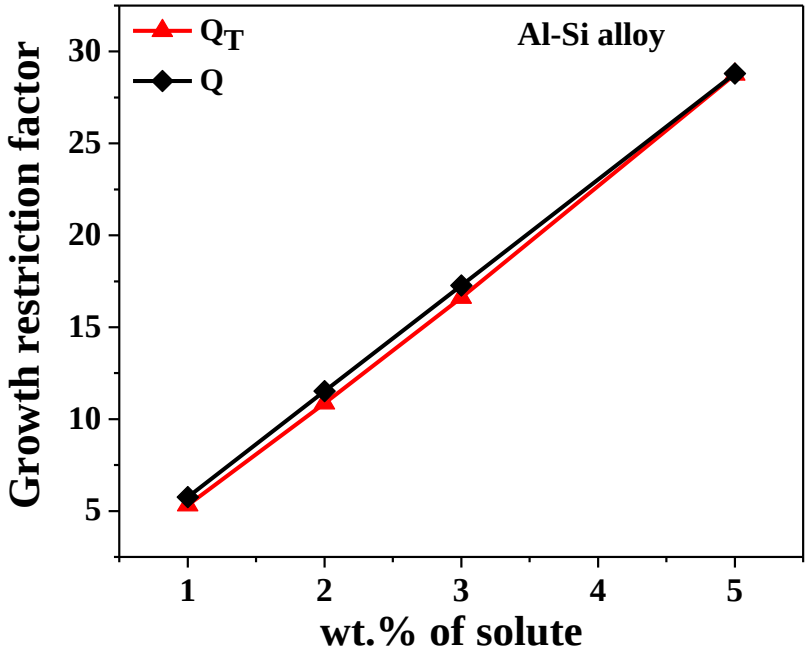

Figure 5.20. Comparison of the values of growth restriction factor by conventional technique and Scheil-Gulliver solidification simulation technique for Al-Si alloys.

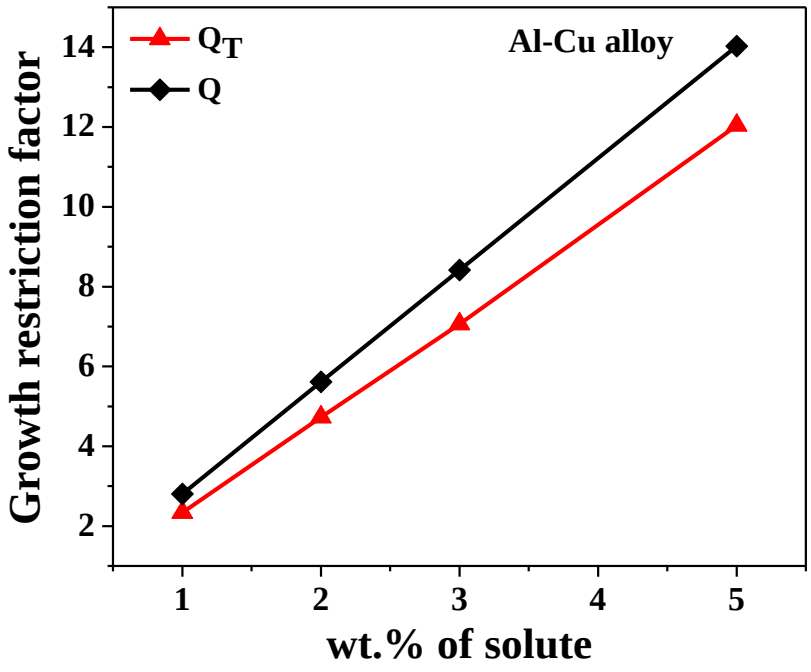

Figure 5.21. Comparison of the values of growth restriction factor by conventional technique and Scheil-Gulliver solidification simulation technique for Al-Cu alloys.

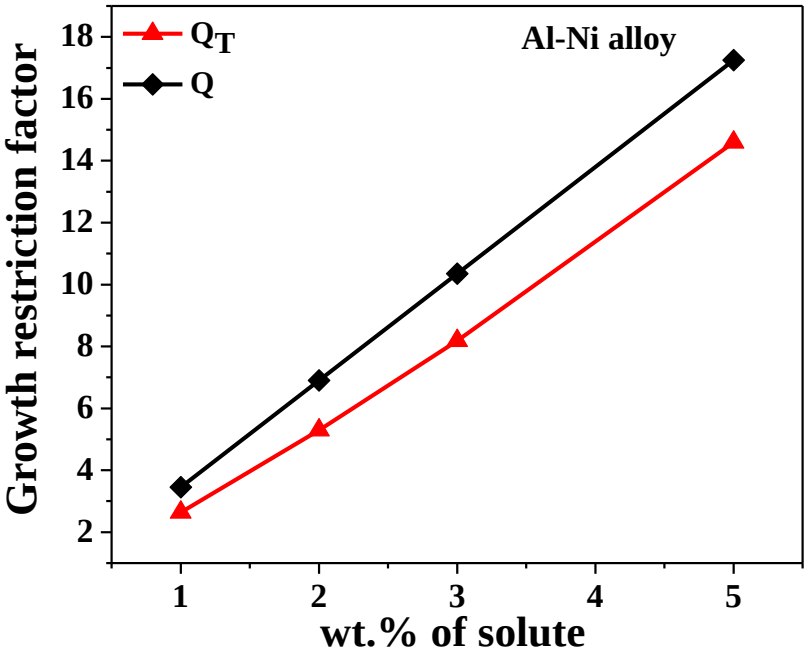

Figure 5.22. Comparison of the values of growth restriction factor by conventional technique and Scheil-Gulliver solidification simulation technique for Al-Ni alloys.

Table 5.3. Percentage error between Q and Q_T.

Alloy	C (solute %)	1	2	3	5
Al-Si alloys	Q_T	5.31	10.86	16.61	28.75
	Q	5.76	11.52	17.72	28.79
	Error (%)	8.5	6	4.201	0.15
Al-Cu alloys	Q_T	2.34	4.73	7.06	12.04
	Q	2.8	5.61	8.41	14.202
	Error (%)	19.87	18.6	19.19	16.48
Al-Ni alloys	Q_T	2.63	5.29	8.18	14.59
	Q	3.45	6.89	10.35	17.24
	Error (%)	31.14	30.4	26.5	18.2

5.2. Freezing range mechanism

The freezing range of an alloy, i.e. the liquidus-solidus gap ($\Delta T_{freezing}$) or the value of Q/k for off-eutectic alloys [201] depends on the solute content for a given alloy system. It can affect the grain refinement of an alloy as first shown by Tarshis et al. [202] on binary Ni-X alloys and then by Abdel-Reihim et al. [203] on the Al-Si and Pb-Sb systems. A small $\Delta T_{freezing}$ means a short solidification time when other conditions are similar. Consequently, only a small proportion of the effective nuclei are likely to have the chance to act as nucleation cites for grain refinement. Hence having an appropriate freezing range is necessary to enable the UST to produce desired grain refining results.

Figures 5.23, 5.24, and 5.25 show the relationship between the average grain size at maximum ultrasonic intensity (1400 W/cm^2) and the freezing range (ΔT) for Al–Si, Al-Cu and Al-Ni alloys, respectively. The value of ΔT is measured using the phase diagrams of binary Al-Si, Al-Cu, and Al-Ni alloys shown in Figures 3.2, 3.3, and 3.4. For Al-Si alloys, the freezing ranges are 79°C, 73°C, 65°C, and 53°C corresponding to 1%, 2%, 3% and 5% silicon, respectively (Figure 5.23). The relatively large values of $\Delta T_{freezing}$ at 1% and 2% silicon can help to understand the grain refinement results obtained at these low silicon contents under different ultrasonic intensity levels (Figures 4.6, 4.7, 4.8 and 4.9), in addition to the relatively large value of $m(k-1)$ for Al-Si alloys (Table 5.1). Al-Cu binary alloys have wide solidification interval values, which are 27°C, 47°C, 63°C, and 92°C (Figure 5.24) corresponding to 1%, 2%, 3% and

5% Cu, respectively. Al-5wt.%Cu alloy thus exhibited excellent ultrasonic grain refining results at maximum ultrasonic intensity. The largest freezing values Al-Cu alloys indicates that, more nucleants particles can be activated for promoting the heterogeneous nucleation in Al-Cu alloys as compared to Al-Ni alloy at comparable growth restriction factor. This factor favors enhanced grain refinement in Al-Cu alloys. The range of freezing range in Al-5wt.%Cu alloy (92°C) is higher than Al-5wt.%Si alloy (54°C) and Al-5wt.%Ni (5°C). This is also confirmed from Figure 4.15, which shows that the grain size of Al-5wt.%Cu alloy (107μm) is smaller than Al-5wt.%Si alloy (120 μm) and Al-5wt.%Ni alloy (140 μm) upon UST.

However, Al-Ni alloys appear to be an exception. Their $\Delta T_{freezing}$ values are very small, being 17°C, 13°C, 10°C, and 5°C corresponding to 1%Ni, 2%Ni, 3%Ni and 5%Ni, respectively (Figure 5.25). Such narrow freezing ranges are not expected to show excellent ultrasonic grain refinement. However, the UST experimental results show that the grain refinement in Al-Ni alloy is larger than Al-Cu alloys at 1, 2 and 3 wt.% solute. These results are contradictory considering the freezing range mechanism. Therefore, freezing range factor alone cannot explain the mechanism of grain refinement in hypoeutectic alloys. It only explains the mechanism of off eutectic alloys (Al-Cu alloy). It tells as to which Al-X system has the largest proportion of potent nuclei in the melt for a fixed solute content for hypoeutectic alloys. However, the results shown in Figures 4.18, 4.19, 4.20, and 4.21 indicate that all four Al-Ni alloys were well grain-refined by UST. This highlights the complexity of understanding the mechanisms for ultrasonic grain refinement. Further studies are needed that focus on the ultrasonic grain refinement of alloys with very small $\Delta T_{freezing}$ values.

5.3. Supercooling parameter

Supercooling parameter (*P*) might be useful for understanding grain refinement mechanism in hypoeutectic alloys. Tarshis et al. [202] observed significant grain refinement in Al and Ni based alloys by adding solute and initially they related the grain size with the supercooling parameter (*P*) for both binary Al-X and Ni-X alloys. Supercooling parameter *P* is defined as [201] [204][13]:

$$P = \frac{m(k-1)C_0}{k} \quad \text{..... (5.2)}$$

Equations. 5.3 and 5.4 are used to calculate *P* for binary off-eutectic and hypoeutectic alloys, respectively [201] [20].

$$P = \Delta T, \qquad C_o \leq C_m \ldots\ldots\ldots\ldots\ldots\ldots\ldots\ldots (5.3)$$

$$\mathrm{P} = Q_T/k, \; C_m < C_o < C_e \ldots\ldots\ldots\ldots\ldots\ldots\ldots (5.4)$$

where C_m, is the maximum solubility of solute in liquid aluminium and C_e is the eutectic composition of alloy [20].

Figures 5.26, 5.27, and 5.28 show the plot between average grain size at maximum ultrasonic intensity and the parameter *P* and ΔT for each aluminium alloy. Figure 5.26 shows that the value of *P* and ΔT is same for Al-1wt.%Si alloy because the composition of 1 wt.% Si lies in the range of off-eutectic alloy, therefore, $P = \Delta T$. Above 1 wt.% of solute, value of ΔT is decreased and the value of P is increased up to 5wt.% of solute because 2, 3 and 5 wt.% composition lies on the range of hypoeutectic alloy. For hypoeutectic alloy $\mathrm{P} = Q_T/k$. The value of P is 83.5, 127.8 and 221.2°C corresponding to 2, 3, and 5 wt.% silicon solute in aluminium, respectively that is higher as compared to the value of ΔT, as shown in Figure 5.26. By increasing the content of solute, the value of *P* is increased significantly and the average grain size is reduced.

For Al-Cu alloys, the value of *P* and ΔT is same because the composition of Cu (1, 2, 3, and 5 wt.%) in aluminium lies in the range of off-eutectic alloy, as shown in Figure 5.27.

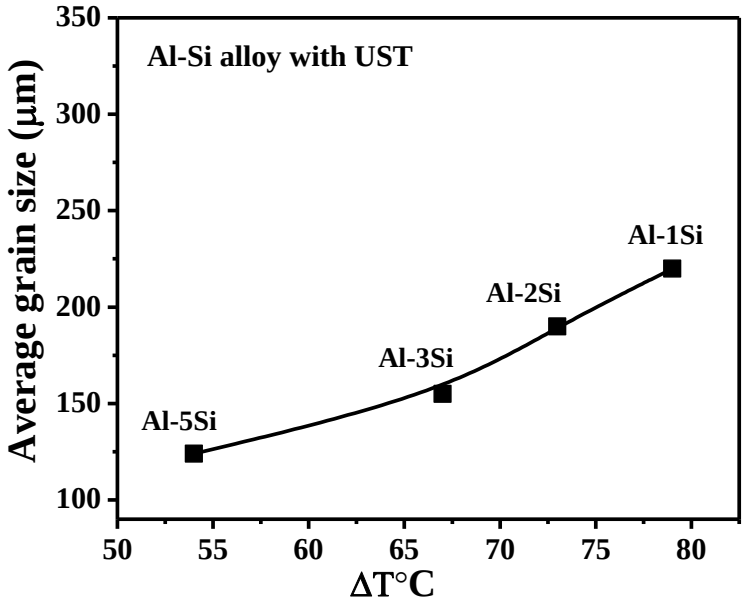

Figure 5.23. The relationship between the average grain size at maximum ultrasonic intensity (1400 W/cm^2) and freezing range (ΔT) in Al–Si hypoeutectic alloys.

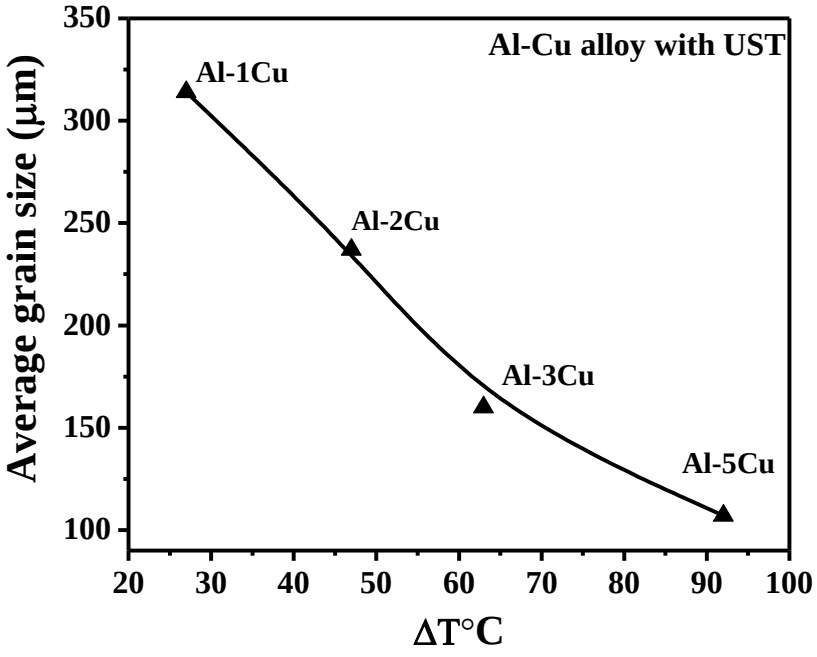

Figure 5.24. The relationship between the average grain size at maximum ultrasonic intensity (1400 W/cm^2) and freezing range (ΔT) in Al–Cu off-eutectic alloys.

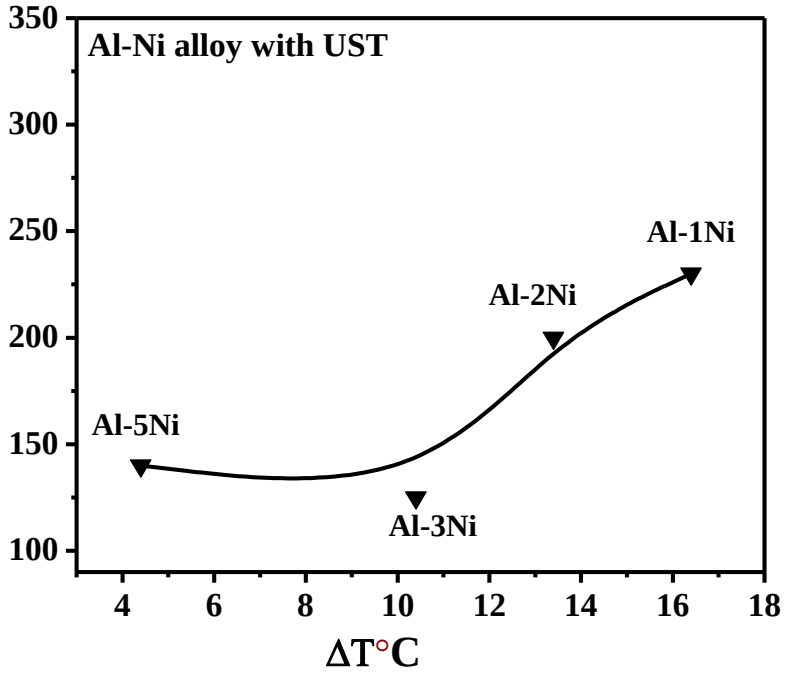

Figure 5.25. The relationship between the average grain size at maximum ultrasonic intensity (1400 W/cm^2) and freezing range (ΔT) in Al–Ni near-eutectic alloys.

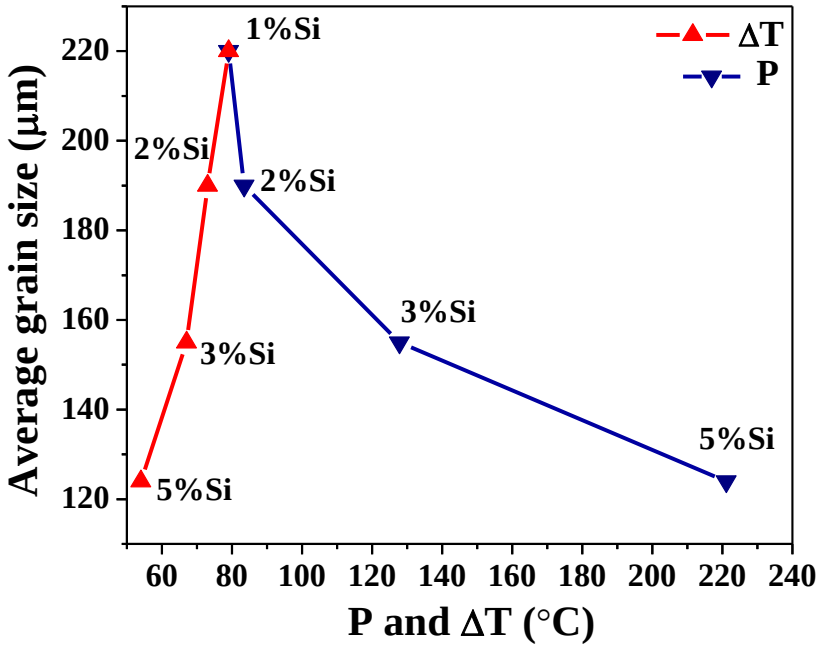

Figure 5.26. The relationship between the average grain size at maximum ultrasonic intensity (1400 W/cm^2) and the parameters P and ΔT in Al–Si hypoeutectic alloys.

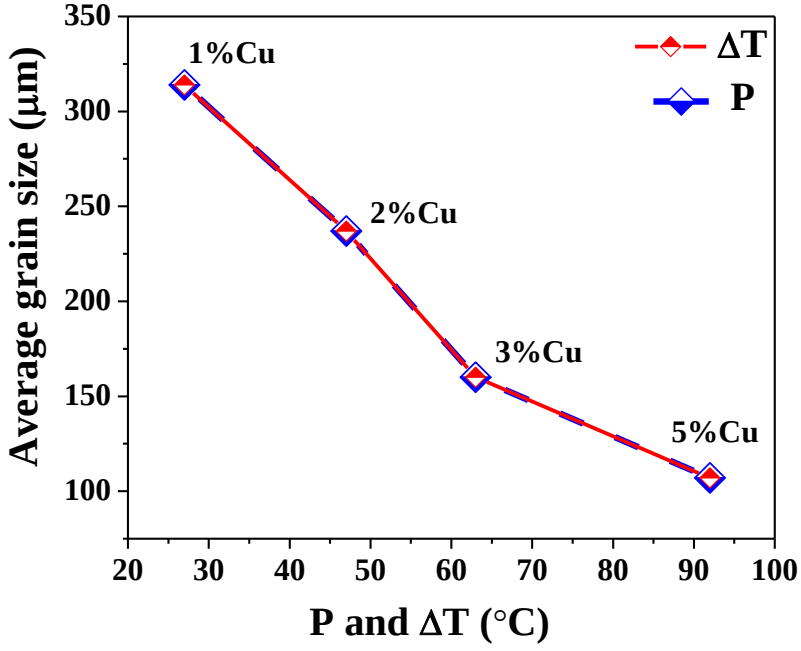

Figure 5.27. The relationship between the average grain size at maximum ultrasonic intensity (1400 W/cm^2) and the P and ΔT parameters in Al–Cu off-eutectic alloys.

For Al-Ni alloys, there is wide difference in the value of P and ΔT, as shown in Figure 5.28. At fixed 5 wt.% content of solute, the value of P is approximately 71 times the value of ΔT.

Its values are 62.6, 125.9, 194.76 and 347.38°C, which correspond to 1, 2, 3 and 5 wt.% of Ni solute. Al-Ni alloys have a large value of *P* as compared to Al-Si and Al-Cu alloys. *P* value of Al-3wt.%Ni alloy is 1.52, which is about three times larger than that of Al-3wt.%Si alloy and Al-3wt.%Cu alloy. This is consistent with the results of Figure 4.22, which shows that grain size of Al-3wt.%Ni alloy is smaller than that of Al-3wt.%Cu alloy and Al-3wt.%Si alloy. *P* values in Al-Cu alloys are smaller as compared to Al-Si and Al-Ni alloys up to 3 wt.% of solute as a result, the grain size of USTed Al-Cu alloys is smaller as compared to other alloys. These results imply that *P* is a very important parameter in explaining the grain refinement of hypoeutectic alloys with the application of UST.

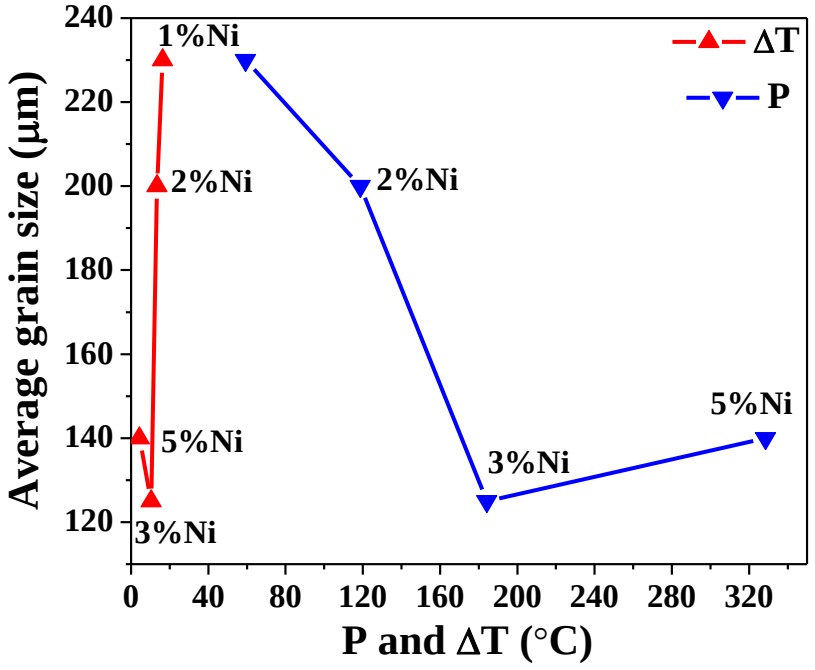

Figure 5.28. The relationship between the average grain size at maximum ultrasonic intensity (1400 W/cm^2) and the *P* and ΔT parameters in Al-Ni near eutectic alloys.

Generally, grain refinement of alloy is closely concerned with dendritic fragmentation, i.e., secondary dendrite arms are fragmented at the dendrite necks [201]. By increasing the value of mC_0/k , size of dendrite necks decreases. Where C_0/k is proportional to the solute enrichment at the dendrite roots. Therefore, the values of *P* represent the temperature depression at the dendrite roots [201]. It is evident that a high *P* value indicates a small dendrite root and thus a high probability of re-melting of the dendrite root by a temperature fluctuation or UST [201].

5.4. Summary of results

The following conclusions are drawn from this chapter:

1. A higher value of growth restriction parameter, *Q*, in hypoeutectic Al-Si alloys explains their increased grain refinement upon UST as compared to Al-Cu alloys, at lower content of solute contents of 1 and 2 wt.%.
2. Among the three binary Al alloy systems studied, the number of potential nucleants that can be activated by ultrasound at the intensity level of 1400 W/cm^2 is more in Al-Cu alloys than in Al-Ni and Al-Si alloys according to StJohn's model.
3. Freezing range (ΔT) mechanism can satisfactorily explain grain refinement of Al-Cu alloys upon UST. ΔT increased with increasing the solute content resulting in increased grain refinement. Al-5wt.%Cu alloy which has a freezing range of 100ºC and the Al-5wt.%Ni alloy which has a freezing range of just 5ºC at the same applied ultrasonic intensity (1400 W/cm^2). However, there is not much difference between the average grain size of Al-5wt.%Cu alloy and Al-5wt.%Ni alloy. Therefore, some focused research on the influence of freezing range on ultrasonic grain refinement of Al alloys appears to be necessary.
4. Supercooling parameter *P* explains the grain refinement mechanism with UST in Al-Ni alloys that have near-eutectic compositions as compared to Al-Cu and Al-Si alloys studied.
5. In each alloy, both the *P* and *Q* values increase with increasing amount of solute. The ΔT value increases in off-eutectic alloy and decreases in hypoeutectic alloys with solute content. Evidently, such discrepancy in average grain size with content of solute cannot be completely described by considering *Q*, ΔT, and *P* values alone.

CHAPTER 6

MECHANICAL PROPERTIES OF ULTRASONICALLY TREATED BINARY ALUMINIUM ALLOYS

In this chapter, the effect of content of solute and UST on the mechanical properties of the binary Al-Si, Al-Cu and Al-Ni alloys is studied by varying the content of the solute (1, 2, 3 and 5 wt.%) and ultrasonic intensity (0, 88 W/cm^2, 350 W/cm^2, 790 W/cm^2, and 1400 W/cm^2).

6.1. Introduction

The combined effects of grain size reduction, grain morphology, amount of porosity and distribution & refinement of eutectic phase significantly influenced the tensile properties, especially total elongation to failure of the investigated aluminium alloys.

6.2. Results and discussion

6.2.1. Mechanical properties

Grain refinement resulting from both the effects of solute and the UST can improve the mechanical behavior of the processed alloys. The Hall-Petch equation relating hardness (H) and average grain size (d) of a polycrystalline material is: [205]

$$H = H_0 + K_H d^{-1/2} \quad \text{..... (6.1)}$$

Where H_0 and K_H are the constants.

Figures 6.1, 6.2, and 6.3 show the variation in hardness of Al−(1-5)%Si alloys, Al−(1-5)%Cu alloys, and Al−(1-5)%Ni alloys at different ultrasonic intensities of 0, 88 W/cm^2, 350 W/cm^2, 790 W/cm^2, and 1400 W/cm^2 for the specimens that were used during continuous cooling. Increasing the amount of solute resulted in a noticeable increase in hardness for all the as-cast and USTed aluminium alloys. It is observed that the hardness of each as-cast aluminium alloy is lower as compared to respective USTed alloy. This is due to the coarse dendritic α-Al phase in as-cast alloys (Figures 4.4, 4.10, and 4.16). UST increases the degree of refinement of α-Al phase and produces globular grains. As a result, the hardness is increased upon UST. The maximum values of hardness are obtained in Al-5wt.%Si alloy, Al-5wt.%Cu alloy, and Al-

3wt.%Ni alloy processed with ultrasonic intensity of 1400 W/cm^2, which are 52, 58 and 36.2 VHN respectively. This is due to the smaller grain size is obtained in Al-5wt.%Si alloy and Al-5wt%Cu alloy upon UST (Figures 4.9 and 4.15). For Al-Ni alloys, there is not much difference between the hardness of Al-3wt.%Ni alloy and Al-5wt.%Ni alloy, as shown in Figure 6.3. This is due to no further decrease in the grain size of Al-5wt.%Ni alloy as compared to Al-3wt.%Ni alloy in each casting condition. It was reported that mechanical properties of Al-Ni alloys are inferior due to comparatively weak primary aluminium matrix of eutectic Al-Ni alloy because of low solubility of nickel solute in aluminium [206]. In the present study, the solute solubility in aluminium, in the descending order is copper, silicon and nickel (see Table 3.2). Thus, low nickel solubility may be a reason for decrease in hardness of as-cast Al-Ni alloys. Hardness of eutectic phase may be the other factor for influencing the hardness of as-cast binary aluminium alloys. For USTed samples, UST improves the mechanical properties of USTed aluminium alloys as compared to respective as-cast alloys, which is discussed later.

The relative effect of solute content and UST on hardness is evaluated through estimating the percentage increase in hardness induced by each factor. For as-cast Al-Si alloys, increasing silicon content by 5 times from 1% to 5% increased the average hardness by ~38% (Figure 6.1). For 1%Si, increasing ultrasonic intensity by ~16 times from 88 W/cm^2 to 1400 W/cm^2 increased average hardness by ~14%. The increase in average hardness is ~23% in the case of USTed Al-5wt.%Si alloy (Figure 6.1).

As for as-cast Al-Cu alloys, increasing the amount of copper from 1% to 5% increased the average hardness by 71% (Figure 6.2). Similarly, increase in ultrasonic intensity from 88 W/cm^2 to 1400 W/cm^2, increased the average hardness by approximately 22% for 1%Cu, and 31% for 5%Cu alloy, which is more pronounced as compared to 1%Si and 5%Si alloy for same case. Addition of 5%Cu solute along with the UST done at maximum ultrasonic intensity of 1400 W/cm^2 shows maximum hardness of 58 VHN. For as-cast Al-Ni alloys (Figure 6.3), the average hardness increases by 26% upon increasing the nickel content from 1% to 5%. At 5 wt.% Ni, the average hardness increased by ~12% upon increasing the ultrasonic intensity from 88 W/cm^2 to 1400 W/cm^2.

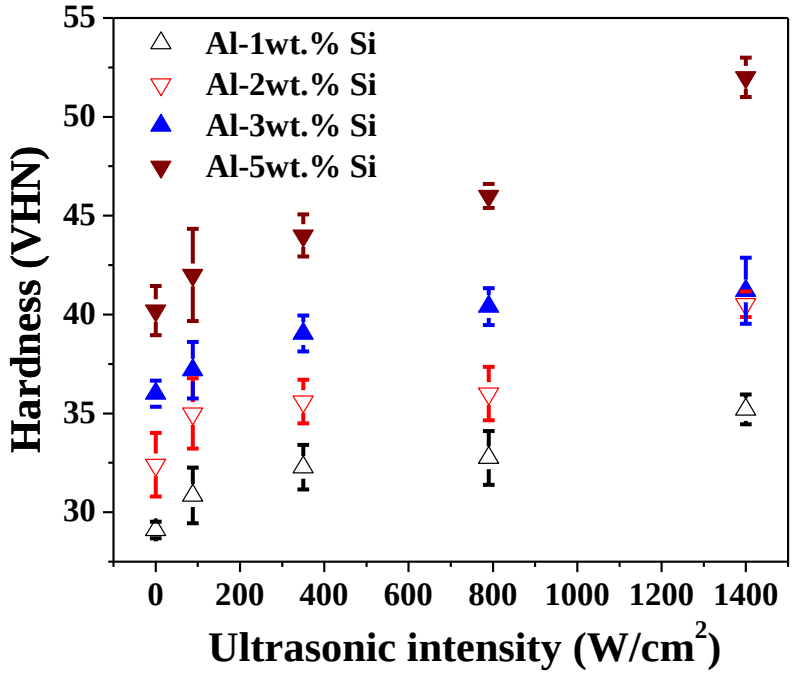

Figure 6.1. Variation of hardness with ultrasonic intensity (W/cm^2) for both as-cast and ultrasonically treated Al-Si alloy: Role of solute content.

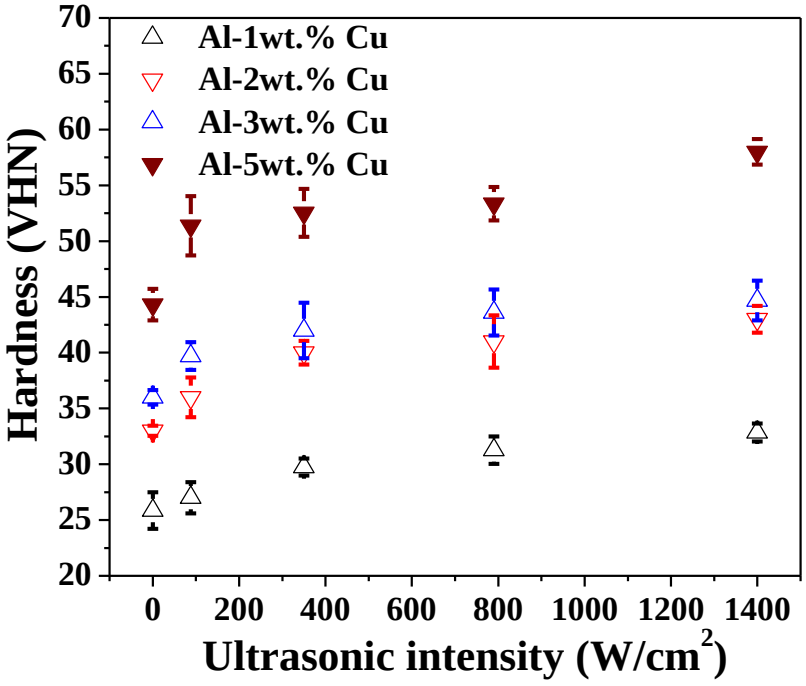

Figure 6.2. Variation of hardness with ultrasonic intensity (W/cm^2) for both as-cast and ultrasonically treated Al-Cu alloy: Role of solute content.

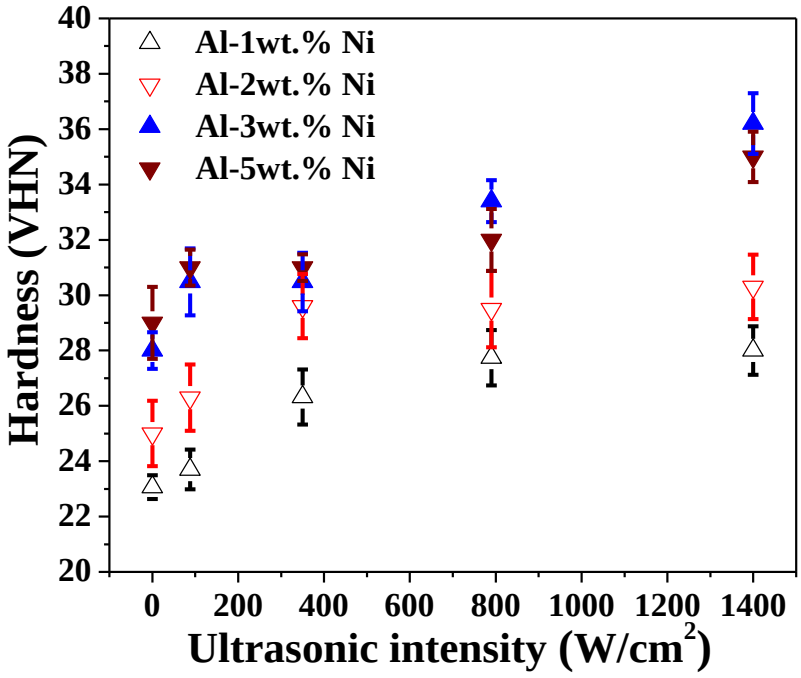

Figure 6.3. Variation of hardness with ultrasonic intensity (W/cm^2) for both as-cast and ultrasonically treated Al-Ni alloy: Role of solute content.

UST refines the eutectic and secondary phase in aluminium alloys, which also enhances their mechanical properties. Several contradictory reports exist in the literature on eutectic modification by UST. Jian et al. reported that UST refined the eutectic Si phase and uniformly distributed it [99]. Similar observations were made by Zhang et al. [113] and Kotadia and Das [26]. In contrast, Zhang et al. observed that eutectic silicon coarsened in Al-5wt.%Si alloy by UST [111]. Feng et al. reported that the eutectic lamellar spacing increased in hypereutectic Al-Si alloys with UST [33]. Eskin and Eskin [207] reported coarsening of eutectic constituents after UST. Kocatepe and Burdett observed that mechanical vibrations produced coarse eutectic silicon in LM6 alloy [208] .

Eutectic solidification occurred in all three Al-5%X (X= Si, Cu, Ni) alloys, although under equilibrium solidification conditions the Al-5wt.%Cu alloy is off-eutectic (<5.65%Cu, see Table 3.2). Figure 6.4 shows higher magnification SEM micrographs of as-cast and with USTed Al- 5wt.%Si alloy, Al-5wt.%Cu alloy, and Al-5wt.%Ni alloy using ultrasonic intensity of 1400 W/cm^2. Coarse acicular and long plate-like eutectic silicon particles distributed non-uniformly among the α-Al dendrites are observed in the as-cast Al-5wt.%Si alloy (Figure 6.4a). In contrast, thin and short Si plates, which exist between the α-Al grains, are observed after UST (Figure 6.4b). At the highest ultrasound intensity, average length and width of the silicon plate reduced

to 37 μm from 68 μm and to 2 μm from 4.7 μm as compared to as-cast Al-5wt.%Si alloy. Eutectic silicon structure is more uniformly dispersed in the USTed microstructure (Figure 6.4b).

Figure 6.4(c, d) shows the SEM micrographs of as-cast and USTed Al-5wt.%Cu alloy at higher magnification. The microstructure of as-cast Al–5wt.%Cu alloy is composed of α-Al rich phase with an inter-dendritic eutectic mixture (α + Al_2Cu). Noticeable influence of UST on the microstructure of the Al–5wt.%Cu alloy is shown in Figure 6.4(c, d). The inter-dendritic eutectic phase (α + Al_2Cu) became much thinner after UST. The average width of eutectic phase decreased to 6.3 μm (Figure 6.4d) from 14 μm (Figure 6.4c) with the application of UST.

As-cast Al-5wt.%Ni alloy consists of eutectic mixture of α-Al + Al_3Ni surrounding the dendritic α-Al (Figure 6.4e). This type of eutectic mixture has alternate α-Al rich phase and Al_3Ni phase [209], which is confirmed from Figure 4.17. It is clear from Figure 6.4(e, f) that Al_3Ni has rod like morphology. Other researchers also reported the rod like shape of Al_3Ni phase [209,210]. With the application of UST, very fine and better dispersion of eutectic phase is observed as compared to as-cast Al-5wt.%Ni alloy.

The mechanism for the refinement of the eutectic phase observed in this research is unclear. Kotadia and Das [26] suggested that finer eutectic Si particles could form in the last stage of solidification due to the limited growth space available and the faster cooling effect resulting from larger contact surface with existing solid.

Figures 6.5, 6.7, and 6..9 show the engineering stress-strain curves of as-cast and USTed (using highest ultrasound intensity of 1400 W/cm^2) Al-Si alloys, Al-Cu alloys, and Al-Ni alloys. Variation in their tensile properties is depicted in Figures 6.6, 6.8, and 6.10, respectively. In these Figures, as-cast Al-1wt.%Si alloy, Al-2wt.%Si alloy, Al-3wt.%Si alloy, Al-5wt.%Si alloy, Al-1wt.%Cu alloy, Al-2wt.%Cu alloy, Al-3wt.%Cu alloy, Al-5wt.%Cu alloy, Al-1wt.%Ni alloy, Al-2wt.%Ni alloy, Al-3wt.%Ni alloy, and Al-5wt.%Ni alloy are named as 1Si, 2Si, 3Si, 5Si, 1Cu, 2Cu, 3Cu, 5Cu, 1Ni, 2Ni, 3Ni, and 5Ni, respectively. Similarly, USTed alloys are named as 1Si-UST, 2Si-UST, 3Si-UST, 5Si-UST, 1Cu-UST, 2Cu-UST, 3Cu-UST, 5Cu-UST, 1Ni-UST, 2Ni-UST, 3Ni-UST, and 5Ni-UST, respectively. It can be seen that the yield strength ($\sigma_{0.2}$), ultimate tensile strength (UTS) and ductility of all the UST aluminium alloys are superior to as-cast alloys.

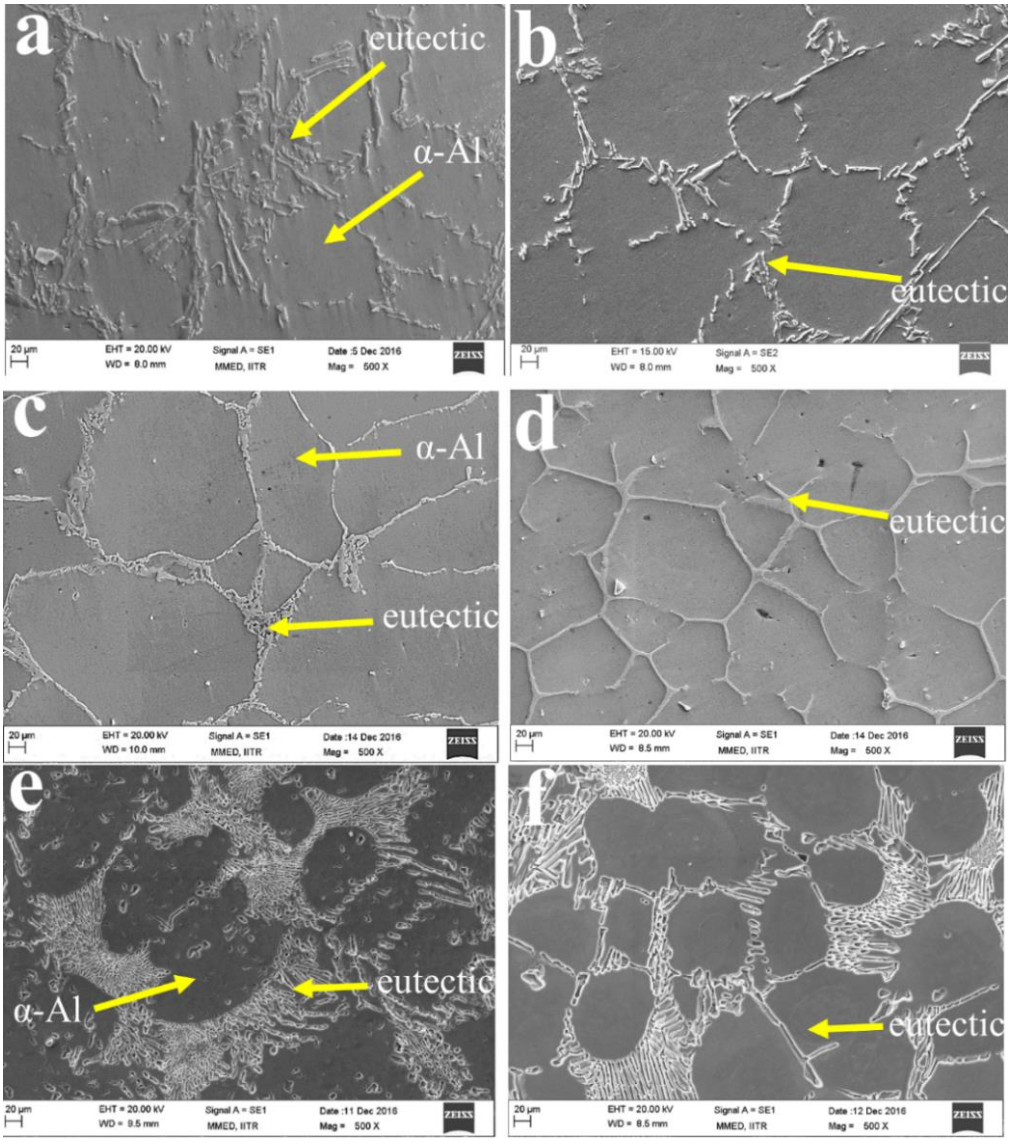

Figure 6.4. Eutectic modification by UST. Al-5wt.%Si alloys- (a) as-cast and (b) with UST (1400 W/cm^2), Al-5wt.%Cu alloys- (c) as-cast and (d) with UST (1400 W/cm^2), and Al-5wt.%Ni alloys- (e) as-cast and (f) with UST (1400 W/cm^2).

Among all the Al-Si alloys, Al-5wt.%Si alloy shows the largest $\sigma_{0.2}$ and UTS values upon UST. It is due to higher amount of solute (Si content) and more refined and globular microstructure as shown in Figure 4.9(d). It can be observed that UTS, $\sigma_{0.2}$, and total elongation to fracture values are lowest for as-cast alloys (Figure 6.6). This is due to higher porosity content of as-cast alloys (see in Table 6.1). UST is known for its degassing ability [19][173], thus it lowers the porosity (Table 6.1).

UTS of the as-cast alloys shows abnormal behavior. Upon doubling the solute content, UTS increased by about 13%. Upon further increase in the Si content to 3 wt.% and 5 wt.%, the UTS is decreased. UTS of USTed Al-1wt.%Si, Al-2wt.%Si, Al-3wt.%Si and Al-5wt.%Si alloys is about 41%, 45%, 56% and 79% higher than those of respective as-cast alloys (Figure 6.6). Further, yield strength and % elongation values of the USTed Al-Si alloys are higher than that of as-cast alloys (Figure 6.6). These results are related to the grain refinement observed after UST. A finer and globular (non-dendritic) microstructure results in higher values of the $\sigma_{0.2}$ and UST. The cavitation phenomenon resulting from UST might have caused degassing of the molten metal and thus decreased porosity. Figure 6.6 shows that total elongation of Al-Si alloy with UST is higher than as-cast alloys for respective solute contents.

At a fixed solute content, USTed Al-Cu alloys and Al-Ni alloys show better mechanical properties as compared to respective as-cast alloy. For all four Al-Cu alloys, it is clearly observed that the UTS remarkably increased with UST as compared to respective as-cast alloys. At a fixed content of solute (5%), the UTS of USTed Al-Cu alloy is ~70% higher than as-cast alloy. Similarly, for Al-5wt.%Ni alloy, the UTS of USTed Al-Ni alloy is ~18% higher than as-cast alloy. This can be explained by the Hall-Petch equation [212] (equation 6.2). According to Hall-Petch equation,

$$\sigma_y=\sigma_0 + k_y d^{-1/2} \ldots\ldots\ldots\ldots (6.2)$$

Where, σ_y is the yield strength, k_y is constant and d is the mean grain diameter. Yield strength of the materials is inversely related to the grain size [212]. In the case of USTed alloys, grain refinement is mainly dependent on solute content and ultrasonic intensity. Significant change in the microstructure with respect to the distribution of eutectic phases such as eutectic phase (α-Al + Si) in Al-Si alloys, eutectic phase (α-Al + Al_2Cu) in Al-Cu alloys, and eutectic phase (α-Al + Al_3Ni) in Al-Ni alloys, also might have had significant influence on the observed mechanical properties of aluminium alloys.

The results show that the mechanical properties of USTed aluminium alloys are better than that of respective as-cast alloys. This is mainly attributed to three aspects:

a. Nearly equiaxed and finer grains are obtained upon UST, which increased the grain boundaries area leading to grain boundary strengthening. As a result, the strength and ductility of USTed aluminium alloys increased of as compared to as-cast aluminium alloys.

b. Relatively finer and better distribution of eutectic phase is achieved upon UST, which is beneficial to improvement of strength and ductility of the alloys.

c. Mechanical properties and micro porosity have a very strong correlation in aluminium alloys. Micro-porosity can initiate cracking during tensile loading. Therefore, mechanical properties of as-cast samples that contained higher porosity are lower than USTed samples. UST has a great potential in degassing of molten metal, resulting in reduced porosity upon UST. This improved the mechanical properties of USTed aluminium alloys.

Therefore, the improvement of strength and ductility upon UST in this present work can could be mainly attributed to the combined effect of the equiaxed refined α-Al grain, refined and better dispersed eutectic phase and reduced porosity.

Table 6.1. Porosity content (vol.%) in as-cast and USTed binary aluminium alloys.

Specimens	**Conditions**	**Measured density (gm/cm^3)**	**Theoretical density (gm/cm^3)**	**Porosity (vol.%)**
Al-1wt.%Si	As-cast	2.61	2.695	3.10
	USTed	2.66	2.695	1.17
Al-2wt.%Si	As-cast	2.58	2.691	3.98
	USTed	2.65	2.691	1.49
Al-3wt..%Si	As-cast	2.56	2.687	4.65
	USTed	2.63	2.687	1.97
Al-5wt.%Si	As-cast	2.53	2.679	5.38
	USTed	2.62	2.679	2.28
Al-1wt.%Cu	As-cast	2.62	2.719	3.63
	USTed	2.68	2.719	1.46
Al-2wt..%Cu	As-cast	2.62	2.738	4.29
	USTed	2.69	2.738	1.87
Al-3wt.%Cu	As-cast	2.64	2.758	4.43
	USTed	2.70	2.758	1.94

Al-5wt.%Cu	As-cast	2.65	2.798	5.20
	USTed	2.73	2.798	2.36
Al-1wt.%Ni	As-cast	2.64	2.719	2.82
	USTed	2.68	2.719	1.51
Al-2wt.%Ni	As-cast	2.64	2.738	3.60
	USTed	2.69	2.738	1.6
Al-3wt.%Ni	As-cast	2.66	2.758	3.63
	USTed	2.70	2.758	1.97
Al-5wt.%Ni	As-cast	2.65	2.797	5.18
	USTed	2.73	2.797	2.46

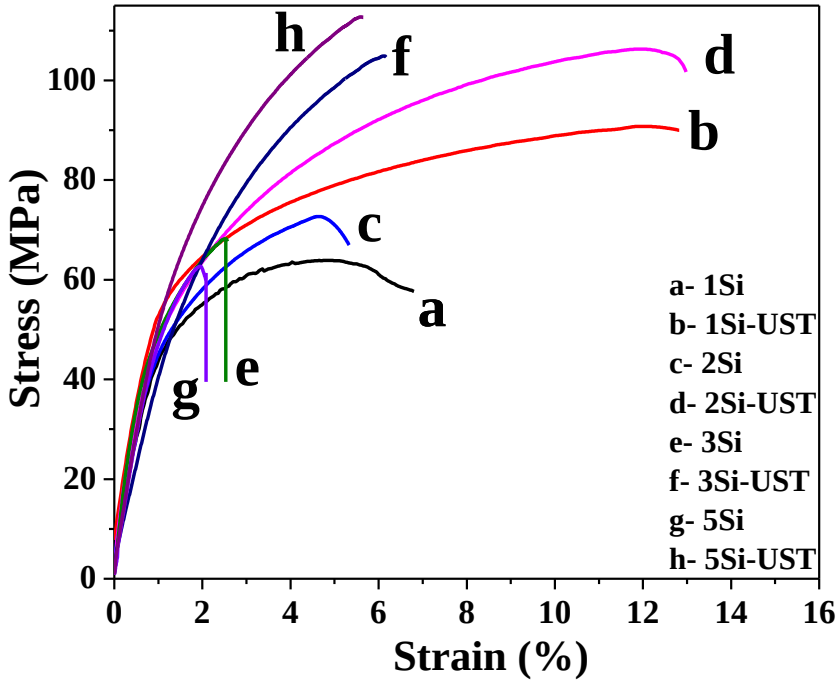

Figure 6.5. Engineering stress-strain curves of Al-(1-5%)Si alloys processed using different processing conditions.

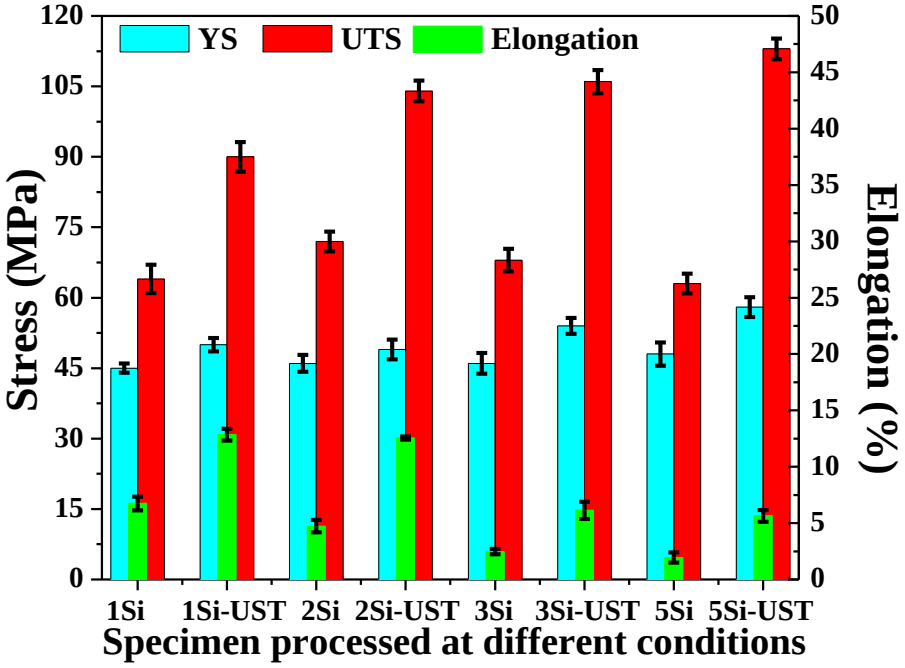

Figure 6.6. Variation of tensile properties of Al-(1-5%)Si alloys processed using different processing conditions.

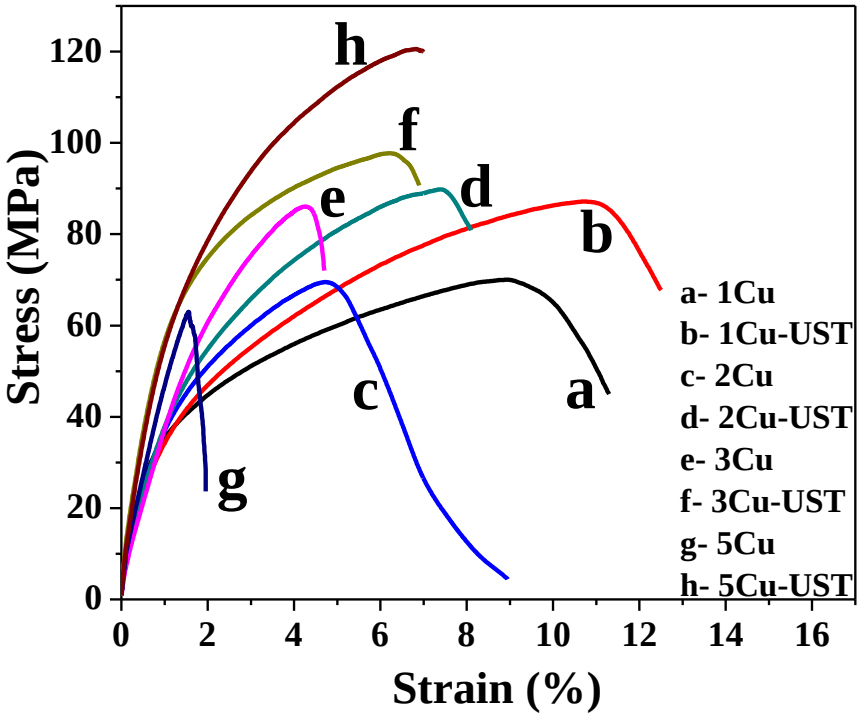

Figure 6.7. Engineering stress-strain curves of Al-(1-5%)Cu alloys processed using different processing conditions.

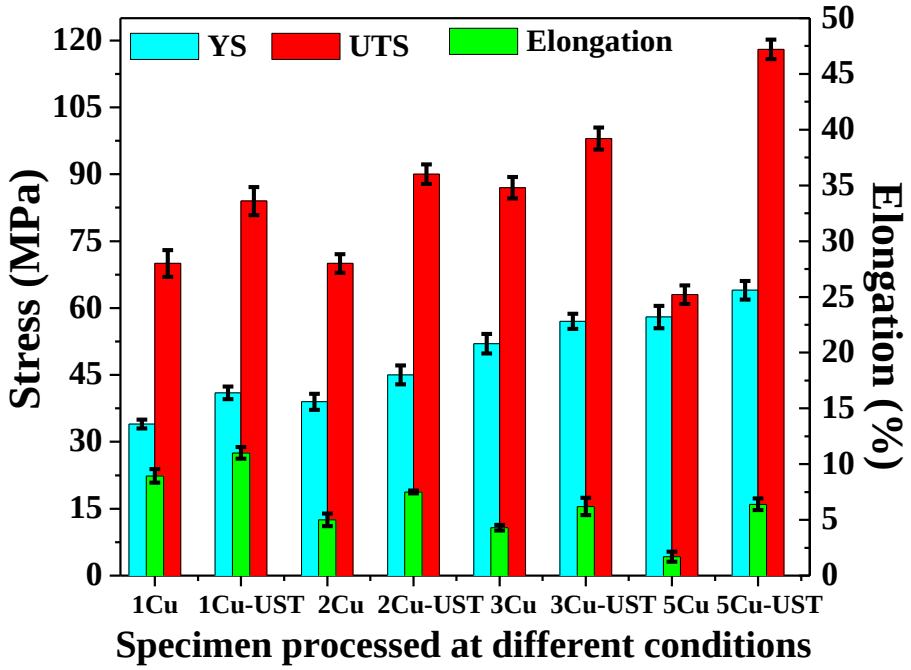

Figure 6.8. Variation of tensile properties of Al-(1-5%)Cu alloys processed using different processing conditions.

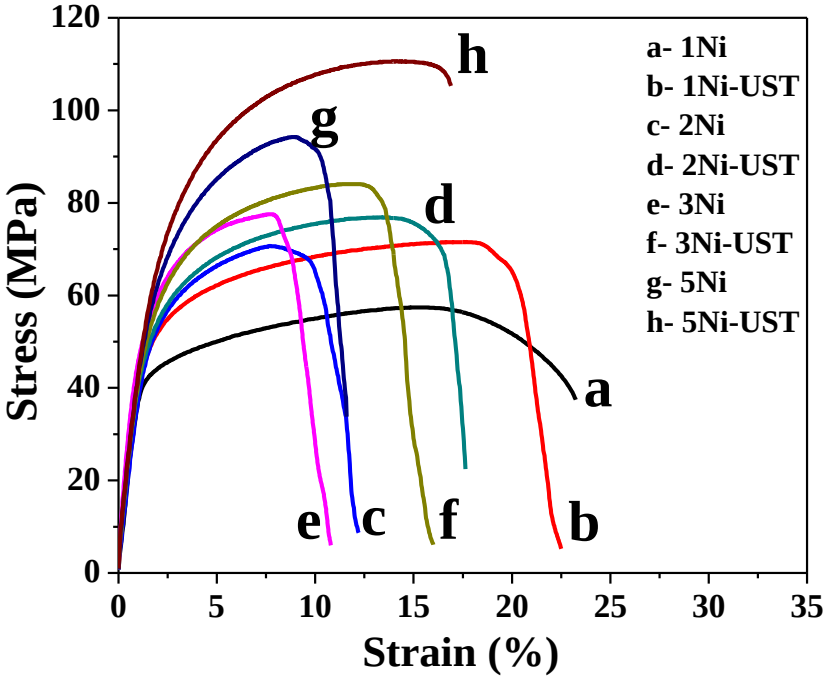

Figure 6.9. Engineering stress-strain curves of Al-(1-5%)Ni alloys processed using different processing conditions.

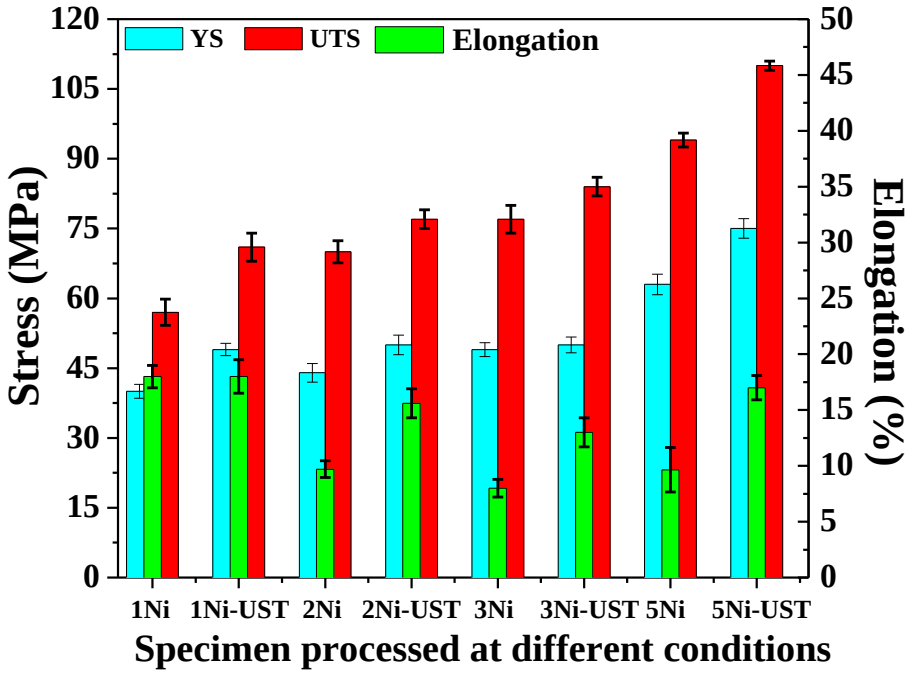

Figure 6.10. Variation of tensile properties of Al-(1-5%)Ni alloys processed using different processing conditions.

6.2.2. Fractography

Figure 6.11 shows the SEM fractographs of Al-(1-5%)Si alloys fabricated in as-cast and USTed (at ultrasonic intensity of 1400 W/cm^2) conditions. For as-cast alloys, dendritic morphology present in the shrinkage porosity is clearly observed (Figures 6.11a, c, e, and g). Amount of shrinkage porosity increased with increasing the content of solute, which is also confirmed from Table 6.1. Due to existence of structural defects in as-cast specimens such as shrinkage porosity, their strength and ductility is decreased (Figure 6.6). Interdendritic crack propagation is responsible for fracture in all the as-cast alloys (Figures 6.11a, c, e and g) [138,213,214]. The UST employed in this work reduced the porosity and refined the microstructure; as a result, shrinkage porosity is approximately eliminated from the USTed specimens (see Figures 6.11b, d, f. and h). As a result, the strength and ductility of the USTed specimens increased as compared to respective as-cast specimens (Figure 6.6). With UST, dendritic fracture surface morphology in as-cast specimens is replaced by cleavage facets, dimples, and tear ridges in USTed specimens. The fracture surfaces of USTed Al–Si specimens show an enhancement in the degree of brittleness with increasing content of solute (see Figures 6.11b, d, f, and h). Abdizadeh reported that the micro-cracks propagate along the interdendritic

aluminium-silicon eutectic phase for as-cast Al-Si alloys [215]. In high silicon alloys, cracks propagated along the embrittled grain boundaries of primary aluminium phase because of existence of brittle and hard eutectic silicon phase [216]. Gupta and Ling reported similar observations [216]. Therefore, ductility of the USTed specimen is also decreased upon increasing the content of silicon. In addition, acicular and fine eutectic silicon phase leads to stress concentration, which further breaks and forms the facets during fracture in USTed specimens [214]. The sizes of dimples decreased with increasing the amount of solute in USTed specimens. Micro-cracks are also observed in USTed specimens. Fracture surface of USTed Al-5wt.%Si alloy is covered mainly by cleavage facets and some tearing ridges, which indicates predominantly brittle fracture.

SEM fractographs of as cast Al-(1-5%)Cu alloys and those USTed at ultrasonic intensity of 1400 W/cm^2 are shown in Figure 6.12. Dendrite arms and shrinkage porosities are observed on the fracture surface of as-cast alloys (Figure 6.12a, c, e, and g). Therefore, interdendritic cracking mechanism appeared to be the leading mechanism for fracture of as-cast Al-(1-5%)Cu alloys (Figure 6.12a, c, e, and g). While dimples, tear ridges and some facets are observed in USTed Al-(1-5%)Cu alloys. Size of dimples decreased with the content of solute in USTed Al-(1-5%)Cu alloys (Figure 6.12b, d, f, and h). Reduction in dimple size in the USTed specimens may be because of the grain refinement of primary aluminium phase and work hardening, which occurs upon plastic deformation of the specimens [217]. In USTed Al-1wt.%Cu alloy, large sized and deeper dimples are observed in fracture surface, which indicates ductile fracture as dominant mechanism for failure. Fracture surface of USTed Al-5wt.%Cu alloy specimen show small sized dimples, some tear ridges, and more cleavage facets, which shows mixed mode fracture behavior. It can be observed that there are more dimples on the fracture surface of the USTed specimens (see Figures 6.12b, d, f. and h), as compared to respective as-cast specimens alloy (Figures 6.12a, c, e and g)). This shows that the ductility of the Al-Cu alloys increased with UST.

Fracture surfaces of as-cast and USTed Al-(1-5%)Ni alloys are shown in Figure 6.13. For the as-cast Al-Ni alloys, (Figure 6.13a, c, e and g), the fracture surfaces consist of dimples, micro voids, and some shrinkage porosity, with ductile fracture features being more dominant. Cante et al. reported that cavities or micro voids in as-cast samples are found due to Al_3Ni particles [209]. The existence of dimples in samples means that an enough amount of plastic deformation occurred before fracture. Therefore, higher ductility is observed in as-cast Al-Ni alloys (Figure

6.10). However, the ductility of USTed samples is higher than respective as-cast samples because of decrease in porosity upon UST, which is reflected in the absence of microvoids in the fractographs (Table 6.1). In addition, Wang reported that fine structure showed high ductility because of inferior particle cracking rate as compared to large and elongated eutectic or secondary phase [206]. In USTed Al-1wt.%Ni alloy sample (Figure 6.12b), some micro-carks are observed along the grain boundary in some regions, suggesting that intergranular fracture occurred in these regions. Whereas, in some regions, no micro-cracks are found along the grain boundary, and transgranular fracture is observed. In other USTed samples (see Figure 6.12d, f, and h), very few micro-cracks are observed along the grain boundary, therefore, transgranular fracture is dominant mechanism for failure of these samples. Some tear ridges, few fine dimples, and some cleavage facets are also observed in these USTed samples. Therefore, mixed mode failure is observed in USTed samples.

These results show that UST changes the fracture mode and thereby leads to increase the strength and ductility of binary aluminium alloys.

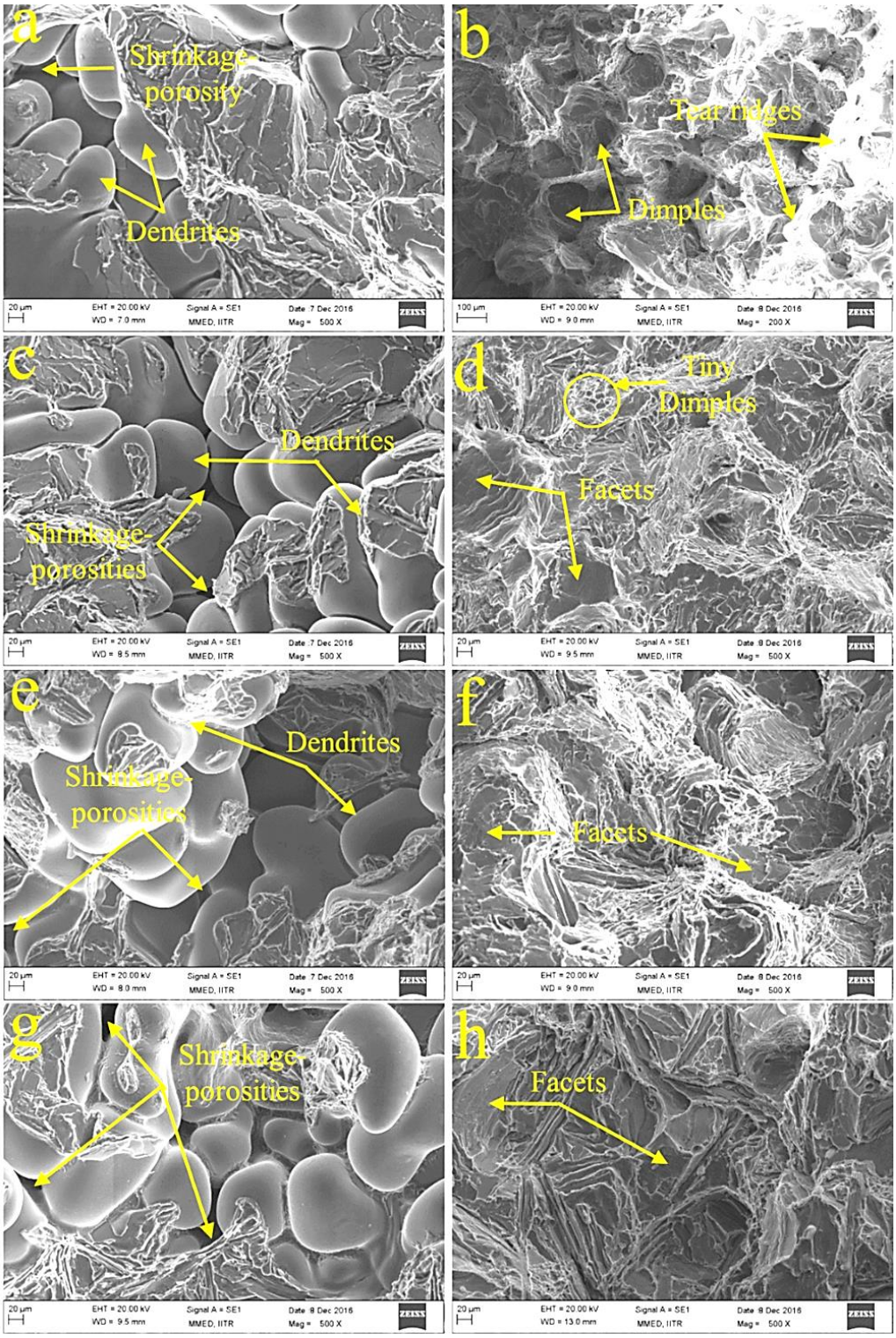

Figure 6.11. SEM fractographs of fractured tensile specimens of Al-1wt.%Si alloys- (a) as-cast and (b) with UST, Al-2wt.%Si alloys- (c) as-cast and (d) with UST, Al-3wt.%Si alloys- (e) as-cast and (f) with UST, and Al-5wt.%Si alloys- (e) as-cast and (f) with UST.

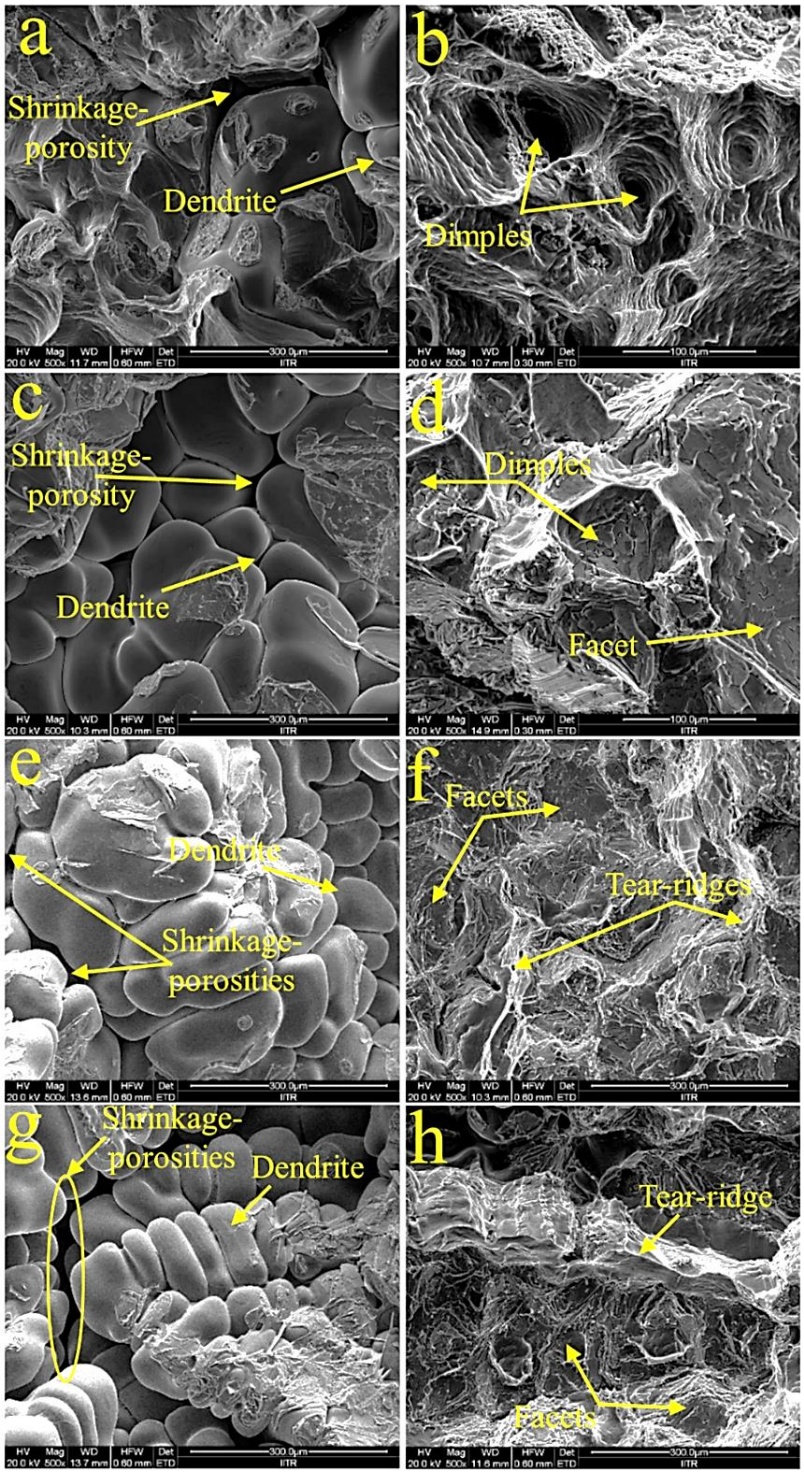

Figure 6.12. SEM fractographs of the tensile fractured surface of Al-1wt.%Cu alloys- (a) as-cast and (b) with UST, Al-2wt.%Cu alloys- (c) as-cast and (d) with UST, Al-3wt.%Cu alloys- (e) as-cast and (f) with UST, and Al-5wt.%Cu alloys (e) as-cast and (f) with UST.

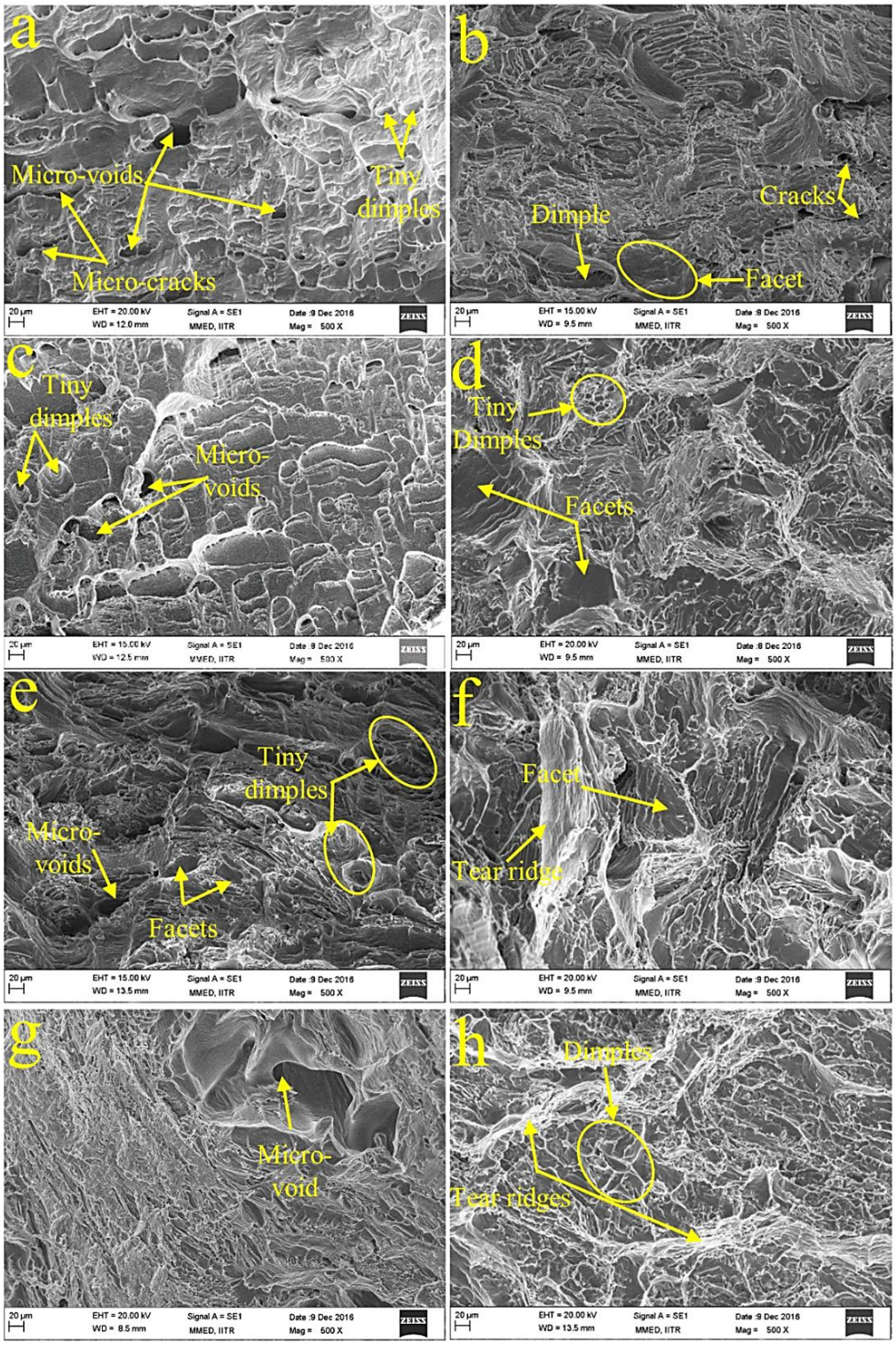

Figure 6.13: SEM fractographs of the tensile fractured surface of Al-1wt.%Ni alloys- (a) as-cast and (b) with UST, Al-2wt.%Ni alloys- (c) as-cast and (d) with UST, Al-3wt.%Ni alloys- (e) as-cast and (f) with UST, and Al-5wt.%Ni alloys- (e) as-cast and (f) with UST.

6.3. Summary of results

1. High-intensity ultrasonic treatment during solidification produced significant refinement of the eutectic structures in the Al-5wt.%Si alloy, Al-5wt.%Cu alloy, and Al-5wt.%Ni alloy.
2. Mechanical properties of USTed alloys are better than respective as-cast alloys due to combined effect of grain refinement of primary aluminium phase, refinement of eutectic phase, and reduction in porosity upon UST.
3. UST also changed the fracture mode from interdendritic fracture in as-cast, Al-1wt.%Si, Al-2wt.%Si, and Al-3wt.%Si alloys to mixed mode in USTed alloys and from interdendritic fracture in as-cast Al-Cu alloys to dominant ductile fracture in USTed alloys. For Al-Ni alloys, fracture mode is changed from dominant ductile fracture in as-cast alloys to dominant mixed mode.

CHAPTER 7

DISPERSION OF NANO-PARTICLES DURING UST

7.1. Introduction

Al6061 alloy is a 6xxx series aluminium alloy, which contains magnesium and silicon as major solute elements [52,218]. Al6061 alloy is widely used in the application of industrial, construction, automobile, and marine applications due to its favorable properties like good weldability, good forgeability & extrudability, high strength-to-weight ratio, and excellent corrosion resistance [52,218,219]. The properties of Al6061 alloy can be further improved by adding the nano-particles reinforcement using UST. Adding ceramic Al_2O_3 particles into aluminium alloy matrix, enhances properties such as high temperature properties, specific stiffness, oxidation resistance, and mechanical properties as compared to base alloy [51,220]. Micron sized Al_2O_3 particles are widely used in fabricating MMC's [221], and now nano-sized Al_2O_3 particles are easily available for fabricating the nano-composites [220].

Because dispersion of nano-particles in molten metals is challenging because of agglomeration and wettability issues, this chapter deals with the effect of temperature of high power ultrasonic processing (700ºC, 725ºC, 750ºC, and 775ºC) on the distribution of 1 wt.% Al_2O_3 nano-particles in Al6061 alloy melt. Al6061 alloy composite is also fabricated with varying content (1, 2 and 3 wt.%) of nano-particles at ultrasonic processing temperature of 775ºC. The microstructural features and mechanical properties of nano-composites are characterized. Various strengthening mechanisms operating in the ultrasonically processed nano-composites are analyzed.

7.2. Effect of UST processing temperature on the microstructure and mechanical properties of nano-composites

7.2.1. Density

Figure 7.1 shows the porosity content of Al6061 alloy and its composites, which are fabricated under the different processing conditions. It can be observed that NC775MS and NC700 specimens show higher porosity as compared to other composites. The porosity is also

higher for the NC775 specimen. Melt temperature influences the viscosity of the melt and thereby plays an important role in the porosity of cast materials. Figure 7.2 shows the effect of processing temperature on viscosity of molten Al6061 and its composites. Relationship between temperature and viscosity of particle dispersed composite (η_c) melt is represented by equation 7.1 [222].

$$\eta_c = \eta_m\left(1 + 2.5\,V_p + 10.5{V_p}^2\right) \ldots\ldots\ldots (7.1)$$

Where, V_p is the volume fraction of dispersed particles. Viscosity of molten matrix (η_m) at temperature T is given by equation (7.2) [223].

$$\eta_m = \eta_0 \exp\left(\frac{E}{RT}\right) \ldots\ldots\ldots\ldots\ldots\ldots\ldots (7.2)$$

where E is the activation energy for viscous flow. By using equations (7.1) and (7.2), η_c is calculated as a function of temperature and the results are shown in Figure 7.2.

Higher melt viscosity at 700°C inhibits the ultrasonic cavitation phenomenon and therefore ultrasonic degassing efficiency is poor. On the other hand, at higher temperature of 775°C, the solubility of hydrogen gas in molten aluminium alloy is high as compared to other processing temperatures [27,181,224]. Some hydrogen is always picked up because of inadequate protection from argon in aluminium melting and degassing is often necessary [225,226]. It is also reported that even after argon degassing, the melt has some amount of hydrogen content [227]. In addition, the clusters of added particles also contain air and in the present work, it is likely that the argon protection was insufficient during stirring and nano-particles addition process. Therefore, UST duration longer than that used in the present work is possibly required for effective degassing and minimization of porosity in the latter case. The mechanism of ultrasonic degassing is thoroughly interrelated to the phenomenon of cavitation in the molten metal. The surface area of pulsating bubbles is many times larger in rarefaction phase when compared to compression phase. At this time, the hydrogen gas diffuses from the surrounding melt in to the bubbles. In rarefaction phase, the amount of hydrogen gas that enters in to the bubble is greater than the amount of hydrogen gas leaving the bubble in compression phase. This is called rectified mass diffusion effect [180], due to which the bubble gains significant amount of hydrogen gas over several cycles. Due to hydrodynamic buoyancy force, large bubbles can float on the surface of the molten metal and escape from the surface [27][228].

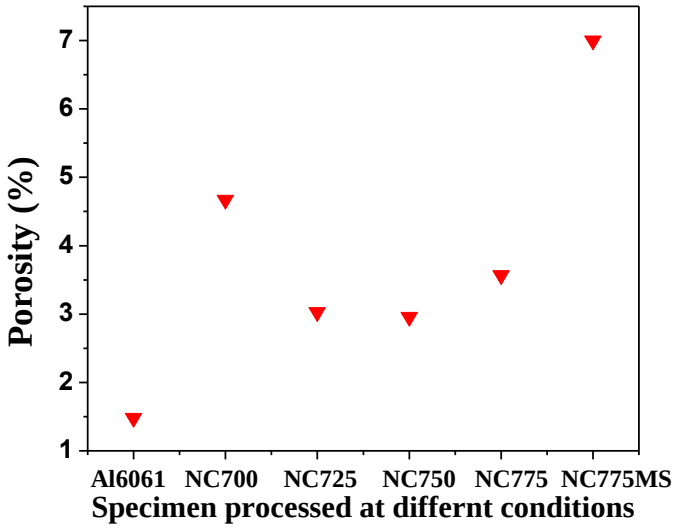

Figure 7.1. Porosity (vol.%) content in Al6061 alloy and its composites.

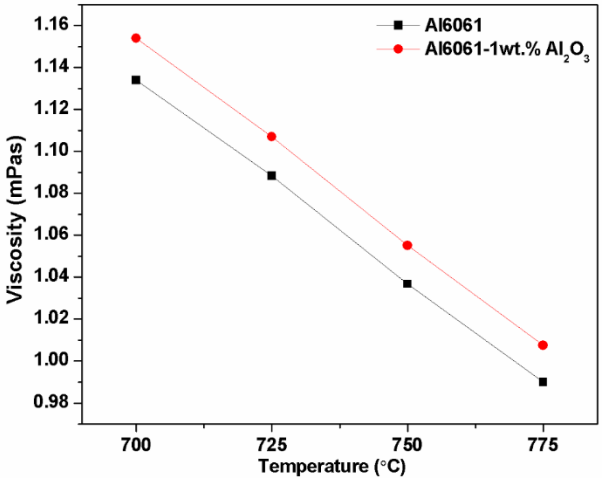

Figure 7.2. Calculated variation of melt viscosity with temperature for Al6061 alloy and its composites.

7.2.2. Microstructural analysis

Figure 7.3 shows the optical micrographs of aluminium alloy and its nano-composites processed at different UST temperatures. The average grain size of as-cast aluminium alloy shown in Figure 7.3a is 310 µm. By adding the 1 wt.% Al_2O_3 reinforcement at 775°C with manual stirring (MS) and at 700°C with UST, grain size reduced drastically by 61% and 41% as compared to as-cast Al6061 alloy (Figure 7.3b and c). By increasing the UST temperature beyond 700°C, a finer dendritic microstructure is obtained (Figure 7.3d, e, and f). It can be observed that the grain size of primary α-Al phase decreased effectively with increasing UST temperature.

Figure 7.4 shows that with increase in the UST temperature to 725°C, 750°C, and 775°C the average grain size by reduced 74%, 77%, and 79%, respectively, with respect to the as-cast Al6061 alloy.

One reason for this refinement is the presence of Al_2O_3 nano-particles in the melt, which provide heterogeneous nucleation sites and thus increase the rate of nucleation. UST further enhances the wetting of non-metallic and reinforcement particles, and uniformly disperses them into the molten metal because of the acoustic streaming effect [16,106,229]. The increased uniformity in the dispersion of nano-particles with UST processing temperature, which is discussed later, further contributed to the grain refinement.

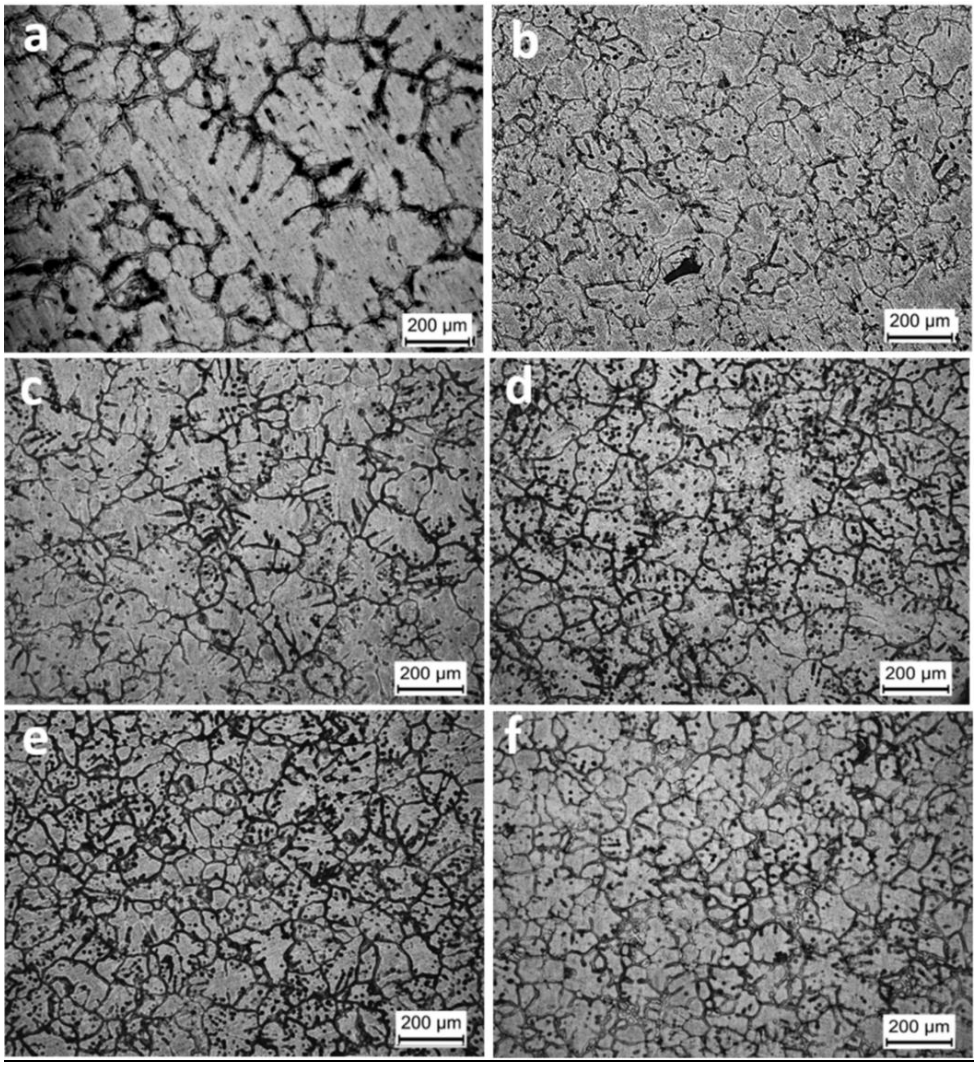

Figure 7.3. Optical micrographs of (a) Al6061 alloy, and its composites- (b) NC7775MS, (c) NC700, (d) NC725, (e) NC775, and (f) NC775.

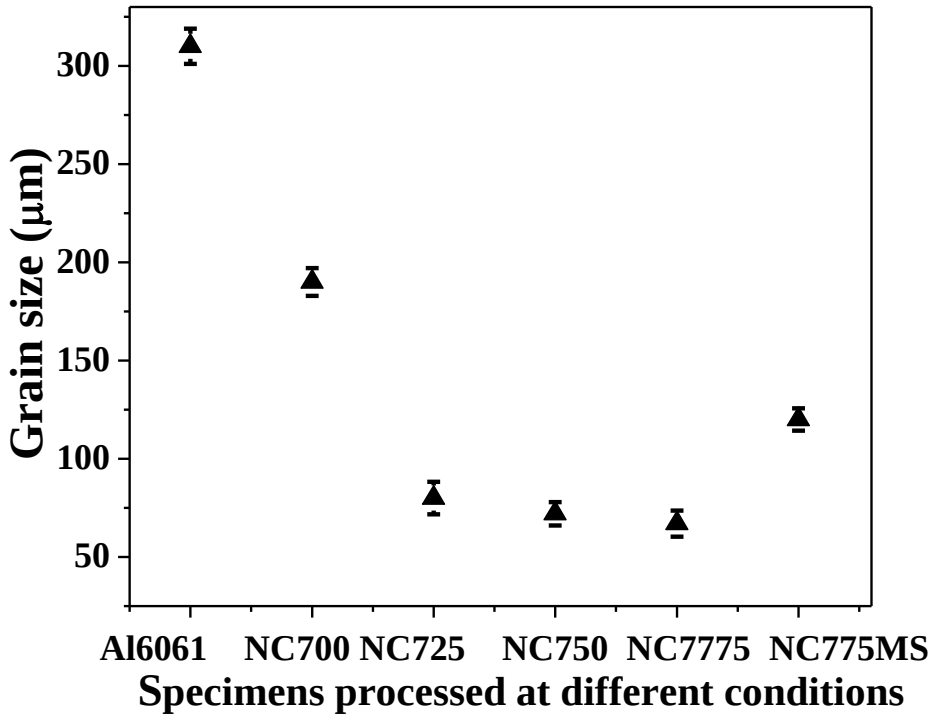

Figure 7.4. Variation in grain size of Al6061 alloy and its composites.

7.2.3. Nano-particles distribution

Figure 7.5 shows the SEM micrographs of Al6061/ Al_2O_3 composites fabricated with MS and with UST. Figures 7.5a and b show sporadic clusters of alumina particles remaining in the melt after manual stirring (1 μm size) and after UST at 700°C (200-250 nm size). Figures 7.5c, d, and e show that Al_2O_3 particles are increasingly well distributed in the aluminium alloy matrix. With increasing processing temperature, the UST broke the clusters effectively and uniformly dispersed the nano-particles inside the grains. The ultrasonic cavitation is weaker at low UST temperature (specimens NC700 and NC725) as compared to at higher temperatures (specimens NC750 and NC775).

Further investigation of the NC775 composite is performed with high magnification bright field TEM image, as shown in Figure 7.6. It shows the dispersion of Al_2O_3 particles in the Al6061 alloy matrix. It can be clearly seen in Figure 7.6a that single nano-particles are dispersed in Al6061 alloy matrix whereas some clustered particles are also observed. Nano-particles are engulfed inside the primary aluminium grain. Uniform distribution of Al_2O_3 nano-particles confers some heterogeneous nucleation sites during solidification. As a result, a more refined

microstructure is observed in NC775 composite as compared to as-cast Al6061 alloy. Dislocation loops are also observed in NC775 composite, as seen in Figure 7.6b, which are generated due to thermal mismatch between the Al6061 alloy matrix and Al_2O_3 nano-particles.

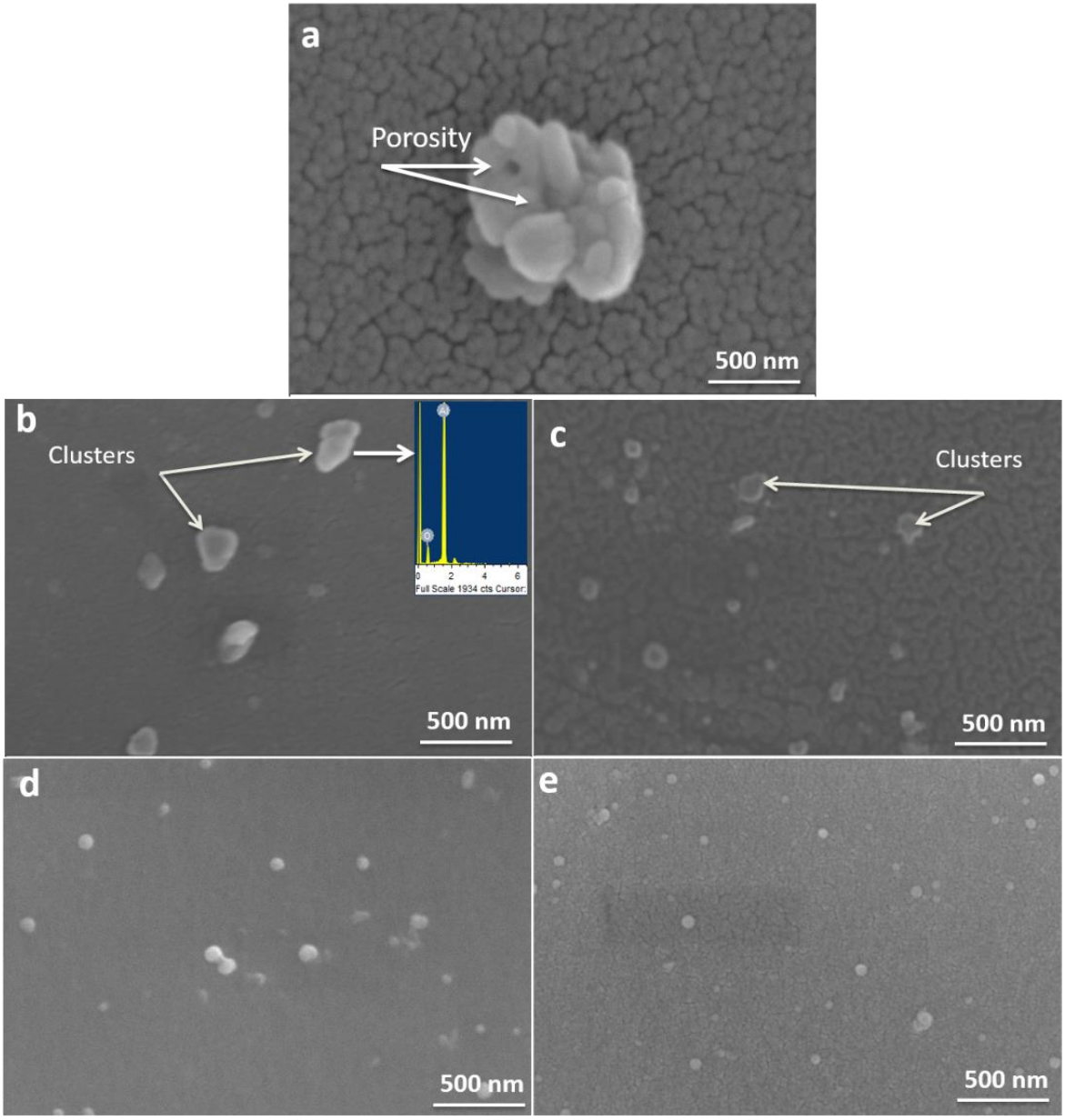

Figure 7.5. SEM micrographs of (a) NC775MS, (b) NC700, (c) NC725, (d) NC750, and (e) NC775 nano-composites showing dispersion of alumina particles. Inset in (b) shows the energy spectra of an alumina cluster.

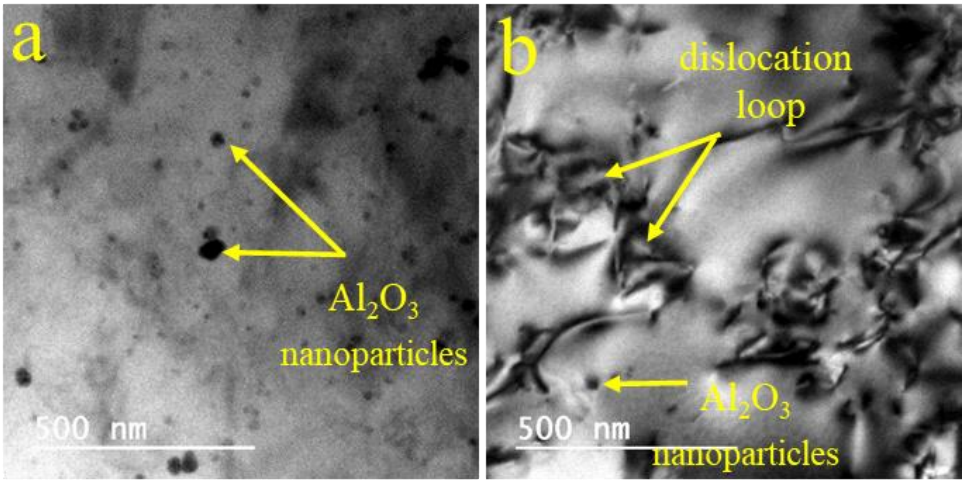

Figure 7.6. TEM micrographs of NC775 nano-composite showing (a) dispersion of alumina particles and the (b) dislocation loops.

7.2.4. Mechanism of improved dispersion during UST

As discussed earlier in Chapter 2, ultrasound assisted solidification is a promising method for uniform dispersion of nano-particles in molten matrix [116,144,153]. During UST, acoustic waves generate tensile stress in the molten metal, which leads to formation of tiny cavities. During the expansion cycles, the cavities grow whereas during the compression cycles they collapse and produce transient (in the order of microseconds) micro "hot spots" [16,169,230], where very high temperatures (5000°C) and pressures (~ 1000 atm) are generated. Equation 7.3 suggests that contact angle θ can be decreased and the wettability of the nano-particles can be increased by increasing their surface energy in vapor phase (σ_{sv}) or by decreasing the surface energy of liquid (molten metal) in vapor phase (σ_{lv}) [231].

$$\sigma_{sv} - \sigma_{sl} = \sigma_{lv} \cos\theta \ldots\ldots\ldots\ldots\ldots\ldots (7.3)$$

Clusters of Al_2O_3 particles, which are filled with air, loosen, and individual dispersed particles act as nuclei for solidification. As discussed earlier, when the ultrasonic probe is inserted into molten metal, the high-pressure pulses and localized high temperature generated by UST induced cavitation [232] enhance the wettability of Al_2O_3 particles by removing or desorbing the gases from the surface of the ceramic particles and filling up of the micro cracks by the melt [46,118]. It increases the surface energy of nano-particles in vapor phase. At very high temperature (5000°C), the surface tension of liquid with vapor is significantly decreased which

further enhances the wettability of the nano-particles. High intensity shock waves generated by UST break the clusters of nano-particles and improve the wettability thereby ensuring their uniform dispersion in the melt [46,57].

7.2.5. Mechanical Properties

Hardness and tensile properties of fabricated aluminium alloy composites are studied as a function of UST processing temperatures. Figure 7.7 shows the average hardness of differently processed nano-composites and the as-cast Al6061 alloy. All the nano-composites have higher hardness as compared to the as-cast Al6061 alloy. Among the UST nano-composites, those processed at higher temperatures exhibit progressively higher hardness. As compared to the as-cast Al6061 alloy, increase in hardness of about 20%, 31%, 42%, 53% and 61% is observed for NC775MS, NC700, NC725, NC750, and NC775 composites respectively. Hardness increases significantly due to combined effect of reduction of grain size and particle strengthening effects.

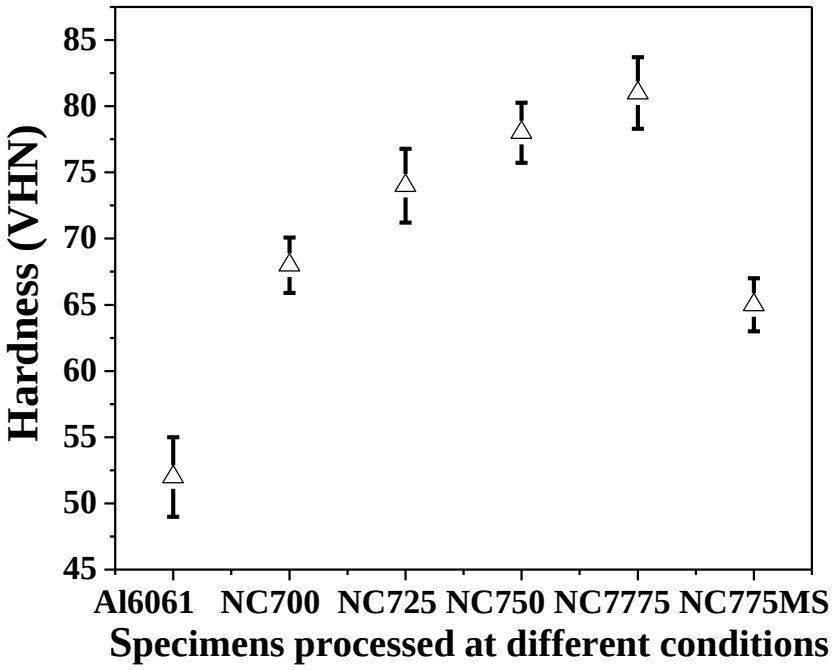

Figure 7.7. Variation in hardness of Al6061 alloy and its composites.

Figure 7.8 shows engineering stress-strain curves of as-cast Al6061 alloy and alloy nano-composites. Variation in tensile properties is depicted in Figure 7.9. It can be seen that the yield strength ($\sigma_{0.2}$) and ultimate tensile strength (UTS) of all the composites are superior as compared to the as-cast Al6061 alloy. The yield strengths of NC775MS and NC775 composite are 20%

and 67% higher than that of the as-cast Al6061 alloy. Tensile strength and ductility of NC775MS composite is inferior to other composites due to poor distribution and more agglomeration of particles (Figure 7.5a). For NC775MS composite, there is no role of Orowan strengthening mechanism for improving the tensile strength of composite because average particle/cluster size is about one μm (Figure 7.5a) and the improvement in tensile strength occurred due to grain refinement and thermal mismatch strengthening mechanisms. The numerical value contributions from these mechanisms are discussed later.

Tensile strength of USTed composites shows improvement with increasing the UST processing temperature because of increasing dislocation density due to larger CTE mismatch between matrix and reinforcement, increment of grain boundary area because of grain refinement, and presence of uniformly distributed Al_2O_3 particles that increase the effect of Orowan strengthening. By increasing the ultrasonic processing temperature, clusters of particles are broken (Fig. 7.5). Therefore, Orowan strengthening acts more effectively in USTed composites as compared to composite processed using manual stirring (NC775MS).

At the highest UST temperature of 775^{o}C, absorption of hydrogen in the molten alloy is more, which increased the percentage of micro porosity in NC775 composite (Figure 7.8). Therefore, it's percent elongation value is lower than those of NC725 and NC750 specimens. NC700 specimen exhibited poor ductility as compared to as-cast Al6061 alloy. Upon adding 1 wt.% nano-particles, viscosity of molten metal is increased which reduced the efficacy of UST. Less efficient UST resulted in poor degassing (higher porosity), and the reinforcement particles remained in clustered form in the matrix (Figure 7.8). Therefore, ductility of NC700 composite is reduced.

7.2.6. Strengthening mechanism

To observe the effect of Al_2O_3 particles on mechanical properties of aluminium alloy composites, mainly two strengthening mechanisms should be considered. One is the classical load transfer from matrix to reinforcement (the continuum mechanics) mechanism, the contribution of which is insignificant because the amount of reinforcement in this work is very small i.e. ~0.7 volume pct. The other mechanism is micromechanics strengthening mechanism. In this, the improvement in yield strength can be attributed to grain refinement, thermal mismatch strengthening, and Orowan strengthening mechanisms.

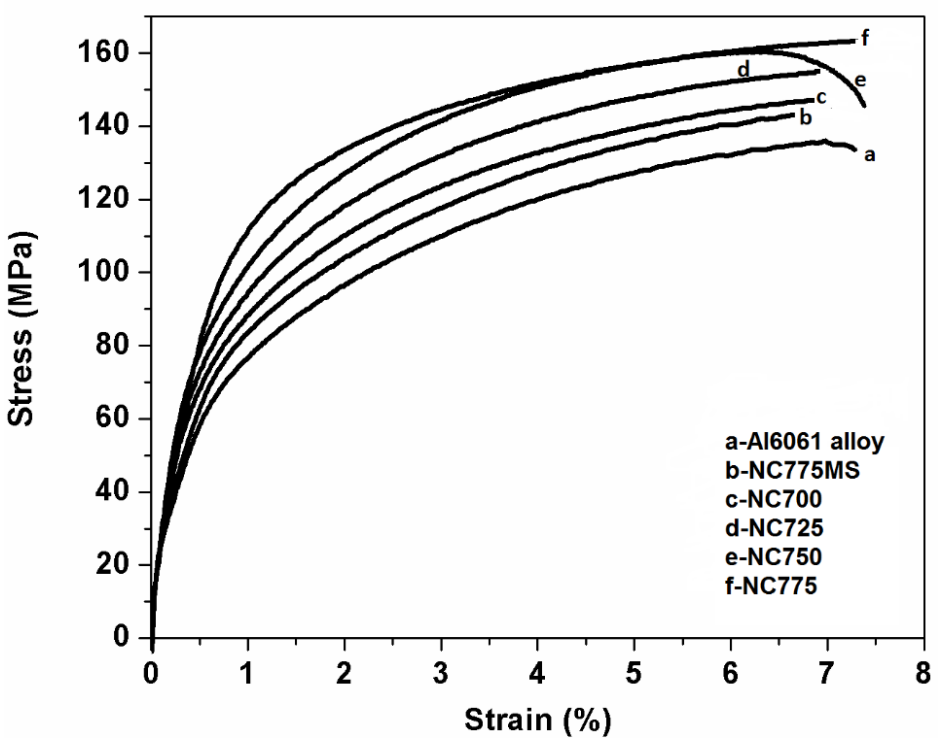

Figure 7.8. Engineering stress-engineering strain curves of Al6061 alloy and its composites.

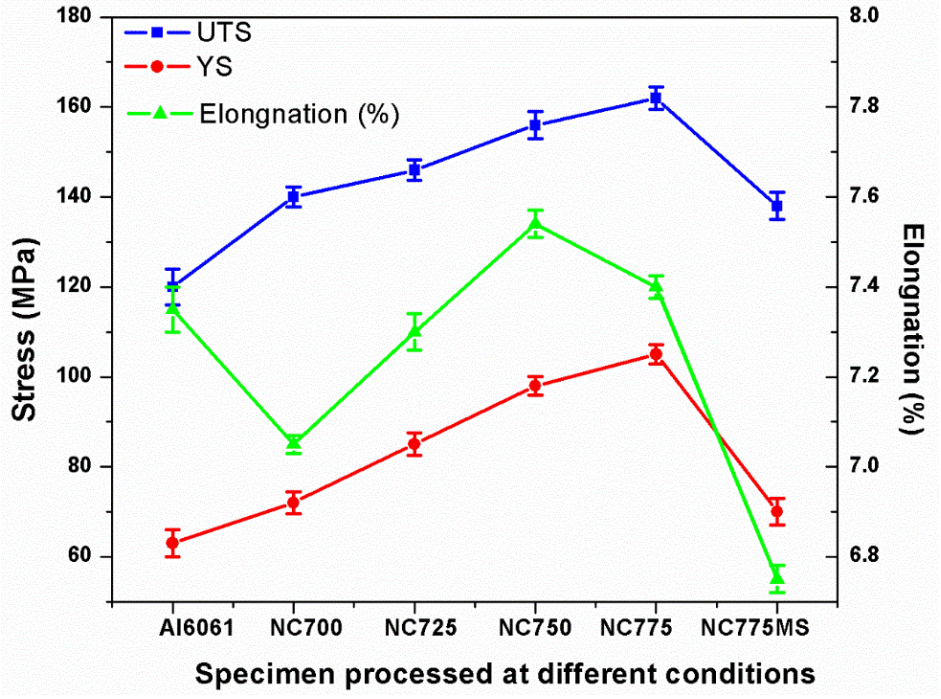

Figure 7.9. Variation in tensile properties of Al6061 alloy and its composites.

7.2.6.1. Grain refinement strengthening mechanism

Decrease in grain size of aluminium alloy increases the yield strength of the composites according to Hall–Petch relationship [48,116,157,212]. The relative increment in yield strength of composite as compared to the base alloy due to grain refinement can be described as:

$$\Delta\sigma_{Hall-Petch} = k\left(\frac{1}{\sqrt{d}} - \frac{1}{\sqrt{d_0}}\right) \ldots\ldots\ldots\ldots\ldots\ldots \quad (7.4)$$

where, d is the average grain size of the composite at different processing temperatures, d_0 is average grain size of as-cast Al6061 alloy, and the value of k (Hall-Petch equation slope) is taken as 74 MPaμm$^{1/2}$ [233]**.**

7.2.6.2 Orowan strengthening mechanism

It is known that Orowan strengthening mechanism is not significant when the reinforcement particles are coarse (micron sized) and inter-particle spacing is large. However, when Al_2O_3 particles of very small size (less than 1 μm) are reinforced in the alloy matrix, as in the present work, it also contributes to strengthening. It is observed that increasing the UST processing temperature dispersed the particles better and inter-particle distance is decreased (Figure 7.5). Therefore, $\Delta\sigma_{Orowan}$ can be calculated for Al6061-1wt.%Al_2O_3 composites by using Orowan Ashby equation [157][151] :

$$\triangle\,\sigma_{\mathrm{Orwan}} = \frac{0.13\mathrm{Gb}}{\lambda}\ln\frac{\mathrm{D}}{2\mathrm{b}} \ldots\ldots\ldots\ldots\ldots\ldots \quad (7.5)$$

Where G is the shear modulus of base alloy, b is the Burgers vector of Al, λ is the average inter-particle spacing, and D is the average diameter of nano-particles. The inter-particle spacing λ is expressed as [157][151]:

$$\lambda = \mathrm{D}\left[\left(\frac{1}{2\mathrm{V_p}}\right)^{1/3} - 1\right] \ldots\ldots\ldots\ldots\ldots\ldots \quad (7.6)$$

7.2.6.3 Thermal mismatch strengthening mechanism:

Aluminium alloy matrix and Al_2O_3 particles have different CTE. During cooling of composite in solidification process, great amount of dislocation density will be generated due to thermal mismatch between the matrix and the reinforcement [234] . Therefore, $\triangle\,\sigma_{\mathrm{CTE}}$ can be calculated as [149]:

$$\triangle \sigma_{CTE} = \eta Gb\sqrt{\rho} \quad \ldots\ldots\ldots\ldots\ldots\ldots\ldots\ldots\ldots\ldots (7.7)$$

Here η is a constant with value close to 1. Dislocation density (ρ) can be calculated as [235,236]:

$$\rho = \frac{12\triangle\alpha\triangle T V_p}{bD(1-V_p)} \quad \ldots\ldots\ldots\ldots\ldots\ldots\ldots\ldots\ldots\ldots (7.8)$$

Where, Δα is the difference in CTE between the Al alloy matrix (25.2×10^{-6} K^{-1}) and the reinforcing particles Al_2O_3 (8.2×10^{-6} K^{-1}). ΔT is the difference between stress free homologous temperature and room temperature. Between the solidus temperature and the stress free homologous temperature, diffusional processes including creep will relieve the stresses. Thus, during cooling until this stress free homologous temperature, the alumina particle and the matrix are stress-free. Assuming that the dislocation punching is initiated at a temperature of 504 K (related to a stress free homologous temperature of 0.59) [237], the value of ΔT is 206 K. For each of the strengthening contributions, the important parameters used in calculating the yield strength are given in Tables 7.1 and 7.2.

Table 7.1. Important parameters used for estimating the value of increment in yield stress due to various strengthening mechanisms for the Al6061-1wt%Al_2O_3 nano-composites.

G (GPa)	**D (nm)**	**k (MPa-μm$^{1/2}$)**	**Δα (K^{-1})**	**b (nm)**	**V_p**
26	50	74	17×10^{-6}	0.286	0.007

Using the parameters in Table 7.1 and using the equations 7.4, 7.5, 7.6, 7.7, and 7.8, different operating strengthening mechanisms are evaluated/discussed. The results showing respective contributions of each mechanism for composites specimen are given in Table 7.2. Average inter-particle distance is decreased significantly by increasing the UST processing temperature. Average inter-particle distance and $\Delta\sigma_{Orowan}$ of NC775 composite is about two times and 1.6 times that of NC700 and NC725 composites. In NC775MS composites, Orowan strengthening mechanism is not applicable because the cluster size is around 1 μm. The $\Delta\sigma_{CTE}$ of NC775 specimen is approximately 6.6 and 1.4 times that of the $\Delta\sigma_{Hall\text{-}Petch}$ and $\Delta\sigma_{Orowan}$, respectively. It is clear that thermal mismatch strengthening mechanism is most efficient one,

followed by Orowan strengthening mechanism and then the grain size strengthening mechanism in all composite specimens.

Table 7.2: The yield stress contributions from various strengthening mechanisms for the NC700, NC725, NC750, NC775, and NC775MS composites.

Al alloy composites	**Average grain size (μm)**	**Average size of nano-particles (nm)**	**Inter-particle distance (nm)**	$\Delta\sigma_{Orowan}$ **(MPa)**	$\Delta\sigma_{CTE}$ **(MPa)**	$\Delta\sigma_{Hall-Petch}$ **(MPa)**
NC700	190	156	390	13.9	14.9	1.31
NC725	80	107	337	15	23.1	4.07
NC750	72	80	288	16.1	28.6	4.51
NC775	67	56	200	22.6	32	4.84
NC775MS	120	1000	**	0	0.239	2.55

** Not applicable because of large cluster size.

7.2.7. Use of various models for calculating the yield strength of composites

Several researchers reported the various superposition methods for analyzing the yield strength enhancement of aluminium alloy nano-composites. These methods are an arithmetic summation, quadratic summation, and compounding methods [157]. In the present, there is no general opinion as to which model is more accurate for predicting the yield strength of composites.

7.2.7.1. Arithmetic summation method

This method is a simply addition of each strengthening mechanisms in a linear manner. It is assumed that different strengthening mechanisms do not influence each other and can freely contribute to the final yield strength of composites [157,158].

$$\Delta\sigma = \Delta\sigma_{Hall-Petch} + \Delta\sigma_{Orowan} + \Delta\sigma_{CTE} + \Delta\sigma_{LOAD} \ldots\ldots\ldots\ldots (7.9)$$

7.2.7.2. Compounding method

This method is differed from the arithmetic summation and quadratic summation methods. In this analysis, improvement of the yield strength due to nano-particles ($\Delta\sigma$) is not added to the yield strength of the base alloy (σ_m), but it is multiplied to the σ_m [157]. According to eq.

$$\sigma_{y,c} = \sigma_m \times \Delta\sigma \ldots\ldots\ldots\ldots\ldots\ldots\ldots\ldots\ldots\ldots\ldots\ldots \text{(7.10)}$$

Where $\Delta\sigma = \left(1 + \frac{\Delta\sigma_{Hall-Petch}}{\sigma_m}\right)\left(1 + \frac{\Delta\sigma_{Orowan}}{\sigma_m}\right)\left(1 + \frac{\Delta\sigma_{CTE}}{\sigma_m}\right)\left(1 + \frac{\Delta\sigma_{LOAD}}{\sigma_m}\right) \ldots\ldots\ldots \text{(7.11)}$

7.2.7.3. Quadratic summation method

Clyne and co-workers proposed a new method for predicated the yield strength of composites, which is quadratic summation method. In this method, assuming that that the each strengthening mechanisms interact with each other and the sum of the squares of each strengthening mechanism is proportional to the square of the total yield strength enhancement [157,238,239]. However, this method is proposed for micron-sized composites. It is reported that the properties of composites alter significantly in nano-composites; therefore, the assumptions for micron-sized composites cannot be essentially applied to nano-composites. In this approach, the square root of the sum of the squares is applied for considering the contributions of different strengthening mechanisms into the yield strength of the composite [157,238,239]. Equation 7.12 is called Sanaty-Zadeh model.

$$\Delta\sigma^2 = \Delta\sigma_{Hall-Petch}{}^2 + \Delta\sigma_{Orowan}{}^2 + \Delta\sigma_{CTE}{}^2 + \Delta\sigma_{LOAD}{}^2 \ldots\ldots\ldots \text{(7.12)}$$

For arithmetic summation and quadratic summation methods, the yield strength of the composites is calculated using the equation 7.11

$$\sigma_{y,c} = \sigma_m + \Delta\sigma. \ldots\ldots\ldots\ldots\ldots\ldots\ldots\ldots\ldots\ldots\ldots\ldots \text{(7.13)}$$

In present research, Orowan and CTE strengthening mechanisms played major roles in the enhancement of the yield strength of nano-composites. On the other hand, there is insignificant effect of Hall-Petch and load bearing strengthening mechanisms on the strength of composite. Therefore, it is necessary to take the square root of the sum of squares of Orowan and CTE strengthening contributions that directly influenced the strength of nano-composites. Hence,

Modified Clyne model is used in present work to evaluate precisely the predicted the yield strength of the aluminium alloy nano-composites [155].

$$\sigma_{y,c} = \sigma_0 + \triangle \sigma_{\text{Hall-Petch}} + + \Delta\sigma_{LOAD} + \sqrt{(\triangle \sigma_{\text{Orowan}})^2 + (\triangle \sigma_{\text{CTE}})^2} \quad \text{..... (7.14)}$$

Where, $\sigma_{y,c}$ is the yield strength of the composite.

The estimated theoretical and experimental yield strength values are summarized in Table 7.3. It shows that theoretically highest value of yield strength is observed by using compounding methods, followed by arithmetic summation method, Modified Clyne model and then quadratic summation method in all composite specimens. For NC700, NC725, NC750 and NC775 nano-composites, the calculated value of yield strength of composite using arithmetic summation method are 1.3, 1.2, 1.14 and 1.2 times higher the experimental values of composite specimens, respectively. Several researchers observed that the value of yield strength of composites, which is calculated by arithmetic summation method, is much higher than the experimental value of yield strength of composites [157,158]. The theoretical value of yield strength of composites calculated using Modified Clyne model and quadratic summation method are very close to experimental value for NC725, NC750 and NC775 nano-composites. In the present study, it is found that the Modified Clyne model is more accurate as compared to quadratic summation method.

For Modified Clyne model, it is estimated that yield strength of NC775 nano-composite is 107 MPa, which is close to experimental value of 105 MPa. The experimental values of yield strengths of NC700 and NC725 nano-composites are 1.2 and 1.1 times smaller than their respective theoretical values. This difference between the theoretical and experimental values can be attributed to non-uniform distribution of nano-particles and retention of some particle clusters. This is because of the inefficiency of UST discussed above which inhibits the cavitation and streaming phenomenon at low processing temperatures, and leads to higher porosity. Clustering of nano-particles decreases the effect of Orowan strengthening by increasing the average inter-particle distance and by offering fewer obstacles for dislocation motion.

Table 7.3. Comparison of calculated and experimental yield strengths for different nano-composites.

Specimens	σ_y, MPa				
	Arithmetic summation method	**Quadratic summation method**	**Compounding method**	**Modified Clyne model**	**Experimental value**
NC700	93.1	83.4	97.06	84.7	72±2.4
NC725	105.2	90.8	113.5	94.6	85±2.5
NC750	112.2	96.1	123.3	100.3	98±2
NC775	122.4	102.5	139	107	105±2.2
NC775MS	66	69.6	65.7	63	65±3

7.2.8. Fractographs of Al6061 alloy and its nano-composites

Figure 7.10 shows SEM fractograph of the fracture surface of tensile specimen of the as-cast Al6061 alloy. It shows that the failure occurs due to a mixed mode fracture. It can be observed from Figure 7.10 that the as-cast Al6061 alloy has mainly failed due to presence of dendritic structure. Dendritic structure looks like clusters of grape and micro-porosities exist in the interdendritic region [240]. Dendritic structure of the base alloy is also confirmed from micrograph of Figure 7.3a. The sample is fractured along the free surface of the dendritic structure and gap between the dendrites. Few tear ridges, micro-voids and tiny dimples are also observed in fracture surface of as-cast Al6061 alloy.

Figure 7.11 shows the SEM fractographs of the fracture surface of tensile specimens of NC700, NC725, NC750, and NC775 nano-composites. In all the nano-composites, there is clear evidence of increase of tear zones (Figure 7.11) as compared to as-cast Al6061 alloy (Figure 7.10) that suggest increase tensile strength of composites as compared to as-cast Al6061 alloy. Few micro-cracks are also observed in all composites, which is probably produced due to casting defects.

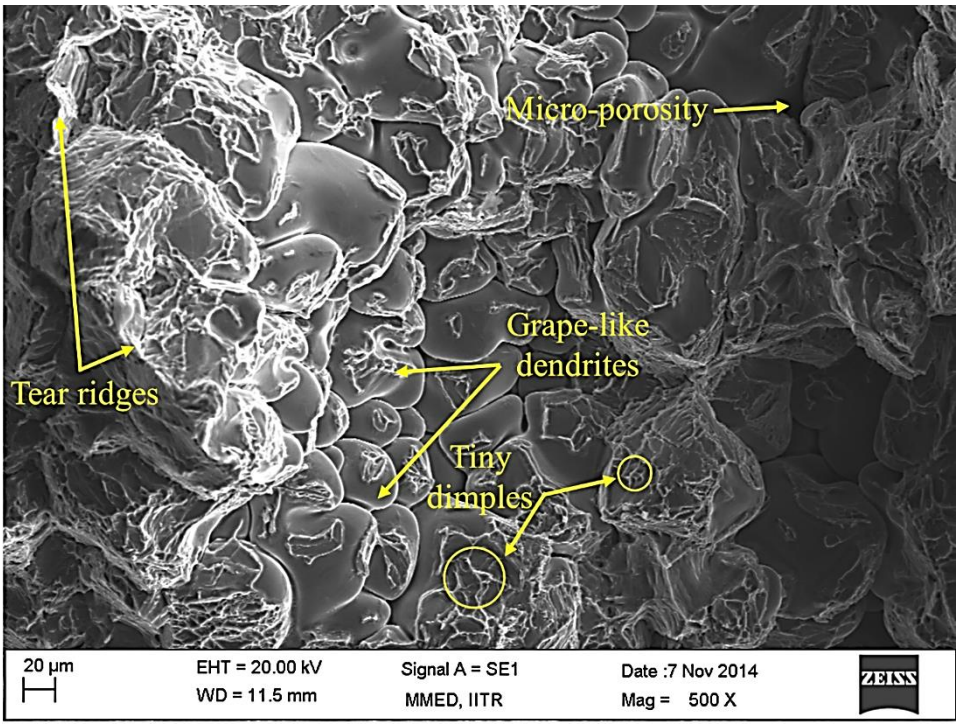

Figure 7.10. SEM fractograph of the fracture surface of tensile specimen of the as-cast Al6061 alloy.

NC700 shows finer dendritic structure (clusters of grapes) and shrinkage porosity in Figure 7.11a that confirmed inter-dendritic cracking as the main mechanism of fracture. Similar observations are made by other researchers about the fracture of cast composites [215,241]. However, Figure 7.11a shows that some regions of the fracture surfaces show tiny dimples and tear ridges. For NC725, NC750, and NC775 nano-composites, there is no evidence of dendritic structure in Figures 7.11b, 7.11c, and 7.11d. The fracture surface of these composites show mixed mode fracture due to presence of tiny dimples, tear ridges, and cleavage facets. In addition, no particle debonding and fracture features are observed in these composites. Figure 7.9 shows that there is not much difference in the ductility of NC750, NC775 nano-composites as result of better distribution of nano-particles (Figure 7.5). The retained ductility of these composites as compared to as-cast Al6061 alloy is confirmed from the existence of higher population of tiny dimples (Figure 7.11c and d). Extensive presence of tear ridges in NC750 and NC775 nano-composites points to a higher degree of ductile plastic deformation that led to improved mechanical behavior of NC750 and NC775 nano-composites as compared to other composites. It is reported that nano-particles could change the way of crack growth as a result of crack bridging, deflection and branching [242]. It is reasonable to infer that more energy would be

dissipated during tensile deformation, thus contributing to the enhancement of ductility of NC750 and NC775 nano-composites as compared to NC700 and NC725 nano-composites. Figure 7.9 shows that the ductility of NC700 and NC725 nano-composites is even lower than that of the as-cast Al6061 alloy. It is due to larger average size of alumina particles of these composite as compared to NC750 and NC775 nano-composites, which is reported in Table. 7.2. Habibnejad-Korayem et al. reported that larger size of particles (>100 nm) resulted to decrease ductility of such composites owing to enhanced the crack initiation and propagation [152], which is confirmed from Figures 7.11a and b, that show more micro-cracks in NC700 and NC725 composites as compared to as-cast Al6061 alloy (Figure 7.10).

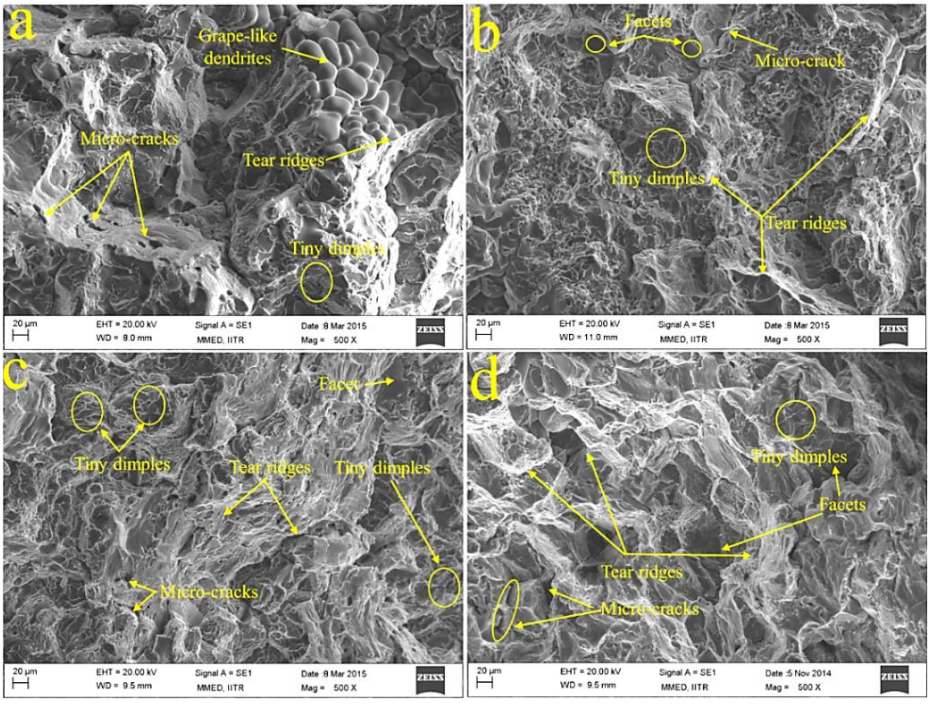

Figure 7.11. SEM fractographs of the tensile fractured surface of (a) NC700, (b) NC725, (c) NC750, and (d) NC775 nano-composites.

7.3. Effect of UST and nano-particles content on the microstructure and mechanical properties of composites

As discussed earlier, uniform distribution of nano-particles is observed at UST temperature of 775°C. In addition, higher UST temperature is used to confirm the satisfactory flowability, when the molten metal was poured into mild steel mould from the graphite crucible. Therefore, Al6061 alloy nano-composites are fabricated with varying the content of nano-particles (2 and 3 wt.%) and USTed at temperature of 775°C. This section deals with study on

the effect of amount of nano-particles, and the UST on the microstructure and mechanical properties of the aluminium alloy composites.

7.3.1. Effect of the amount of nano-particles on the melt viscosity

Table 7.4 shows the value of melt viscosity at different content of nano-particles at UST temperature of 775°C. Melt viscosity is calculated with the help of equations 7.1 and 7.2. Table 7.4 shows that the viscosity of molten aluminium alloy melts increases with increased amount of alumina nano-particles. With increasing content of nano-particles, the contact surface area of nano-particles with air will be increased and more amount of the gas will enter into the molten metal during processing [52]. Therefore, porosity is higher at 3 wt.% of nano-particles as compared to 1 wt.% and 2 wt.% of nano-particles in Al6061 alloy composite, as shown in Figure 7.12. Similar observations are reported by some researchers that the porosity of composites is enhanced with increasing the content of particles [243][244]. In addition, this is because of the influence of low wettability and large agglomeration at higher content of nano-particles and easier pore nucleation at the interface of Al6061 matrix and Al_2O_3 particles [30,31]. Furthermore, ultrasonic cavitation phenomenon will be poor at the higher content of nano-particles (3 wt.%) due to higher melt viscosity, which will be affect the mechanical properties and distribution of nano-particles in Al6061 alloy nano-composites. Wang also reported that high viscosity of the melt decreases the influence of UST [121].

Table 7.4. Effect of content of nano-particles on the melt viscosity.

Al_2O_3 nano-particles (wt.%)	**Viscosity (mPas) of the melt at ultrasonic processing temperature of 775°C**
1	1.007
2	1.025
3	1.040

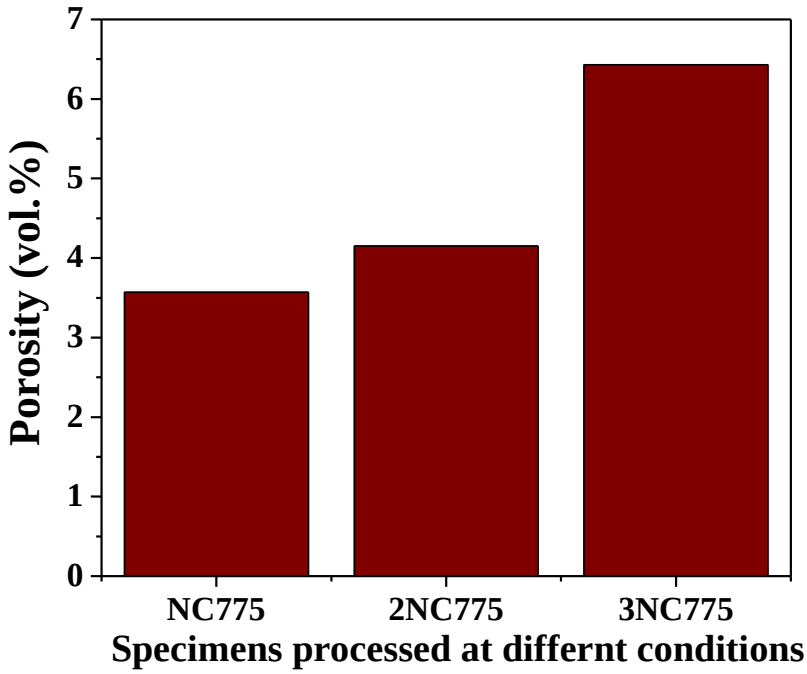

Figure 7.12. Porosity content (vol.%) in NC775, 2NC775, and 3NC775 nano-composites.

7.3.2 Microstructural evolution

Figure 7.13 shows the EBSD images of as-cast Al6061 alloy and its nano-composites, containing different amount of nano-particles and USTed at 775°C. Figure 7.13 shows that the reinforcing of Al_2O_3 nano-particles in Al6061 alloy matrix decreases the average grain size of primary aluminium phase. Figure 7.14 shows the variation in grain size of Al6061 alloy, NC775, 2NC775, and 3NC775 nano-composites, with grain sizes being determined from EBSD data of Figure 7.13. Figure 7.15 shows the SEM microstructures of NC775, 2NC775, and 3NC775 nano-composites, which is used to highlight the dispersion of alumina particles in the composites.

For nano-composite specimens, the average grain size of the primary aluminium phase is mainly dependent upon the content of nano-particles. Upon adding of 1 wt.% of nano-particles, the average grain size decreases significantly when ultrasonic processing is done at temperature of 775°C, as compared to the as-cast Al6061 alloy. Upon adding of 2 wt.% of nano-particles, a few clusters of particles and fine single particles are observed in Figure 7.15a, where the apparent particle size varied from of 80-110 nm with average particle size of 95 nm in 2NC775 nano-composite. As a result, there is not much improvement in the average grain size of 2NC775 nano-composite as compared to NC775 nano-composite. However, the grain size of 2NC775 composite is significantly reduced by 74% as compared to the as-cast Al6061 alloy (Figure 7.14).

Addition of 3 wt.% of nano-particles resulted in large agglomeration and poor distribution of Al_2O_3 particles with an average particle size of 228 nm for 3NC775 nano-composite, as shown in Figure 7.15c. It is due to low wettability, more gas entrapment in molten metal and higher amount of nano-particles. It is extremely difficult to obtain better distribution of alumina nano-particles in molten Al6061 alloy when the amount of alumina nano-particles is more than 2 wt.% in present research, because of poor wettability and large surface-to-volume ratio. In addition, the efficiency of UST is inhibited at higher viscosity of 3NC775 melt. These problems induce agglomeration, micro-porosities and clustering in the 3NC775 nano-composite. Due to this effect, the average grain size of 3NC775 nano-composite (170 μm) is larger as compared to NC775 and 2NC775 nano-composites. Yet, the grain size of 3NC775 nano-composite is decreased by 41% as compared to as-cast Al6061 alloy (Figure 7.14).

As discussed earlier, refinement of α-Al phase occurs due to better dispersion of nano-particles by UST that confers heterogeneous nucleation sites by Al_2O_3 particles and thereby increase the rate of nucleation, dominantly in the NC775 and 2NC775 nano-composites. Some micro-cracks are also observed in 2NC775 and 3NC775 nano-composites (Figure 7.15). The sizes of micro-cracks are larger in 3NC775 nano-composite as compared to 2NC775 nano-composite. This is likely to influence the mechanical properties of 3NC775 nano-composite mode adversely, which is discussed in following section.

7.3.3. Mechanical Properties

Hardness and tensile properties of the fabricated aluminium alloy nano-composites synthesized at UST temperature of 775°C are investigated as a function of content of nano-particles. The average hardness of these nano-composites and as-cast Al6061 alloy is shown in Figure 7.16 at different content of nano-particles. NC775, 2NC775 and 3NC775 nano-composites show higher hardness as compared to as-cast Al6061 alloy. An increment in average hardness of about 61%, 76%, and 23% is observed for NC775, 2NC775 and 3NC775 nano-composites as compared the as-cast Al6061 alloy, respectively. Hardness increased significantly due to combined effect of decrease of grain size and particle strengthening effects. In addition, the hardness of composites increases due to the obstruction in the movement of dislocations by thermal strain [118,245], which developed due to difference in CTE between the alumina particles and Al60061 alloy matrix. The hardness of 3NC775 composites is lower as compared

to NC775 and 2NC775 nano-composites due to presence of agglomeration of particles and micro-porosities, which inhibit the particle strengthening effects.

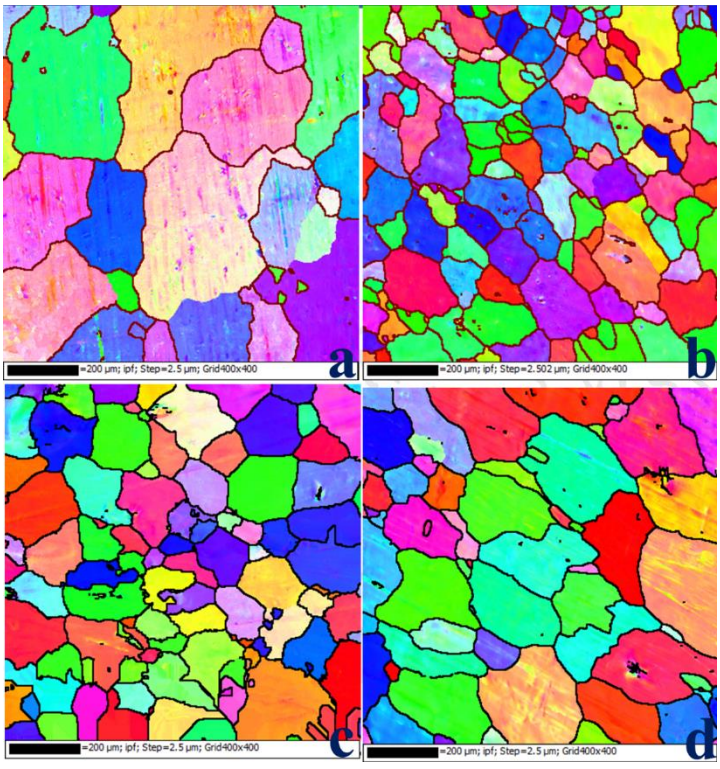

Figure 7.13. EBSD micrographs of (a) as-cast Al6061 alloy and its composites (b) NC775, (c) 2NC775, and (d) 3NC775.

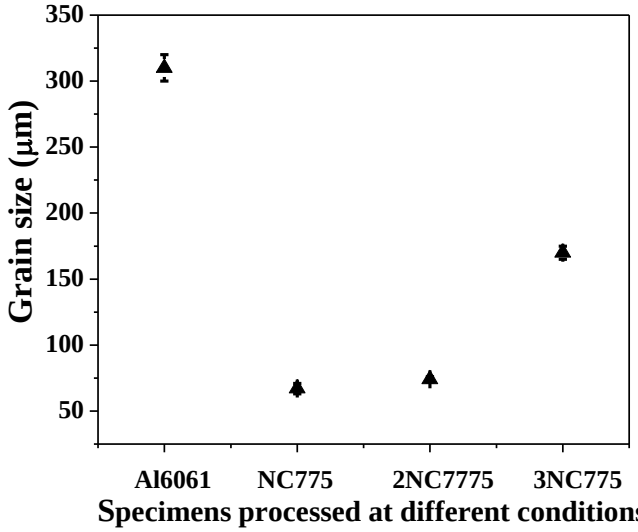

Figure 7.14. Comparison of grain size of as-cast Al6061 alloy, NC775, 2NC775, and 3NC775 nano-composites.

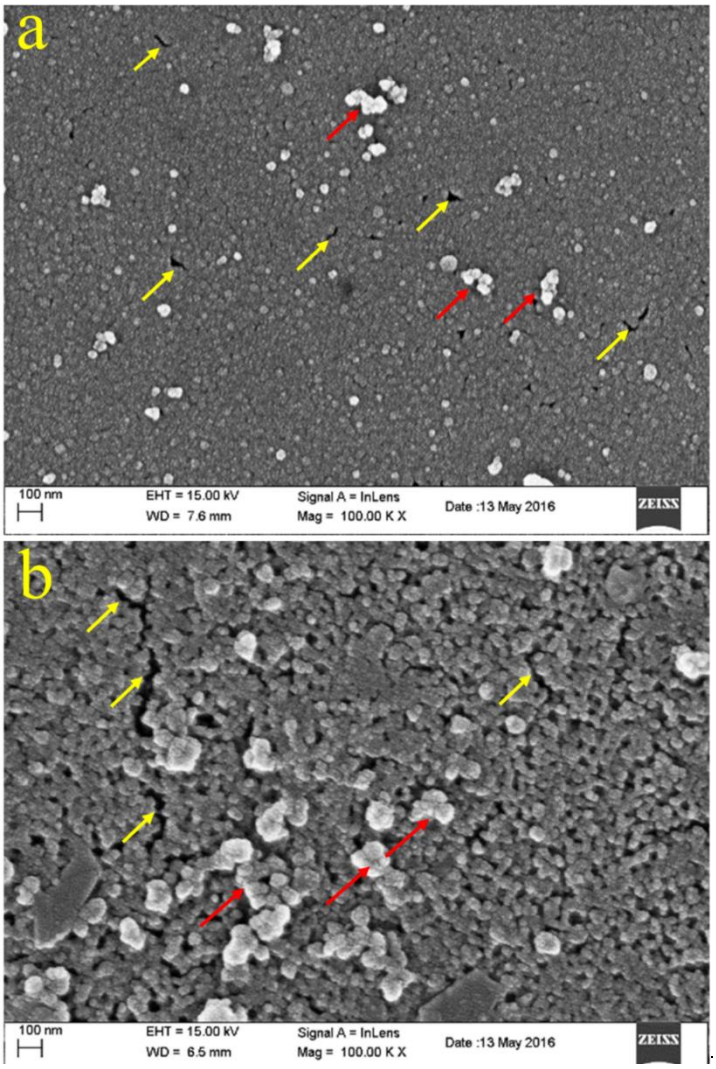

Figure 7.15. SEM micrographs of (a) 2NC775 and (b) 3NC775 nano-composites showing dispersion of alumina particles (Red arrows show clusters of alumina particles and yellow arrows indicate micro-cracks).

The engineering stress-strain curves of base alloy and its nano-composites are shown in Figure 7.17. Figure 7.18 shows the variation in the tensile properties. It can be observed that the yield strength ($\sigma_{0.2}$) and ultimate tensile strength (UTS) of all the nano-composites is higher than that of the base alloy. The yield strengths of NC775, 2NC775 and 3NC775 nano-composites are 67%, 81%, and 11% higher as compared to the as-cast Al6061 alloy. It is due to combined influences of enhancement in grain boundary area due to refinement of primary phase, Orowan strengthening and the massive thermal stress is generated due to thermal mismatch between the

Al6061 alloy matrix and alumina particles. Improvement in tensile strength is observed up to 2 wt.% of nano-particles as the result increasing the dislocation density due to CTE mismatch between Al6061 alloy matrix and alumina particles and Orowan strengthening. After that, tensile strength decreased for 3NC775 nano-composite as compared to NC775 and 2NC775 nano-composites due to more clustering of nano-particles. Clusters of particles are reported adversely affect the mechanical properties of composites. Tszeng et al. [32] also observed that the micro-cracks were prone to initiate at the interface between the metal matrix and particle clusters that eventually cause severe degradation in the strength of composites.

It is observed from Figure 7.18 that the percent elongation decreased gradually with increasing the content of nano-particles. This may be the result of less efficiency of UST, which lead to more clusters of nano-particles and higher content of porosity (see in Figure 7.12) observed in the nano-composite with higher alumina nano-particles content.

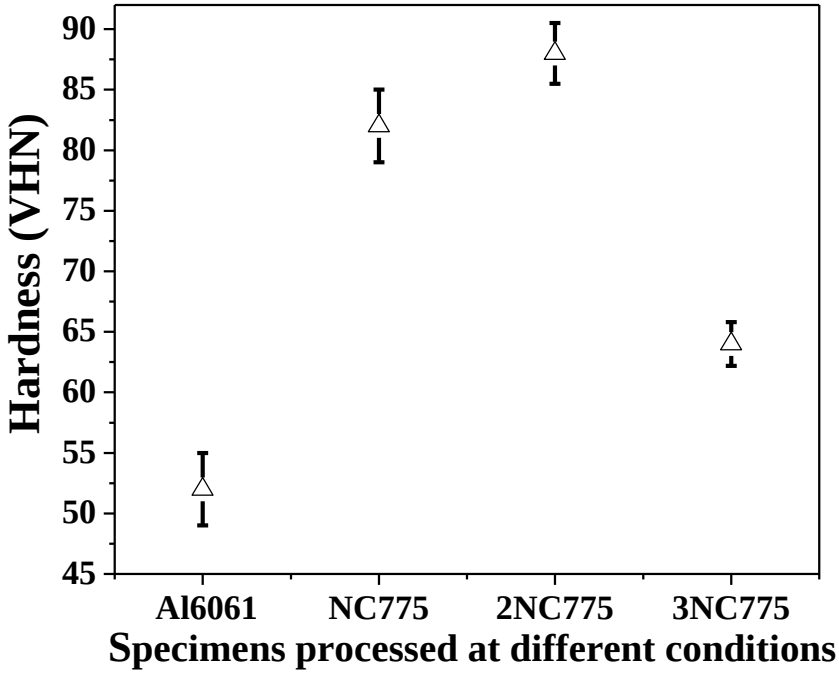

Figure 7.16. Comparison of hardness of as-cast Al6061 alloy, NC775, 2NC775, and 3NC775 composites.

At the highest 3 wt.% content of nano-particles, the percentage of micro-porosities and particles agglomeration in 3NC775 composites is more as compared to NC775 and 2NC775 nano-composites. Thus, its percent elongation value is inferior to that of the NC775 and 2NC775

and as-cast Al6061 alloy specimens. For 3NC775 nano-composites, viscosity of melt was higher which decreased the efficacy of UST. Less efficient UST resulted in higher porosity, and the reinforcement particles remained in clustered form in the Al6061 alloy matrix (Figure 7.15b). Therefore, ductility of 3NC775 nano-composite is reduced.

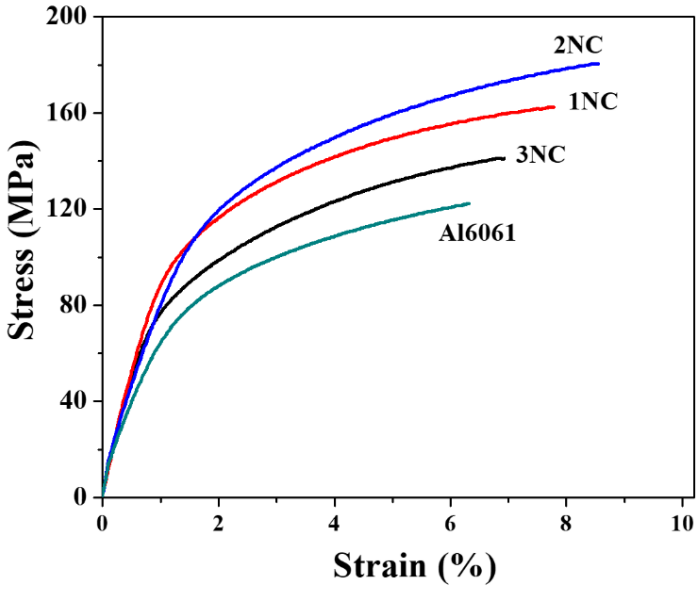

Figure 7.17. Engineering stress-strain curve of as-cast Al6061 alloy, NC775, 2NC775, and 3NC775 composites.

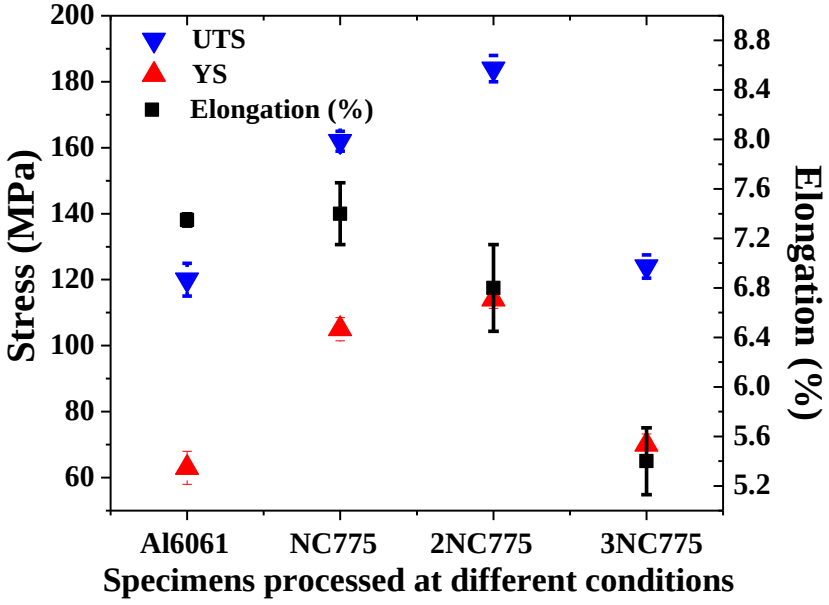

Figure 7.18. Variation in tensile properties of as-cast Al6061 alloy, NC775, 2NC775, and 3NC775 composites.

7.3.4. Strengthening mechanisms

As discussed earlier, Hall-Petch strengthening, Orowan strengthening, and coefficient of thermal expansion (CTE) strengthening mechanisms contribute to the enhancement yield strength of composites. For higher content of reinforcement (3 wt.%), load bearing strengthening mechanism may be play an important role. Thus, load-bearing strengthening mechanism is also considered in the present analysis.

Table 7.5 shows that the $\Delta\sigma_{CTE}$ of NC775, 2NC775 and 3NC775 specimens are approximately 6.6 & 1.4 times, 9.2 & 1.1 times, and 18.3 & 1.6 times that of the $\Delta\sigma_{Hall\text{-}Petch}$ and $\Delta\sigma_{Orowan}$, respectively. It is clear that CTE mismatch strengthening mechanism is the main dominating mechanism for the enhancement of the yield strength of nano-composites. Contribution to strengthening from CTE mismatch and Orowan are increased up to 2 wt.% of reinforcement, after that its decreased at 3 wt.% of alumina reinforcement. $\Delta\sigma_{Orowan}$ of NC775 and 2NC775 nano-composites are about 1.3 times and two times that of 3NC775 composites. It is due to agglomeration and non-uniform distribution of particles, which increases the inter-particle distance in the 3 wt.% of alumina in Al6061 alloy matrix. $\Delta\sigma_{load}$ does not contribute to increment the yield strength of NC775 and 2NC775 nano-composites much due to its lower value. Even in 3NC775 nano-composite, $\Delta\sigma_{load}$ contribution for the enhancement of yield strength is very less.

Table 7.5. The yield strength contributions from various strengthening mechanisms for the NC775, 2NC775, and 3NC775 nano-composites.

Specimens	**Avg. grain size (μm)**	**Avg. size of nano-particles (nm)**	**Inter-particle distance (nm)**	$\Delta\sigma_{Orowan}$ **(MPa)**	$\Delta\sigma_{CTE}$ **(MPa)**	$\Delta\sigma_{Hall-Petch}$ **(MPa)**	$\Delta\sigma_{load}$ **(MPa)**
NC775	67	56	200	22.6	32	4.84	0.4347
2NC775	78	82	135	34	37.6	4.07	0.8694
3NC775	170	228	341	17	27	1.47	1.3041

The experimental results for nano Al_2O_3/Al6061 composites with different weight percentage of reinforcement are compared with the calculated values, as shown in Table 7.6. It

can be observed from Table 7.6 that the theoretical values of yield strength for Al60661 alloy nano-composites obtained using the quadratic summation method and Modify Clyne method, are approximately equal to the experimental values up to 2 wt.% of alumina reinforcement. At 3 wt.% of alumina nano-particles, the experimental value of yield strength of 3NC775 nano-composite is approximately 35% lower than the theoretical values. This is attributed to the presence of large amount of porosity and clusters of alumina particles in the 3NC nano-composite.

Table 7.6. Comparison of calculated and experimental yield strengths for the NC775, 2NC775, and 3NC775 nano-composites.

	σ_y, MPa				
Specimens	**Arithmetic summation method**	**Quadratic summation method**	**Compounding method**	**Modified Clyne model**	**Experimental value**
NC775	122	102	139	107	105
2NC775	140	114	169	118	113
3NC775	109	94	119	96	71

7.3.5. Fractography

Figure 7.19 shows the SEM micrographs of 2NC775 and 3NC775 nano-composites. Mixed mode fracture is clearly appeared in all the composites. In 2NC775 nano-composite (Figure 7.19a), population of tiny dimples is more as compared to the as-cast Al6061 alloy (Figure 7.10). Deeper, smaller dimples, and tear ridges point to relatively ductile fracture of 2NC775 nano-composite that accompanied with significant plastic deformation. However, some shear fracture regions, containing facets/step-wise facets are also observed which shows less significant, brittle character of the fracture in 2NC775 nano-composite.

In 3NC775 nano-composite, population of cleavage facets is more as compared to NC775 nano-composite and 2NC775 nano-composite, which can be seen from Figure 7.19b. However, few tiny dimples are also seen in Figure 7.19b. Cleavage facets and smaller population of dimple suggests predominantly brittle behavior of 3NC775 nano-composite. Many pores are observed on the fracture surface of 3NC775 nano-composite, which are mainly attributed to improper distribution of alumina particles, clusters of particles, poor bonding between matrix and

reinforcement. As a result, ductility and strength of 3NC775 nano-composite is reduced as compared to NC775 nano-composite and 2NC775 nano-composite. In addition, clusters of particles segregate along the grain boundary because of inhomogeneous distribution and particle pushing nature. Due to this effect, clusters of particles generate cracking under lower stress which creates the low energy path along the grain boundaries for crack propagation [246]. Micro-cracks also worked as stress raisers that led to propagation of cracks at lower stress, which decreased the ductility of composite. Micro-cracks are also observed in 3NC775 nano-composites.

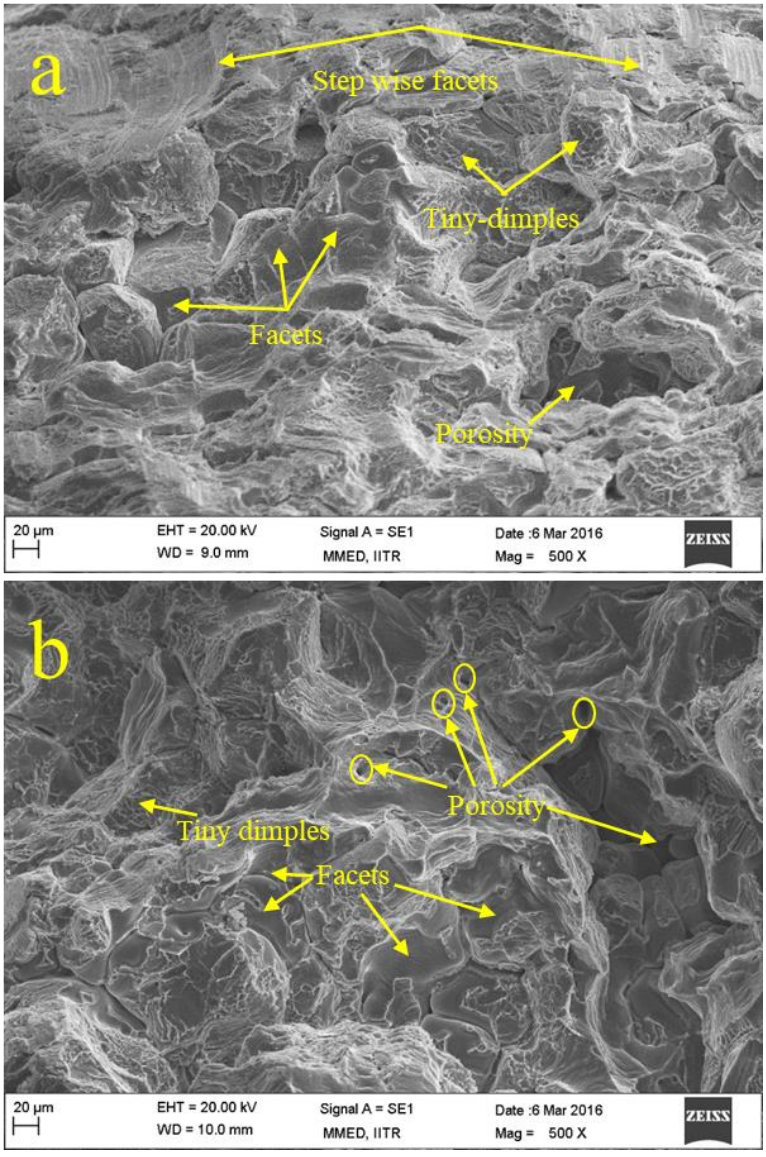

Figure 7.19. SEM fractographs of the fractured surface of (a) 2NC775 and (b) 3NC775, nano-composites.

7.4. Summary of results

1. An excellent distribution of Al_2O_3 nano-particles is obtained in NC775 composite specimens after ultrasonic treatment. Some agglomerates of particles are observed in NC700 specimen because of less effectiveness of UST due to higher melt viscosity.
2. Increasing the ultrasonic processing temperature resulted in more uniform distribution of Al_2O_3 nano-particles that caused enhanced heterogeneous nucleation and significantly decreased the grain size of composites as compared to base aluminium alloy.
3. NC750 nano-composite exhibited the best combination of mechanical properties with yield strength, ultimate tensile strength, and ductility, which are 55%, 30% and 3% higher than that of the base alloy.
5. Melt viscosity increased with increasing the content of nano-particles, which affected the distribution of nano-particles. Poor distribution of nano-particles and clusters of particles are observed in 3NC775 nano-composite.
6. Al6061 based nano-composites with Al_2O_3 nano-particles addition were successfully made using ultrasonic processing up to 2 wt.% of nano-particles. These nano-composites showed marked improvement in strength and ductility when compared to unreinforced alloys.
7. There is not much improvement in grain size of 2NC775 nano-composite as compared to NC775 nano-composite.
8. 2NC775 nano-composite shows good mechanical properties with yield strength and ultimate tensile strength, which are 81% and 53% higher than the base alloy. 3NC775 nano-composite shows poor yield strength and ultimate tensile strength as compared to NC775 nano-composite and 2NC775 nano-composite due to agglomeration of particles.
9. In all the nano-composites, thermal mismatch strengthening mechanism is most dominant one followed by Orowan strengthening, and grain-size strengthening mechanisms.

CHAPTER 8
CONCLUSIONS

This chapter deals with the major findings of this work. The role of solute and ultrasonic intensity on the microstructural and mechanical properties of binary hypoeutectic and off-eutectic aluminium alloys are investigated. Further investigations involved the effect of ultrasonic processing temperature and content of nano-particles on the dispersion, other microstructural features, and mechanical properties of nanocomposites. The following conclusions are drawn based on the present work.

1. Content of solute and UST had significant effect on the grain refinement of binary Al-Si, Al-Cu and Al-Ni alloys. Increased grain refinement occurred with increase in ultrasound intensity and content of the solute. Maximum grain refinement was observed at higher content of solute (5 wt.%) and highest ultrasound intensity (1400 W/cm^2) for Al-Si and Al-Cu alloys. For Al-Ni alloy, highest grain refinement was obtained at 3 wt.% of solute and maximum ultrasound intensity of 1400 W/cm^2. At ultrasound intensity of 1400 W/cm^2, the values of minimum grain size were about 124 µm, 107 µm, and 120 µm for Al-5wt.%Si alloy, Al-5wt.%Cu alloy, and Al-3wt.%Ni alloy, respectively.
2. Combination of higher content of solute (3 and 5 wt.%) and maximum ultrasound intensity produced non-dendritic, nearly-equiaxed, and globular grains.
3. By increasing the amount of solute from 1% to 5%, grain size was reduced by ~52%, 58%, and 23% for as-cast Al-Si alloys, as-cast Al-Cu alloys, and as-cast Al-Ni alloys, respectively. At fixed amount of solute (5wt.%), the reduction in average grain size was about ~48%, 85%, and ~40%, with increasing ultrasonic intensity from 88 W/cm^2 to 1400 W/cm^2 for Al-Si alloy, Al-Cu alloy, and Al-Ni alloy, respectively.
4. Grain density of Al-Si alloys and Al-Cu alloys increased with increasing the content of solute at fixed ultrasonic intensity. Increase in grain density was about 6 times, 58 times, 9 times by increasing the ultrasonic intensity 16 times from 88 to 1400 W/cm for Al-5wt.%Si alloy, Al-5wt.%Cu alloy, and Al-5wt.%Ni alloy, respectively.
5. Growth restriction factor (Q) increased with increasing the amount of solute. Q for Al-1wt.%Si alloy was two and 1.7 times higher than Al-1wt.%Cu alloy and Al-1wt.%Ni alloy,

respectively. *Q* could not fully explain the mechanism of ultrasonic grain refinement for hypoeutectic alloys studied in present study.

6. According to StJohn's model, the value of largest intercept ($a \approx 1094$ μm) was found for as-cast Al-Ni alloys. Both the potency of solutes and the number of active nucleants increased with increase in the ultrasonic intensity from 88 to 1400 W/cm^2. The intercept (*a)* and the slope (*b*) decreased from 229 μm to 115 μm & 737 μm°C to 570 μm°C, 386 μm to 78 μm & 1582 μm°C to 697 μm°C, and 277 μm to 109 μm & 585 μm°C to 442 μm°C with increasing ultrasonic intensity from 88 to 1400 W/cm^2 for Al-Si alloys, Al-Cu alloys, and Al-Ni alloys, respectively. Potency in Al-Ni alloys were higher than that in Al-Si and Al-Cu alloys at the highest ultrasonic intensity used in this work.
7. Freezing range (ΔT) mechanism satisfactorily explains the grain refinement mechanism of off-eutectic Al-Cu alloys upon UST. The ΔT value increased in off-eutectic alloy and decreased in hypoeutectic alloys with solute content. Supercooling parameter (*P*) explained the ultrasonic grain refinement mechanism of near eutectic Al-Ni alloys. Clearly, such inconsistency in average grain size with UST and amount of solute could not be completely explained by considering *Q*, ΔT, and *P* values alone.
8. UST refined the eutectic phase. As a result, the average length of the Si plate decreased to 37 μm from 68 μm for the as-cast Al-5wt.%Si alloy. Similarly, the average width of eutectic phase reduced to 6 μm from 14 μm for USTed Al-5wt.%Cu alloy.
9. The yield strength, UTS, and total elongation of each USTed alloys were higher than respective as-cast alloy due to combined influence of refinement of primary aluminium phase and eutectic phase, and reduction in porosity content upon UST. At ultrasonic intensity of 1400 W/cm^2, the highest values of hardness found in Al-5wt.%Si alloy, Al-5wt.%Cu alloy, and Al-3wt.%Ni alloy, were 52, 58 and 36.2 VHN, respectively. The UTS of USTed Al-5wt.%Si, Al-5wt.%Cu alloy and Al-5wt.%Ni alloy was ~79%, ~69%, and ~18% higher than respective as-cast alloys.
10. Upon adding 1 wt.% of nano-particles in Al6061 alloy, the average grain size decreased with increasing the ultrasonic processing temperature. This is because of better distribution of nano-particles with increasing ultrasonic processing temperature, which increased the rate of nucleation from increased heterogeneous nucleation sites provided by alumina particles.

As a result, the average grain size of NC725, NC750, and NC775 nano-composites reduced by 74%, 77%, and 79%, respectively, with respect to the as-cast Al6061 alloy.

11. UST uniformly dispersed the alumina nano-particles in the Al6061 alloy matrix for NC775 composite due to low melt viscosity, which increased the efficiency of UST. The average size of alumina nano-particles/clusters was about 156 nm, 107 nm, 80 nm, and 56 nm for NC700, NC725, NC750, and NC775 nano-composites, respectively.
12. Increment in hardness of about 20%, 31%, 42%, 53% and 61% respectively was obtained for NC775MS, NC700, NC725, NC750, and NC775 nano-composites with respect to as-cast Al6061 alloy due to refinement of primary aluminium phase and particle strengthening effect. Mechanical properties of composites improved with increasing UST processing temperature that better dispersed the Al_2O_3 particles. As a result, the CTE mismatch and Orowan strengthening contributions increased. Yield strength of NC775 nano-composites increased by about 67% as compared to that of the as-cast Al6061 alloy.
13. Al6061 alloy nano-composites were successfully fabricated using 1 and 2 wt.% of alumina nano-particles at ultrasonic processing temperature of 775°C. At higher alumina additions, i.e. in 3NC775 composite, higher melt viscosity reduced the efficiency of UST. 3NC775 composite showed poor mechanical properties as compared to NC775 and 2NC775 composites due to agglomeration and poor dispersion of Al_2O_3 particles in Al6061 matrix. Yield strength of NC775, 2NC775 and 3NC775 nano-composites is about 67%, 81%, and 11% higher than that of base alloy. 2NC775 nano-composite showed best mechanical properties among all the composites.
14. In all the nano-composites, thermal mismatch strengthening mechanism was the dominant one followed by Orowan strengthening, and grain-size strengthening mechanisms. $\Delta\sigma_{CTE}$ of NC775, 2NC775 and 3NC775 nano-composites were about 6.6 & 1.4 times, 9.2 & 1.1 times, and 18.3 & 1.6 times higher as compared to $\Delta\sigma_{Hall\text{-}Petch}$ and $\Delta\sigma_{Orowan}$, respectively. Quadratic summation method and modified Clyne method for calculating the yield strength of 1NC775, 2NC775, and 3NC775 nano-composites showed best agreement with the experimental value of yield strength of these composites.

Chapter 9

SCOPE OF FUTURE WORK

Further studies could include investigation of the following:

- Numerical simulation of acoustic pressure field for ultrasonic grain refinement of Al-Si alloys, Al-Cu alloys, and Al-Ni alloys can be done and studied.
- Al-Ni alloys are promising new generation of eutectic alloys, which can be used for high-temperature applications. Therefore, mechanical properties of eutectic Al-Ni alloy can be studied at high temperature, and improved upon by adding suitable solutes and reinforcements for high temperature applications.
- The Al6061 alloy nano-composite has been successfully fabricated with UST. These nano-composites showed increase in yield strength and ultimate tensile strength as compared to base alloy. As these materials can be investigated further for fatigue and creep behavior, for automobile and aerospace applications.
- Detailed TEM analysis of aluminium alloy nano-composites can be done.
- Effect of heat treatment on the microstructural and mechanical properties of these materials can be studied.

REFERENCES

[1] F. Ubaid, P. Matli, R. Shakoor, G. Parande, V. Manakari, A. Mohamed, M. Gupta, Using B4C nanoparticles to enhance thermal and mechanical response of aluminum, Materials (Basel). 10 (2017) 621. doi:10.3390/ma10060621.

[2] S.L. Pramod, S.R. Bakshi, B.S. Murty, Aluminum-based cast in situ composites: A review, J. Mater. Eng. Perform. 24 (2015) 2185–2207. doi:10.1007/s11665-015-1424-2.

[3] P. Matli, R. Shakoor, A. Amer Mohamed, M. Gupta, Microwave rapid sintering of Al-metal matrix composites: A review on the effect of reinforcements, microstructure and mechanical properties, Metals (Basel). 6 (2016) 143. doi:10.3390/met6070143.

[4] M. Zamani, H. Dini, A. Svoboda, L.-E. Lindgren, S. Seifeddine, N.-E. Andersson, A.E.W. Jarfors, A dislocation density based constitutive model for as-cast Al-Si alloys: Effect of temperature and microstructure, Int. J. Mech. Sci. 121 (2017) 164–170. doi:10.1016/j.ijmecsci.2017.01.003.

[5] C. Blawert, N. Hort, K.U. Kainer, Automotive applications of magnesium and its alloys, Trans. Indian Inst. Met. 57 (2004) 397–408. doi:10.4028/www.scientific.net/MSF.419-422.67.

[6] F.C. Robles Hernandez, J.H. Sokolowski, Effects and on-line prediction of electromagnetic stirring on microstructure refinement of the 319 Al-Si hypoeutectic alloy, J. Alloys Compd. 480 (2009) 416–421. doi:10.1016/j.jallcom.2009.02.109.

[7] J. Mathew, A. Mandal, S.D. Kumar, S. Bajpai, M. Chakraborty, G.D. West, P. Srirangam, Effect of semi-solid forging on microstructure and mechanical properties of in-situ cast Al-Cu-TiB2 composites, J. Alloys Compd. 712 (2017) 460–467. doi:10.1016/j.jallcom.2017.04.113.

[8] P.P. Bhingole, G.P. Chaudhari, Synergy of nano carbon black inoculation and high intensity ultrasonic processing in cast magnesium alloys, Mater. Sci. Eng. A. 556 (2012) 954–961. doi:10.1016/j.msea.2012.07.104.

[9] Z. Chen, T. Wang, L. Gao, H. Fu, T. Li, Grain refinement and tensile properties improvement of aluminum foundry alloys by inoculation with Al-B master alloy, Mater. Sci. Eng. A. 553 (2012) 32–36. doi:10.1016/j.msea.2012.05.088.

[10] N. Kumar, R.S. Mishra, C.S. Huskamp, K.K. Sankaran, Microstructure and mechanical behavior of friction stir processed ultrafine grained Al-Mg-Sc alloy, Mater. Sci. Eng. A. 528 (2011) 5883–5887. doi:10.1016/j.msea.2011.03.109.

[11] G.S. Reddy, J.A. Sekhar, Microstructure refinement with forced convection in aluminium and superalloys, J. Mater. Sci. 20 (1985) 3535–3544. doi:10.1007/BF01113760.

[12] B.S. Murty, S. a. Kori, M. Chakraborty, Grain refinement of aluminium and its alloys by heterogeneous nucleation and alloying, Int. Mater. Rev. 47 (2002) 3–29. doi:10.1179/095066001225001049.

[13] A.L. Greer, A.M. Bunn, A. Tronche, P. V. Evans, D.J. Bristow, Modelling of inoculation of metallic melts: application to grain refinement of aluminium by Al-Ti-B, Acta Mater. 48 (2000) 2823–2835. doi:10.1016/S1359-6454(00)00094-X.

[14] F. Wang, D. Eskin, T. Connolley, J. Mi, Effect of ultrasonic melt treatment on the refinement of primary Al3Ti intermetallic in an Al-0.4Ti alloy, J. Cryst. Growth. 435 (2016) 24–30. doi:10.1016/j.jcrysgro.2015.11.034.

[15] T.E. Quested, A.L. Greer, The effect of the size distribution of inoculant particles on as-cast grain size in aluminium alloys, Acta Mater. 52 (2004) 3859–3868. doi:10.1016/j.actamat.2004.04.035.

[16] T. V. Atamanenko, D.G. Eskin, L. Zhang, L. Katgerman, Criteria of grain refinement induced by ultrasonic melt treatment of aluminum alloys containing ZR and Ti, Metall. Mater. Trans. A Phys. Metall. Mater. Sci. 41 (2010) 2056–2066. doi:10.1007/s11661-010-0232-4.

[17] M. Easton, D. StJohn, Grain refinement of aluminum alloys: Part II. Confirmation of, and a mechanism for, the solute paradigm, Metall. Mater. Trans. A. 30 (1999) 1625–1633. doi:10.1007/s11661-999-0099-4.

[18] F. Wang, D. Qiu, Z.L. Liu, J.A. Taylor, M.A. Easton, M.X. Zhang, The grain refinement mechanism of cast aluminium by zirconium, Acta Mater. 61 (2013) 5636–5645. doi:10.1016/j.actamat.2013.05.044.

[19] F. Wang, Z.L. Liu, D. Qiu, J.A. Taylor, M.A. Easton, M.X. Zhang, The influence of the effect of solute on the thermodynamic driving force on grain refinement of Al alloys, Metall. Mater. Trans. A. 46 (2015) 505–515. doi:10.1007/s11661-014-2599-0.

[20] Z. Liu, F. Wang, D. Qiu, J.A. Taylor, M. Zhang, The effect of solute elements on the grain refinement of cast Zn, Metall. Mater. Trans. A Phys. Metall. Mater. Sci. 44 (2013) 4025–4030. doi:10.1007/s11661-013-1861-1.

[21] D. Shu, B. Sun, J. Mi, P.S. Grant, A quantitative study of solute diffusion field effects on heterogeneous nucleation and the grain size of alloys, Acta Mater. 59 (2011) 2135–2144. doi:10.1016/j.actamat.2010.12.014.

[22] B. Nagasivamuni, K.R. Ravi, An analytical approach to elucidate the mechanism of grain refinement in calcium added Mg-Al alloys, J. Alloys Compd. 622 (2015) 789–795. doi:10.1016/j.jallcom.2014.10.185.

[23] M. Payandeh, A.E.W. Jarfors, M. Wessén, Solidification sequence and evolution of microstructure during rheocasting of four Al-Si-Mg-Fe alloys with low Si content, Metall. Mater. Trans. A Phys. Metall. Mater. Sci. 47 (2016) 1215–1228. doi:10.1007/s11661-015-3290-9.

[24] X.T. Li, T.J. Li, X.M. Li, J.Z. Jin, Study of ultrasonic melt treatment on the quality of horizontal continuously cast Al-1%Si alloy, Ultrason. Sonochem. 13 (2006) 121–125. doi:10.1016/j.ultsonch.2005.08.005.

[25] B. Patel, G.P. Chaudhari, P.P. Bhingole, Microstructural evolution in ultrasonicated AS41 magnesium alloy, Mater. Lett. 66 (2012) 335–338. doi:10.1016/j.matlet.2011.08.113.

[26] H.R. Kotadia, A. Das, Modification of solidification microstructure in hypo- and hyper-eutectic Al-Si alloys under high-intensity ultrasonic irradiation, J. Alloys Compd. 620 (2015) 1–4. doi:10.1016/j.jallcom.2014.09.089.

[27] G.I. Eskin, Ultrasonic treatment of light alloy melts, Gordon and Breach Science, Amsterdam, 1998.

[28] E.Q. Wang, G. Wang, M.S. Dargusch, M. Qian, D.G. Eskin, D.H. StJohn, Grain refinement of an Al-2 wt%Cu alloy by Al3Ti1B master alloy and ultrasonic treatment, IOP Conf. Ser. Mater. Sci. Eng. 117 (2016) 12050. doi:10.1088/1757-899X/117/1/012050.

[29] G.I. Eskin, Improvement of the structure and properties of ingots and worked aluminum alloy semifinished products by melt ultrasonic treatment in a cavitation regime, Metallurgist. 54 (2010) 505–513. doi:10.1007/s11015-010-9331-0.

[30] J.R.G. Sander, B.W. Zeiger, K.S. Suslick, Sonocrystallization and sonofragmentation, Ultrason. Sonochem. 21 (2014) 1908–1915. doi:10.1016/j.ultsonch.2014.02.005.

[31] K.S. Suslick, Y. Didenko, M.M. Fang, T. Hyeon, K.J. Kolbeck, W.B. McNamara III, M.M. Mdleleni, M. Wong, Acoustic cavitation and its consequences, Philos. Trans. R. Soc. A. 357 (1999) 335–353. doi:10.1098/rsta.1999.0330.

[32] H. Puga, S. Costa, J. Barbosa, S. Ribeiro, M. Prokic, Influence of ultrasonic melt treatment on microstructure and mechanical properties of AlSi9Cu3 alloy, J. Mater. Process. Technol. 211 (2011) 1729–1735. doi:10.1016/j.jmatprotec.2011.05.012.

[33] H.K. Feng, S.R. Yu, Y.L. Li, L.Y. Gong, Effect of ultrasonic treatment on microstructures of hypereutectic Al-Si alloy, J. Mater. Process. Technol. 208 (2008) 330–335. doi:10.1016/j.jmatprotec.2007.12.121.

[34] X. Jian, H. Xu, T.T. Meek, Q. Han, Effect of power ultrasound on solidification of aluminum A356 alloy, Mater. Lett. 59 (2005) 190–193. doi:10.1016/j.matlet.2004.09.027.

[35] N.Q. Tuan, H. Puga, J. Barbosa, A.M.P. Pinto, Grain refinement of Al-Mg-Sc alloy by ultrasonic treatment, Met. Mater. Int. 21 (2015) 72–78. doi:10.1007/s12540-015-1008-6.

[36] A. Das, H.R. Kotadia, Effect of high-intensity ultrasonic irradiation on the modification of solidification microstructure in a Si-rich hypoeutectic Al-Si alloy, Mater. Chem. Phys. 125 (2011) 853–859. doi:10.1016/j.matchemphys.2010.09.035.

[37] G. Wang, M.S. Dargusch, M. Qian, D.G. Eskin, D.H. StJohn, The role of ultrasonic treatment in refining the as-cast grain structure during the solidification of an Al-2Cu alloy, J. Cryst. Growth. 408 (2014) 119–124. doi:10.1016/j.jcrysgro.2014.09.018.

[38] P.K. Ghosh, S. Ray, P.K. Rohatgi, Incorporation aluminium-magnesium of alumina particles alloy by stirring in in melt, Trans. Japan Inst. Met. 25 (1984) 440–444.

[39] P.K. Ghosh, S. Ray, Effect of porosity and alumina content on the high temperature mechanical properties of compocast aluminium alloy-alumina particulate composite, J. Mater. Sci. 22 (1987) 4077–4086. doi:10.1007/BF01133361.

[40] Y. Yang, J. Lan, X. Li, Study on bulk aluminum matrix nano-composite fabricated by

ultrasonic dispersion of nano-sized SiC particles in molten aluminum alloy, Mater. Sci. Eng. A. 380 (2004) 378–383. doi:10.1016/j.msea.2004.03.073.

[41] G. Cao, H. Choi, H. Konishi, S. Kou, R. Lakes, X. Li, Mg-6Zn/1.5%SiC nanocomposites fabricated by ultrasonic cavitation-based solidification processing, J. Mater. Sci. 43 (2008) 5521–5526. doi:10.1007/s10853-008-2785-9.

[42] S.C. Tjong, Novel nanoparticle-reinforced metal matrix composites with enhanced mechanical properties, Adv. Eng. Mater. 9 (2007) 639–652. doi:10.1002/adem.200700106.

[43] I.B. Ozsoy, G. Li, H. Choi, H. Zhao, Shape effects on nanoparticle engulfment for metal matrix nanocomposites, J. Cryst. Growth. 422 (2015) 62–68. doi:10.1016/j.jcrysgro.2015.04.025.

[44] J.B. Ferguson, G. Kaptay, B.F. Schultz, P.K. Rohatgi, K. Cho, C.S. Kim, Brownian motion effects on particle pushing and engulfment during solidification in metal-matrix composites, Metall. Mater. Trans. A Phys. Metall. Mater. Sci. 45 (2014) 4635–4645. doi:10.1007/s11661-014-2379-x.

[45] L.Y. Chen, J.Y. Peng, J.Q. Xu, H. Choi, X.C. Li, Achieving uniform distribution and dispersion of a high percentage of nanoparticles in metal matrix nanocomposites by solidification processing, Scr. Mater. 69 (2013) 634–637. doi:10.1016/j.scriptamat.2013.07.016.

[46] X. Li, Y. Yang, X. Cheng, Ultrasonic-assisted fabrication of metal matrix nanocomposites, J. Mater. Sci. 39 (2004) 3211–3212. doi:10.1023/B:JMSC.0000025862.23609.6f.

[47] G. Govender, L. Ivanchev, H. Burger, A. Mulaba, H. Chikwande, Evaluation of HEBM mechanical alloying of Al2O3—356/7075 powder mixture, Open J. Compos. Mater. 2 (2012) 48–53. doi:10.4236/ojcm.2012.22007.

[48] H. Ferkel, B.L. Mordike, Magnesium strengthened by SiC nanoparticles, Mater. Sci. Eng. A. 298 (2001) 193–199. doi:10.1016/S0921-5093(00)01283-1.

[49] J.Q. Xu, L.Y. Chen, H. Choi, X.C. Li, Theoretical study and pathways for nanoparticle capture during solidification of metal melt, J. Phys. Condens. Matter. 24 (2012) 255304. doi:10.1088/0953-8984/24/25/255304.

[50] S.A. Sajjadi, H.R. Ezatpour, H. Beygi, Microstructure and mechanical properties of Al-Al2O3 micro and nano composites fabricated by stir casting, Mater. Sci. Eng. A. 528 (2011) 8765–8771. doi:10.1016/j.msea.2011.08.052.

[51] M. Karbalaei Akbari, H.R. Baharvandi, O. Mirzaee, Fabrication of nano-sized Al2O3 reinforced casting aluminum composite focusing on preparation process of reinforcement powders and evaluation of its properties, Compos. Part B Eng. 55 (2013) 426–432. doi:10.1016/j.compositesb.2013.07.008.

[52] H.R. Ezatpour, S.A. Sajjadi, M.H. Sabzevar, Y. Huang, Investigation of microstructure and mechanical properties of Al6061-nanocomposite fabricated by stir casting, Mater. Des. 55 (2014) 921–928. doi:10.1016/j.matdes.2013.10.060.

[53] S.A. Sajjadi, H.R. Ezatpour, M. Torabi Parizi, Comparison of microstructure and mechanical properties of A356 aluminum alloy/Al2O3 composites fabricated by stir and compo-casting processes, Mater. Des. 34 (2012) 106–111. doi:10.1016/j.matdes.2011.07.037.

[54] H. Su, W. Gao, Z. Feng, Z. Lu, Processing, microstructure and tensile properties of nano-sized Al2O3 particle reinforced aluminum matrix composites, Mater. Des. 36 (2012) 590–596. doi:10.1016/j.matdes.2011.11.064.

[55] D.B. Miracle, Metal matrix composites - From science to technological significance, Compos. Sci. Technol. 65 (2005) 2526–2540. doi:10.1016/j.compscitech.2005.05.027.

[56] K.B. Nie, X.J. Wang, X.S. Hu, L. Xu, K. Wu, M.Y. Zheng, Microstructure and mechanical properties of SiC nanoparticles reinforced magnesium matrix composites fabricated by ultrasonic vibration, Mater. Sci. Eng. A. 528 (2011) 5278–5282. doi:10.1016/j.msea.2011.03.061.

[57] J. Lan, Y. Yang, X. Li, Microstructure and microhardness of SiC nanoparticles reinforced magnesium composites fabricated by ultrasonic method, Mater. Sci. Eng. A. 386 (2004) 284–290. doi:10.1016/j.msea.2004.07.024.

[58] S. Song, X. Zhou, L. Li, W. Ma, Numerical simulation and experimental validation of SiC nanoparticle distribution in magnesium melts during ultrasonic cavitation based processing of magnesium matrix nanocomposites, Ultrason. Sonochem. 24 (2015) 43–54. doi:10.1016/j.ultsonch.2014.12.010.

[59] M. Qian, A. Ramirez, A. Das, D.H. Stjohn, The effect of solute on ultrasonic grain refinement of magnesium alloys, J. Cryst. Growth. 312 (2010) 2267–2272. doi:10.1016/j.jcrysgro.2010.04.035.

[60] K. Raju, S.N. Ojha, Effect of spray forming on the microstructure and wear properties of Al – Si alloys, Procedia Mater. Sci. 5 (2014) 345–354. doi:10.1016/j.mspro.2014.07.276.

[61] S.K. Shaha, F. Czerwinski, W. Kasprzak, J. Friedman, D.L. Chen, Effect of solidification rate and loading mode on deformation behavior of cast Al-Si-Cu-Mg alloy with additions of transition metals, Mater. Sci. Eng. A. 636 (2015) 361–372. doi:10.1016/j.msea.2015.03.077.

[62] S. Jia, L. Nastac, The influence of ultrasonic stirring on the solidification microstructure and mechanical properties of A356 alloy, Chem. Mater. Eng. 1 (2013) 69–73. doi:10.13189/cme.2013.010301.

[63] L. Lu, A.K. Dahle, D.H. Stjohn, Grain refinement efficiency and mechanism of aluminium carbide in Mg-Al alloys, Scr. Mater. 53 (2005) 517–522. doi:10.1016/j.scriptamat.2005.05.008.

[64] Y.C. Lee, a. K. Dahle, D.H. StJohn, The role of solute in grain refinement of magnesium, Metall. Mater. Trans. A. 31 (2000) 2895–2906. doi:10.1007/BF02830349.

[65] D. Kurz, W and Fisher, Fundamentals of solidification (3rd edition), Trans Tech Publications, Switzerland, 1980.

[66] Porter D.A and Easterling K.E, Phase transformations in metals and alloys, Springer-Science+Business Media, B.V., 1992.

[67] E. Fras, K. Wiencek, M. Gorny, H. Lopez, Theoretical model for heterogeneous nucleation of grains during solidification, Mater. Sci. Technol. 19 (2003) 1653–1660. doi:10.1179/026708303225004585.

[68] J. Wannasin, R. Canyook, S. Wisutmethangoon, M.C. Flemings, Grain refinement behavior of an aluminum alloy by inoculation and dynamic nucleation, Acta Mater. 61 (2013) 3897–3903. doi:10.1016/j.actamat.2013.03.029.

[69] M.A. Easton, D.H. Stjohn, A model of grain refinement incorporating alloy constitution and potency of heterogeneous nucleant particles, Acta Mater. 49 (2001) 1867–1878. doi:10.1016/S1359-6454(00)00368-2.

[70] D.H. StJohn, A. Prasad, M.A. Easton, M. Qian, The contribution of constitutional supercooling to nucleation and grain formation, Metall. Mater. Trans. A Phys. Metall. Mater. Sci. 46 (2015) 4868–4885. doi:10.1007/s11661-015-2960-y.

[71] W.A. Tiller, K.A. Jackson, J.W. Rutter, B. Chalmers, The redistribution of solute atoms during the solidification of metals, Acta Metall. 1 (1953) 428–437. doi:10.1016/0001-6160(53)90126-6.

[72] J.A. Spittle, S. Sadli, Effect of alloy variables on grain refinement of binary aluminium alloys with Al–Ti–B, Mater. Sci. Technol. 11 (1995) 533–537. doi:10.1179/026708395790165273.

[73] I. Maxwell, A. Hellawell, A simple model for grain refinement during solidification, Acta Metall. 23 (1975) 229–237. doi:10.1016/0001-6160(75)90188-1.

[74] M.A. Easton, D.H. Stjohn, Grain refinement of aluminum alloys : Part I . The nucleant and solute paradigms — A review of the literature, Metall. Mater. Trans. A. 30 (1999) 1613–1623. doi:10.1007/s11661-999-0098-5.

[75] J.D. Hunt, Steady state columnar and equiaxed growth of dendrites and eutectic, Mater. Sci. Eng. 65 (1984) 75–83. doi:10.1016/0025-5416(84)90201-5.

[76] G. Chai, L. Backerud, L. Arnberg, Relation between grain size and coherency paralmeters in aluminium alloys, Mater. Sci. Technol. 11 (1995) 1099–1103.

[77] P. Desnain, Y. Fautrelle, J.L. Meyer, J.P. Riquet, F. Durand, Prediction of equiaxed grain density in multicomponent alloys, stirred electromagnetically, Acta Metall. Mater. 38 (1990) 1513–1523. doi:10.1016/0956-7151(90)90119-2.

[78] D.H. StJohn, M. Qian, M.A. Easton, P. Cao, Z. Hildebrand, Grain refinement of magnesium alloys, Metall. Mater. Trans. A Phys. Metall. Mater. Sci. 36 (2005) 1669–1679. doi:10.1007/s11661-005-0030-6.

[79] M. Qian, P. Cao, M.A. Easton, S.D. McDonald, D.H. StJohn, An analytical model for constitutional supercooling-driven grain formation and grain size prediction, Acta Mater. 58 (2010) 3262–3270. doi:10.1016/j.actamat.2010.01.052.

[80] D.H. Stjohn, P. Cao, M. Qian, M.A. Easton, A new analytical approach to reveal the

mechanisms of grain refinement, Adv. Eng. Mater. 9 (2007) 739–746. doi:10.1002/adem.200700157.

[81] M. Easton, D. St John, An analysis of the relationship between grain size, solute content, and the potency and number density of nucleant particles, Metall. Mater. Trans. A Phys. Metall. Mater. Sci. 36 (2005) 1911–1920. doi:10.1007/s11661-005-0054-y.

[82] A. Ramirez, M. Qian, B. Davis, T. Wilks, High-intensity ultrasonic grain refinement of magnesium alloys: role of solute, Int. J. Cast Met. Res. 22 (2009) 260–263. doi:10.1179/136404609X367894.

[83] D.G. McCartney, Grain refining of aluminium and its alloys using inoculants, Int. Mater. Rev. 34 (1989) 247–260. doi:10.1179/imr.1989.34.1.247.

[84] M.A. Martinez-Villalobos, I.A. Figueroa, M.A. Suarez, G.A.L. Rodriguez, O.N. Peralta, G.G. Reyes, I.A. Lopez, J. V Martinez, C.D. Trujillo, Microstructural evolution of rapid solidified Al-Ni alloys, J. Mex. Chem. Soc. 60 (2016) 67–72.

[85] A.N. Turchin, D.G. Eskin, L. Katgerman, Effect of melt flow on macro- and microstructure evolution during solidification of an Al-4.5% Cu alloy, Mater. Sci. Eng. A. 413–414 (2005) 98–104. doi:10.1016/j.msea.2005.09.020.

[86] A.S. Chaus, E.I. Marukovich, M. Sahul, Microstructure and properties of secondary Al-12%Si alloy rapidly quenched from the melt, J. Mater. Eng. Perform. 25 (2016) 4776–4784. doi:10.1007/s11665-016-2367-y.

[87] D. Eskin, Q. Du, D. Ruvalcaba, L. Katgerman, Experimental study of structure formation in binary Al-Cu alloys at different cooling rates, Mater. Sci. Eng. A. 405 (2005) 1–10. doi:10.1016/j.msea.2005.05.105.

[88] R. Haghayeghi, E.J. Zoqui, D.G. Eskin, H. Bahai, Grain refinement of an Al-10% Mg alloy by intensive shearing in the liquid state, J. Alloys Compd. 485 (2009) 807–811. doi:10.1016/j.jallcom.2009.06.085.

[89] H.T. Li, Y. Wang, Z. Fan, Mechanisms of enhanced heterogeneous nucleation during solidification in binary Al-Mg alloys, Acta Mater. 60 (2012) 1528–1537. doi:10.1016/j.actamat.2011.11.044.

[90] B. Silva, I. Araujo, W. Silva, P. Goulart, A. Garcia, J. Spinelli, Correlation between dendrite arm spacing and microhardness during unsteady-state directional solidification of Al-Ni alloys, Philos. Mag. Lett. 91 (2011) 337–343. doi:10.1080/09500839.2011.559911.

[91] V.C. Srivastava, G.B. Rudrakshi, V. Uhlenwinkel, S.N. Ojha, Wear characteristics of spray formed Al-alloys and their composites, J. Mater. Sci. 44 (2009) 2288–2299. doi:10.1007/s10853-008-2924-3.

[92] K. Raju, A.P. Harsha, S.N. Ojha, Evolution of microstructure and its effect on wear and mechanical properties of spray cast Al-12Si alloy, Mater. Sci. Eng. A. 528 (2011) 7723–7728. doi:10.1016/j.msea.2011.06.078.

[93] V. Abramov, O. Abramov, V. Bulgakov, F. Sommer, Solidification of aluminium alloys

under ultrasonic irradiation using water-cooled resonator, Mater. Lett. 37 (1998) 27–34. doi:10.1016/S0167-577X(98)00064-0.

[94] T.V. Atamanenko, D.G. Eskin, L. Katgerman, Experimental study of grain growth in aluminium melts under the influence of ultrasonic melt treatment, Mater. Sci. Forum. 561–565 (2007) 987–990. doi:10.4028/www.scientific.net/MSF.561-565.987.

[95] T. V. Atamanenko, D.G. Eskin, L. Katgerman, Temperature effects in aluminium melts due to cavitation induced by high power ultrasound, Int. J. Cast Met. Res. 22 (2009) 26–29. doi:10.1179/136404609X367254.

[96] J.-G. Jung, J.-M. Lee, Y.-H. Cho, W.-H. Yoon, Combined effects of ultrasonic melt treatment, Si addition and solution treatment on the microstructure and tensile properties of multicomponent Al-Si alloys, J. Alloys Compd. 693 (2017) 201–210. doi:10.1016/j.jallcom.2016.11.305.

[97] J. Ferguson, B. Schultz, K. Cho, P. Rohatgi, Correlation vs. Causation: The effects of ultrasonic melt treatment on cast metal grain size, Metals (Basel). 4 (2014) 477–489. doi:10.3390/met4040477.

[98] Y. Fukui, Y. Tsunekawa, M. Okumiya, Nucleation with collapse of acoustic cavitation in molten Al-Si alloys, Adv. Mater. Res. 89–91 (2010) 190–195. doi:10.4028/www.scientific.net/AMR.89-91.190.

[99] X. Jian, T.T. Meek, Q. Han, Refinement of eutectic silicon phase of aluminum A356 alloy using high-intensity ultrasonic vibration, Scr. Mater. 54 (2006) 893–896. doi:10.1016/j.scriptamat.2005.11.004.

[100] R. Jiang, X. Li, P. Chen, R. Li, X. Zhang, Effect and kinetic mechanism of ultrasonic vibration on solidification of 7050 aluminum alloy, AIP Adv. 4 (2014) 0–9. doi:10.1063/1.4891035.

[101] R.P. Jiang, X.Q. Li, M. Zhang, Investigation on the mechanism of grain refinement in aluminum alloy solidified under ultrasonic vibration, Met. Mater. Int. 21 (2015) 104–108. doi:10.1007/s12540-015-1012-x.

[102] W. Khalifa, Y. Tsunekawa, M. Okumiya, Effect of ultrasonic melt-treatment on the eutectic silicon and iron intermetallic phases in Al-Si cast alloys, Mater. Sci. Forum. 642 (2010) 431–436. doi:10.4028/www.scientific.net/MSF.638-642.431.

[103] W. Khalifa, Y. Tsunekawa, M. Okumiya, Ultrasonic grain refining effects in A356 Al-Si cast alloy, in: AFS Trans., 2010: pp. 1–8.

[104] W. Khalifa, Microstructure modification of Al-4.5%Mg alloy using ultrasonic treatment, in: World Foundry Organ., Bilbao, 2014.

[105] J.-W. LI, T. Momono, Y. FU, Z. JIA, Y. Tayu, Effect of ultrasonic stirring on temperature distribution and grain refinement in Al-1.65%Si alloy melt, Trans. Nonferrous Met. Soc. China. 17 (2007) 691–697. doi:10.1016/S1003-6326(07)60158-7.

[106] Y.L. Li, H.K. Feng, F.R. Cao, Y.B. Chen, L.Y. Gong, Effect of high density ultrasonic on the microstructure and refining property of Al-5Ti-0.25C grain refiner alloy, Mater. Sci.

Eng. A. 487 (2008) 518–523. doi:10.1016/j.msea.2007.11.067.

[107] K. Matsuda, T. Takehara, M. Yang, H. Uno, T. Kubo, G. Miyano, M. Yoshida, Verification of the mechanism of grain refinement by ultrasonic treatment of aluminum-4 wt pct silicon molten alloy, Metall. Mater. Trans. A. 47 (2016) 2509–2516. doi:10.1007/s11661-016-3377-y.

[108] H. Puga, J. Barbosa, S. Costa, S. Ribeiro, A.M.P. Pinto, M. Prokic, Influence of indirect ultrasonic vibration on the microstructure and mechanical behavior of Al-Si-Cu alloy, Mater. Sci. Eng. A. 560 (2013) 589–595. doi:10.1016/j.msea.2012.09.106.

[109] S.R. Yu, H.K. Feng, Y.L. Li, L.Y. Gong, Study on the properties of Al-23%Si alloy treated by ultrasonic wave, J. Alloys Compd. 484 (2009) 360–364. doi:10.1016/j.jallcom.2009.04.104.

[110] L. Zhang, D.G. Eskin, L. Katgerman, Influence of ultrasonic melt treatment on the formation of primary intermetallics and related grain refinement in aluminum alloys, J. Mater. Sci. 46 (2011) 5252–5259. doi:10.1007/s10853-011-5463-2.

[111] L. Zhang, D.G. Eskin, A. Miroux, L. Katgerman, Formation of microstructure in Al-Si alloys under ultrasonic melt treatment, in: Light Met. 2012, 2012: pp. 18–21.

[112] L. Zhang, D.G. Eskin, a G. Miroux, L. Katgerman, On the mechanism of the formation of primary intermetallics under ultrasonic melt treatment in an Al-Zr-Ti alloy, IOP Conf. Ser. Mater. Sci. Eng. 27 (2012) 12002. doi:10.1088/1757-899X/27/1/012002.

[113] S. Zhang, Y. Zhao, X. Cheng, G. Chen, Q. Dai, High-energy ultrasonic field effects on the microstructure and mechanical behaviors of A356 alloy, J. Alloys Compd. 470 (2009) 168–172. doi:10.1016/j.jallcom.2008.02.091.

[114] S.C. Sharma, A. Ramesh, Effect of heat treatment on mechanical properties of particulate reinforced Al6061 composites, J. Mater. Eng. Perform. 9 (2000) 557–561.

[115] S. Jia, D. Zhang, Y. Xuan, L. Nastac, An experimental and modeling investigation of aluminum-based alloys and nanocomposites processed by ultrasonic cavitation processing, Appl. Acoust. 103 (2016) 226–231. doi:10.1016/j.apacoust.2015.07.016.

[116] R. Harichandran, N. Selvakumar, Effect of nano/micro B4C particles on the mechanical properties of aluminium metal matrix composites fabricated by ultrasonic cavitation-assisted solidification process, Arch. Civ. Mech. Eng. 16 (2016) 147–158. doi:10.1016/j.acme.2015.07.001.

[117] I. Mobasherpour, A.A. Tofigh, M. Ebrahimi, Effect of nano-size Al2O3 reinforcement on the mechanical behavior of synthesis 7075 aluminum alloy composites by mechanical alloying, Mater. Chem. Phys. 138 (2013) 535–541. doi:10.1016/j.matchemphys.2012.12.015.

[118] I. Narasimha Murthy, D. Venkata Rao, J. Babu Rao, Microstructure and mechanical properties of aluminum-fly ash nano composites made by ultrasonic method, Mater. Des. 35 (2012) 55–65. doi:10.1016/j.matdes.2011.10.019.

[119] X. Li, Y. Yang, D. Weiss, Theoretical and experimental study on ultrasonic dispersion of

nanoparticles for strengthening cast Aluminum Alloy A356, Metall. Sci. Technol. 26 (2008).

[120] X. Li, Y. Yang, D. Weiss, Ultrasonic cavitation based dispersion of nanoparticles in aluminum melts for solidification processing of bulk aluminum matrix nanocomposite: Theoretical study, fabrication and characterization, in: AFS Trans., Schaumburg, IL USA, 2007: pp. 1–12.

[121] X.J. Wang, N.Z. Wang, L.Y. Wang, X.S. Hu, K. Wu, Y.Q. Wang, Y.D. Huang, Processing, microstructure and mechanical properties of micro-SiC particles reinforced magnesium matrix composites fabricated by stir casting assisted by ultrasonic treatment processing, Mater. Des. 57 (2014) 638–645. doi:10.1016/j.matdes.2014.01.022.

[122] P.K. Ghosh, S. Ray, Influence of annealing on the mechanical properties of compocast Al(Mg) -Al203 particulate composite, J. Mater. Sci. 28 (1993) 3783–3788.

[123] S.T. Kumaran, M. Uthayakumar, A. Slota, S. Aravindan, J. Zajac, Machining behavior of AA6351– SiC–B4C hybrid composites fabricated by stir casting method, Part. Sci. Technol. 34 (2016) 586–592. doi:10.1080/02726351.2015.1093050.

[124] S.T. Kumaran, M. Uthayakumar, S. Aravindan, S. Rajesh, Dry sliding wear behavior of SiC and B4C-reinforced AA6351 metal matrix composite produced by stir casting process, J. Mater. Des. Appl. 230 (2016) 484–491. doi:10.1177/1464420715579302.

[125] R. Yamanoglu, E. Karakulak, A. Zeren, M. Zeren, Effect of heat treatment on the tribological properties of Al-Cu-Mg/nanoSiC composites, Mater. Des. 49 (2013) 820–825. doi:10.1016/j.matdes.2013.02.026.

[126] W.A. Uju, I.N.A. Oguocha, A study of thermal expansion of Al–Mg alloy composites containing fly ash, Mater. Des. 33 (2012) 503–509. doi:10.1016/j.matdes.2011.04.056.

[127] K.K. Alaneme, A.O. Aluko, Fracture toughness (K1C) and tensile properties of as-cast and age-hardened aluminium (6063)-silicon carbide particulate composites, Sci. Iran. Transcations A Civ. Eng. 19 (2012) 992–996. doi:10.1016/j.scient.2012.06.001.

[128] K.B. Khan, T.R.G. Kutty, M.K. Surappa, Hot hardness and indentation creep study on Al-5% Mg alloy matrix-B4C particle reinforced composites, Mater. Sci. Eng. A. 427 (2006) 76–82. doi:10.1016/j.msea.2006.04.015.

[129] S. Ozden, R. Ekici, F. Nair, Investigation of impact behaviour of aluminium based SiC particle reinforced metal-matrix composites, Compos. Part A Appl. Sci. Manuf. 38 (2007) 484–494. doi:10.1016/j.compositesa.2006.02.026.

[130] O. Yılmaz, S. Buytoz, Abrasive wear of Al2O3-reinforced aluminium-based MMCs, Compos. Sci. Technol. 61 (2001) 2381–2392.

[131] A. Baradeswaran, A. Elaya Perumal, Influence of B4C on the tribological and mechanical properties of Al 7075-B4C composites, Compos. Part B Eng. 54 (2013) 146–152. doi:10.1016/j.compositesb.2013.05.012.

[132] Y. Li, T.G. Langdon, Creep behavior of a reinforced Al-7005 alloy: impications for the creep process in metal matrix composite, Acta Mater. 46 (1998) 1143–155.

[133] A. Mazahery, M.O. Shabani, Characterization of cast A356 alloy reinforced with nano SiC composites, Trans. Nonferrous Met. Soc. China (English Ed. 22 (2012) 275–280. doi:10.1016/S1003-6326(11)61171-0.

[134] Y. Li, T.G. Langdon, Creep behavior of an Al-6061 metal matrix composite reinforced with alumina particulates, Acta Mater. 45 (1997) 4797–4806.

[135] A. El-Sabbagh, M. Soliman, M. Taha, H. Palkowski, Hot rolling behaviour of stir-cast Al 6061 and Al 6082 alloys - SiC fine particulates reinforced composites, J. Mater. Process. Technol. 212 (2012) 497–508. doi:10.1016/j.jmatprotec.2011.10.016.

[136] M.M. Benal, H.K. Shivanand, Effects of reinforcements content and ageing durations on wear characteristics of Al (6061) based hybrid composites, Wear. 262 (2007) 759–763. doi:10.1016/j.wear.2006.08.022.

[137] T.S. Srivatsan, Microstructure, tensile properties and fracture behaviour of Al2O3 particulate-reinforced aluminium alloy metal matrix composites, J. Mater. Sci. 31 (1996) 1375–1388.

[138] H.R. Ezatpour, S.A. Sajjadi, M.H. Sabzevar, Y.Z. Huang, An investigation of the tensile and compressive properties of Al6061 and its nanocomposites in as-cast state and in extruded condition, Mater. Sci. Eng. A. 607 (2014) 589–595. doi:10.1016/j.msea.2014.04.036.

[139] K. Mahadevan, K. Raghukandan, B.C. Pai, U.T.S. Pillai, Influence of precipitation hardening parameters on the fatigue strength of AA 6061-SiCp composite, J. Mater. Process. Technol. 198 (2008) 241–247. doi:10.1016/j.jmatprotec.2007.06.075.

[140] S. Mula, S.K. Pabi, C.C. Koch, P. Padhi, S. Ghosh, Workability and mechanical properties of ultrasonically cast Al–Al2O3 nanocomposites, Mater. Sci. Eng. A. 558 (2012) 485–491. doi:10.1016/j.msea.2012.08.032.

[141] S. Mula, P. Padhi, S.C. Panigrahi, S.K. Pabi, S. Ghosh, On structure and mechanical properties of ultrasonically cast Al-2% Al2O3 nanocomposite, Mater. Res. Bull. 44 (2009) 1154–1160. doi:10.1016/j.materresbull.2008.09.040.

[142] K.B. Nie, X.J. Wang, X.S. Hu, L. Xu, K. Wu, M.Y. Zheng, Microstructure and mechanical properties of SiC nanoparticles reinforced magnesium matrix composites fabricated by ultrasonic vibration, Mater. Sci. Eng. A. 528 (2011) 5278–5282. doi:10.1016/j.msea.2011.03.061.

[143] K.B. Nie, X.J. Wang, K. Wu, X.S. Hu, M.Y. Zheng, Development of SiCp/AZ91 magnesium matrix nanocomposites using ultrasonic vibration, Mater. Sci. Eng. A. 540 (2012) 123–129. doi:10.1016/j.msea.2012.01.112.

[144] G. Cao, H. Konishi, X. Li, Mechanical properties and microstructure of SiC-reinforced Mg-(2,4)Al-1Si nanocomposites fabricated by ultrasonic cavitation based solidification processing, Mater. Sci. Eng. A. 486 (2008) 357–362. doi:10.1016/j.msea.2007.09.054.

[145] Y. Xuan, L. Nastac, The role of ultrasonic cavitation in refining the microstructure of aluminum based nanocomposites during the solidification process, Ultrasonics. (2017) 15–17. doi:10.1016/j.ultras.2017.06.023.

[146] K.M. Shorowordi, T. Laoui, A.S.M.A. Haseeb, J.P. Celis, L. Froyen, Microstructure and interface characteristics of B4C, SiC and Al2O3 reinforced Al matrix composites: A comparative study, J. Mater. Process. Technol. 142 (2003) 738–743. doi:10.1016/S0924-0136(03)00815-X.

[147] X. QU, L. Zhang, M. WU, S. Ren, Review of metal matrix composites with high thermal conductivity for thermal management applications, Prog. Nat. Sci. Mater. Int. 21 (2011) 189–197. doi:10.1016/S1002-0071(12)60029-X.

[148] M. Esmaily, N. Mortazavi, J.E. Svensson, M. Halvarsson, M. Wessen, L.G. Johansson, A.E.W. Jarfors, A new semi-solid casting technique for fabricating SiC-reinforced Mg alloys matrix composites, Compos. Part B Eng. 94 (2016) 176–189. doi:10.1016/j.compositesb.2016.02.019.

[149] W.S. Miller, F.J. Humphreys, Strengthening mechanisms in particulate metal matrix composites, Scr. Metall. Mater. 25 (1991) 33–38. doi:10.1016/0956-716X(91)90349-6.

[150] A.M. Redsten, E.M. Klier, A.M. Brown, D.C. Dunan, Mechanical properties and microstructure of cast aluminum, Mater. Sci. Eng. A. 201 (1995) 88–102.

[151] Z. Zhang, D.L. Chen, Contribution of Orowan strengthening effect in particulate-reinforced metal matrix nanocomposites, Mater. Sci. Eng. A. 483–484 (2008) 148–152. doi:10.1016/j.msea.2006.10.184.

[152] M. Habibnejad-Korayem, R. Mahmudi, W.J. Poole, Enhanced properties of Mg-based nano-composites reinforced with Al2O3 nano-particles, Mater. Sci. Eng. A. 519 (2009) 198–203. doi:10.1016/j.msea.2009.05.001.

[153] A. Erman, J. Groza, X. Li, H. Choi, G. Cao, Nanoparticle effects in cast Mg-1wt% SiC nano-composites, Mater. Sci. Eng. A. 558 (2012) 39–43. doi:10.1016/j.msea.2012.07.048.

[154] J.B. Ferguson, F. Sheykh-Jaberi, C.S. Kim, P.K. Rohatgi, K. Cho, On the strength and strain to failure in particle-reinforced magnesium metal-matrix nanocomposites (Mg MMNCs), Mater. Sci. Eng. A. 558 (2012) 193–204. doi:10.1016/j.msea.2012.07.111.

[155] A. Sanaty-Zadeh, Comparison between current models for the strength of particulate-reinforced metal matrix nanocomposites with emphasis on consideration of Hall-Petch effect, Mater. Sci. Eng. A. 531 (2012) 112–118. doi:10.1016/j.msea.2011.10.043.

[156] B.Q. Han, D.C. Dunand, Microstructure and mechanical properties of magnesium containing high volume fractions of yttria dispersoids, Mater. Sci. Eng. A277. 277 (2000) 297–304. doi:10.1016/S0921-5093(99)00074-X.

[157] C.S. Kim, I. Sohn, M. Nezafati, J.B. Ferguson, B.F. Schultz, Z. Bajestani-Gohari, P.K. Rohatgi, K. Cho, Prediction models for the yield strength of particle-reinforced unimodal pure magnesium (Mg) metal matrix nanocomposites (MMNCs), J. Mater. Sci. 48 (2013) 4191–4204. doi:10.1007/s10853-013-7232-x.

[158] M. Wang, D. Chen, Z. Chen, Y. Wu, F. Wang, N. Ma, H. Wang, Mechanical properties of in-situ TiB2/A356 composites, Mater. Sci. Eng. A. 590 (2014) 246–254. doi:10.1016/j.msea.2013.10.021.

[159] Z. Szaraz, Z. Trojanova, M. Cabbibo, E. Evangelista, Strengthening in a WE54 magnesium alloy containing SiC particles, Mater. Sci. Eng. A. 462 (2007) 225–229. doi:10.1016/j.msea.2006.01.182.

[160] R. Zheng, J. Chen, Y. Zhang, K. Ameyama, C. Ma, Fabrication and characterization of hybrid structured Al alloy matrix composites reinforced by high volume fraction of B4C particles, Mater. Sci. Eng. A. 601 (2014) 20–28. doi:10.1016/j.msea.2014.02.032.

[161] D. Zhang, L. Nastac, Numerical modeling of the dispersion of ceramic nanoparticles during ultrasonic processing of aluminum-based nanocomposites, J. Mater. Res. Technol. 3 (2014) 296–302. doi:10.1016/j.jmrt.2014.09.001.

[162] G.M. Swallowe, J.E. Field, C.S. Rees, A. Duckworth, A photographic study of the effect of ultrasound on solidification, Acta Metall. 37 (1989) 961–967.

[163] O. V. Abramov, Action of high intensity ultrasound on solidifying metal, Ultrasonics. 25 (1987) 73–82. doi:10.1016/0041-624X(87)90063-1.

[164] G. Cao, H. Konishi, X. Li, Recent developments on ultrasonic cavitation based solidification processlng of bulk magnesium nanocomposites, Int. J. Met. 2 (2008) 57–65.

[165] I. Tzanakis, G.S.B. Lebon, D.G. Eskin, K. Pericleous, Effect of input power and temperature on the cavitation intensity during the ultrasonic treatment of molten aluminium, Trans. Indian Inst. Met. 68 (2015) 1023–1026. doi:10.1007/s12666-015-0639-0.

[166] H. Dieringa, Properties of magnesium alloys reinforced with nanoparticles and carbon nanotubes: A review, J. Mater. Sci. 46 (2011) 289–306. doi:10.1007/s10853-010-5010-6.

[167] F. Wang, D. Eskin, T. Connolley, J. Mi, Effect of ultrasonic melt treatment on the refinement of primary Al3Ti intermetallic in an Al-0.4Ti alloy, J. Cryst. Growth. 435 (2016) 24–30. doi:10.1016/j.jcrysgro.2015.11.034.

[168] M. Technologies, Influence of indirect ultrasonic vibration on the microstructure and mechanical behavior of Al-Si-Cu alloy H. Puga, J. Barbosa, S. Costa, S. Ribeiro, A.M.P.Pinto, M. Prokic, (n.d.).

[169] T. Leong, M. Ashokkumar, K. Sandra, The fundamentals of power ultrasound - A review, Acoust. Aust. 39 (2011) 54–63. doi:ISSN 0814-6039.

[170] M. Qian, A. Ramirez, A. Das, Ultrasonic refinement of magnesium by cavitation: Clarifying the role of wall crystals, J. Cryst. Growth. 311 (2009) 3708–3715. doi:10.1016/j.jcrysgro.2009.04.036.

[171] J.D. Hunt, K.A. Jackson, Nucleation of solid in an undercooled liquid by cavitation, J. Appl. Phys. 37 (1966) 254–257. doi:10.1063/1.1707821.

[172] L. Nastac, Modeling and simulation of microstructure evolution in solidifying alloys, Kluwer Academic Publishers, 2004.

[173] H. Xu, X. Jian, T.T. Meek, Q. Han, Degassing of molten aluminum A356 alloy using ultrasonic vibration, Mater. Lett. 58 (2004) 3669–3673. doi:10.1016/j.matlet.2004.02.055.

[174] N. Alba-Baena, T. Pabel, N. Villa-Sierra, D.G. Eskin, Effect of ultrasonic melt treatment on degassing and structure of aluminium alloys, Mater. Sci. Forum. 765 (2013) 271–275. doi:10.4028/www.scientific.net/MSF.765.271.

[175] D. Eskin, Kinetics of ultrasonic degassing of aluminum alloys, Light Met. 2013. (2013) 957–962. doi:10.4028/www.scientific.net/MSF.783-786.155.

[176] R. Haghayeghi, H. Bahai, P. Kapranos, Effect of ultrasonic argon degassing on dissolved hydrogen in aluminium alloy, Mater. Lett. 82 (2012) 230–232. doi:10.1016/j.matlet.2012.05.112.

[177] H. Puga, J. Barbosa, E. Seabra, S. Ribeiro, M. Prokic, The influence of processing parameters on the ultrasonic degassing of molten AlSi9Cu3 aluminium alloy, Mater. Lett. 63 (2009) 806–808. doi:10.1016/j.matlet.2009.01.009.

[178] G.I. Eskin, Broad prospects for commercial application of the ultrasonic (cavitation) melt treatment of light alloys, Ultrason. Sonochem. 8 (2001) 319–325. doi:10.1016/S1350-4177(00)00074-2.

[179] W.W. Xu, I. Tzanakis, P. Srirangam, W.U. Mirihanage, D.G. Eskin, A.J. Bodey, P.D. Lee, Synchrotron quantification of ultrasound cavitation and bubble dynamics in Al-10Cu melts, Ultrason. Sonochem. 31 (2016) 355–361. doi:10.1016/j.ultsonch.2016.01.017.

[180] A.R.N. Meidani, M. Hasan, A study of hydrogen bubble growth during ultrasonic degassing of Al-Cu alloy melts, J. Mater. Process. Technol. 147 (2004) 311–320. doi:10.1016/j.jmatprotec.2003.11.012.

[181] G.I. Eskin, Cavitation mechanism of ultrasonic melt degassing, Ultrason. Sonochem. 2 (1995) S137–S141. doi:10.1016/1350-4177(95)00020-7.

[182] ASM Handbook Vol. 3, Alloy Phase Diagrams, 1992.

[183] S.L. Pramod, A.K. Prasada Rao, B.S. Murty, S.R. Bakshi, Effect of Sc addition on the microstructure and wear properties of A356 alloy and A356-TiB2 in situ composite, Mater. Des. 78 (2015) 85–94. doi:10.1016/j.matdes.2015.04.026.

[184] H. Choi, H. Konishi, X. Li, Al2O3 nanoparticles induced simultaneous refinement and modification of primary and eutectic Si particles in hypereutectic Al-20Si alloy, Mater. Sci. Eng. A. 541 (2012) 159–165. doi:10.1016/j.msea.2012.01.131.

[185] H. Ye, An overview of the development of Al-Si-Alloy based material for engine applications, J. Mater. Eng. Perform. 12 (2003) 288–297. doi:10.1361/105994903770343132.

[186] S.L. Pramod, Ravikirana, A.K.P. Rao, B.S. Murty, S.R. Bakshi, Effect of Sc addition and T6 aging treatment on the microstructure modification and mechanical properties of A356 alloy, Mater. Sci. Eng. A. 674 (2016) 438–450. doi:10.1016/j.msea.2016.08.022.

[187] A.P. Kumar, V.M.S. Muthaiah, S. Mula, Effect of Nb, Y and Zr on thermal stability of nanocrystalline Al-4.5 wt.% Cu alloy prepared by mechanical alloying, J. Alloys Compd. 722 (2017) 617–627. doi:10.1016/j.jallcom.2017.06.089.

[188] J. Dziedzic, S. Winczewski, J. Rybicki, Structure and properties of liquid Al-Cu alloys:

Empirical potentials compared, Comput. Mater. Sci. 114 (2016) 219–232. doi:10.1016/j.commatsci.2015.12.014.

[189] M. Zamani, S. Seifeddine, A.E.W. Jarfors, High temperature tensile deformation behavior and failure mechanisms of an Al-Si-Cu-Mg cast alloy -The microstructural scale effect, Mater. Des. 86 (2015) 361–370. doi:10.1016/j.matdes.2015.07.084.

[190] A.E. Al-Rawajfeh, S.M.A. Al Qawabah, Investigation of copper addition on the mechanical properties and corrosion resistance of commercially pure aluminum, Emirates J. Eng. Res. 14 (2009) 47–52.

[191] Y. Fan, M.M. Makhlouf, The effect of introducing the Al-Ni eutectic composition into Al-Zr-V alloys on microstructure and tensile properties, Mater. Sci. Eng. A. 654 (2016) 228–235. doi:10.1016/j.msea.2015.12.044.

[192] W.R. Osorio, L.C. Peixoto, M. V. Cante, A. Garcia, Microstructure features affecting mechanical properties and corrosion behavior of a hypoeutectic Al-Ni alloy, Mater. Des. 31 (2010) 4485–4489. doi:10.1016/j.matdes.2010.04.045.

[193] S. Shankar, Y.W. Riddle, M.M. Makhlouf, Nucleation mechanism of the eutectic phases in aluminum-silicon hypoeutectic alloys, Acta Mater. 52 (2004) 4447–4460. doi:10.1016/j.actamat.2004.05.045.

[194] Q. Du, D.G. Eskin, A. Jacot, L. Katgerman, Two-dimensional modelling and experimental study on microsegregation during solidification of an Al-Cu binary alloy, Acta Mater. 55 (2007) 1523–1532. doi:10.1016/j.actamat.2006.10.035.

[195] M. Qian, A. Ramirez, An approach to assessing ultrasonic attenuation in molten magnesium alloys, J. Appl. Phys. 105 (2009). doi:10.1063/1.3054374.

[196] A. Radjai, K. Miwa, Structural refinement of gray iron by electromagnetic vibrations, Metall. Mater. Trans. A. 33 (2002) 3025–3030. doi:10.1007/s11661-002-0287-y.

[197] A. Ramirez, M. Qian, B. Davis, T. Wilks, D.H. StJohn, Potency of high-intensity ultrasonic treatment for grain refinement of magnesium alloys, Scr. Mater. 59 (2008) 19–22. doi:10.1016/j.scriptamat.2008.02.017.

[198] J.I.I. Youn, Y.J. Kim, Nucleation enhancement of al alloys by high intensity ultrasound, Jpn. J. Appl. Phys. 48 (2009). doi:10.1143/JJAP.48.07GM14.

[199] D.H. StJohn, M.A. Easton, M. Qian, J.A. Taylor, Grain refinement of magnesium alloys: A review of recent research, theoretical developments, and their application, Metall. Mater. Trans. A. 44 (2013) 2935–2949. doi:10.1007/s11661-012-1513-x.

[200] R. Schmid-Fetzer, A. Kozlov, Thermodynamic aspects of grain growth restriction in multicomponent alloy solidification, Acta Mater. 59 (2011) 6133–6144. doi:10.1016/j.actamat.2011.06.026.

[201] H. Xu, L.D. Xu, S.J. Zhang, Q. Han, Effect of the alloy composition on the grain refinement of aluminum alloys, Scr. Mater. 54 (2006) 2191–2196. doi:10.1016/j.scriptamat.2006.02.035.

[202] L.A. Tarshis, J.L. Walker, J.W. Rutter, Experiments on the solidification structure of alloy

castings, Metall. Trans. 2 (1971) 2589–2597. doi:10.1007/BF02814899.

[203] M. Abdel-Reihim, N. Hess, W. Reif, M.E.J. Birch, Effect of solute content on the grain refinement of binary alloys, J. Mater. Sci. 22 (1987) 213–218. doi:10.1007/BF01160574.

[204] H. Men, Z. Fan, Effects of solute content on grain refinement in an isothermal melt, Acta Mater. 59 (2011) 2704–2712. doi:10.1016/j.actamat.2011.01.008.

[205] X. Yang, J. Yi, S. Ni, Y. Du, M. Song, Microstructural evolution and structure-hardness relationship in an Al-4wt.%Mg alloy processed by high-pressure torsion, J. Mater. Eng. Perform. 25 (2016) 1909–1915. doi:10.1007/s11665-016-2044-1.

[206] E. Cadirli, A. Aker, Y. Kaygisiz, M. Sahin, Influences of growth velocity and Fe content on microstructure, microhardness and tensile properties of directionally solidified Al-1.9Mn-xFe ternary alloys, Mater. Res. 20 (2017) 801–813. doi:10.1590/1980-5373-MR-2017-0048.

[207] G.I. Eskin, D.G. Eskin, Some control mechanisms of spatial solidification in light alloys, Z. Met. 95 (2004) 682–690.

[208] K. Kocatepe, Effect of low frequency vibration on porosity of LM25 and LM6 alloys, Mater. Des. 28 (2007) 1767–1775. doi:10.1016/j.matdes.2006.05.004.

[209] M. V. Cante, J.E. Spinelli, N. Cheung, A. Garcia, The correlation between dendritic microstructure and mechanical properties of directionally solidified hypoeutectic Al-Ni alloys, Met. Mater. Int. 16 (2010) 39–49. doi:10.1007/s12540-010-0039-2.

[210] S. Engin, U. Buyuk, N. Marasli, The effects of microstructure and growth rate on microhardness, tensile strength, and electrical resistivity for directionally solidified Al-Ni-Fe alloys, J. Alloys Compd. 660 (2016) 23–31. doi:10.1016/j.jallcom.2015.11.080.

[211] G.I. Eskin, D.G. Eskin, Production of natural and synthesized aluminum-based composite materials with the aid of ultrasonic (cavitation) treatment of the melt, Ultrason. Sonochem. 10 (2003) 297–301. doi:10.1016/S1350-4177(02)00158-X.

[212] G.E. Dieter, Mechanical Metallurgy, McGraw Hill Book Inc, U.S.A., 1986.

[213] X. Li, Q. Cai, B. Zhao, Y. Xiao, B. Li, Effect of nano TiN/Ti refiner addition content on the microstructure and properties of as-cast Al-Zn-Mg-Cu alloy, J. Alloys Compd. 675 (2016) 201–210. doi:10.1016/j.jallcom.2016.03.091.

[214] S. Tahamtan, A. Fadavi Boostani, Microstructural characteristics of thixoforged A356 alloy in mushy state, Trans. Nonferrous Met. Soc. China. 20 (2010) s781–s787. doi:10.1016/S1003-6326(10)60581-X.

[215] H. Abdizadeh, M.A. Baghchesara, Investigation on mechanical properties and fracture behavior of A356 aluminum alloy based ZrO2 particle reinforced metal-matrix composites, Ceram. Int. 39 (2013) 2045–2050. doi:10.1016/j.ceramint.2012.08.057.

[216] M. Gupta, S. Ling, Microstructure and mechanical properties of hypo/hyper-eutectic Al-Si alloys synthesized using a near-net shape forming technique, J. Alloys Compd. 287 (1999) 284–294. doi:10.1016/S0925-8388(99)00062-6.

[217] S.K. Panigrahi, R. Jayaganthan, A study on the mechanical properties of cryorolled Al-Mg-Si alloy, Mater. Sci. Eng. A. 480 (2008) 299–305. doi:10.1016/j.msea.2007.07.024.

[218] G. Chunlei, X. Yongdong, W. Mengjun, Prediction of the flow stress of Al6061 at hot deformation conditions, Mater. Sci. Eng. A. 528 (2011) 4199–4203. doi:10.1016/j.msea.2011.02.004.

[219] G.B.V. Kumar, C.S.P. Rao, N. Selvaraj, M.S. Bhagyashekar, Studies on Al6061-SiC and Al7075-Al2O3 metal matrix composites, J. Miner. Mater. Charact. Eng. 9 (2010) 43–55. doi:10.4236/jmmce.2010.91004.

[220] Y. Yang, Z. Zhang, X. Zhang, Processing map of Al2O3 particulate reinforced Al alloy matrix composites, Mater. Sci. Eng. A. 558 (2012) 112–118. doi:10.1016/j.msea.2012.07.092.

[221] R. Senthilkumar, N. Arunkumar, M. Manzoor Hussian, A comparative study on low cycle fatigue behaviour of nano and micro Al2O3 reinforced AA2014 particulate hybrid composites, Results Phys. 5 (2015) 273–280. doi:10.1016/j.rinp.2015.09.004.

[222] D.. Lloyd, The solidification microstructure of particulate reinforced aluminum/SiC composites., Compos. Sci. Technol. 35 (1989) 159–179.

[223] T.E. Quested, A.T. Dinsdale, A.L. Greer, Thermodynamic modelling of growth-restriction effects in aluminium alloys, Acta Mater. 53 (2005) 1323–1334. doi:10.1016/j.actamat.2004.11.024.

[224] D.G. Eskin, Ultrasonic processing of molten and solidifying aluminium alloys: overview and outlook, Mater. Sci. Technol. 836 (2016) 1–10. doi:10.1080/02670836.2016.1162415.

[225] A. Mitrasinovic, F.C. Robles Hernandez, M. Djurdjevic, J.H. Sokolowski, On-line prediction of the melt hydrogen and casting porosity level in 319 aluminum alloy using thermal analysis, Mater. Sci. Eng. A. 428 (2006) 41–46. doi:10.1016/j.msea.2006.04.084.

[226] D. Casari, T.H. Ludwig, M. Merlin, L. Arnberg, G.L. Garagnani, The effect of Ni and V trace elements on the mechanical properties of A356 aluminium foundry alloy in as-cast and T6 heat treated conditions, Mater. Sci. Eng. A. 610 (2014) 414–426. doi:10.1016/j.msea.2014.05.059.

[227] Qingyou Han, Ultrasonic processing of materials, Metall. Mater. Trans. B. 46B (2015) 1603–1614. doi:10.2172/859314.

[228] H. Xu, T.T. Meek, Q. Han, Effects of ultrasonic field and vacuum on degassing of molten aluminum alloy, Mater. Lett. 61 (2007) 1246–1250. doi:10.1016/j.matlet.2006.07.012.

[229] T. V. Atamanenko, D.G. Eskin, M. Sluiter, L. Katgerman, On the mechanism of grain refinement in Al-Zr-Ti alloys, J. Alloys Compd. 509 (2011) 57–60. doi:10.1016/j.jallcom.2010.09.046.

[230] K.B. Nie, X.J. Wang, K. Wu, X.S. Hu, M.Y. Zheng, L. Xu, Microstructure and tensile properties of micro-SiC particles reinforced magnesium matrix composites produced by semisolid stirring assisted ultrasonic vibration, Mater. Sci. Eng. A. 528 (2011) 8709–8714. doi:10.1016/j.msea.2011.08.035.

[231] G.W. Liu, M.L. Muolo, F. Valenza, A. Passerone, Survey on wetting of SiC by molten metals, Ceram. Int. 36 (2010) 1177–1188. doi:10.1016/j.ceramint.2010.01.001.

[232] X. Liu, Y. Osawa, S. Takamori, T. Mukai, Microstructure and mechanical properties of AZ91 alloy produced with ultrasonic vibration, Mater. Sci. Eng. A. 487 (2008) 120–123. doi:10.1016/j.msea.2007.09.071.

[233] F. Chen, Z. Chen, F. Mao, T. Wang, Z. Cao, TiB2 reinforced aluminum based in situ composites fabricated by stir casting, Mater. Sci. Eng. A. 625 (2015) 357–368. doi:10.1016/j.msea.2014.12.033.

[234] T.S. Srivatsan, M. Al-Hajri, C. Smith, M. Petraroli, The tensile response and fracture behavior of 2009 aluminum alloy metal matrix composite, Mater. Sci. Eng. A. 346 (2003) 91–100. doi:10.1016/S0921-5093(02)00481-1.

[235] S. Scudino, G. Liu, K.G. Prashanth, B. Bartusch, K.B. Surreddi, B.S. Murty, J. Eckert, Mechanical properties of Al-based metal matrix composites reinforced with Zr-based glassy particles produced by powder metallurgy, Acta Mater. 57 (2009) 2029–2039. doi:10.1016/j.actamat.2009.01.010.

[236] S. Jayalakshmi, S. Gupta, S. Sankaranarayanan, S. Sahu, M. Gupta, Structural and mechanical properties of Ni60Nb40 amorphous alloy particle reinforced Al-based composites produced by microwave-assisted rapid sintering, Mater. Sci. Eng. A. 581 (2013) 119–127. doi:10.1016/j.msea.2013.05.072.

[237] D.C. Dunand, A. Mortensen, On plastic relaxation of thermal stresses in reinforced metals, Acta Metall. Mater. 39 (1991) 127–139. doi:10.1016/0956-7151(91)90261-X.

[238] T.W. Clyne, P.J. Withers, An introduction to metal matrix composites, Cambridge University Press, Cambridge, 1993.

[239] D. Hull, T.W. Clyne, An Introduction to Composite Materials, Cambridge University Press, Cambridge, 1996.

[240] H.R. Ezatpour, M.T. Parizi, S.A. Sajjadi, G.R. Ebrahimi, A. Chaichi, Microstructure , mechanical analysis and optimal selection of 7075 aluminum alloy based composite reinforced with alumina nanoparticles, Mater. Chem. Phys. 178 (2016) 119–127. doi:10.1016/j.matchemphys.2016.04.078.

[241] M. Karbalaei Akbari, O. Mirzaee, H.R. Baharvandi, Fabrication and study on mechanical properties and fracture behavior of nanometric Al2O3 particle-reinforced A356 composites focusing on the parameters of vortex method, Mater. Des. 46 (2013) 199–205. doi:10.1016/j.matdes.2012.10.008.

[242] R. Yang, Z. Zhang, Y. Zhao, G. Chen, M. Liu, L. Jiao, L. Chen, Microstructure-property analysis of ZrB2/6061Al hierarchical nanocomposites fabricated by direct melt reaction, Mater. Charact. 112 (2016) 51–59. doi:10.1016/j.matchar.2015.12.012.

[243] K. Ponappa, S. Aravindan, P.V. Rao, Influence of Y2O3 particles on mechanical properties of magnesium and magnesium alloy (AZ91D), J. Compos. Mater. 47 (2012) 1231–1239. doi:10.1177/0021998312446501.

[244] S. Aravindan, P. V Rao, K. Ponappa, Evaluation of physical and mechanical properties of AZ91D / SiC composites by two step stir casting process, J. Magnes. Alloy. 3 (2015) 52–62. doi:10.1016/j.jma.2014.12.008.

[245] M. Shanthi, G.L.X. Xia, M. Gupta, Effect of Mg/nano-Al2O3 interaction time during stirring on microstructure and mechanical properties of Mg–Al2O3 composite, Mater. Sci. Technol. 27 (2011) 1341–1346. doi:10.1179/026708310X12701095964568.

[246] A.F. Boostani, R.T. Mousavian, S. Tahamtan, S. Yazdani, R.A. Khosroshahi, D. Wei, J.Z. Xu, D. Gong, X.M. Zhang, Z.Y. Jiang, Graphene sheets encapsulating SiC nanoparticles: A roadmap towards enhancing tensile ductility of metal matrix composites, Mater. Sci. Eng. A. 648 (2015) 92–103. doi:10.1016/j.msea.2015.09.050.

LIST OF PUBLICATIONS

JOURNAL PAPERS

1. **Neeraj Srivastava**, G.P. Chaudhari, M. Qian "Grain refinement of cast binary Al-Si, Al-Cu and Al-Ni alloys fabricated by ultrasound solidification technique" in **Journal of Materials Processing and Technology,** Vol. 249, pp. 367–378, 2017.
2. **Neeraj Srivastava**, G.P. Chaudhari, "Strengthening in Al alloy nanocomposites fabricated by ultrasound assisted solidification technique", in **Materials Science & Engineering A**, Vol. 651, pp. 241-247, 2016.
3. Neeraj Srivastava, G.P. Chaudhari, Microstructural evolution and mechanical behavior of ultrasonically synthesized Al6061-nano alumina composites, **Materials Science & Engineering A** (Accepted 2018). https://doi.org/10.1016/j.msea.2018.03.092
4. **Neeraj Srivastava,** G.P. Chaudhari, Rahul Gupta, "Effect of solute and high power ultrasound on mechanical properties of Al-Si alloys with different solute concentrations", in Material Science and Engineering: Conference Series - IOP Science, Accepted, 2017.
5. **Neeraj Srivastava**, G.P. Chaudhari, M. Qian, "Grain growth restriction in ultrasonicated binary Al alloys using the Scheil-Gulliver model" (To be communicated).

CONFERENCE ABSTRACTS

1. **Neeraj Srivastava**, Rahul Gupta, G.P. Chaudhari, " Effect of solute and high power ultrasound on mechanical properties of Al-Si alloys with different solute concentrations", in International Conference (ICRAMME, Hyderabad), 2017.
2. **Neeraj Srivastava**, G.P. Chaudhari, "Effect of power ultrasound on solidification of Al-Cu alloys with different solute concentrations", in International Conference (PFAM, IIT ROORKEE), 2014.
3. **Neeraj Srivastava**, G.P. Chaudhari, "Effect of power ultrasound on solidification of Al alloys with different solute concentrations", in Conference (NMD-ATM), 2013.